Beyond whole-cell motion – reactive interpenetrating flow and elliptic Voronoi tessellation in two dimensions

Dissertation
zur
Erlangung des Doktorgrades (Dr. rer. nat.)
der
Mathematisch-Naturwissenschaftlichen Fakultät
der
Rheinischen Friedrich-Wilhelms-Universität Bonn

vorgelegt von

Martin Bock

aus
Kösching

Bonn 2012

Angefertigt mit Genehmigung der
Mathematisch-Naturwissenschaftlichen Fakultät der
Rheinischen Friedrich-Wilhelms-Universität Bonn

1. Gutachter: Prof. Dr. Wolfgang Alt (Theoretische Biologie)
2. Gutachter: Prof. Dr. Rolf Klein (Informatik)

Tag der Promotion: 11.03.2013
Erscheinungsjahr: 2013

Zusammenfassung: Eine wichtige Eigenschaft von höher entwickelten Lebensformen ist ihre Fähigkeit zur Erneuerung des Körpers. Dazu teilen sich Zellen, die mikrometergroßen ,,Atome" des Lebens, und bilden daraufhin spezialisierte Gewebe. In der Haut, aber auch während der Embryogenese, vollführen die Zellen gerichtete Bewegungen, um ihren genetisch vorgesehenen Platz einzunehmen. Nur einige wenige Moleküle bestimmen die relevanten Kraftgesetze zur Zellmigration, nämlich Aktin, Integrin, Cadherin und Myosin.

Die Dynamik des Zytoplasmas innerhalb der Zelle kann durch eine hydrodynamische Kontinuumstheorie beschrieben werden, welche ,,Reactive Interpenetrating Flow" (reaktive, sich durchdringende Strömung) genannt wird. Die zentrale Annahme der Theorie lautet, dass das Zytoplasma im Wesentlichen eine inkompressible Flüssigkeit darstellt, welche aus einer Mischung von Aktin-Netzwerk und wässrigem Zytosol besteht. Dabei werden die Synthese des Aktin-Netzwerks durch Polymerisierung, dessen Transport, sowie der dazwischenliegende Fluß des Zytosols berücksichtigt. In den isotropen Bewegungsgleichungen überwiegen die Rei-

bungskräfte, und es treten sowohl aktive als auch passive Spannungsterme auf. Die passiven Spannungen gründen auf dem Mischungscharakter der Flüssigkeit, und beinhalten den Quelldruck des Netzwerks sowie Reibung aufgrund von Viskosität und der Durchdringung der Komponenten. Die aktiven Spannungen entstehen durch Kontraktionen im Netzwerk, welche von Myosin-Motorproteinen erzeugt werden.

Bezieht man Integrin-Moleküle mit ein, die Adhäsionskräfte zum Substrat vermitteln, so kann man eine eindimensionale Modellzelle konstruieren, welche zwei charakteristische dynamische Zustände einnimmt: 1. im symmetrischen und ruhenden Zustand kompensieren sich die Zugkräfte aus beiden Richtungen, so dass sich die Zelle nicht bewegen kann; 2. im polaren und migrierenden Zustand entsteht eine Assymetrie in den Zugkräften, welche die Zelle antreibt und persistent bewegt. Beide Zustände sind relativ stabil und autonom in dem Sinne dass sie keine Regulierung außerhalb des bestehenden Modells benötigen, etwa wenn man das vordere oder hintere Zellende künstlich vorschreiben würde. Ein vereinfachtes, zwei-dimensionales Zellmodel zeigt charakteristische Korrelationen, wie sie bei Migrationstrajektorien aus Experimenten an menschlichen Hautzellen auftreten.

Die Form von wechselwirkenden Einzelzellen innerhalb einer einlagigen Schicht läßt sich mathematisch durch eine neue Art von Voronoi-Diagramm beschreiben, wobei Ellipsen als sogenannte Erzeuger fungieren. Diese Ellipsen werden als Parameter gewählt, und beschreiben Position, bevorzugte Größe und die Orientierung der betrachteten Zellen. Jeder Erzeuger ordnet einem beliebigen Punkt in der Ebene ein gewisses Gewicht zu, nämlich den Quotienten aus dem Abstand Erzeuger-Punkt und dem Radius der Ellipse in diesselbe Richtung. Mit Hilfe der Punktgewichte werden die expliziten Nachbarschaftsbeziehungen sowie die Form der Kontakte zwischen den einzelnen Modellzellen des Voronoi-Diagramms bestimmt. Als Vorgabe für die Erzeugerellipsen läßt sich die Lage von Zellkernen verwenden, etwa wie man sie auf gängigen Fluoreszenzaufnahmen erkennen kann. Das daraus erstellte Voronoi-Diagramm zeichnet die Zell-Zell Kontakte aus dem Experiment nach.

In Gruppen oder im Gewebe vermitteln sogenannte Cadherine auf der Außenseite der Zellmembran die Adhäsionskräfte zwischen den Zellen. Ausgehend vom Voronoi-Diagramm als Modell für die Zellgeometrie werden geeignete Kraftgleichungen aufgestellt, mit denen man die Wechselwirkungen von Zellen in Gruppen quantitativ untersuchen kann. Berücksichtigt man auftetende Variationen in der Zellgröße sowie stochastische Kräfte, so gibt es in kleinen dynamischen Zellgruppen mehrere topologis-

che Möglichkeiten, die Zellen relativ stabil anzuordnen. Die Kohäsion des Modellgewebes in Bewegung hängt essentiell von der relativen Lamellenbreite der Zellen sowie der Homogenität ihrer Größenverteilung ab. Diese beiden wichtigen Größen sind geometrischer Natur und deswegen mit Hilfe der Phasenkontrastmikroskopie experimentell bestimmbar. Wie es auch an embryonalen Zellextrakten beobachtbar ist, werden die Zellen im Modell langsam in zusammengehörige Gruppen sortiert. Dazu wird der Exprimierungsgrad von Cadherin für beide Zellarten separat eingestellt. Die sogenannte Elongation des Keimbandes während der Entwicklung der *Drosophila*-Fliege erwächst aus der Änderung der topologischen Nachbarschaftsbeziehungen zwischen den Zellen. Bereits kleine Anisotropien in der Interaktionskraft zwischen den Zellen reichen aus, um das Gewebe persistent zu verformen.

Summary: A crucial property of higher-developed living beings is the ability to continuously exchange and renew their body. This is achieved by division and redistribution of cells, the micron-sized and autonomous "atoms" of life. In the skin and during embryogenesis, these cells undergo directed motion to arrive at their native place within dedicated tissue environments. Only few molecular players essentially determine the involved physical force balances, namely actin, integrin, cadherin and myosin.

The intracellular dynamics of actin network polymerisation, transport and the interstitial flow of the aqueous cytosol can be described by a two-component hydrodynamical continuum theory called the Reactive Interpenetrating Flow. The central underlying assumption in this theory is, that the cytoplasm is essentially an incompressible fluid, consisting of the dynamic actin network and the aqueous cytosol. The force balances in the fluid are dominated by friction and involve both active and passive isotropic stresses. Passive stresses arise from the presence of two fluid components, leading to network swelling and friction due to viscosity and fluid permeation. Active stresses in the fluid relate to the presence of myosin motor proteins that induce contractions in the actin network.

Including the adhesion of the cell towards the substrate by means of integrin molecules, one can construct a one-dimensional model cell that exhibits two characteristic dynamical cell states: 1. in the symmetric resting state, traction from front and back balances so that the cell adheres to the substratum without moving, and 2. in the polarized migrating state, an asymmetry in traction drives persistent cell locomotion. These two

steady states are rather stable and autonomous in the sense that they do not need any out-of-model regulation prescribing front and back of the cell. A simplified two-dimensional model exhibits the characteristic correlation features from trajectories of human epidermal keratinocyte cells as determined in experiments.

The shapes of individual interacting cells in a monolayer can be mathematicaly quantified by means of a novel type of Voronoi tessellation, which involves ellipses as so-called generators. These generator ellipses are prescribed and encode the positions of the cells, their preferred size and orientation. To every point in the plane each generator attributes a certain power, given by the center distance divided by the colinear local radius of the ellipse. From these point powers, the proposed Voronoi tessellation constructs explicit neighbor relations and the shape of the cell-cell contacts within groups of model cells. By taking cell nuclei from fluorescence micrographs as model input for the generator ellipses, the resulting Voronoi tesselation is able to recapitulate the corresponding cell-cell contacts as observed simultaneously in the experiment.

Central to cell-cell adhesion in groups and tissue are cadherin receptors on the exterior cell membranes, providing for a force link between cells in contact. Employing the Voronoi tesselation as cell geometry model, one can construct compatible in-tissue force balances and thereby elucidate the interactions of cells in groups. The explicit consideration of size variation and stochastic forces leads to several relatively stable topological cell arrangements in small groups. The cohesion of the model tissue crucially depends on the relative lamella width and the homogeneity of the cell size distribution, both of which are geometric quantities accessible in phase-contrast microscopy. As observed in cell extracts from embryos, the model is able to slowly sort mixed cells into matching groups by attributing differential cadherin expression levels to the individual cells. Finally, the so-called convergent extension during the development of the *Drosophila* fly relies on topological rearrangements induced by only small anisotropies in the cellular interaction force.

Teile dieser Arbeit sind bereits veröffentlicht worden:
Parts of this work have already been published:

- M. Bock, A. K. Tyagi, J.-U. Kreft, and W. Alt. Generalized Voronoi tessellation as a model of two-dimensional cell tissue dynamics. *Bulletin of Mathematical Biology*, 72:1696, 2010.

- W. Alt, M. Bock, and C. Möhl. Coupling of cytoplasm and adhesion dynamics determines cell polarization and locomotion. In A. Chauvière, L. Preziosi, and C. Verdier, editors, *Cell Mechanics: From Single Scale-Based Models to Multiscale Modeling*, pages 86–125. Chapman & Hall / CRC, 2010.

- M. Bock and C. Wollnik. How do biological cells move? *European Communications in Mathematical and Theoretical Biology*, 14:54–69, Oct. 2011.

This work is dedicated to all my teachers.

Contents

1. How do biological cells move?[1]

Summary: Taking a historical perspective, we revisit selected key experiments and methods that have lead to the current understanding of the motion of biological cells. As it turns out, only few molecular players essentially determine the involved physical force balances, namely (i) actin, (ii) myosin, (iii) integrin, and (iv) cadherin. By identifying their function in isolation and mutual cooperation, we put forward a general conceptual framework, which allows for the classification and unification of various cell migration phenomena.

1.1. On microscopes, cells and animalculae

Back in 1665, Robert Hooke (1635–1703)[2] delivered his book "Micrographia" to his contractors, the "Council of the Royal Society of London for Improving of Natural Knowledge" [108]. This groundbreaking work marks the advent of the empirical method – justifying knowledge from repeated observations and measurements. This concept still provides for an essential basis of science today. In this spirit and by his duty as a curator of the scientific devices of the Royal Society, Robert Hooke had been ordered to make "some physiological descriptions of minute bodies made by magnifying glasses with observations and inquiries thereupon" [108]. Hooke presented his findings in 38 schemes, comprising micrographs from cloth to plants, animals, fossils, and even the surface of the moon. In his observation XVIII, "Of the Schematisme or Texture of Cork, and of the Cells and Pores of some other such frothy Bodies" Hooke makes a striking and peculiar observation:[3]

> "[...] I could exceeding plainly perceive it to be all perforated and porous, [...] but that the pores of it were not regular;

[1] With some modifications, this chapter appeared as an article in the European Communications in Mathematical and Theoretical Biology [32]. This article was written jointly by M.B. and Carina Wollnik.

[2] Unless indicated otherwise, all historical dates in this chapter are taken from the book by Ilse Jahn [115]. For a historical perspective specifically on cell mechanics, see [175].

[3] Compare "Schem. XI, Fig: 1" in [108].

> [...] the Interstitia, or walls (as I may so call them) or partitions of those pores were neer as thin in proportion to their pores, [...] these pores, or cells, were not very deep, but consisted of a great many little Boxes [...] there were usually about threescore of these small Cells placed end-ways in the eighteenth part of an Inch in length [...]" [108, Observ. XVIII]

Apparently without knowing, Hooke had observed plant cells in their typical box-like structure with enforced walls, thereby laying the foundation to the current notion of *cell* in biology. As we know now, the biological implications of his results have proven their significance in the subsequent centuries.

Another pioneer of early microscopy was Antonie van Leeuwenhoek (1632–1723). Being clothier by profession, he had – despite of being a layman – constructed optical devices allowing a magnification of up to 270 fold. In 1677, he sent a letter to the publisher of the "Philosophical Transactions", the Royal Society's scientific journal. In this letter he reported the observation of little "animulculae" immersed in rain water stored for a few days in a "new earthen pot" [220]. Moreover, the size of some of these *animulculae* was about one thousand times smaller than the eye of a louse[4]. He also described that the *animulculae* use tails and little feets as tool to move about.

By using single spherical lenses of very small diameter, van Leeuwenhoek was able outperform the multi-lens microscopes of contemporary vintage. This is due to the favorable imaging properties of such a simple device: it does not inherit the multiplicative propagation of imaging errors from lens to lens. Indeed, Leeuwenhoek got a glimpse into a new world, for he discovered *protozoa* and *bacteria*. However, the lack of independent observations and the difficulty of integrating empirical observations into a consistent and comprehensive framework prevented a quicker scientific progress: it was not before the 19th century, that van Leeuwenhoek's *animalculae* could be observed with conventional microscopes of two or more lenses.

In 1847, the English translation of a remarkable treatise by the German researcher Theodor Schwann appeared. Schwann opens his preface with:

> "It is one of the essential advantages of the present age, that the bond of union connecting the different branches of natural science is daily becoming more intimate, and it is to the

[4] "Schem. XXXV" in [108].

Figure 1.1.: Cartilage cells from the from the frog *Rana esculenta* (left) and tadpole pigment cells (right) as sketched by Theodor Schwann in [195, Plate II Fig. 8 and Plate II Fig. 1].

> contributions which they reciprocally afford each other that we are indebted for a great portion to the progress which the physical sciences have lately made." [195]

Two years earlier, in 1845, the Royal society had awarded the Copley Medal to Schwann (1810–1882). Together with his colleague Matthias Jakob Schleiden (1804–1881) he laid the foundation to the cell theory, essentially stating that life is made of cells. The anecdote goes that the initial spark to this theory came up when Schwann and Schleiden discussed their microscopical observations during dinner. Coming from the formerly distant fields of physiology and botany, respectively, they found striking coincidences in animals and plants – on the microscopic scale. Apparently there are "elementary particles" in animals that function in several respects like the cells long known in the kingdom of plants. Figure 1.1 shows some original sketches of Schwann from his far reaching work.

1.2. On proteins, muscle and the cytoskeleton

The advances of microscopy during the 19th century – among the most notable being those made by Ernst Karl Abbe (1840–1905) – lead to the development of microscopes working at the fundamental diffraction limit imposed by the wavelength of visual light. In this way, for the first time, researchers were able to observe structures on the micron-scale and slightly below. In particular, the cytoskeleton falls into this 'microscopic' length-scale. The cytoskeleton comprises protein structures that stabilize a cell's form, enable the cell to move and help transporting proteins and organelles inside the cell.

1. Intracellular actin and myosin: Contraction in muscle was one of the first driving force for the study of cytoskeletal structures. Already in 1864, Wilhelm Kühne described a protein called myosin [134]. Later, in 1942, Albert Szent-Györgyi and co-workers found two myosin-proteins called myosin A and myosin B [19], which by now are called myosin and acto-myosin (i.e. actin bound to myosin). Furthermore, they found another protein that was thought to activate myosin and therefore called it actin. It was first described in 1942 by F.B. Straub [203], a co-worker of Szent-Györgyi. Actin, however, had already been purified long before by W.D. Halliburton (1887) [95, 176], when its significance was not yet discovered and it therefore had no name.

As we know by now, actin is a central component of the cytoskeleton: the small actin monomers aggregate into elongated filaments by converting energy stored in ATP[5]. Importantly, filamentous actin is of polar structure, so that a certain quasi-stationary state called *treadmilling* may emerge during polymerization and depolymerization [34]. This state is characterized by the filament polymerization being faster at the plus (barbed) end than at the minus (pointed) end. Thus, the chemical reaction kinetics effectively establish a net transport velocity towards the minus end of the filament, which usually happens to be directed inwards to the cell body.

Along these possibly treadmilling actin filaments, certain types of motor proteins, for example myosin-II (animals) or myosin-V (plants), move and transport vesicles or cell organelles throughout the cytoplasm. In muscle cells one observes a complex called acto-myosin or sarcomer. There, the myosin head regions move along opposite directions of aligned actin filaments, so that tension is created and the whole muscle contracts. In non-muscle cells, actin and myosin play an analogous role and thereby form an integral part of the migration machinery. Specifically, the cellular contraction force is provided by actin and myosin-II interaction [222].

2. Transcellular receptors: Other proteins are responsible for the cell's interaction with its surroundings. There are four distinct families of proteins which connect a cell to its environment, like substrate, extra-cellular matrix, or other cells. These families are:

- the immunoglobulin family of cell adhesion molecules (Ig-CAMs), which are involved in connections to other cells, cell adhesion, signal transduction and regulation of gene expression,

[5]ATP = adenosine triphosphate

- the cadherin family, which is central to cell adhesion and cell-cell contacts,
- the integrin family, which links the cytoskeleton to substrate and activates intracellular signaling pathways,
- the selectin family, which is involved in vascular cell adhesion and signalling,

Here we give further details on two of these families:

(i) Cadherin: The force-bearing connections in cell-cell contacts are mostly formed by a certain family of Ca^{2+} dependent adhesion proteins, the cadherins. The first described member of this family was the E-cadherin. Also known as L-CAM, Warren J. Gallin and co-workers described it as cell adhesion molecule in chicken in 1983 [84], whereas Reinhard Schuh and co-workers as uvomorulin in mice in 1986 [194]. The main cadherin types are E-cadherin (epidermal), N-cadherin (neural) and R-cadherin (retinal tissue). All of them are either involved in cell adhesion or cell-cell contacts.

One usually differentiates between classical and proto-cadherins. For cell migration and aggregation, the most important ones are certain classical cadherins, like E- and N-cadherin. They participate in so-called strong cell-cell adhesions [94]. Under normal circumstances, breaking of these strong adhesions occurs only with the help of other molecules, e.g. by means of phosphorylation.

(ii) Integrin: The integrin family provides the most important cellular receptor molecules for connections of a migrating cell to the substrate, and is also involved in transmembrane signaling processes. Integrin was initially described in the 1960s and 1970s as oxypertine, a tranquilizing drug against schizophrenia [12, 162]. Later on, in 1987, Richard O. Hynes introduced the name 'integrin' [112]. Integrins are composed of two chains termed α and β. These chains vary in their composition, giving rise to multiple types of integrins with distinct properties. In mammals there are 24 different kinds of integrins, which are composed of 18 distinct α-subunits and 8 distinct β-subunits [113]. Despite of this compositional variety, all integrins are approximately horseshoe-shaped. The two leg regions extend sideways and join at the prominent "head", where both α- and β-chains are connected.

Integrins can be in either of two conformational states, active or inactive. In the inactive state, the head region faces the cell membrane by bending over towards the leg regions, whereas in the active state the head region is freely accessible. The binding sites for other proteins are situated in the head region, so that the binding affinity is modulated by the integrins' activation state. Usually, most integrins are in the inactive state and have to be activated by divalent cations like Mn^{2+} or by the attachment of certain ligands [185].

Before coming to further details of integrin cooperation, we visit some fairly recent methodological advances.

1.3. On rubber sheets, traction and fluorescence

Modern microscopic techniques provide many possibilities for the visualization of different properties of the objects under study. One perhaps surprising yet very exciting imaging technique allows for the quantification of forces. The basic idea is to measure the deformation of the substrate on which the cell migrates.

1. Soft substrate traction force microscopy: In the 1980s, Harris invented the elastic substrate method, whereby a thin layer of a liquid silicone surface is polymerized [97]. When seeded on such a substrate, a migrating cell causes the surface to wrinkle. Unfortunately the precise mathematical relation of wrinkles and forces is unknown, and the initially assumed proportionality did not yield consistent results. In a next step, in 1994, Lee and co-workers stabilized the substrate by connecting the surface edges to a rigid box [140]. To measure the substrate deformation, silicon beads were added to the polymer sheet. Yet the bulk modulus was quite high, so that the beads would displace only by a very small amount. The breakthrough came in 1997, when Pelham and Wang improved synthesized polyacrylamide substrates [174]. The crosslinker to monomer ratio of polyacrylamids can be freely adjusted so to match the applied forces of different cell types with a suitable substrate stiffness. In 1999, Dembo and Wang used smaller beads and fluorescence to further increase the resolution [63]. By now, traction force microscopy has seen several modifications and refinements. Mutual limitations and benefits are discussed in [187].

2. Micro-needle traction force microscopy: Other groups measured the forces applied by the cell to the substrate by means of micro-needles. Initially, in 1997, Galbraith and Sheetz used small needles to measure forces at adhesion sites [80]. In 2001, Balaban and co-workers invented stress measurement at focal adhesion sites with micro-patterned surfaces [18] and finally in 2003, Tan used arrays of regularly spaced micro-needles, which made the method more precise [209]. When employing this method, care has to be taken that the relation between force and elongation or needle displacement is known precisely.

3. Fluorescing proteins: An important tool to further analyze the cells' cytoskeleton *in-vivo* or *in-vitro* are fluorescent proteins, such as GFP[6]. GFP was first discovered in the jellyfish *Aequorea victoria*, but by now it has been found in several other animals. The first description was given by F.H. Johnson and co-workers in 1962 [119]. As often in science, the true benefit of this discovery has not been identified until much later. The first paper in connection with proteins marked by other fluorescent proteins was written by M. Chalfie and co-workers in 1994 [44]. Already in 2008, the Nobel prize in chemistry was awarded to O. Shimomura, M. Chalfie and R. Y. Tsien for GFP and similar blue and yellow colored fluorescent proteins. Today, a lot of different fluorescence protein constructs are available in various different colors, acting as specific markers for other proteins. It is even possible to employ several distinct fluorescence markers at the same time, which is useful to distinguish different proteins in a cell or even in the same spot.

4. Comprehensive integration in quantitative models: What set out with the observation of *animalculae* has now grown into a vivid field, in which researchers seek to understand the inner mechanisms of biological cells, be it prokaryotes or eukaryotes. Here we are interested in the phenomena of cellular motion. With the detailed data on intra- and transcellular protein interactions at hand, our task is now to integrate these data into a common and widely applicable theory. Such a theory should be able to account for the behavior observed in selected model systems. In the process of theory building we should generalize, refine or adapt our framework, and reiterate until the cell-level theory describes the motion of various types of cells, possibly with additional specializing modifications. Since biological phenomena are inherently diverse and

[6]GFP = green fluorescent protein

mutually interrelated, the process of finding a suitable theory typically takes a long time – often so long that the impression might arise that there will never be a complete theory for biological systems. With this in mind we turn to the seminal works of the current paradigm, which sorted out the details and assembled a unified picture of the migration of specific cells on two-dimensional substrata.

1.4. "Cell migration: a physically integrated molecular process"

The title of this section is the one of a famous opinion article by Doug Lauffenburger and Alan Horwitz [138], of which the science portal `http://webofknowledge.com` lists over 2100 citations by December 2012. In this article, the authors provide a kind of taxonomic description of the cellular migration process, which organizes a plenitude of detailed observations into a single conceptual framework. The key steps of cell migration in this framework are exhibited in the section titles of [138]:

1. "Morphological Polarization" provides for the initial starting point, since there should be some direction as to what is forward. This aspect of cell motility is observable in many distinct kinds of cells, e.g. keratinocytes, fibroblasts, neutrophils.

2. "Membrane Extension" encompasses a kind of forward-step of the cell, and is approximately centered around the forward direction as set by the cell's morphology.

3. "Formation and Stabilization of Attachments" mostly at the cell front leads to the transmembrane connection of the cell to the substrate.

4. "Contractile Forces and Traction" due to cytoskeleton and adhesions generate a net pulling/pushing effect for the cell in forward direction.

5. "Rear Release" and breaking of no longer needed attachments at the rear end enables the cell to actually translocate upon traction generation.

6. "Overall Coordination" somehow has to take place to carry out steps 1–5 in a efficient and/or controlled manner.

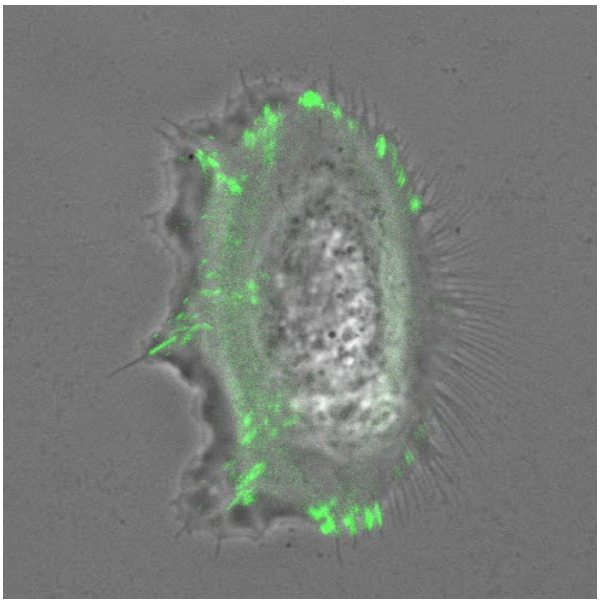

Figure 1.2.: A human epidermal keratinocyte migrates on a fibronectin substrate from right to left. At the front (left), the membrane is pushed out to enable subsequent adhesion formation (green). In this way, intracellular forces couple to the substrate and give rise to the translocation of the cell body (bright, elliptical region in the middle of the cell). At the cell's rear end, retraction fibers form at sites of breaking adhesions, hindering the cell in its forward translocation. The fluorescing marker (green) is Zyxin, which colocalizes with focal adhesion complexes containing transmembrane integrins.

The appeal to this scheme is that it allows to separately investigate the single steps in specific submodels or experiments. Moreover, it is sufficiently concise that it can be grasped as a whole. Indeed, the work by Lauffenburger and Horwitz [138] has inspired many cartoons explaining cellular migration in later publications (e.g. [135, 150]). In figure 1.2, some of the elementary steps are already visible from a micrograph of a human epidermal keratinocyte.

1. Polymerization and tip dynamics: It is perhaps not surprising that many researchers focused on the first two steps to further explain cell motility. Somehow, morphology and membrane extension seem to be related concepts, for they both affect the observable outline of the cell.

Also, Lauffenburger and Horwitz note in their article that "response to migratory stimuli is almost universally found to be coupled with local actin polymerization" [138, Section "Membrane Extension"]. The resulting effect on the cell's morphology can also be seen in figure 1.2, where the cell exhibits a prominent, wide and flat lamella at the front (left), together with several spike-like filopodia extending forward. Consequently, in 2003, Thomas D. Pollard and Gary G. Borisy found that the "Cellular motility [is] driven by assembly and disassembly of actin filaments" [179].

The rationale for this hypothesis is the following: actin filaments polymerize at the cell front in such a way that the membrane is pushed outward, away from the central cell body. This process is driven by the orientational polarity inherent in actin filaments. The spatial regulation of the polymerization zone then leads to the formation of a polarized cell morphology. In order to enhance the overall polymerization rate at the lamella tip, branching proteins like Arp2/3[7] and membrane-anchored WASP[8] complexes provide for additional nucleation points for actin filaments. These polymerization agents are believed to be produced only at the membrane. Correspondingly, polymerization occurs mostly at the very cell tip. Inhibition of polymerization by capping proteins in an intermediate zone and severing of filaments further back, e.g. by ADF/cofilin (actin depolymerizing factor), recycles the actin monomers so that they again may be incorporated into polymerizing filaments [151, 179]. These and other molecular players in the polymerization processes at the lamella tip are summarized in figure 1.3 which was originally proposed in [179, Figure 3].

2. Cellular adhesion-velocity relation: In this way, key steps 1 & 2 of the scheme above can be explained. A fairly detailed understanding of steps 3 & 5 had already been achieved by the end of the 90s. In 1997, Palacek and co-workers had found that in CHO[9] cells, the migration speed depends on integrin, such that even small changes in integrin concentration can significantly affect the migration speed. If the concentration of available ligands on the substrate is low, speed increases upon increasing the amount of expressed integrin. In contrast, when the concentration of available substrate ligands is high, the migration speed increases with decreasing expression of integrins. In between these two regimes, the

[7] Arp2/3 = actin related proteins 2 and 3
[8] WASP = Wiskott-Aldrich syndrome protein
[9] CHO = Chinese hamster ovary

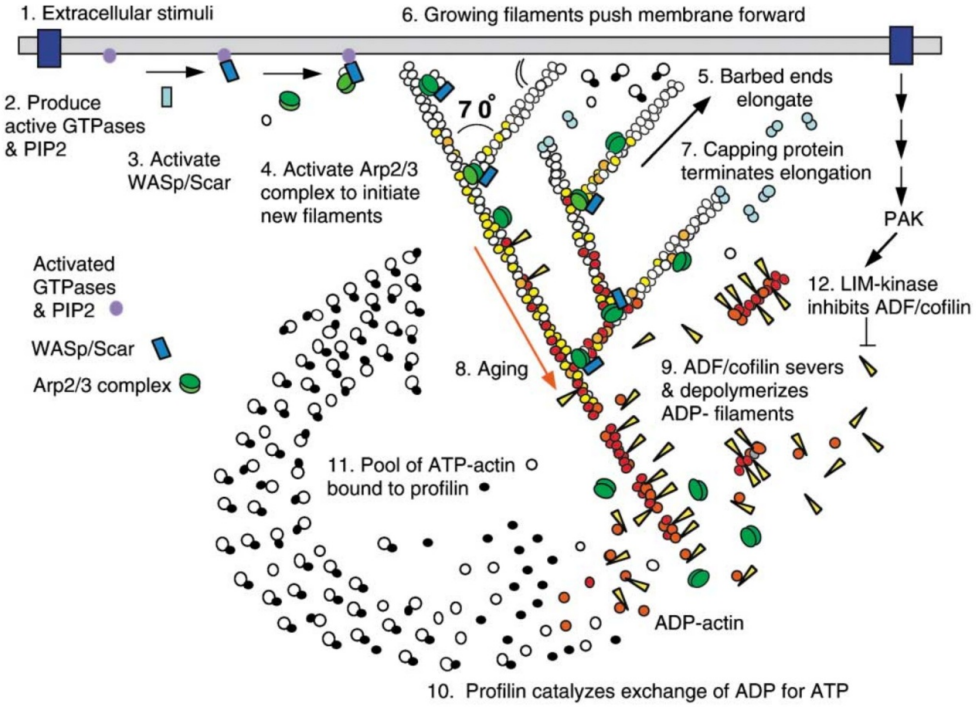

Figure 1.3.: Cartoon picture of the dendridic actin nucleation at the tip of migrating cells. The polymerization of actin is faster at the barbed ends of the filaments, which mostly point towards the cell membrane, in a characteristic pattern of dendritic branches. The Arp2/3 complex is activated at the membrane and creates additional branches in the filament network, which enhances the effective actin polymerization close to the membrane. This polymerization then advances the membrane, so that the network falls behind the zone of enhanced polymerization. Due to filament aging involving the dephosphorylation in the actin monomers, the network becomes susceptible to depolymerization, which is additionally enhanced by severing agents. The released pool of actin monomers is subsequently again phosphorylated while diffusing back to the membrane, which completes the actin polymerization cycle. The presented cartoon is reprinted from [179, Figure 3], with kind permission by Thomas D. Pollard.

maximum migration speed for these cells was 10–20 μm/h [169]. These effects can be explained from a 4-state model of the kinetics of the binding complex, which connects cell-internal F-actin and cell external substrate by intermediate integrin [170]. Specifically, the involved binding affinities give rise to inherent reaction time constants, which – depending on cell type and substrate stickiness – influence the mutual effectiveness of the processes in 3 & 5. Consequently, some cells are faster than others.

3. Active contraction and traction: From the traditional results of acto-myosin in muscle, the details of step 4 seem to be reasonably understood. As described before, myosin colocalizes with actin, crosslinks the filaments and creates a net tensile force due its ATP consuming motor activity. Therefore, only step 6 of aforementioned scheme needs further clarifications. To this end, we further review several polarization mechanisms in a broad sense, which have been implicated to be at work in certain model systems.

1.5. Cellular polarization mechanisms

1. Mechanisms occurring close to the membrane: The most common theme in cell polarization is certainly the regulatory aspect of the actin polymerization cascade at the lamella tip. Extracellular signals somehow have to make their way inside to initiate certain effects. It is believed, that the Rho/Rac family of proteins processes external chemical signals [184], whereby one specific complex involved in polymerization is WASP. While the molecular details are quite puzzling and not yet completely understood [168], the basic working principle goes like this: Being sterically auto-inhibited to actin or Arp2/3 binding, WASP gets activated by deformation in the presence of transmembrane PIP2[10] and cytosolic Cdc42[11]. Subsequently, Arp2/3 may attach to actin so that polymerization is induced.

Even though not all details of molecular regulation processes on the nano-scale are known completely, there is a common denominator on the whole cell level, which can resemble and summarize various specific pathways. In fairly abstract mathematical terms, stimulation of polymerization can be recapitulated from local-excitation global-inhibition models [232], or several other mathematically distinct but conceptually

[10]PIP2 = phosphatidylinositol biphosphate
[11]Cdc42 = cell division control protein 42

related schemes [116], usually involving actin-polymerizing agents at the membrane. When solving the underlying equations on a roughly cell-like geometry like a circle, these mechanisms give rise to a spatial pattern localizing a leading edge, the region of predominant actin polymerization. For further details we refer to [116], which also gives an account on capability and limitations of three model classes on membrane-initiated cell polarization.

Once the cell has established a spatial regulation pattern designating the leading edge, actin polymerization has to adapt so that protrusion forces are generated in the corresponding direction. There are two theoretical frameworks how force generation works at the interior surface of the cell membrane:

(i) In the Brownian Ratchet model [150,152–154], actin filaments directly support the membrane with their plus ends. When there is enough space due to thermal fluctuations of membrane or filament, an actin monomer squeezes in between and the filament grows. Averaging over many of these polymerization events, a net protrusion force emerges, which pushes the membrane forward.

(ii) Alternatively or coincidentally, polymerization may be initiated at motor proteins anchored in the cell membrane. Careful force and energy estimates lead to the postulate that such an mechanism is actually at work in migrating cells [65, 66]. Originally, this mode of force generation was observed in listeria. These bacteria infect host cells and propel themselves by creating an actin polymerization tail at their rear ends. Since insertion of monomers is an active process, the emerging motion is step-like.

Certainly, the phenomena described above play an important role to the cell's sense of direction. However, to ensure overall and cell-wide coordination, these purely membrane-associated processes do not seem to suffice. Taking place mostly at the very tip of the lamella front, the rear release, for example, cannot be influenced from this regulation circuitry. Indeed, during the last years, some other mechanisms have been implicated to participate in directing a cell.

2. Mechanisms occurring in the cell bulk: One of those other mechanisms depart from the membrane relies on internal processes in the actomyosin bulk of the cell. Suppose a cell is at rest, entirely symmetric,

i.e. circular, and the retrograde flow is directed radially inward, pointing from the lamella tip to the cell body/nucleus, which is enclosed by a shell of peripheral actin fibers. Initially, all forces are balanced in this system: contractions in the fiber shell are compensated by the retrograde flow from the periphery. Thereby, the fiber shell around the cell body contracts in centripetal direction, whereas the incoming retrograde flow builds a pressure acting in centrifugal direction. If however contraction is enhanced/decreased in a particular region, the initial symmetry will break and some morphological polarization of the cell will occur. These effects have been observed in fish keratocytes [229, 233], and suggested to be an effective response to inhibitory extracellular chemical gradients [52].

Reorientation works as follows: if some repelling stimulus is received, strong contractions are induced in the corresponding region of the cell. These cytoskeletal contractions lead to localized compressions of the cell bulk. At the same time, the cytosol is squeezed away from the contractile region, which affects the overall flow equilibrium. In this way the membrane at the opposite end of the cell bulges out, and the overall morphology starts to change. A similar phenomenon occurs when the contraction is decreased in a particular cell region, except that the membrane then extends in the same place, not at the opposite cell end. These effects can be nicely observed in blebbing cells, for example L929 fibroblasts [216]. However, the underlying mechanisms have been conceptualized much earlier. Already in the 1970s, Taylor and co-workers developed the idea in a series of papers on certain amoeba and *Dictyostelium discoideum* [212, 213]. Also, experiments on *Xenopus laevis* from the 1980s seem to support the general idea of contraction-induced polarization [204].

3. Fluctuations and spontaneous polarization: It is important to realize that both cell bulk and membrane associated polarization mechanisms can also arise spontaneously, i.e. without relying on external cues. Concentrations of all involved proteins vary, so that locally there might occur fluctuations, effectively shifting the relevant reaction equilibrium. Depending on the strength of the fluctuation, the cell system as a whole might be stable or unstable under these perturbations. Notably, close to equilibrium most extracellular signals are in the strong-fluctuation regime, because in this "homeostatic" state there are only very few signaling molecules at work. Of course, whether such effects are actually important to the cell's function should be clarified in experiments. We expect, however, that ubiquitous fluctuations are not only involved in cel-

lular regulation, but rather have been explored by nature so to participate in almost all processes that jointly comprise life.

4. Checking with phenomenology – repetitive protrusion cycles: It was known by the mid-90s, that cultured human epidermal keratinocytes exhibit characteristic ruffle dynamics at their lamella tips. In repeating periods of approximately two minutes, lamellipodia protrude at 2–6 μm/min and subsequently retract again with 1–4 μm/min, whereas filopodia protrude and retract at slightly higher velocities [7]. Similar observations had previously been made in the lamellae of amoeboid cells and even cell extracts. If one stimulates human epidermal keratinocytes with epidermal growth factor, the ruffle velocity and frequency increases [103].

This phenomenon is remarkable for several reasons. Apparently, there seems to be an inherent rhythm to the cell's protrusion/retraction behavior. Next, the protrusion velocity is similar for both lamellipodia and filopodia. Finally, the observed dynamics of the leading edge can serve as fairly easy benchmark for protrusion/polarization models, namely by comparing kymographs of lamella tip positions from *in-vitro* and *in-silico* cells. Recently, related effects have been observed in the filament-based leading edge models by Falcke and coworkers [75, 236]. By coupling the polymerizing F-actin brush at the lamella tip to a cross-linked gel-like bulk further in the back, they find several distinct protrusion phenotypes in their simulations. Notably, these phenotypes share some common characteristics with the ruffle dynamics reported in [7, 103] and already recapitulated in simulations [8].

Our observations of the lamella of human epidermal keratinocytes suggest to interpret the rhythmic protrusion cycles of a cell as a way of sensing and exploring its environment. Some experimental attempts have already been made to relate a cell's protrusion dynamics with its morphological polarity [142]. If protrusion indeed constitutes a kind of environmental sensing, one would expect a correlation between protrusive activity and the course of the subsequent migration trajectory. Moreover, one could further test this hypothesis by studying protrusion behavior of cells while controlling the persistence of their migration trajectory [173].

5. Polarization of polymerization, protrusion, and morphology: Here, we argue that steps 1, 2 and 6, i.e. "Morphological Polarization", "Membrane Extension" and "Overall Coordination" from the scheme in section 1.5 should be combined and understood jointly on the whole-cell level.

Protrusion activity is affected both by actin polymerization at the lamella tip and fluid streaming upon local cell contraction. Overall coordination – e.g. from front to back – can be reached by chemical agents, but also directly via the force equilibrium in the cytoskeleton. The cell's morphology ultimately arises from a combination of all these effects, and also depends on the adhesive properties of its environment. The actual loci of membrane extension are a mere consequence of this interplay.

1.6. Revisiting cellular adhesion and tension

1. Actin, myosin and stress fibers: If actin filaments align in antiparallel orientational polarity and connect with the help of cross-linker proteins, the emerging bundles are called stress fibers. Thereby, α-actinin and myosin alternate in linking the fibers, which leads to an overall bundle contractility, similar to the phenomena known from muscle cells. According to [110], there are three different types of stress fibers, cf. figure 1.4:

1. Dorsal stress fibers develop through actin polymerization induced by formin proteins, which occurs close to focal adhesions. At the one end, they point to the leading edge of the cell, while their other end extends towards the cell center. In this central region, dorsal stress fibers are sometimes connected to stress fibers of type 2.

2. Transverse arcs are bent actin filament bundles, which are nucleated by the Arp2/3 complex and attached to myosin bundles. Transverse arcs are usually not connected to focal adhesion complexes.

3. Ventral stress fibers are converted dorsal fibers or transverse arcs that end up at the rear end of the cell. These ventral fibers are connected to focal adhesions on both ends.

In this light, we may regard stress fibers as a machinery that transduces forces from one position of the cell to another. Furthermore, structures such as the bulk actin network, intermediate filaments or even microtubuli participate in this cell-scale force distribution. The cytoskeleton-mediated force propagation also provides for a direct regulative hook from the cell's front to its back, and is involved in the stabilization of cell shape [41]. If only the membrane were to support overall cell cohesion, there would occur instabilities causing rupture, so that fragments of the cell would separate from the rest. In migration models of fibroblasts, this instability has been reported as the "dripping faucet instability", in analogy to a drop parting from a not entirely closed faucet [99].

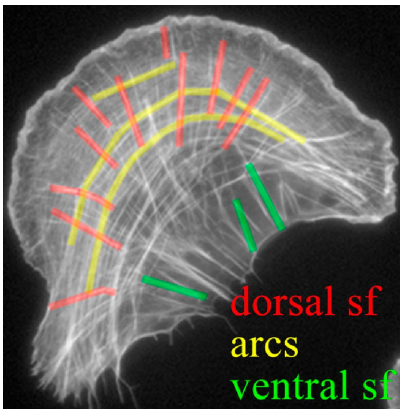

Figure 1.4.: There are different kinds of stress fibers distributed at different loci of a migrating cell (picture here: human osteosarcoma cell, "U2OS"). 1. Dorsal stress fibers (red) extend radially throughout the lamella and connect cell body and focal adhesions. 2. Transverse arc stress fibers (yellow) provide for lateral tension and are bent in the direction of migration. 3. Ventral stress fibers (green) facilitate rupture of adhesions at the rear end of the cell by propagating tension from transverse arcs to the retraction zone. The picture shown here is reproduced from [110] with permission by P. Hotulainen.

2. Effective fluidity of the cell bulk: The here postulated analogy of cell bulk and drop is not coincidental. Indeed, we share the opinion that the cytoplasm mostly behaves like a fluid. This perhaps controversial view has a rather simple explanation: the inherent time-scale of chemical processes in the cytoplasm, most notably of the actin cytoskeleton, is much smaller than the relevant time-scale of cellular migration. Actin monomers turn over in seconds, whereas cell motility and translocation happens in minutes to hours. Fluidity arises because there are almost no bonds between actin monomers that would stay connected long enough to determine cellular motion. Instead, due to chemical turnover, the cytoskeleton bulk appears as fluid when investigating the long time-scale of motility. In a similar manner, crosslinkers like myosin attach and dissociate to/from actin filaments rather quickly – again compared to the time-scale of cell motion of minutes to hours. This "fluid" view becomes more and more common in whole-cell models [6, 118, 123] and is already well established at the tissue-level [94, 145, 198]. Nevertheless, actin and crosslinker bonds do influence the material properties of the cytoplasm.

It is to be expected that their kinetic turnover speed would modulate the effective viscosity of the cytoplasmic fluid.

3. Integrin and focal adhesions: During migration, it is important for the cell to connect itself to the underlying substrate. To this end, focal adhesion complexes assemble at the interface between cell and substratum, so that locomotion forces can be transmitted. For human epidermal keratinocytes it has been reported that initially small adhering connections are assembled below filopodia, i.e. spike-like thin, and elongated cytoskeletal protuberances. This assembly process is mediated by a small protein called VASP[12] [190]. After that, right behind VASP, slightly larger connecting sites are formed from proteins like tensin, paxillin, talin, zyxin, β-integrin, vinculin and even VASP itself. These larger connections are called small focal adhesion sites. A small focal adhesion will grow to a larger one as soon as the lamellipodium arrives at the corresponding region [190]. As the focal adhesion site grows, there is a steady phosphorylation and turnover of vinculin molecules. Subsequent size maintenance and shrinking of the focal adhesion site is modulated by vinculin dephosphorylation [158].

Apparently, there also seems to be an inherent time-scale in focal adhesion formation, maturing and subsequent disassembly. Fluorescence recovery after photo-bleaching (FRAP) measurements on the exchange dynamics of vinculin pose a lower boundary of approximately 1 min to this ripening or maturing process [156, 158]. In mature focal adhesions, the residence time of integrin is approximately 1–3 min [180].

Moreover, adhesion sites to the substrate also seem to be important for the cell shape. When seeding cells on substrates with localized adhesive spots, they exhibit a characteristic outline, whereby tip-like extensions anchor to the adhesive spots. At the same time, the intermediate arcs sharply curve inward, approximately in a circular fashion [28]. Based on an energy-minimizing principle, the emerging cell shape can be related to the forces acting on the adhesive spots, and the cell outline thus becomes directly predictable [28]. This shows that the distribution and strength of adhesion spots contribute to whole-cell shape generation.

4. Mutual feedback of cytoskeleton and focal adhesions: Finally, focal adhesion sites are also influenced by stresses in the actin cytoskeleton. Upon ATP hydrolysis, the actomyosin-complex contracts, which creates

[12]VASP = Vasodilator-stimulated phosphoprotein

a tension in the focal adhesion complexes [224]. Some of the molecular bonds in the focal complex are sensitive to tensile forces and therefore tend to break upon load, which leads to an incomplete detachment of the focal adhesions. In this way, a crawling cell leaves a so-called migration track behind, which mostly contains integrin clusters [124]. This suggests to combine steps 4 "Contractile Forces and Traction" and 5 "Rear Release" of the scheme in section 1.5. The inverse phenomenon does occur as well. In nascent focal adhesions, force-induced tensile load as provided e.g. by stress fibers or retrograde actin flow facilitates the further assembly and clustering process of the complex [81, 89, 180]. Consistent with these observations, focal adhesions of MDCK[13] cells enlarge on stiffer substrates [188].

5. Cadherin and intercellular junctions: Cadherin is an elongated molecule, with two characteristic functional groups at its opposite ends, namely the C-terminal region (ending with a carboxyl group COOH) and the N-terminal region (ending with an amino group NH_2) [139]. At the N-terminal domain, there are five different extracellular repeat units EC1–EC5, of which the first three are believed to dominate the formation of homophilic cadherin-cadherin bonds. These bonds develop in two distinct kinetic phases: In the first phase, cadherins mostly form EC1–EC2 bonds, whereby the corresponding probability of accomplishing the cell-cell contact is relatively low. Then, after a short lag phase, cadherins engage in EC3 bonds, which provides for stronger coupling of the cells and keeps them connected [139].

Similar to integrin, cadherin forms adhesions in patches involving several individual molecules. Functionally most important are the so-called adherens junctions, which are composed of clustered cadherins [107, 235]. Initially, few E-cadherins connect to those of the other cell in a small number of bonds. Then, other cadherins approach the region by means of diffusion, where they engage in dimers and thus become trapped. Subsequently, so-called catenins attach to the cell-interior domains of the cadherins. This enforces the present cluster structure and at the same time provides for connections to the cytoskeleton, so that cohesive stresses may propagate from one cell to the other. Once established, the adherens junction is fairly stable, because there is a certain energy cost for a cadherin to leave the cluster, leading to a half residence time of approximately 2 minutes [107]. In figure 1.5, one can recognize a cadherin-mediated adhesion

[13] MDCK = Madin-Darby canine kidney epithelial cells

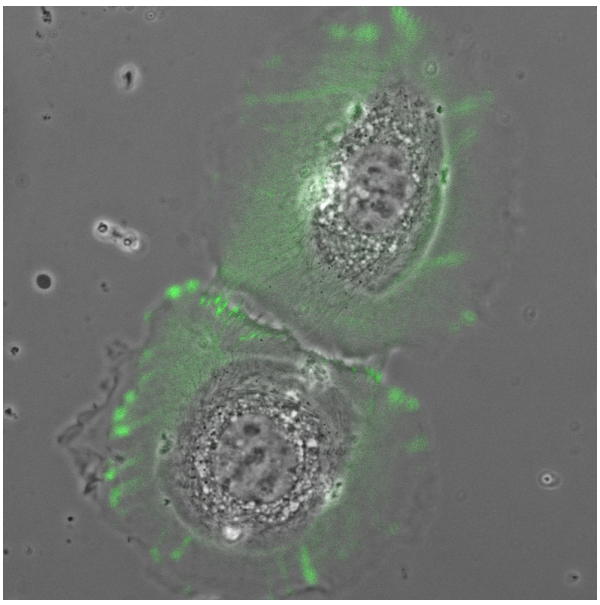

Figure 1.5.: This pair of human epidermal keratinocytes has formed a cadherin-mediated adhesion zone. The fluorescent marker (green) is Zyxin, which colocalizes both with focal and transcellular adhesion complexes. A possible adhesion mechanism has been suggested in [35]. Thereby, one cell touches the other with its filopodia. The other, in turn, responds by generating localized stresses in its actin cytoskeleton. In this way, cadherin adhesion is initiated and a stable cell-cell adhesion emerges. In the picture above we see two connected cells with an already mature cell-cell contact zone. The strong focal adhesions towards the substrate (also green) show that the cells have been in this constellation for a longer time.

zone between two human epidermal keratinocytes. The striking stability of such an adherens junction can be understood in terms of a receptor-ligand binding model on fluctuating membranes [225]. Thereby, membrane fluctuations lead to the preferential formation of receptor/ligand pairs close to existing clusters, which constitutes a positive, self-enhancing feedback of adherens junctions [131].

There are two distinct kinds of catenins, namely α-catenin and β-catenin [33,94]. Both species are involved in cadherin clustering, whereby the latter forms a complex with E-cadherin. The former can bind in several states: as a monomer, it attaches to β-catenin in the E-cadherin–β-catenin complex, whereas in its homo-dimer conformation, it only binds to actin filaments. In this way, actin filaments may restrain the E-cadherin diffusion into the junction. Additionally, α-catenin may also prevent the Arp2/3 complex from binding to actin, thereby inhibiting actin polymerization [33, 94].

6. Clustering and force-induced adhesion modulation: One early and important model of the dynamics at cell-cell contacts has been by by George I. Bell, from 1978. The central idea is quite simple: connections between adjacent cells are realized by their surface proteins, which eventually bind to one another. Bond disconnection is modulated by the applied force. Thereby, the dissociation rate (off rate) of cell-cell bonds increases exponentially with the applied force (load) [21]. In the late 90s, Evans and Ritchie showed by means of simulations, that under high loading rates the number of rupture events is also high. Conversely, under low loading rates, there seem to appear very low bond strengths [76]. Meanwhile, the measurement of forces on single bonds is quite a standard technique, by which these theoretical predictions have been verified [147].

We believe that this force-induced speed up of molecular bond breaking is a very central motif of cellular motility. Ultimately, migration follows force transduction. Therefore, in any motility process leading to translocation, there must be some forces involved. Since force affects chemical bonds, this certainly comprises a very direct regulation circuitry. Specifically, the sensed forces can provide for feedback onto the macromolecular aggregates involved in cellular motility processes.

The inverse effects may also occur at sites of adhesion. We have already seen that adhesion formation involves clustering of multiple receptors. In the preceding paragraph we have found that actin in cooperation with α-catenin is involved in the cadherin clustering process. When a cadherin

molecule close to the cluster is connected to an actin filament, the forces pulling on that filament – or even its Brownian fluctuations – might navigate the cadherin into the cluster, which subsequently enhances the local adhesion strength. Similar processes are also at work during the maturation of focal adhesion sites [81]. Additionally, integrins might be activated by mere pulling in the suitable directions [180, Fig. 1]. Finally, imposing tensile load on an immature adhesion complex increases its size [158].

Altogether, these effects comprise a conceptually simple and powerful mechanism for a crosstalk of actin and cell-cell and cell-substratum adhesion molecules. In the initial phase of adhesion formation, external load on the adhesion molecules enhances the clustering effect, so that the adhesion matures more quickly. When the adhesion site has aged, fairly strong pulling forces are able to overcome the barrier of the connecting bonds in the adhesion molecules. After some time, this would induce subsequent rupture and disassembly of the adhesion site.

1.7. Modes of motion of selected kinds of vertebrate cells

1. Length-scale, timescale and molecular key players: Modeling cell migration easily gets complex and considering every single involved protein complicates the matter even more. Therefore, one needs to focus on the main functional themes. Here we identify three important locations for the processes driving cellular motility:

- the cell bulk,
- the contact zone between two adjacent cells,
- the contact zone between cell and substrate or extracellular matrix.

When describing whole-cell motility, the corresponding dimensions give rise to approximately three different length-scales:

- molecular scale $\approx$ membrane thickness ($\sim$ 10 nm),
- intermediate scale $\approx$ cell lamellipodium ($\sim$ 1 μm),
- cell scale $\approx$ one to few cell radii ($\sim$ 50 μm).

Similarly, there are three distinct time scales:

- chemical reaction scale ($\sim$ 5 s),
- intermediate scale $\approx$ protrusion, adhesion maturation ($\sim$ 2 min),
- cell translocation scale ($\sim$ 1 h).

These time- and length-scales help to organize and categorize specific phenomena in the sense of a taxonomy. At the same time, they allow for a certain modularity in the construction of models. Commonly, things that happen at a different time- and/or length-scale can be neglected or their effects can be conveniently summarized without resorting to detailed submodel development.

According to section 1.6, there are usually four dominant chemical players related to force transduction in cell motility:

- actin (cytoskeleton),
- myosin (contraction),
- integrin (cell-matrix or cell-substrate adhesion),
- cadherin (cell-cell adhesion).

Here we do not list any upstream or downstream chemical signaling species. Such species ultimately regulate only detailed aspects of the aforementioned force machinery. Any regulation circuitry should therefore be a modular ingredient to the model and tuned to the specific cell type at hand.

2. Physical mechanisms jointly at work: In the light of the previous considerations, there are fairly few mechanisms that jointly constitute the majority of cellular motility phenomena:

1. actin polymerization (usually mostly at the tip),
2. motor-induced cytoskeletal contraction (cell bulk),
3. long range force transduction (across cell bulk),
4. force-induced molecular clustering and breaking of chemical bonds (adhesion sites, possibly cytoskeleton),
5. fluid-like behavior of cytoplasm/cytoskeleton (cell bulk).

Location and effect of these few mechanisms are combined and explored *in-vivo* so that many different modes of cellular motion and morphology have been developed.

Certainly, the item 5 of the preceding list is the most controversial one: it might be difficult to imagine long-range force transduction in wobbling fluids. Central to a fluid's cohesion, however, are its interior stresses, which jointly contribute to the overall surface tension. In the cell, this function is provided by two players: (i) the membrane as flexible container of the cytoplasm, and (ii) the cytoskeleton inside of that container, including but not limited to the cortex underneath the membrane. Importantly, the tension provided by the membrane does not suffice in all cases to achieve cohesion of the whole cell. In these cases, the cytoskeleton serves by enforcing and strengthening the effective cellular surface tension.

Our findings are summarized in table 1.1, and in line with the inspiring work by Denise Montell [159]. We try to relate the biological phenomena to their location, the underlying physical mechanisms, and the involved chemicals.

When idealizing a complex real-live system into a coherent model, not all details can be captured exhaustively. On the other hand, one would like to summarize omitted facts so to at least partially account for them. One summarizing technique is the incorporation of stochastic perturbations.

Perturbations, however, are not only a useful ingredient to idealized model systems. In fact, fluctuations occur in any system involving the spatial distribution of chemical reactants. Diffusion is inherent to such systems, which is a stochastic process driven by Brownian motion of the particles in the surrounding solvent fluid. Effectively, this leads to variations in the concentration profile of the reactants, which constitutes a direct source of fluctuations. It is therefore to be expected that nature has somehow explored these fluctuations to help in the ubiquitous self-organization processes that we observe at all stages of life. The considerations of fluctuations might even proof to be essential in order to explain certain biological phenomena.

Yet to a modeler, the immediate practical benefits of perturbations are more mundane: increasing noise serves as a quick benchmark for the robustness of the system. After all, robustness is a central characteristic of all living beings.

Biological phenomenon	**Location**	**Physical mechanism**	**Chemical players**
cell-wide coordination	whole cell	chemical signalling; force transduction, adhesion modulation by force	various; actin, myosin
sensing, polarization	lamella tip, cell bulk	chemical signalling, polymerization, fluid flow	PIP2, ..., Arp2/3, actin; actin, myosin
protrusion, membrane extension	lamella; cell bulk	fluid flow	Arp2/3, actin, actin, myosin
cell-matrix adhesion	below cell	adhesion modulation by force	integrin, ...; actin, myosin
contraction	cell bulk, backside	motor activity	actin, myosin
rear release	below cell, backside	adhesion modulation by force	integrin, ..., actin, myosin
cell-cell adhesion	between two cells, close to membranes	adhesion modulation by force	cadherin, ...; actin, myosin
tissue cohesion	cell bulk, between cells	trans-cellular adhesion and force-transduction	actin, myosin, cadherin, ...
collective migration	tissue bulk	trans-cellular adhesion, force-transduction, substratum tension	actin, myosin, cadherin, ..., integrin, ...

Table 1.1.: Taxonomy of force-involving phenomena in cellular migration. Migration combines the mechanisms in the third column in a modular way. Generic parameters to these mechanisms, e.g. strength, speed/time-scale, and noise-driven fluctuations, need to be ajdusted according to cell type. In this way, typical migrating cell systems, such as keratinocytes and fibroblasts, can be understood within this common conceptual framework (see also example paragraph 1.7.3 in the text).

3. Some tangible biological examples: Human epidermal keratinocytes exhibit several typical morphological modes on two-dimensional substrates, see figure 1.6. In their sessile state A, as attained after spreading on a substrate, they are circular. This corresponds to a force equilibrium between radial retrograde flow, adhesion induced expansion and lateral tangential contraction, e.g. by stress fibers around the cell body, cf. also paragraph 1.5.2.The migrating state B is polarized and exhibits a broad front of polymerization, with adhesion "carpet" maturing shortly behind the leading edge, so that a lamella develops in the direction where the cell is crawling. At the rear end, stress-fiber contractions help in breaking adhesion bonds. Most of these phenomena could already be conceived in whole-cell continuum descriptions [6, 135]. Since switching is possible between the two states, the emerging cell trajectories exhibit intervals of persistent and fast locomotion with slow reorientation phases in between. The bimodal morphology C with two protrusion zones on opposite cell ends facilitates these reorientations.

Fish keratocytes are in many ways similar to human epidermal keratinocytes. In their canoe-shaped migratory mode, the recycling of actin monomers is slightly more efficient, and possibly adhesions are regulated more tightly, so that the leading edge is sufficiently smooth, as typical for this type of cells. Strongest traction is situated at the lateral parts, i.e. shifted outwards as compared to human keratinocytes. Altogether, this leads to very persistent and fast locomotion [123, 233].

Depending on their state, there are one or more distinct tip regions of active actin polymerization in fibroblasts, see e.g. [178, 206]. Accordingly, there are usually several protruding lamellipodia, giving rise to a multi-modal cell shape. At the same time, removal of remaining adhesions at the back is also fairly localized [99]. Radial stress fibers in long rupture podia are under high tension towards the cell center. In this way, forward traction and backward retraction forces are under continuous competition. Thus, fibroblasts reorient frequently during migration, leading to rather slow overall translocation speeds.

Neutrophils are morphologically distinct, because they follow a guiding chemical cue. They attain a drop-like like shape, with the so-called uropod being the thin part, situated at the back. While hunting a bacterium[14], the blob-like front quickly adapts to directional changes. This is achieved by reducing the overall cellular surface tension. Being softer

[14]See the famous movie by David Rogers, `http://www.biochemweb.org/neutrophil.shtml`.

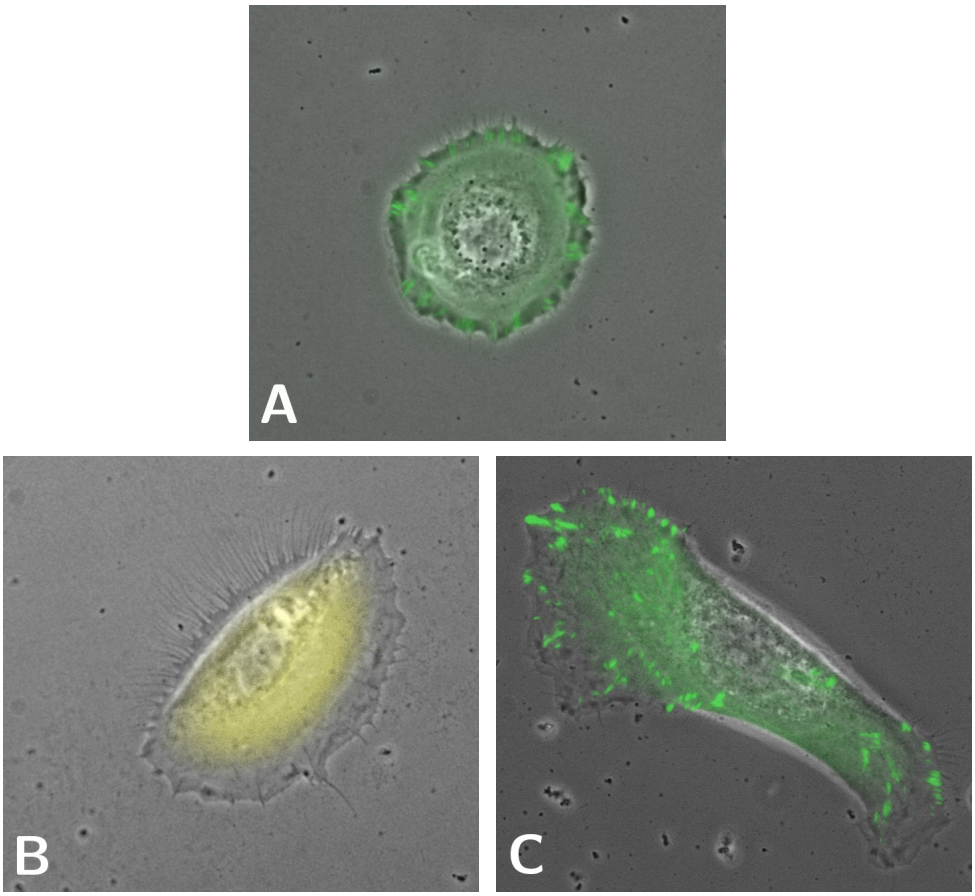

Figure 1.6.: When seeded on fibronectin substrata, human epidermal keratinocytes attain distinct morphological states. In the sessile state A, cells are round and attain a fried-egg shape. The migrating state B is characterized by a broad lamella in the direction of the cell's crawling motion. Sometimes, keratinocytes also attain a bimodal shape C, where there are two lamella at opposite ends of the cell. In A and C, the green fluorescence staining is for vinculin, which co-localizes with the cellular focal adhesions involving also integrin. In B, staining is for tubulin, which is a part of the cytoskeletal network and mostly situated within the cell body. The presented micrographs are by courtesy of Carina Wollnik [231].

and more deformable obviously facilitates the migration through the surrounding tissue. However, also the adhesions have to be reorganized very quickly. We speculate that this works by keeping the focal adhesions in the nascent state before maturation. Due to their task, neutrophil trajectories are expected to be closely related to the pattern set by the chemical cues.

Finally, neuronal growth cones share some of the aforementioned motion principles. Recently, it has been shown that growth cones are exceptionally soft mechanical structures [24]. This means that only weak adhesions are needed for translocation. At the same time, the protrusional "sensing" is excessive, which could arise from the need of integrating extracellular signals very precisely. Also, the trailing axon certainly plays a role, however it is not clear whether the axon is pulled or rather assembled on-the-fly. All in all, a straight growth trajectory emerges, whereby the speed of the cone is very slow [23].

2. The Reactive Interpenetrating Flow model describes the dynamics of the cytoplasm

Summary: In this chapter we derive a hydrodynamic continuum theory for the cytoplasm of motile cells. The model presented here was originally proposed by Alt and Dembo, and is usually referred to as Reactive Interpenetrating Flow (RIF) model [6, 8, 50, 58, 60, 62]. The central underlying assumption in this theory is, that the cytoplasm is essentially of fluid nature, where tensile and pressure like forces are generated from active components in the fluid. RIF distinguishes two phases in the cytoplasm, namely (i) the filamentous cytoskeleton and (ii) the aqueous cytosol phase. There is a separate mass and force balance for each of these phases. The mass balances are constructed in a way that the total volume flux is incompressible. Moreover, the Stokes-type force balances contain an isotropic, active, and bistable stress. Also, there is a Darcy type friction between the filamentous and aqueous phase. Both active stress and inter-phase friction are prescribed as constitutive equations.

2.1. Mass balances involve the volume fraction

1. Three distinct mass balances in the cytoplasm: In order to represent and quantify the physical cytoplasm mechanisms 1 & 5 from paragraph 1.7.2, we treat the cytoplasm as a compound fluid, whereby we initially start with three constituents.[1] To this end, we consider the mass densities of (i) filamentous F-actin ρ_f, (ii) monomeric G-actin ρ_g, and (iii) aqueous solvent ρ_s. Accordingly, we write the three mass balances,

$$\text{F-actin:} \qquad \partial_t \rho_\mathrm{f} + \boldsymbol{\nabla} \cdot \big(\rho_\mathrm{f} \mathbf{v}_\mathrm{f}\big) = \quad J', \tag{2.1}$$

$$\text{G-actin:} \qquad \partial_t \rho_\mathrm{g} + \boldsymbol{\nabla} \cdot \big(\rho_\mathrm{g} \mathbf{v}_\mathrm{g} + \mathbf{j}_\mathrm{g}\big) = -J', \tag{2.2}$$

$$\text{solvent:} \qquad \partial_t \rho_\mathrm{s} + \boldsymbol{\nabla} \cdot \big(\rho_\mathrm{s} \mathbf{v}_\mathrm{s} - \mathbf{j}_\mathrm{g}\big) = \quad 0. \tag{2.3}$$

[1] This chapter relies heavily on the notions of hydrodynamics. A brief and accessible introduction to the matter is given in [177, chapter 12]. The classic reference is [137], however the treatment of fluid mixtures differs from the approach pursued here. To this end, the underlying ideas are most clearly exposed in the early RIF papers [57, 61].

Here, bold symbols indicate vectors, and we have employed the $\boldsymbol{\nabla}$-notation familiar from vector analysis, indicating the divergence in the second terms on the left-hand side. Moreover, the three fluid components $\rho_\mathrm{f}, \rho_\mathrm{g}, \rho_\mathrm{s}$ are transported with their respective advection velocities $\mathbf{v}_\mathrm{f}, \mathbf{v}_\mathrm{g}, \mathbf{v}_\mathrm{s}$. The G-actin diffusion current $\mathbf{j}_\mathrm{g}$ is embedded in the advection flow with $\mathbf{v}_\mathrm{g}$. A similar diffusion of F-actin has been neglected, because the filaments are connected in a cross-linked structure. Importantly, we separately retain a distinct velocity field for each phase. Finally, the polymerization rate J' describes the chemical reaction $\rho_\mathrm{f} \leftrightarrow \rho_\mathrm{g}$ and quantifies both F-actin filament assembly and disassembly from/to surrounding G-actin monomers.

2. Mass density rescaling and volume fractions: Let m_a be the mass of a single actin monomer, and V_a its volume, both when dissolved and embedded in a filament. Correspondingly, let $m_\mathrm{s}, V_\mathrm{s}$ be mass and volume of one element of solvent. With the help of these quantities, we express the mass densities $\rho_\mathrm{f}, \rho_\mathrm{g}, \rho_\mathrm{s}$ in terms of the respective volume fractions $\theta_\mathrm{f}, \theta_\mathrm{g}, \theta_\mathrm{s}$, namely

$$\theta_\mathrm{f} = \frac{V_a}{m_a}\rho_\mathrm{f}, \qquad \theta_\mathrm{g} = \frac{V_a}{m_a}\rho_\mathrm{g}, \qquad \theta_\mathrm{s} = \frac{V_s}{m_s}\rho_\mathrm{s}. \tag{2.4}$$

Accordingly, dividing the actin equations (2.1, 2.2) by $m_\mathrm{a}/V_\mathrm{a}$, and the solvent equation (2.3) by $m_\mathrm{s}/V_\mathrm{s}$ gives us the mass balance equations in terms of volume fractions,

$$\text{F-actin:} \qquad \partial_t\theta_\mathrm{f} + \boldsymbol{\nabla}\cdot\left(\theta_\mathrm{f}\mathbf{v}_\mathrm{f}\right) = \frac{V_\mathrm{a}}{m_\mathrm{a}}J', \tag{2.5}$$

$$\text{G-actin:} \qquad \partial_t\theta_\mathrm{g} + \boldsymbol{\nabla}\cdot\left(\theta_\mathrm{g}\mathbf{v}_\mathrm{g} - D_\mathrm{g}\boldsymbol{\nabla}\theta_\mathrm{g}\right) = -\frac{V_\mathrm{a}}{m_\mathrm{a}}J', \tag{2.6}$$

$$\text{solvent:} \qquad \partial_t\theta_\mathrm{s} + \boldsymbol{\nabla}\cdot\left(\theta_\mathrm{s}\mathbf{v}_\mathrm{s} + D_\mathrm{g}\boldsymbol{\nabla}\theta_\mathrm{g}\right) = 0, \tag{2.7}$$

$$\text{bulk:} \qquad \theta_\mathrm{f} + \theta_\mathrm{g} + \theta_\mathrm{s} = 1. \tag{2.8}$$

Specifically, the G-actin diffusion current was assumed to be $\mathbf{j}_\mathrm{g} = -D_\mathrm{g}\boldsymbol{\nabla}\rho_\mathrm{g}$, and D_g denotes the G-actin diffusion constant. We stress that both m_s and V_s are effective quantities. If the solvent were to consist of water only, m_s and V_s would be precisely the mass and volume of one single H_2O molecule. However, because the cytosolic solvent contains many different molecules, we have to think of m_s and V_s as average values, without accounting for variations in the cytosolic composition. Of course one could always add additional mass balances if the model is required to resolve further details. Moreover, the molecular actin mass m_a and

volume V_a in solution is not exactly the same as that of a monomer in a filament. Both might be modified slightly due to interactions with the solvent. However, such meticulous details are generally neglected in RIF models [6, 8, 50, 58, 60, 62], since their effect on the flow in a whole-cell level description is expected to be small.

3. Combination of G-actin and solvent mass balance: Since the actin monomers with volume fraction θ_g are distributed throughout the aqueous solvent θ_s, we assume the monomer and solvent velocities to coincide, $\mathbf{v}_\mathrm{g} = \mathbf{v}_\mathrm{s} =: \mathbf{w}$. Denoting the combined volume fraction of G-actin and solvent by $\theta_\mathrm{w} := \theta_\mathrm{g} + \theta_\mathrm{s}$, we obtain a single effective mass balance by addition of the two relations (2.6, 2.7). Adding the result to (2.5) yields

$$\partial_t \theta_\mathrm{f} + \boldsymbol{\nabla} \cdot \big(\theta_\mathrm{f} \mathbf{u}\big) = \frac{V_\mathrm{a}}{m_\mathrm{a}} J', \tag{2.9}$$

$$\boldsymbol{\nabla} \cdot \big(\theta_\mathrm{f} \mathbf{u} + \theta_\mathrm{w} \mathbf{w}\big) = 0, \tag{2.10}$$

$$\theta_\mathrm{f} + \theta_\mathrm{w} = 1, \tag{2.11}$$

where we introduced the abbreviation $\mathbf{u} := \mathbf{v}_\mathrm{f}$. Here, the second equation expresses the incompressibility of the overall volume flux. Together with the third equation, the solvent velocity $\mathbf{w}$ could be expressed in terms of the actin network volume fraction θ_g and its velocity $\mathbf{u}$. We stress that there is no simple scaling conversion between the effective cytosol volume fraction θ_w and its mass density analogue ρ_w. Specifically we have

$$\rho_\mathrm{w} := \rho_\mathrm{g} + \rho_\mathrm{s} = \frac{m_a}{V_a}\theta_\mathrm{g} + \frac{m_s}{V_s}\theta_\mathrm{s}, \tag{2.12}$$

$$\theta_\mathrm{w} := \theta_\mathrm{g} + \theta_\mathrm{s} = \frac{V_a}{m_a}\rho_\mathrm{g} + \frac{V_s}{m_s}\rho_\mathrm{s}, \tag{2.13}$$

which follows from the density scaling relations (2.4). The reason for this delicacy is that both ρ_w and θ_w represent the density or volume fraction of a combined quantity, which contains both reactive and non-reactive chemical species. The possibility for writing simple conversion equations involving only one scaling factor like (2.4) requires that all chemically reacting species have their own mass balance equation.

2.2. Both in-phase force balances are friction-dominated

1. Navier-Stokes fluid force balances: In order to find the transport velocities $\mathbf{u}, \mathbf{w}$, we have to construct expressions for the momentum balances of the corresponding phases. We have argued in paragraph 1.6.2

that the dynamical behavior of the cellular cytoplasm is essentially that of a fluid. Since there are two fluid phases in RIF flows, we have two separate momentum balances of Navier-Stokes type,

$$\rho_{\mathrm{f}}\big(\partial_t + \mathbf{u}\cdot\boldsymbol{\nabla}\big)\mathbf{u} - \boldsymbol{\nabla}\cdot\big(\mathbb{S}_{\mathrm{f}} + \eta_{\mathrm{f}}\widetilde{\boldsymbol{\nabla}}\mathbf{u}\big) = \mathbf{f}_{\mathrm{f}}^{\mathrm{ext}}, \tag{2.14}$$

$$\rho_{\mathrm{w}}\big(\partial_t + \mathbf{w}\cdot\boldsymbol{\nabla}\big)\mathbf{w} - \boldsymbol{\nabla}\cdot\big(\mathbb{S}_{\mathrm{w}} + \eta_{\mathrm{w}}\widetilde{\boldsymbol{\nabla}}\mathbf{w}\big) = \mathbf{f}_{\mathrm{w}}^{\mathrm{ext}}. \tag{2.15}$$

with the combined G-actin/solvent mass density of the aqueous cytosol $\rho_{\mathrm{w}} := \rho_{\mathrm{g}} + \rho_{\mathrm{s}}$. The first term in both equations represents the inertia due to the fluid mass. The second term on the left-hand side represents stresses within the respective phase of the compound fluid. Specifically, we consider the viscous stresses $\eta_{\mathrm{f}}\widetilde{\boldsymbol{\nabla}}\mathbf{u}, \eta_{\mathrm{w}}\widetilde{\boldsymbol{\nabla}}\mathbf{w}$ in filament and aqueous phase, respectively. The involved symmetrized velocity gradient has tensorial structure and reads $\widetilde{\boldsymbol{\nabla}}\mathbf{v} := (\partial_i v_k + \partial_k v_i)$ for $\mathbf{v} = \mathbf{u}, \mathbf{w}$ in explicit components. Any other in-phase stress is represented by the two tensors $\mathbb{S}_{\mathrm{f}}$ and $\mathbb{S}_{\mathrm{w}}$, which will be specified later. Forces not arising in the corresponding fluid phase are summarized by the external forces $\mathbf{f}_{\mathrm{f}}^{\mathrm{ext}}, \mathbf{f}_{\mathrm{w}}^{\mathrm{ext}}$ on the right hand sides.

2. Dimensional considerations: In order to simplify these momentum balances, we estimate typical values of several involved key quantities. These values are presented in table 2.1 and further discussed in the appendix A.1. Using these typical values, we can render the momentum balances (2.14, 2.15) dimensionless. This is achieved by dividing both sides by $\rho_{\mathrm{f}}^0|\mathbf{u}^0|^2/L_0$ or $\rho_{\mathrm{w}}^0|\mathbf{w}^0|^2/L_0$, respectively, where $\rho_{\mathrm{f}}^0, \rho_{\mathrm{w}}^0$ are the characteristic mass densities, and L_0 is the typical length scale of the flow. With the characteristic advection velocities $u_0 := |\mathbf{u}^0|, w_0 := |\mathbf{w}^0|$, the scaled derivatives $\partial_t^u := L_0\partial_t/u_0, \partial_t^w := L_0\partial_t/w_0$ in time and $\boldsymbol{\nabla}_{L_0} := L_0\boldsymbol{\nabla}, \widetilde{\boldsymbol{\nabla}}_{L_0} := L_0\widetilde{\boldsymbol{\nabla}}$ in space we obtain

$$\frac{\rho_{\mathrm{f}}}{\rho_{\mathrm{f}}^0}\Big(\partial_t^{u_0} + \frac{\mathbf{u}}{u_0}\boldsymbol{\nabla}_{L_0}\Big)\frac{\mathbf{u}}{u_0} - \boldsymbol{\nabla}_{L_0}\cdot\Big(\frac{\mathbb{S}_{\mathrm{f}}}{\rho_{\mathrm{f}}^0 u_0^2} + \frac{\eta_{\mathrm{f}}}{L_0\rho_{\mathrm{f}}^0 u_0}\widetilde{\boldsymbol{\nabla}}_{L_0}\frac{\mathbf{u}}{u_0}\Big) = \frac{L_0\mathbf{f}_{\mathrm{f}}^{\mathrm{ext}}}{\rho_{\mathrm{f}}^0 u_0^2}, \tag{2.16}$$

$$\frac{\rho_{\mathrm{w}}}{\rho_{\mathrm{w}}^0}\Big(\partial_t^{w_0} + \frac{\mathbf{w}}{w_0}\boldsymbol{\nabla}_{L_0}\Big)\frac{\mathbf{w}}{w_0} - \boldsymbol{\nabla}_{L_0}\cdot\Big(\frac{\mathbb{S}_{\mathrm{w}}}{\rho_{\mathrm{w}}^0 w_0^2} + \frac{\eta_{\mathrm{w}}}{L_0\rho_{\mathrm{w}}^0 w_0}\widetilde{\boldsymbol{\nabla}}_{L_0}\frac{\mathbf{w}}{w_0}\Big) = \frac{L_0\mathbf{f}_{\mathrm{w}}^{\mathrm{ext}}}{\rho_{\mathrm{w}}^0 w_0^2}. \tag{2.17}$$

The dimensionless viscosities of the F-actin $\eta_{\mathrm{f}}/\big(L_0\rho_{\mathrm{f}}^0 u_0\big)$ and the cytosol phase $\eta_{\mathrm{w}}/\big(L_0\rho_{\mathrm{w}}^0 w_0\big)$ in the last summands on the left-hand side represent the inverse Reynolds numbers of the corresponding flow. If the Reynolds number is very low, the viscosity terms $\propto \eta$ will dominate over the mass

quantity	symbol	typical value	comment
F-actin density	ρ_{f}^0	$\sim 1.5\,\mathrm{g/cm^3}$	slightly higher than water
F-actin velocity	$\lvert\mathbf{u}^0\rvert$	$\lesssim 0.25\,\mu\mathrm{m/s}$	in fish keratocytes [78, 192, 229, 233]
F-actin viscosity	η_{f}^0	$\sim 500\,\mathrm{Pa\cdot s}$	in neutrophils [101, 104]
cell size	L_0	$\sim \mu\mathrm{m}$	up to $50\,\mu\mathrm{m}$
cytosol density	ρ_{w}^0	$\approx 1.1\,\mathrm{g/cm^3}$	similar to water
cytosol velocity	$\lvert\mathbf{w}^0\rvert$	$\lesssim 0.7\,\mu\mathrm{m/s}$	in fish keratinocytes [123]
cytosol viscosity	η_{w}^0	$\sim 10^{-3}\,\mathrm{Pa\cdot s}$	[202, table I]

Table 2.1.: The characteristic dimensions of cytoplasm flow can be estimated from various measurements. All these estimates are presented in appendix A.1, together with a short critique and further explanations. Note that the mass densities $\rho_{\mathrm{f}}^0, \rho_{\mathrm{w}}^0$ can also be measured in units of $\mathrm{pg}/\mu\mathrm{m}^3 \equiv \mathrm{g/cm^3}$.

inertia terms $\propto \rho$ on the left-hand side. In this way, inertia could be neglected, and the preceding equations would be much simpler. Indeed, with the numbers from table 2.1 and as discussed in appendix A.1, we obtain the Reynolds numbers

$$\text{F-actin network phase:} \qquad \mathrm{Re_f} := \frac{L_0 \rho_{\mathrm{f}}^0 u_0}{\eta_{\mathrm{f}}} \sim 10^{-12}, \tag{2.18}$$

$$\text{aqueous solvent phase:} \qquad \mathrm{Re_w} := \frac{L_0 \rho_{\mathrm{w}}^0 w_0}{\eta_{\mathrm{w}}} \sim 10^{-6}. \tag{2.19}$$

In order to ensure that the first terms in the equations (2.16, 2.17) can really be neglected safely, we have to take into account possible deviations of the dimensionless densities $\rho_{\mathrm{f}}/\rho_{\mathrm{f}}^0, \rho_{\mathrm{w}}/\rho_{\mathrm{w}}^0$ from unity. The overall concentration of actin monomers is usually rather low, e.g. some $500\,\mu\mathrm{M}$ at the leading edge of certain highly motile mouse melanoma cells [129]. Therefore it is clear that the dimensionless mass density of the cytosol $\rho_{\mathrm{w}}/\rho_{\mathrm{w}}^0$ is very close to 1, because the monomers would comprise only a very small part of the cytosolic solvent.[2] However, in the cytoskeleton phase we have to expect more variation in the concentration $\rho_{\mathrm{f}}/\rho_{\mathrm{f}}^0$,

[2]Compare the physiological actin concentration of $500\,\mu\mathrm{M} \equiv 0.0005$ mol/l with the concentration of densely packed "actin monomer" balls with diameter of 2.7 nm,

because actin filaments preferentially assemble at the leading edge. Nevertheless, considering the value Re_f, there is plenty of room for F-actin density variations, even if the inertia term in (2.16) is neglected. Indeed, if the estimated η_f were off by two orders of magnitude, cf. discussions in the appendix A.1, neglecting inertia in the cytoskeleton phase would still be valid at least for $\rho_\mathrm{f}/\rho_\mathrm{f}^0 < 10^8$, where we have allowed for an additional safety margin of two orders of magnitude.

3. Neglecting inertia terms: In conclusion, the force balances (2.14, 2.15) can be treated in the friction-dominated regime, and therefore it is sufficient to consider the corresponding Stokes equations,

$$-\boldsymbol{\nabla}\cdot\left(\mathbb{S}_\mathrm{f}+\eta_\mathrm{f}\widetilde{\boldsymbol{\nabla}}\mathbf{u}\right)=\mathbf{f}_\mathrm{f}^\mathrm{ext}, \tag{2.20}$$

$$-\boldsymbol{\nabla}\cdot\left(\mathbb{S}_\mathrm{w}+\eta_\mathrm{w}\widetilde{\boldsymbol{\nabla}}\mathbf{w}\right)=\mathbf{f}_\mathrm{w}^\mathrm{ext}. \tag{2.21}$$

In the following section, we take a closer look at the involved model stresses and forces.

2.3. Force balances include isotropic active stresses and Darcy permeation

In order to close the RIF system of equations for cytoplasm flow, we have to make several model assumptions regarding the effective stresses in the force balances. These assumptions are made in the sense of phenomenological constitutive laws, so that most important features of cytoplasm motion can be captured. Therefore, the chosen relations have to prove their usefulness a-posteriori, when comparing RIF theory with experiments.

1. External forces acting on the phases: Apart from possibly other contributions, e.g. due to substratum friction, the external forces on the right-hand side of equations (2.20, 2.21) contain a permeation term which represents the friction forces between filamentous actin network and aqueous solvent. According to the phenomenological Darcy law [53,161], such a permeative friction is proportional to the velocity difference. Moreover, it is generally assumed in RIF models, that this inter-phase friction is

which is approximately 0.12 M. Conversely, the mass density of "pure" F-actin of 1.5 g/cm^3 quoted in the table is equivalent to a concentration of 0.03 M, since a single actin monomer has the approximate mass of 42000 atomic mass units.

also proportional to the product of the two volume fractions $\theta_\mathrm{f}\theta_\mathrm{w}$, which is taken as a measure for the effective drag between the two phases. Noting that the inter-phase friction opposes the flow velocity of the respective phase, we write

$$\mathbf{f}_\mathrm{f}^\mathrm{ext} = \theta_\mathrm{f}\theta_\mathrm{w}\phi_\mathrm{ph}\big(\mathbf{w}-\mathbf{u}\big) + \mathbf{f}_\mathbf{u}, \qquad \mathbf{f}_\mathrm{w}^\mathrm{ext} = \theta_\mathrm{f}\theta_\mathrm{w}\phi_\mathrm{ph}\big(\mathbf{u}-\mathbf{w}\big), \tag{2.22}$$

with the friction coefficient ϕ_ph. The additional summand $\mathbf{f}_\mathbf{u}$ in the first equation represents possible other interactions of the cytoskeleton with the cell exterior, which shall play an important role in the following chapter. A similar contribution for the solvent has been dropped. To this end, one could think – for example – of osmotic effects due to ions in and around the cell. However, such contributions can alternatively be absorbed in the boundary conditions. We note that an extension of the present model including external cytosol forces is straight forward, and has already been proposed in [5, cf. $\mathbf{F}_a$].

2. Internal stresses in the phases: Now we turn to the in-phase stress tensors $\mathbb{S}_\mathrm{f}$ and $\mathbb{S}_\mathrm{w}$. Comparing the dimensionless viscosities or inverse Reynolds numbers of the two phases, c.f. equations (2.18, 2.19), we find that the F-actin viscosity exceeds the cytosol viscosity by approximately six orders of magnitude. In this way, F-actin poses a rather rigid obstacle for the cytosol. We therefore neglect the viscous term $\eta_\mathrm{w}\widetilde{\boldsymbol{\nabla}}\mathbf{w}$ in equation (2.21), because the effective inter-phase friction appears to be much higher. Since the aqueous phase is essentially passive, we do not consider any active contributions to its stresses. Therefore, we write for the corresponding cytosol stress

$$\boldsymbol{\nabla}\cdot\mathbb{S}_\mathrm{w} = -\theta_\mathrm{w}\boldsymbol{\nabla}p, \tag{2.23}$$

where we assume that forces arising from gradients in the hydrostatic pressure p split across the two phases according to their volume fraction.

Correspondingly, the pressure gradient appears with θ_f in the network phase. Next, we clearly have to retain the viscosity term in (2.20), because η_f is rather high. Indeed, the estimated F-actin viscosity as characterized by the dimensional number η_f is comparable to that of molten glass [59]. Moreover, we assume the model stress $\mathbb{S}_\mathrm{f}$ for the network to be isotropic, $\mathbb{S}_\mathrm{f} := S\mathbb{I}$, where $\mathbb{I}$ denotes the identity matrix $\mathbb{I} := \mathrm{diag}\big(1,\ldots,1\big)$, with the model function S to be specified later. A thermodynamically amenable construction of anisotropic stresses has been undertaken in the so-called Active Polar Gel (APG) theory [118], which is comparable to the one

presented here. In order to derive such anisotropic stresses, one introduces the mean orientation of the local F-actin network as new hydrodynamic variable called polarity [133]. However, this entails a plethora of cross-couplings, for example between the actin polymerization kinetics J', cf. equation (2.9), and the F-actin velocity $\mathbf{u}$ [42, 117]. For simplicity we therefore neglect these anisotropic stresses. In this way, we have

$$\boldsymbol{\nabla} \cdot \mathbb{S}_\mathrm{f} = \boldsymbol{\nabla}\big[S(\theta_\mathrm{f})\big] - \theta_\mathrm{f}\boldsymbol{\nabla} p. \tag{2.24}$$

In the past, various model functions have been considered for S, which all can be summarized by a difference of two functionally distinct terms,

$$S(\theta_\mathrm{f}) = \psi(\theta_\mathrm{f}) - \sigma(\theta_\mathrm{f}), \tag{2.25}$$

where ψ represents contractions in the F-actin network, and σ its osmotic swelling pressure. Even though being termed osmotic, this swelling pressure resides exclusively within the cell's cytoplasm and does not involve the cell membrane in any way. It arises because local regions with high F-actin volume fractions attract surrounding solvent cytosol in the same manner as salt attracts water.

Another possible interpretation of the two stress contributions is that ψ includes any active effects arising in the cell due to the consumption of energy in dedicated molecular machines. In contrast, σ encompasses purely passive effects which arise from the presence of concentration gradients in thermodynamic systems. A common assumption in RIF-type models is, that the network contraction is proportional to the network volume fraction θ_f. Moreover, contraction may be enhanced or inhibited by specific regulation factors, for example myosin. Again, swelling is generally considered to represent purely passive stress contributions. It has often been omitted from RIF models, or modeled by non-linear expressions involving some logarithm of θ_f, which arises from a suitably chosen thermodynamic potential.

The actual relations that have been published as models for S are summarized in table 2.2. Together with the external and internal model stresses (2.22, 2.23, 2.25), the resulting Stokes equations (2.20, 2.21) for the momentum balance in the two phases are

$$\text{F-actin:}\quad -\boldsymbol{\nabla}\cdot\big(\eta_\mathrm{f}\widetilde{\boldsymbol{\nabla}}\mathbf{u}\big) - \boldsymbol{\nabla}S(\theta_\mathrm{f}) + \theta_\mathrm{f}\boldsymbol{\nabla}p = \theta_\mathrm{f}\theta_\mathrm{w}\phi_\mathrm{ph}\big(\mathbf{w}-\mathbf{u}\big) + \mathbf{f}_\mathbf{u}, \tag{2.26}$$

$$\text{cytosol:}\quad \theta_\mathrm{w}\boldsymbol{\nabla}p = \theta_\mathrm{f}\theta_\mathrm{w}\phi_\mathrm{ph}\big(\mathbf{u}-\mathbf{w}\big). \tag{2.27}$$

By adding the latter equation to the former, we can eliminate the explicit dependence on the solvent variables $\theta_\mathrm{w}, \mathbf{w}$ from the F-actin momentum

#	**contraction** ψ	**swelling** σ	**viscosity** η_{f}	**references**
1.	$\psi_0\theta_{\mathrm{f}}$	0	$\eta_0\theta_{\mathrm{f}}$	[101, 136]
2.	$-\psi_0\theta_{\mathrm{f}}m$	0	$\eta_0\theta_{\mathrm{f}}$	[99]
3.	$\psi_0\theta_{\mathrm{f}}$	$\sigma_0\big\lvert\theta_{\mathrm{f}}+\ln(1-\theta_{\mathrm{f}})\big\rvert$	$\eta_0\theta_{\mathrm{f}}$	[57, 61]
4.	$\psi_0\theta_{\mathrm{f}}^2$	$\sigma_0\big\lvert\ln(1-\theta_{\mathrm{f}}/\theta_\sigma)\big\rvert$	$\eta_0\theta_{\mathrm{f}}$	[218]
5.	$\psi_0\theta_{\mathrm{f}}m$	$\sigma_0\big\lvert\ln(1-\theta_{\mathrm{f}})\big\rvert$	$\eta_0\theta_{\mathrm{f}}$	[6]
6.	$\psi_0\theta_{\mathrm{f}}^2/(1+\theta_{\mathrm{f}}/\theta_\psi)^2$	$\sigma_0\big\lvert\ln(1-\theta_{\mathrm{f}})\big\rvert$	$\eta_0\theta_{\mathrm{f}}$	[135]
7.	$\psi_0\theta_{\mathrm{f}}^2\exp\big(-\theta_{\mathrm{f}}/\theta_\psi\big)$	$\sigma_0\big\lvert\ln(1-\theta_{\mathrm{f}})\big\rvert$	$\eta_0\theta_{\mathrm{f}}$	[8]
8.	$\psi_0\theta_{\mathrm{f}}(m-m_0)$ and $\psi_0\theta_{\mathrm{f}}\ln(m/m_0)$	0	$\eta_0\theta_{\mathrm{f}}\exp(\theta_{\mathrm{f}}/\theta_\eta)$	[59]
9.	$\psi_0\theta_{\mathrm{f}}$ and 0	0	$\eta_0\theta_{\mathrm{f}}\exp(\theta_{\mathrm{f}}/\theta_\eta)$	[100]
10.	$\psi_0\theta_{\mathrm{f}}^2\exp\big(-\theta_{\mathrm{f}}/\theta_\psi\big)$	0	η_0	[200]

Table 2.2.: In earlier applications of RIF-type models, various phenomenological stress functions have been explored. They are presented in the table without any particular order. Here $\theta_{\mathrm{f}} \geq 0$ indicates the F-actin volume fraction, and $m \geq 0$ the dimensionless density of of a messenger modulating network contraction. All other quantities are positive constants in specific models. Note that by equations (2.20, 2.25), the contraction ψ has the same sign as the viscosity term η_{f}, whereas the swelling σ has the opposite sign. Specifically, the "contraction" ψ in 2. actually represents a polymerization pressure at the leading edge of crawling cells. The non-linear viscosity in 8. is a necessary ingredient so that separated endo- and ectoplasm zones emerges in a model of the fountain flow in *Amoeba proteus*.

balance, because the ϕ_{ph}-terms cancel and the volume fractions add up, $\theta_{\mathrm{f}} + \theta_{\mathrm{w}} = 1$, see equation (2.11). Moreover, we can solve (2.27) for the velocity $\mathbf{w}$ of the aqueous solvent, and insert it into the divergence relation for the total volume flux (2.10), which yields

$$\boldsymbol{\nabla} \cdot \Big(\frac{1 - \theta_{\mathrm{f}}}{\phi_{\mathrm{ph}} \theta_{\mathrm{f}}} \boldsymbol{\nabla} p \Big) = \boldsymbol{\nabla} \cdot \mathbf{u}, \tag{2.28}$$

where again (2.11) was employed. This represents the compressibility of the F-actin flow as embedded in the solvent. Naturally, compressibility in the network phase does not affect the incompressibility of the bulk cytoplasm (2.10), because the aqueous solvent flow is present to compensate.

3. Reactive interpenetrating flow field equations: Putting all the pieces together again, the RIF field equations are given by (2.9), (2.26+2.27), and (2.28) for

$$\text{F-actin volume fraction } \theta: \qquad \partial_t \theta + \boldsymbol{\nabla} \cdot \big(\theta \mathbf{u} \big) = J, \tag{2.29}$$

$$\text{F-actin transport velocity } \mathbf{u}: \qquad - \boldsymbol{\nabla} \cdot \big(\eta_{\mathrm{f}} \widetilde{\boldsymbol{\nabla}} \mathbf{u} \big) - \boldsymbol{\nabla} S + \boldsymbol{\nabla} p = \mathbf{f}_{\mathbf{u}}, \tag{2.30}$$

$$\text{Hydrostatic pressure } p: \qquad \boldsymbol{\nabla} \cdot \Big(\frac{1 - \theta_{\mathrm{f}}}{\phi_{\mathrm{ph}} \theta_{\mathrm{f}}} \boldsymbol{\nabla} p \Big) = \boldsymbol{\nabla} \cdot \mathbf{u}, \tag{2.31}$$

respectively. Here, the index f at F-actin volume fraction θ was dropped for convenience, and the chemical reaction term on the right-hand side of (2.29) has been condensed, $J := V_{\mathrm{a}} J' / m_{\mathrm{a}}$, cf. (2.9). For solving the the preceding system of equations for $\theta, \mathbf{u}, p$, the fields for the aqueous solvent phase do not need to be computed explicitly. Instead, for given $\theta, \mathbf{u}, p$ they directly follow from the relations (2.11) and (2.27), namely

$$\text{cytosol volume fraction } \theta_{\mathrm{w}}: \qquad \theta_{\mathrm{w}} = 1 - \theta, \tag{2.32}$$

$$\text{cytosol transport velocity } \mathbf{w}: \qquad \mathbf{w} = \mathbf{u} - \frac{1}{\phi_{\mathrm{ph}} \theta} \boldsymbol{\nabla} p. \tag{2.33}$$

In this way, the quantitative RIF description of the dynamics of the cytoplasm is closed. Note that the pressure p effectively serves as Lagrange multiplier to enforce the incompressibility constraint (2.10), stating that the bulk flux velocity $\theta \mathbf{u} + (1 - \theta) \mathbf{w}$ is divergence free. This is an important property of most generic liquids like e.g. water, and one of the checkmarks to distinguish fluids from gases, because in general the latter are highly compressible.

2.4. The Active Polar Gel is an alternative cytoplasm theory

1. Active Polar Gel theory: The initial starting point for the RIF theory was, that the cytoplasm should be described as a multi-component fluid. During the last couple of years, an alternative theory was developed based on the same underlying idea. This theory is usually called "Active Polar Gel" (APG) [117, 118, 133] and based on linear irreversible thermo-hydrodynamics [54].

In APGs, there is in principle only one independent velocity in the fluid, namely the center-of-mass velocity. This velocity derives from one single force balance, however it appears in the mass balances of all modeled molecular species. For the cytoplasm, one typically considers (i) polymer/F-actin, (ii) monomer/G-actin and (iii) aqueous solvent, as in RIF described above. The relative mixing between these three phases is accomplished by augmenting the center-of-mass advection with an additional so-called diffusion flux in each phase. Importantly, these fluxes incorporate all kinds of possible transportation, including diffusion due to both thermal and concentration gradients, relative advection of different molecular species, and several other mechanisms.

Starting from the Helmholtz free energy[3], one derives source terms of the entropy density. These source terms have a characteristic structure, each being a product of a so-called thermodynamic flux with a so-called conjugate force. For the constitutive equations, one makes a general ansatz by writing fluxes as linear functions of forces and their gradients. Possible coupling coefficients have to obey the Curie principle [54, chapters IV, VI] and Onsager reciprocal relations [54,165,166], which all follow from fundamental symmetry principles, such as the expected behavior under time- and/or space inversion. As a result, the emerging entropy source is a non-negative definite expression in the forces and their gradients, so that Clausius inequality[4] holds.

A central prerequisite to express the thermodynamic fluxes as linear ansatz of the forces is the presence of anisotropy in the APG. This is implemented by introducing a new, vector-valued hydrodynamic variable called polarity. For example, a thin slab of an Active Polar Gel spontaneously starts to flow in the direction of its polarity [42]. Active

[3]The (Helmholtz) free energy is an important quantity in classical thermodynamics, see [43] for an introduction.

[4]In a closed thermodynamic system, the entropy $\mathcal{S}$ cannot decrease, $\Delta\mathcal{S} \geq 0$.

contractions in APGs are considered to be eventually driven by chemical fuels like ATP. The dominant contributions to these contractions are, however, mediated by aforementioned polarity vector, because it provides for an inter-conversion instance from scalar- to vector-valued variables in the constructed entropy source. Thus, Active Polar Gels can only be "active" whence they are anisotropic. Without polarity, there cannot be active contractions in the otherwise passive gel.

Recently, APG theory has been extended by Callan-Jones and Jülicher [42] to exhibit a permeation term similar to the Darcy law involved in RIF, cf. equation (2.22). In section 2.2 of this paper, they present the RIF-like limit of APG theory. Under several fairly strong assumptions they rewrite the linear ansatz for the polymer/solvent diffusion current to yield force balances much akin to the ones of RIF. Naturally, as RIF models are isotropic, the APG in the RIF limit is actually passive, i.e. it does not involve the polarity vector and therefore does not exhibit active contractions of the polymer phase. Surprisingly, and in contrast to RIF, the viscosity and pressure terms appear in the solvent force balance [42, equation (37)].

2. Differences between APG and RIF: Even though both theories start from the same basic idea, there seem to be several essential differences between Active Polar Gels and Reactive Interpenetrating Flow:

1. RIF models are isotropic. Nevertheless, the general assumption is that there are active contractile stresses in the polymer of F-actin phase.

2. In RIF, each phase has a transport velocity on its own, together with a corresponding force balance.

3. Diffusion currents in RIF are not included in the corresponding in-phase transport velocities. They do not "come out" of the theory by a kind of linear ansatz. Instead, they are explicitly modeled, cf. the D_g-terms in equations (2.6, 2.7).

Moreover, one commonly assumes non-linear chemical reactions in RIF-type models, for example for the actin polymerization kinetics J', cf. equation (2.1). Since the underlying linear irreversible thermo-hydrodynamics [54] cultivates the linear ansatz as virtue, inclusion of similar effects in APGs is somewhat against the spirit of the theory. Indeed, as pointed out in [54, chapter X, §2], chemical reactions commonly call for non-linear

modeling expressions, which cannot be faithfully represented by linear irreversible thermo-hydrodynamics. In order to circumvent this limitation in APGs, one could – of course – choose suitable non-linear coupling coefficients depending e.g. on the actin monomer concentration in the cytosol. In doing so, one then has to ensure that the resulting entropy source obeys to Clausius inequality.

2.5. Specific assumptions inherit intrinsic model limitations

1. Main assumptions of RIF models: The central assumptions of the RIF cytoplasm model presented in this chapter can be summarized as follows:

(i) The total cytoplasm mass is conserved and consists of two phases, $\rightsquigarrow$ equation (2.32).

(ii) There is material transport and turnover in both phases, $\rightsquigarrow$ equations (2.30, 2.33).

(iii) The total cytoplasm flux is incompressible, $\rightsquigarrow$ equation (2.31).

(iv) The cytoskeleton motion effectively comprises a friction-dominated Stokes flow, $\rightsquigarrow$ equation (2.30).

(v) There are active and isotropic contractile stresses in the cytoskeleton phase, $\rightsquigarrow$ equation (2.25).

(vi) The friction between cytoskeleton and cytosol is Darcy-like, $\rightsquigarrow$ equation (2.22).

Importantly, the time scale envisioned for such a cytoplasm model is given by typical dynamical features of cellular migration. According to the arguments in paragraph 1.7.1, this time scale would range from minutes to hours. On the seconds time-scale, the elastic response of the cytoskeleton would have to be considered. At the other end of the time-scale window, we would have to account for cell reorganization as induced by genetic regulation or the progress of the cell cycle.

2. Coarse-graining of particles into continuum densities: Common to all continuum models is the assumption of a intermediate time- and length-scale, in which averages of particle and momentum densities can be defined in a meaningful way. In order for a model to be useful, the details of common experiments should be clearly resolved. For example, the typical concentration of F-actin on the leading edge of crawling cells is $\sim 500\,\mu\mathrm{M}$[5] [129]. Neglecting advanced techniques involving fluorescence or near-field imaging, the typical resolution limit of an optical microscope is $\sim 200\,\mathrm{nm}$. Also, the lamella at the leading edge of the cell is roughly 100 nm high. We have therefore an averaging volume of approximately $200\cdot 200\cdot 100\,\mathrm{nm}^3$ at the crucial intermediate-scale averaging of our continuum description. Correspondingly, this volume contains around 1200 G-actin monomers. Naturally, if the concentration of the involved molecules is much lower, e.g. in the nM region for typical messenger species, this limitation becomes more severe. However, as a positive side-effect, we can safely choose a simulation grid with fairly wide compartment spacing. Not only does this ensure the validity of the continuum description, it also speeds up computations significantly.

3. Number of distinct mass equations: In the derivation of the RIF theory, we had to rescale the initial continuity equations for the mass densities. This rescaling has to be performed using constant scalars, otherwise additional terms would arise from the derivatives in the equations. For example, starting from the mass balance equations for (i) F-actin density (ii) G-actin/solvent density, the rescaling of (ii) cannot be done without the additional assumption that the local amount of G-actin would be constant in the combined G-actin/solvent density. Luckily, such problems can be circumvented by starting from a sufficient number of continuity equations. Specifically, both educt and product of a chemical reaction in the cytoplasm need to be included as separate mass balances. One can reduce the number of equations after scaling, by simple addition of the relations to be lumped together.

4. Is the pressure p negligible? The authors of [186, page 1856] argue that one can neglect the pressure term p in equation (2.30). Indeed, for keratocytes they estimate the corresponding stress to be approximately 10% of the viscoelastic or contractile contributions of the cytoskeleton

[5]The unit μM indicates the number of micro-moles per liter.

phase. Therefore, the additional equation of the Darcy law is not necessary in their approach. However, here we model both cytoskeleton and cytoplasm phase, so that the pressure is an essential ingredient to implement the incompressibility of the composite cytoplasm. The latter can be pictured as internally condensing sponge, where actin turnover changes the local two-phase material composition. In this way, each phase is separately compressible. At the same time, when exerting external pressure on a wet sponge, it will respond by releasing some of its contained fluid, so that the total volume of sponge and water remains constant. In the RIF description, the cytoplasm would respond in the same way, and the pressure is required to enforce this dynamical behavior. Note however that the wet sponge analogy is limited, because the network phase in actual cytoplasm is highly diluted as compared to the pores of a sponge.

5. RIF force balances and their dissipation functional: Both Stokes equation (2.30), and the divergence relation (2.31) can be derived by minimizing a functional that can be interpreted as the power dissipated in the RIF cytoplasm at each time instant. Moreover, the construction of this functional involves the mathematically weak formulation of (2.30, 2.31) and opens the possibility to construct numerical solutions with the help of finite elements. The derivation of the RIF equations from such a power dissipation functional was proposed in [5]. Interestingly, a similar formulation of a so-called two-fluid model of polymer blends and melts has been given by Doi and Onuki in 1992 [70]. In order to formulate and minimize dissipation functional, they employ the method of Onsager [165, 166] which is at the heart of linear irreversible thermo-hydrodynamics [54]. Recently, these models have been applied to the growth and invasion of skin tumors [22,46]. All these efforts show that two-phase models are a versatile tool and promise a wide applicability in the biological sciences.

3. Coupling of cytoplasm and adhesion dynamics determines single cell polarization and locomotion[1]

Summary: In this chapter we describe whole-cell motion by means of a one-dimensional model system. Thereby, we consider both the internal cytoplasm dynamics as well as the exterior adhesion site formation. The cytoplasm dynamics in the cell is represented by the Reactive Interpenetrating Flow equations from chapter 2. Cytoskeletal contraction is active and mediated by an additional density variable resembling the role of myosin as tension-inducing agent. Moreover, explicit consideration of an adhesion mediator akin to integrin provides for connections to the substratum so that the model cell can exert traction. When all these ingredients are combined in a coupled system of equations, the model cell exhibits two distinct steady states:

(i) In the symmetric resting state, traction from front and back balances so that the cell adheres to the substratum without moving.

(ii) In the polarized migrating state, an asymmetry in traction drives persistent cell locomotion.

These two steady states are rather stable and autonomous in the sense that they do not need any out-of-model regulation e.g. like prescribing front and back of the cell. Here we induce the transition between resting and migrating state by a super-threshold external stimulus. Various emerging characteristics of the simulation model compare favorably with experimental data obtained from highly motile cells.

A simplified version of the model above can be cast in a quasi two-dimensional form. To this end, we write actin, integrin, substratum ligands and the local lamella width as freely evolving fields on the unit circle, and assume a basic molecular transport mechanism relating to the cellular migration velocity. The resulting model cell is capable of exhibiting shape fluctuations and migration trajectories in the plane.

[1]Data presented in sections 3.1–3.7 of this chapter have been published in [6], which was jointly written by Wolfgang Alt, M.B., and Christoph Möhl.

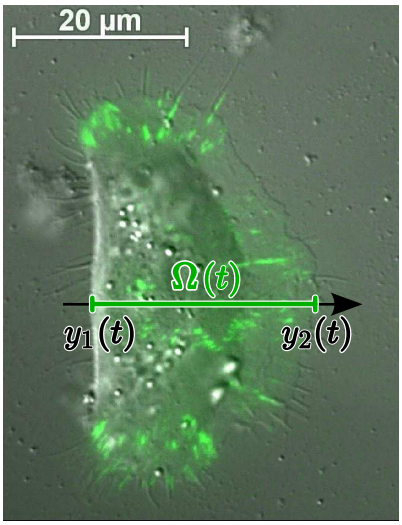

Figure 3.1.: Certain cells develop characteristic fan-like shape during migration. Specifically, the anterior-posterior axis of the cell is given by direction of its motion. Here we define the model variables on the time dependent one-dimensional interval $\Omega(t) = [y_1(t), y_2(t)]$ along the anterior-posterior axis of the cell. Marked by the fluorescence dye are the focal adhesion contacts which connect the cell to the underlying substratum. The presented microscopic picture of a human epidermal keratinocyte is courtesy of Claudia Schäfer, Merkel group, Forschungszentrum Jülich [189, movie 05].

3.1. Myosin leads to cytoskeletal contraction

1. Simulation domain: Human epidermal keratinocytes polarize into a fan-like shape with a rather straight posterior retracting end and the roughly semi-elliptical, protruding lamella at the anterior front, cf. figure 3.1. Therefore it is natural to approximate the domain $\Omega(t)$ of the cytoplasmic equations of motion by the interval

$$\Omega(t) = \big[y_1(t), y_2(t)\big], \tag{3.1}$$

aligned on the posterior-anterior axis of a crawling cell. Thus, we model a section through the cell, from posterior to anterior end, and approximately through the center of the cell nucleus. In figure 3.1, this section is indicated by the green bar and bounded by the intersections of the horizontal axis with the cell outline. The ends of the cell are denoted by

the spatial coordinates $y_1(t)$ and $y_2(t)$, whereby it is not specified a-priori which of these ends will be the anterior or posterior one. Importantly, all velocities in following model equations are measured in the lab frame at rest.

2. Two molecular states of myosin motors: The filaments in the cytoskeleton phase may be connected to various specialized kinds of linker molecules, each of which is responsible for specific functions. In particular, we are interested in molecules involved in physical mechanisms such as force generation and transduction. As we have seen in paragraphs 1.2.1 and 1.6.1, myosin proteins attach to the actin filaments of the cytoskeletal phase and create contractile forces by means of sliding the adjacent filaments in opposite directions. Here we consider two main states of this process:

1. bound myosins m_b are connected with the filamentous phase and give rise to contractions therein,

2. free myosins m_f are immersed in the solvent phase and diffuse freely.

Importantly, m_b and m_f describe the respective molecular concentrations with a dimension of dimension number/volume.

3. Scalar reaction, diffusion and transport equations: In one spatial dimension we can write all quantities as scalars, including the previously introduced F-actin transport velocity $\mathbf{u} \equiv u$. Denoting the spatial coordinate by $y \in \Omega \equiv [y_1, y_2]$, the mass balances for bound and free myosin are

$$\partial_t m_b + \partial_y\big(m_b u\big) = \quad \alpha_m \theta m_f - \delta_m(\theta) m_b, \tag{3.2}$$

$$\partial_t m_f - \partial_y\big(D_m \partial_y m_f\big) = -\alpha_m \theta m_f + \delta_m(\theta) m_b. \tag{3.3}$$

The second terms on the left-hand sides represent material transport. Since m_b is bound to the F-actin network, it is convected with the cytoskeleton transport velocity u. In contrast, the free myosins m_f merely diffuse with constant D_m, because there is no specific anchoring for m_f in the cytosol. The kinetic terms with α_m, δ_m quantify the local turnover in the reversible chemical reaction $m_f \leftrightarrow m_b$. The association rate α_m on the right-hand sides describes the bond formation between free myosins

m_f and cytoskeletal filaments. The bond dissociation rate $\delta_m = \delta_m(\theta)$ is exponential in the volume fraction of the cytoskeleton phase θ,

$$\delta_m(\theta) = \delta_{m0} \exp\Big(\frac{\theta}{\theta_m}\Big), \tag{3.4}$$

which resembles steric inhibition or competition for binding sites.[2] The two constants δ_{m0} and θ_m are model parameters, see appendix table A.2. The boundary conditions for the two myosin mass balances will be discussed in section 3.4.

From equations (3.2, 3.3) we can obtain the chemical equilibrium concentration for m_b. Setting the left-hand sides to zero, i.e. vanishing transport $\partial_y \dots$ and concentration change $\partial_t \dots$, we solve the remaining expressions for

$$m_b = \frac{\alpha_m \theta}{\delta_m(\theta)} m_f, \tag{3.5}$$

where m_f now represents the constant base-level concentration of free myosin.

4. Myosin and active stresses: When in contact with the cytoskeleton, bound myosin m_b gives an active contribution to the model stress S from equation (2.25). The specific form of this active stress contribution will be introduced in section 3.3.

3.2. Integrin connects cytoskeleton and substratum

1. Four integrin binding states: In the introduction, paragraphs 1.2.1 and 1.6.3, we have already seen how integrin affects the cellular migration machinery. Recall that integrin is a trans-membrane receptor, which has binding sites for both intracellular and extracellular ligands. In this way, integrin provides for the links of the cell to the substratum or the extracellular matrix fabric. Notably, the fairly complex process of assembling and disassembling so-called focal adhesion sites involves various regulation hooks [87]. Based on the already present ingredients of our model, we here employ a four-state model for the integrin binding kinetics, which was originally proposed by Palacek and coworkers [170] and subsequently applied in a model of cell fragment motion [135]. In these four-state

[2] In [6, eq. 8], the dissociation rate δ_m was $\propto (1 + \theta^2/\theta_m^2)$. However, the model modification (3.4) with exponential was actually used in [6, section 4.2].

models, one separately takes into account the state of both exterior and interior binding sites:

(i) free integrins b_f diffuse in the cell membrane,

(ii) actin bound integrins b_a are connected with the cell's actin cytoskeleton on their interior binding site,

(iii) substratum bound integrins b_s are attached to the extracellular matrix on their exterior binding site,

(iv) bound integrins b_b maintain connections on both binding sites, providing the link between substratum and cytoskeleton.

A cartoon summary of the four binding states is presented in figure 3.2.

2. Integrin reaction, diffusion and transport equations: According to figure 3.2, we write four mass balance equations for the respective number of integrins per basal cell area,

$$\partial_t b_f - \partial_y\big(D_f \partial_y b_f\big) = -\beta_{fsa} b_f + \delta_{sf} b_s, \tag{3.6}$$

$$\partial_t b_a + \partial_y\big(b_a u\big) = \alpha_{fa} b_f - \beta_{fab} b_a + \delta_{ba} b_b, \tag{3.7}$$

$$\partial_t b_s = \alpha_{fs} b_f - \beta_{fsb} b_s + \delta_{bs} b_b, \tag{3.8}$$

$$\partial_t b_b = + \alpha_{sb} b_s + \alpha_{ab} b_a - \beta_{sab} b_b. \tag{3.9}$$

For the sake of better readability, we introduced the combined reaction constants

$$\begin{aligned} \beta_{fsa} &\equiv \alpha_{fa} + \alpha_{fs}, \qquad & \beta_{fab} &\equiv \delta_{af} + \alpha_{ab}, \\ \beta_{fsb} &\equiv \alpha_{sb} + \delta_{sf}, \qquad & \beta_{sab} &\equiv \delta_{ba} + \delta_{bs}. \end{aligned} \tag{3.10}$$

Several reaction constants depend on the amount of present actin θ and the local force f_u,

$$\alpha_{fa} = \alpha^0_{fa} \cdot \theta, \qquad \alpha_{sb} = \alpha^0_{sb} \cdot \theta, \tag{3.11}$$

$$\delta_{ba} = \delta^0_{ba} \cdot \exp\big(\rho_{ba}|f_u|\big), \qquad \delta_{bs} = \delta^0_{bs} \cdot \exp\big(\rho_{bs}|f_u|\big). \tag{3.12}$$

The first two identities mean that integrins are recruited to the cytoskeleton in an auto-catalyzed manner proportional to the local amount of F-actin. The second two equations resemble the dependence of chemical bond rupture on the applied force f_u in focal adhesions b_b. For further details on this force-induced rupture mechanism see section 1.6.6. All the

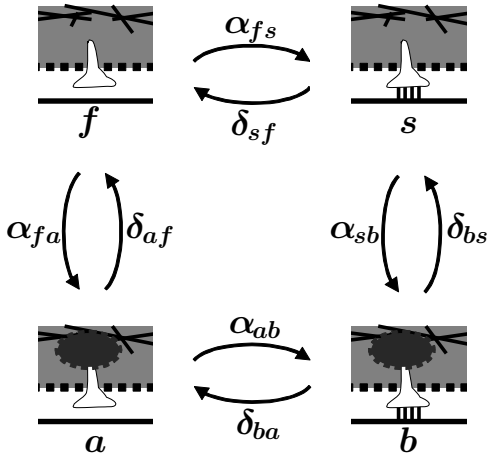

Figure 3.2.: The adhesion of cells to the extracellular matrix or substrata is mediated by so-called integrins. This whole class of transmembrane molecules connects the intracellular cytoskeleton to the extracellular matrix, for example to fibronectin. If we do not consider any further mediator proteins, this leaves four distinct binding states for a single integrin molecule: (i) free integrins (f) diffuse on the cell membrane, (ii) actin bound integrins (a) are linked with the cytoskeleton within the cell, (iii) substratum bound integrins (s) are attached to the adhesion sites on the extracellular matrix, and (iv) bound integrins (b) have connections to both substratum and the cytoskeleton. In the text, we denote the corresponding integrin concentrations by b_f, b_a, b_s, b_b, respectively. The association and dissociation rates $\alpha., \delta.$ characterize the formation and subsequent bond breaking kinetics of the integrins. Initially, such an adhesion model has been proposed in [170]. The cartoons presented here are courtesy of Esa Kuusela [135].

remaining coefficients and reaction constants are model parameters, see appendix table A.2. Finally, the specific form of f_u will be introduced in equations (3.14, 3.38).

In addition to the chemical kinetics, we consider material transport in equations (3.6–3.9). Being immersed in the cell membrane, free integrins diffuse with the diffusion constant D_f, see equation (3.6). Moreover, actin bound integrins b_a are advected with the F-actin cytoskeleton velocity u, cf. equation (3.7). Finally, due to their rigid connections with the substratum, both substratum and double bound integrins b_s, b_b are at rest. Therefore, equations (3.8, 3.9) lack a transport term with ∂_y. As for myosin, the boundary conditions will be discussed in section 3.4.

3. Parameter estimates: Regarding the model parameters presented in this section, only few rather rough estimates can be extracted from experimental data. Integrin transport properties like velocities and diffusion constants have been measured in Chinese hamster ovary cells by means of image correlation microscopy [230, table 1]. The reported diffusion constants are approximately $0.5 \ldots 6$ times the value from appendix table A.2. For all the chemical parameters α, δ, we refer to the original model [170, table 1] and references therein.

3.3. Cytoplasm contractions and adhesion sites join forces in whole-cell migration

In this section we combine the equations for reactive interpenetrating flow, myosin reaction/transport and four-state integrin reaction/transport into a coupled system jointly describing cytoplasm and adhesion dynamics of a one-dimensional migrating model cell.

1. Reactive interpenetrating flow: In one spatial dimension, the general equations (2.29, 2.31, 2.30) for the combined cytoskeleton and cytosol flow read

$$\partial_t \theta + \partial_y\big(\theta u\big) = J, \tag{3.13}$$

$$-\partial_y\big(\eta \partial_y u\big) - \partial_y\big(S - p\big) = f_u, \tag{3.14}$$

$$\partial_y\Big(\frac{1-\theta}{\phi_{\mathrm{ph}}\theta} \cdot \partial_y p\Big) = \partial_y u, \tag{3.15}$$

where all quantities have been replaced by their scalar representation, i.e. $\mathbf{u} \equiv u, \mathbf{f_u} \equiv f_u$ and $\boldsymbol{\nabla} = \widetilde{\boldsymbol{\nabla}} \equiv \partial_y$. As in chapter 2, θ denotes the

F-actin volume fraction, u its transport velocity, and p the hydrostatic pressure. The force f_u on the right-hand side of (3.14) will be specified later in equation (3.38).

2. Viscosity and actin polymerization: The viscosity η is assumed to be linear in the F-actin volume fraction,

$$\eta = \eta_0 \theta, \tag{3.16}$$

because denser filament networks are more viscous due to increased entanglement [69].

The actin polymerization J is believed to be mostly determined by the amount of available barbed or plus ends θ_+ in the filamentous network phase [179]. Following [151], we write $\partial_t \theta_+ = \beta_n(\theta) - \omega\theta_+$ for the corresponding kinetic evolution equation, where β_n is denotes the F-actin branching rate and ω the rate of branch number reduction due to capping proteins. Assuming that the preceding chemical reaction quickly reaches its equilibrium, this relation reduces to

$$\theta_+(\theta) = \beta_n(\theta)/\omega. \tag{3.17}$$

This equilibrium assumption relies on the idea that the reaction kinetics is fast as compared to the other processes occuring in the cell during migration. The effective F-actin branching rate β_n has two contributions,

$$\beta_n = \varepsilon + \nu \frac{\theta}{\theta_\beta + \theta}. \tag{3.18}$$

Here, ε summarizes the spontaneous actin nucleation rate, which is expected to be low, because most actin monomers associate with the polymerization inhibitor thymosin (S.A. Koestler, private communication). The second term on the right hand side of (3.18) represents stimulated filament branching of the actin network. Thereby, $\nu = \nu_0 \cdot [\mathrm{Arp2/3}]$ is proportional to the concentration of activated Arp2/3 complexes inducing branches. Also, branching begins to saturate at the characteristic volume fraction θ_β. The net F-actin polymerization J includes these ingredients in a specific manner,

$$J = \big(\alpha_B \theta_g - \delta_B\big)\theta_+(\theta) - \delta_a \theta + \text{perturbations}. \tag{3.19}$$

Again, F-actin polymerization mostly occurs at the barbed ends θ_+ of the filaments, which comprises a mechanism of auto catalysis. Thus the

polymerization term $\alpha_B \theta_g \theta_+$ depends linearly on the amount of available barbed ends θ_+, but also on the present G-actin monomers θ_g. Actin disassembly occurs in two distinct ways, namely (i) via the depolymerization δ_B at plus or barbed ends θ_+, and (ii) via other mechanisms like filament severing, pointed-end depolymerization or other degradation, with the lumped rate δ_a. Since we do not explicitly resolve the G-actin monomers as a separate phase in the compound fluid, we have to prescribe their volume fraction as constant $\theta_g < 1 - \theta$ as part of the aqueous cytosolic phase. This assumption is not problematic because the F-actin volume fraction θ is expected to not exceed $\theta \sim 0.1$, even under the rather extreme conditions at the leading edge of the cell. The last term in the preceding equation contains contains the small stochastic perturbations that were employed as a robustness check during the simulations. As usual, the constant model parameters $\eta_0, \omega, \varepsilon, \nu_0$, [Arp2/3], $\theta_\beta, \alpha_B, \theta_g, \delta_B$ and δ_a are given in appendix table A.2.

3. Myosin induced contraction and cytoskeleton swelling: The bound myosins m_b are attached to the F-actin cytoskeleton θ, and induce a certain contractile stress ψ in the filament phase. Together with the swelling pressure σ we obtain the effective cytoplasm stress

$$S = \psi - \sigma = \psi_0 \theta m_b - \sigma_0 \big|\ln(1-\theta)\big|, \tag{3.20}$$

cf. also row 5 in table 2.2 As mentioned in paragraph 2.3.2, the second term σ on the right hand side arises due to osmotic effects, because regions with high F-actin volume fractions attract solvent cytosol in the same manner as salt attracts water.

In order to better understand the first term ψ, we insert the equation (3.5) corresponding to the situation when bound myosin m_b is in chemical equilibrium with respect to a certain fixed free myosin concentration m_f. With the help of this approximation we have

$$\text{myosin equilibrium:} \qquad \psi \overset{(3.5)}{=} \psi_0 \frac{\alpha_m m_f}{\delta_{m0}} \cdot \frac{\theta^2}{\exp(\theta/\theta_m)}, \tag{3.21}$$

In this way, the active cytoskeleton stress S depends only on the F-actin volume fraction θ, and we can plot the emerging $S(\theta)$, see figure 3.3. However we emphasize that in the actual simulations the more complete model expression from equation (3.20) has been employed, and the concentrations of both myosin species m_b, m_f have been retained as free variables.

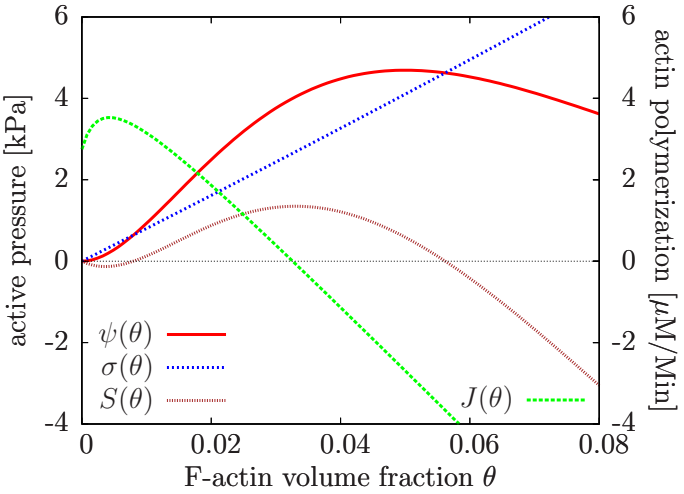

Figure 3.3.: Stress model functions according to equation (3.20) with the simplification (3.21). Both active contractile stress ψ and osmotic swelling pressure σ depend on the F-actin volume fraction θ, and jointly constitute the active cytoplasm stress $S = \psi - \sigma$. This stress should be compared with the F-actin assembly rate $J(\theta)$. In the low concentration regime, strong polymerization overcomes the weak expanding pressure from S. In contrast, in the high concentration regime, strong depolymerization and strong pressure join forces to spread and dissolve all the F-actin. In the intermediate regime, the contractile stress causes the filaments to aggregate. For the plot of ψ, the free myosin concentration was $m_f = 10\,\mu\text{M}$.

3.4. Boundary conditions describe phenomena close to the plasma membrane

1. Lab frame coordinates and velocities: In the cell migration model presented here, all quantities are written in terms of the lab frame attached to the resting substrate underneath the cell. As already mentioned, the moving domain $\Omega(t)$ is delimited by the set of time-dependent boundary points $\Gamma := \partial\Omega = \{y_1(t), y_2(t)\}$, see figure 3.1. The motion of the free boundary $\dot{\Gamma}$ can therefore be conveniently expressed in terms of the boundary point velocities,

$$\dot{\Gamma}\big|_{y_1} = \dot{y}_1 \cdot \nu_\Gamma\big|_{y_1}, \qquad \dot{\Gamma}\big|_{y_2} = \dot{y}_2 \cdot \nu_\Gamma\big|_{y_2}, \tag{3.22}$$

where we again stress that these boundary point velocities $\dot{y}_1, \dot{y}_2$ are measured in the lab frame.

As we have seen in paragraph 1.5.1, actin polymerization induces a certain boundary stress at the outer edge of crawling cells. This stress will appear in the boundary conditions, which are necessary to close the mathematical RIF description (3.13–3.15) of the cytoplasm flow. Since these boundary conditions are quite peculiar, we take the remainder of this section to develop them in detail.

2. The tip expansion velocity V: In general, since the cell membrane is impermeable to actin filaments, we have to impose a zero efflux condition on the F-actin mass balance (3.13). This means that the F-actin network θ cannot cross the free boundary Γ. However, in principle, the network may as well fall back and leave the membrane by moving towards the cell center. The resulting boundary condition for the F-actin mass balance (3.13) is therefore an inequality,

$$y = y_1, y_2 : \qquad \theta V \cdot \nu_\Gamma \geq 0, \qquad \text{with } V := \dot{y}_{1,2} - u. \tag{3.23}$$

For convenience, we have condensed the boundary velocities $\dot{y}_{1/2} \equiv \dot{y}_1, \dot{y}_2$, because the last equation of (3.23) holds for both respective boundary positions $y = y_1, y_2$ in the lab frame. The quantity V indicates the amount of membrane advancement as compared to the amount of F-actin network advection u on both ends $y = y_1, y_2$ of the cell. It therefore represents the intracellular expansion velocity between membrane an cytoskeleton at the outer tip of the cell, so that we briefly shall refer to V as "tip expansion velocity". Clearly, the F-actin volume fraction $\theta \geq 0$, so that the F-actin boundary flux inequality (3.23) is fulfilled in the following scenarios for the tip dynamics:

1a. $V \cdot \nu_\Gamma > 0,\ \theta|_\Gamma > 0$ **:** F-actin flux away from membrane

1b. $V \cdot \nu_\Gamma > 0,\ \theta|_\Gamma = 0$ **:** zero F-actin flux with non-zero tip expansion

2. $V \cdot \nu_\Gamma = 0,\ 0 \leq \theta|_\Gamma \leq 1$ **:** zero F-actin flux at the boundary.

The generic case is 1a. The non-zero tip expansion V means that the F-actin velocity u tends to remove the network from the tip. Simultaneously, however, the emerging gap towards the membrane is closed by enhanced actin polymerization, so that V can here be interpreted as effective tip polymerization speed. In the special case 1b, the solvent flow enlarges the gap between cell boundary Γ and the F-actin network θ, which can be observed in biological cells during blebbing [216]. In case 2, the F-actin network always has contact to the membrane, which happens at regions of active retraction or stalled tip advancement. In any case, both protrusion and retraction naturally emerge from our model system.

3. Motion of the free boundary $\dot{\Gamma}$: For the cell to translocate, the tip has to extend and the rear has to retract. This kind of boundary motion is determined from the total volume flux,

$$\dot{y}_{1/2} = \theta u + (1-\theta)w. \tag{3.24}$$

However, the RIF dynamics from above have been written in terms of θ, u, p exclusively, so that we want to eliminate the cytosol velocity w. To this end, we again employ the original equation (2.33) for the cytosol velocity w and insert it into equation (3.24),

$$\dot{y}_{1/2} = u - \frac{1-\theta}{\phi_{\mathrm{ph}}\theta}\partial_y p. \tag{3.25}$$

Replacing the left-hand side with $\dot{y}_{1/2}$ from equation (3.23), we see that tip expansion is related to the pressure gradient at the boundary,

$$y = y_1, y_2 : \qquad V = -\frac{1-\theta}{\phi_{\mathrm{ph}}\theta}\partial_y p. \tag{3.26}$$

4. Boundary pressure balances: Since there is a separate force balance in each phase, cf. equations (2.26, 2.27), there are two distinct boundary pressure balances at $y = y_1, y_2$ [5, section 2.4],

F-actin:
$$-\nu_\Gamma \cdot \eta(\theta)\partial_y u - \psi(\theta, m_b) + \theta p = \overline{\kappa}_\Gamma \theta \tau + P_{\mathrm{poly}}\big(\theta, m_b, V\big), \tag{3.27}$$

cytosol:
$$\sigma(\theta) + (1-\theta)p = (1 - \overline{\kappa}_\Gamma\theta)\tau - P_{\mathrm{poly}}\big(\theta, m_b, V\big). \tag{3.28}$$

The F-actin contractile stress $\psi(\theta, m_b)$ and the swelling pressure $\sigma(\theta)$ have been introduced in equation (3.20). Moreover, $\overline{\kappa}_\Gamma \in [0,1]$ represents the relative influence of the membrane tension τ on the cytoskeleton phase at the tips y_1, y_2. As a side note, τ itself is an independent field variable $\tau = \tau(t,y)$ of the dimension of an effective pressure, which describes the tension of those parts of the membrane that are situated below the cell. Other effects which could arise from the membrane dynamics atop – but not below – the cell are neglected. Finally, the lamella tip polymerization pressure P_{poly} has three contributions,

$$P_{\text{poly}}\big(\theta, m_b, V\big) = P_{\text{clamp}}(\theta) + P_{\text{ratchet}}(\theta) - \eta_\Gamma\big(\theta, m_b\big)V. \tag{3.29}$$

Here we take into account boundary pressures that arise from the clamp-motor P_{clamp} and Brownian ratchet P_{ratchet} mechanism. They both arise from the localized polymerization of F-actin at the cell boundary Γ, see paragraph 1.5.1 for details. The resistance against polymerization originates from cross-linked filaments that are situated slightly behind the membrane edge. This resistance limits the tip expansion velocity V and is assumed to be purely viscous on the considered time- and length-scale, see paragraphs 1.6.2 and 2.2.2. The related effective viscosity η_Γ depends on both the present actin θ and the cross-linking motor myosin m_b. In order to keep the focus on the boundary conditions, we refer to appendix A.2 for details on the model functions $P_{\text{clamp}}, P_{\text{ratchet}}, \eta_\Gamma$.

5. Actin boundary conditions and free boundary motion: With the ingredients from the preceding paragraphs, we can now write the actin boundary conditions. First, we sum the boundary pressure balances (3.27, 3.28),

$$y = y_1, y_2: \qquad -\nu_\Gamma \cdot \eta(\theta)\partial_y u - S(\theta) + p = \tau, \tag{3.30}$$

where $S = \psi - \sigma$ as before. Next, we eliminate the pressure p with the help of the cytosol boundary balance (3.28),

$$\nu_\Gamma \cdot \eta(\theta)\partial_y u + S(\theta) = \frac{1}{1-\theta}\Big[\theta(1-\overline{\kappa}_\Gamma)\tau - \sigma(\theta) - P_{\text{poly}}\big(\theta, m_b, V\big)\Big], \tag{3.31}$$

which can be employed as a boundary expression for u.[3] Importantly, however, since the tip expansion velocity reads $V = u - \dot{y}_{1/2}$, equation

[3] A slightly simplified relation follows from writing the swelling σ in the F-actin boundary pressure balance 3.27. Dropping $\overline{\kappa}_\Gamma$ and splitting τ according to volume fraction θ, one obtains $\nu_\Gamma \cdot \eta(\theta)\partial_y u + S(\theta) + P_{\text{poly}}\big(\theta, m_b, V\big) = 0$.

(3.31) constitutes a mixed Dirichlet-Neumann expression in u, cf. also the polymerization pressure (3.29).

The actual choice of boundary conditions for the RIF system (3.13–3.15) depends on the aforementioned scenarios for the tip dynamics:

1a. $V \cdot \nu_\Gamma > 0,\ \theta|_\Gamma > 0$ **:** The zero efflux condition for the F-actin mass balance is fulfilled since $V \cdot \nu_\Gamma > 0$. Equation (3.31) constitutes a mixed condition for u, while the cytosol boundary pressure balance (3.28) represents a Dirichlet condition for p. The motion of the free boundary $\dot{y}_{1/2}$ is then determined from u and $\partial_y p$ according to (3.25), which is an implicit relation because the boundary conditions for u and p contain $\dot{y}_{1/2}$ via V in the polymerization pressure term $\propto P_{\text{poly}}$. Since membrane and F-actin network move in opposite directions, the boundary influx for the F-actin mass transport equation (3.13) has to vanish.

1b. $V \cdot \nu_\Gamma > 0,\ \theta|_\Gamma = 0$ **:** Here, the F-actin efflux vanishes because $\theta = 0$. This case can arise at boundary points with vanishing polymerization pressure P_{poly}. There, the volume fraction $\theta \to 0$ degenerates, so that all summands of the F-actin boundary pressure balance (3.27) vanish independently. The solvent boundary pressure balance (3.28) breaks down to the Dirichlet condition $p = \tau$ for p. Finally, by (3.25, 3.26) we have $V = \dot{y}_{1/2}$, whereby $\dot{y}_{1/2}$ follows from the L'Hospital limit of the expression $\propto \partial_y p$ for $y \to y_1, y_2$ from the interior.

2. $V \cdot \nu_\Gamma = 0,\ 0 \leq \theta|_\Gamma \leq 1$ **:** The F-actin efflux vanishes again, since $V = 0$. The tip expansion relation (3.26) therefore yields a zero-Neumann condition for p. Conversely, (3.30) constitutes a pure Neumann condition for u, because it does not contain the polymerization pressure P_{poly}.

The quite subtle case 1b is desirable only for specific biological phenomena like the aforementioned blebbing. The earlier formulation [135] of the present model has taken into account such a possibility. For the pursued modeling aim of explaining relatively fast cell migration this complication is however not needed. In the remaining part of this chapter, we therefore assume for simplicity

$$\forall y \in \overline{\Omega} : \qquad \theta > 0, \tag{3.32}$$

so that the F-actin cytoskeleton always sticks to the membrane. Moreover, since the extension of steadily crawling cells like human epidermal

keratinocytes along the anterior-posterior axis does not change very much during migration, we also assume

$$y_2(t) - y_1(t) = \text{const.} =: \lambda, \tag{3.33}$$

where the model cell length λ is parameter, see appendix table A.2. In this way, the boundary velocities $\dot{y}_1 = \dot{y}_2 \equiv \dot{y}_{1/2}$ are identical and constitute the migration velocity of the model cell.

Under the remaining tip scenarios 1a & 2 and together with the respective boundary conditions from above, the hyperbolic-elliptic system (3.13–3.15) for actin turnover and flow is closed and therefore accessible to its numerical solution. The motion of the time-dependent domain $\Omega(t)$ follows from equation (3.25). The only remaining undetermined quantity is the effective membrane surface tension τ. As will turn out, it provides for a Lagrange multiplier needed to implement the cellular force balance constraint as introduced in the following section, cf. 3.5. Before coming to that, however, we also have to close the transport, reaction and diffusion systems for myosin and integrin.

6. Myosin boundary conditions: Since the myosin evolution equations (3.2, 3.3) involve transport terms, they also require the specification of suitable boundary conditions describing the mass transport at the domain border Γ. For bound myosin m_b, the situation is similar to that of F-actin discussed above. However, since the role of m_b does not involve the peculiarities of polymerization at the cell boundary Γ, we can take a simpler approach here and require zero flux without inequality,

$$y = y_1, y_2: \quad m_b\big(u - \dot{y}_{1/2}\big)\cdot\nu_\Gamma = 0 \;\Leftrightarrow\; \begin{cases} m_b = 0 & \text{for } V\cdot\nu_\Gamma > 0, \\ m_b \text{ free} & \text{for } V\cdot\nu_\Gamma = 0. \end{cases} \tag{3.34}$$

The corresponding zero flux identity $D_m\partial_y m_f = 0$ for free myosin gives rise to the Neumann condition,

$$y = y_1, y_2: \qquad \partial_y m_f = 0. \tag{3.35}$$

7. Integrin boundary conditions: The boundary conditions for the two integrin mass balances (3.6, 3.7) are also zero flux. In full analogy to the corresponding myosin relations, we therefore write

$$y = y_1, y_2: \qquad \partial_y b_f = 0, \tag{3.36}$$

$$b_a\big(u - \dot{y}_{1/2}\big)\cdot\nu_\Gamma = 0 \quad\Leftrightarrow\quad \begin{cases} b_a = 0 & \text{for } V > 0, \\ b_a \text{ free} & \text{for } V = 0. \end{cases} \tag{3.37}$$

Having found suitable boundary conditions for the coupled system for cytoplasm and adhesion dynamics, we come now to the mechanism generating the locomotion forces of the model cell.

3.5. Cell-substratum adhesive slip mediates locomotion forces

1. Traction arising from frictional slip: As argued in paragraph 1.6.3, the forces for cellular locomotion arise at the interface between the cell and the substratum. At this interface, integrins connect the cell-interior F-actin and the cell-exterior substrate or extracellular matrix. Importantly, these connections appear to be non-rigid on the time-scale of cellular migration. Bond formation and breakup are in a dynamical chemical equilibrium, where both the forward and the backward reaction occur simultaneously. In this sense and in the time average relevant to cellular migration, the instantaneous assembly of substratum adhesion bonds allows only for transient force transduction. Accordingly, the F-actin retrograde flow is only transiently connected to focal adhesion sites, and therefore does not stop by mere integrin binding.

This transiency of the cellular adhesion mechanism can be conceptualized in terms of a molecular clutch [45]. Instantaneously, force transmission is possible at seemingly fixed or rigid focal adhesions, while on a longer time-scale, the whole focal adhesion complex is well capable of moving relative to the substrate. The same holds also for F-actin moving over the integrin substratum contact. Indeed, this molecular clutch has been shown to be effective in human osteosarcoma cells [11]. Experimental evidence indicates that α-actinin is involved in increasing the slip at the actin-integrin binding complex [38, table 1]. The apparent mutual relation of focal adhesions and actin speed [3,86] also seems to be consistent with the general idea of a molecular clutch at focal adhesions.

Since the integrin bonds are transient only, the actin retrograde flow generates friction-type forces, which ultimately give rise to forward translocation of the cell. Here, we model this cytoskeleton-initiated traction via a slip of F-actin dragging over the integrin-mediated substratum adhesions,

$$f_u = -\phi_u b_b \theta u. \tag{3.38}$$

The parameter ϕ_u describes the amount of effective friction due to the interactions of F-actin θ with bound integrins b_b. Importantly, the drag

force f_u appears also as external force on the right-hand side of the Stokes equation (3.14).

2. Cell-level force balance: Recall that the domain Ω of the migrating model cell has the fixed length λ. Therefore, the cellular migration velocity v coincides with the velocity $\dot{y}_{1/2}$ driving the free boundary $\Gamma = \partial\Omega$. Assuming that the lower plasma membrane moves along with the whole cell, the local friction towards the substratum is

$$f_v = -\phi_v v \equiv -\phi_v \dot{y}_{1/2}, \tag{3.39}$$

whereby ϕ_v denotes the membrane friction coefficient. The resulting substratum force balance reads

$$\int_{y_1}^{y_2} \big(f_u + f_v\big)\, \mathrm{d}y = 0 \quad \Leftrightarrow \quad \lambda\phi_v \dot{y}_{1/2} = \int_{y_1}^{y_2} \big(\phi_u b_b \theta u\big)\, \mathrm{d}y. \tag{3.40}$$

Substituting f_u from the Stokes equation (3.14) into the first summand of the friction integral (3.40), one obtains the Stokes boundary terms

$$\int_{y_1}^{y_2} f_u \, \mathrm{d}y = \big(-\nu_\Gamma \cdot \eta \partial_y u - S + p\big)\big|_{y_1}^{y_2} = \tau\big|_{y_1}^{y_2}, \tag{3.41}$$

where we used the boundary condition (3.30) for the last equality. From the total friction integral we therefore conclude

$$\lambda\phi_v \dot{y}_{1/2} = \tau|_{y_1}^{y_2}. \tag{3.42}$$

This reveals that, similar to p, τ acts as a Lagrange multiplier. As mentioned in paragraph 2.3.3, p enforces the incompressibility condition (2.10) on the bulk cytoplasm flux velocity $\theta u + (1-\theta)w$. In contrast, $\tau(t, y)$ causes the lower plasma membrane to move with the uniform velocity $\dot{\Gamma}$ over the substrate for all positions $y \in [y_1, y_2]$. Alternatively one could also impose the incompressibility of the membrane, see [6, section 3.2.4] for details.

Equation (3.42) also shows that the determination of the variable pair u, p in the tip expansion scenarios 1b & 2 is implicit as well. For 1b, the Dirichlet condition (3.28) for the pressure reads $p = \tau$ and relates the original identity (3.25) for $\dot{y}_{1/2}$ indirectly with τ. In scenario 2, the relation (3.42) indirectly affects the employed Neumann condition (3.30) for u via τ, while at the same time $\dot{y}_{1/2} = u$ from equation (3.25). Thus,

in any case $u, \dot{y}_{1/2}$ and τ are given in an implicit way and the equations have to be numerically iterated until the system is self-consistent. Since the τ-equation (3.42) determines only the tension difference between the two cell ends, we assume a small baseline tension parameter $\tau_0 = \min\big[\tau(y_1), \tau(y_2)\big]$ in the numerical iteration, see table A.2.

3.6. Cell polarization is either spontaneous or induced by taxis cues

1. Symmetric and polarized model cell mode: When seeding human epidermal keratinocytes on fibronectin substrata, these cells exhibit several dynamical states at sufficiently low density, compare figure 1.6. The most common dynamical states of the cells are (i) the symmetric state in which the cells are circular and do not move, and (ii) the polarized state with prominent leading lamella extending in the direction of the cellular migration. The same two states have also been observed in fish keratocytes [233], and in celloids without nucleus [221]. Here we want to understand the nature of these two dynamical cell modes and their underlying molecular structure.

2. Symmetric non-motile cell mode: Starting from evenly distributed actin, myosin and integrin concentrations $\theta, m_f, m_b, b_f, b_a, b_s, b_b$, the model cell quickly settles and exhibits the symmetric state, see figure 3.4 (a1) & (a2). This sessile cell mode is characterized by the concentrations being distributed in symmetric manner with respect to the center of the cell. Apparently, actin, myosin and bound integrin pile up in the middle of the cell. This can be understood in terms of the F-actin flow velocity u, see the black dotted line in figure 3.4 (a1). Since this flow is directed towards the cell center, there is a tendency to remove actin associated species from the outer ends and advect them to the central region.

Accordingly, since b_a integrins are actin-bound, they are transported with the F-actin flow velocity u. Thus, there is a general trend for the majority of the overall integrin pool to accumulate at the cell center. In contrast, free and substrate-bound integrins b_f, b_s extend towards the outer ends of the cell. Recall that by equations (3.11, 3.12), both actin θ and force $f_u = -\phi_u b_b \theta u$ (red dashed line in figure 3.4 (a1)) affect the integrin association and dissociation rates, respectively. Since $\alpha_{fa}, \alpha_{sb} \propto \theta$, the relatively low amount of actin at the ends of the cell shifts the chemical integrin equilibrium towards b_f, b_s. In the intermediate range,

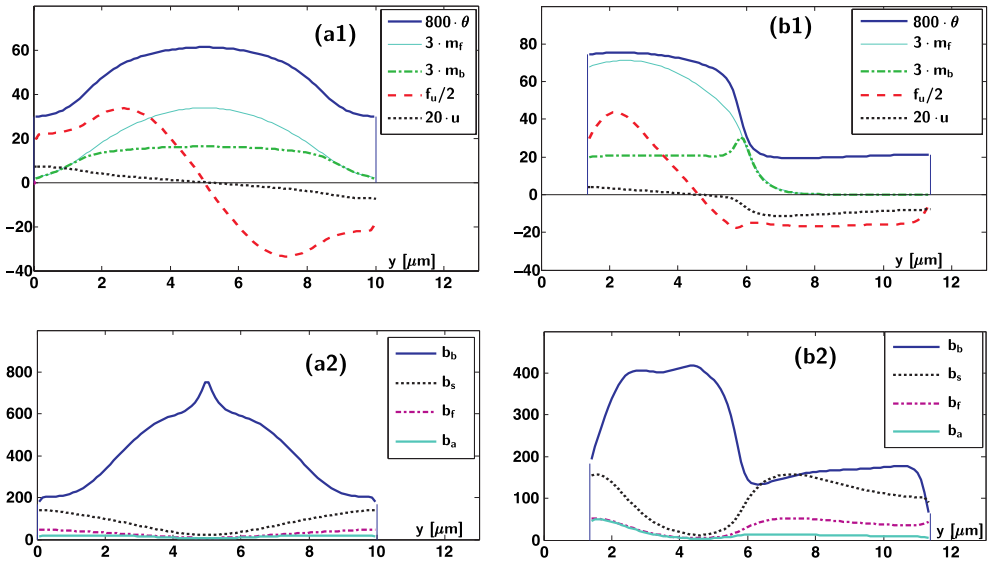

Figure 3.4.: Keratinocytes at rest attain a circular, symmetric and unpolarized state, while migrating ones are of asymmetric shape and the polarized lamella is oriented towards the direction of the motion. Here we consider central sections through the cell, along the posterior-anterior axis. The emerging concentration profiles of the quantities in the simulated, one-dimensional model cell exhibit both of these two, clearly distinct motility states. On the left hand side, the cytoskeletal F-actin θ together with the contractile myosin m_b and the bound integrin b_b is symmetric with respect to the cell center. Since the cytoskeleton flow u is evenly oriented in centripetal direction towards the cell center, the cell the net locomotive force of the cell vanishes. In contrast, on the right hand side the concentrations θ, m_b and b_b are asymmetric. The interplay of the posterior cytoskeletal contraction and the anterior polymerization drive at the lamella tip leads to a prominent asymmetry in the F-actin flow profile u. Due to the enhanced retrograde flow at the cell front, the integrated overall force leads to forward translocation in positive y-direction.

where $|f_u|$ is rather high, focal adhesions are quickly disrupted yielding increased amounts of b_a, b_s, even despite of the already high actin level θ. In the center of the cell, the very high amount of actin θ and the relatively low force $|f_u|$ favor the double-bound state b_b of integrins.

The cellular migration force f_u from equation (3.38) is determined from the joint action of integrin adhesion sites b_b and the centripetal F-actin mass flux θu. As can be observed in figure 3.4 (a1) & (a2), the profiles of both F-actin θ and integrin b_b are symmetric about the cell center $y \sim 5$ μm. In contrast, the profile of the F-actin transport velocity u is antisymmetric, so that the resulting profile of the traction force f_u is antisymmetric. Thus, the centripetal pulling forces from both cell ends mutually compensate in the cellular traction force integral $\int_\Omega f_u \, \mathrm{d}y$ from equation (3.40). In this way, the cell remains stationary and rests at its place, even though the underlying cytoskeleton machinery turns over in a highly dynamic manner.

3. Polarized and migrating cell mode: Cell polarization arises from contractile or polymerization stimuli as discussed in the following paragraph. Once the full polarity has been established, the model cell migrates and exhibits asymmetric concentration profiles, see figure 3.4 (b1) & (b2). In the plots, we see the resulting protrusion front on the right hand side of the model cell. This lamella-like region is characterized by low levels of bound myosin m_b and a prominent retrograde flow velocity u. At the rear end of the cell, the F-actin flow u is almost vanishing, whereas the amount of bound myosin m_b is generally high. Note that in the presented plots, u is measured in cell-centric coordinates, so that the F-actin velocity in the lab frame is $u_{\mathrm{lab}} = u_{\mathrm{plot}} + v$, whereby $v \approx 0.12$ μm/min denotes the migration velocity of the cell.

The particular distribution of actin in figure 3.4 (b1) is somewhat at odds with the general behavior as observed in experiments like [192, 221]. However, here we do not model the presence of a cell body or nucleus. Its presence would impose a spatial obstacle within the cytoplasmic flow. During migration, this obstacle is situated at the back of the cell, so that the accumulation of actin at the rear end would be hindered. In spite of this model limitation, we emphasize that the obtained distributions of F-actin exhibit the correct profile at the outer ends of the cell, see also the experimental data below.

The behavior of the bound myosin mostly arises from its transport properties. Since it is bound to the F-actin cytoskeleton, it moves with the

corresponding velocity u, and is thus constantly shuffled away from the front towards the rear. Due to the permanent mutual turnover between bound and free myosins, depletion of one leads to the depletion of the other. Therefore, also free myosin m_f is low at the front. The converse situation arises at the rear of the cell, where the general trend is similar as for actin.

The mechanism underlying the observed integrin distributions is much alike the one in the symmetric cell mode. The now asymmetric flow shuffles actin-bound integrins b_a to the back. The transition from the bound kinetic state b_b to the semi-bound ones b_a, b_s is mediated by the force-dependent disruption rates δ_{ba}, δ_{bs}. Therefore, integrin recycling occurs predominantly at the cell rear, where the forces f_u give rise to strong retraction.

The motion of the cell arises from the specific profile of f_u, which – in contrast to the symmetric cell state – does not balance in the cellular traction force integral $\int_\Omega f_u \, \mathrm{d}y$ from equation (3.40). Recall that by equation (3.38) we have $f_u \propto b_b \theta u$. Inspecting figure 3.4 (b1) & (b2), we find that the asymmetry in f_u follows almost exclusively from the F-actin transport velocity u. Surprisingly, both F-actin θ and integrin b_b profiles rather seem to antagonize the forward asymmetry of f_u toward the right-hand side of the plots. Nevertheless, since the retrograde flow is prominent enough throughout the tip region $y \sim 7 \ldots 11$ μm, and also because there is a small overlap of high θ and b_b values with still negative u at $y \sim 6$ μm, the model cell migrates due to aforementioned asymmetry in the force integral. This shows that the consideration of a dynamical F-actin transport velocity u is essential for the model cell's migration capability.

4. Transition and robustness of the two cell modes: Here we consider two scenarios for the stimulus that causes the model cell to polarize. As we have seen in section 1.5, the Rho/Rac family of proteins is involved in initiating a F-actin polymerization stimulus [168, 184]. In order to mimic the effect of a chemotactic gradient, we permanently increase the F-actin polymerization rate J from equations (3.13, 3.19) at one end of the model cell in its sessile and unpolarized mode. As expected, the cell slowly polarizes and engages in persistent migration, see [6, section 4.2] for further details.

On the other hand, polarization might also arise due an asymmetry in the stress distribution throughout the cell, see again section 1.5. A

corresponding stimulus would affect the contractile machinery in the cell, which also has been associated with downstream effectors of Rho [168]. Here we directly modify the myosin-actin association rate α_m, which leads to an increased contractile stress ψ according to equation (3.21). If we prescribe $\alpha_m = 20/\text{min}$ at one end of the unpolarized cell for 0.5 min, the cell returns to its initial sessile state after a short period of overshooting migration. However, if we impose a stimulus of $\alpha_m = 50/\text{min}$ for the same time, the polarization is persistent and migration prevails, see [6, figure 8] for the emerging cell velocity curves. Importantly, the polarizing stimulus has to exceed a certain threshold so that persistent cell migration may emerge.

Finally, we also impose stochastic perturbations on the F-actin polymerization rate J from equation (3.19). This particular robustness check demonstrates that both the sessile and the migrating cell mode are able to withstand occurring fluctuations in all force-bearing chemical reaction processes. Together with the *in-silico* experiments on stimulated cell polarization mentioned above, we conclude that the fundamental modes of migrating cells in two dimensions are autonomous, self-organizing, and self-stabilizing. Indeed, from a biological perspective, such a robustness is highly desirable, in particular with respect to signal reception and transduction. When the dynamical system of the force-generating cellular migration machinery is able to sustain the fundamental morphological modes autonomously, then the associated signalling relay merely needs to control the switch between these modes. Consequently, any logic that just maintains a specific mode would – in principle – be superfluous. Conversely, such a logic could be neglected until the mechanical cell modes and their upstream signalling switch are understood in a satisfactory manner.

5. Comparison with experimental data: Here we present relevant concentration, traction and flow fields of HEK cells, see figure 3.5. The data contain the information extracted from several different time-lapse movies that have been averaged according to a novel method involving the circular normalization of the cell outline [157]. Thereby, the cell shape is approximated by a polygon with ~ 12 nodes, for each frame in the involved movies. The cell center is identified with the center-of-mass of the polygon, and the cell's velocity is computed from the time derivative of the center position, see A & E in figure 3.5. Then, the individual frames are rotated, so that the turned cell always migrates towards the top, cf. B

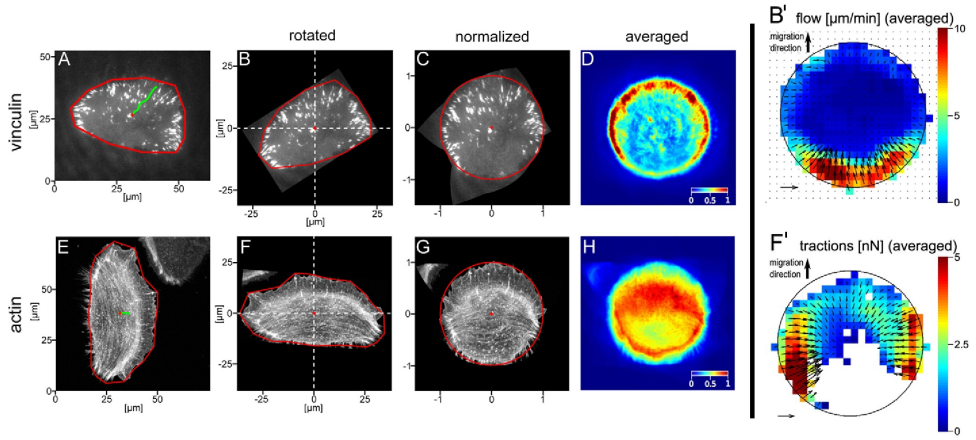

Figure 3.5.: Experimental data on human epidermal keratinocytes (HEK) compares favorably with the results from the simulation model. Note that these data are averaged, see the text for a brief description of the averaging procedure. The connections between experimental and model quantities are (i) vinculin $\approx$ bound integrins b_b, (ii) actin $\sim$ cytoskeletal F-actin θ, (iii) cytoplasm flow $\sim$ F-actin velocity u, and (iv) traction $\approx$ traction force f_u. The nature of these correspondences is further explained in the text. This figure has been reproduced from [157, figure 1 A-H, figure 3 B & F], with kind permission by Christoph Möhl.

& F. Since the cell center is known, the cell contours can be morphed to a circle of fixed radius, which is again done for each frame. Each of the resulting micrographs of the time-lapse movie frames thus exhibits an almost circular cell and therefore they all can be averaged in a meaningful way. Here, we compare these experimental data to the migrating state of our model cell, because the cells in the time-lapse movies were also migrating. Note that the model plots from figure 3.4 feature the anterior-posterior cell axis from left to right, cf. the simulation domain $[y_1, y_2]$ as drawn in figure 3.1. In contrast, the anterior-posterior cell axis stretches from bottom to top in the experimentally determined reference pictures from figure 3.5.

Vinculin is known to co-localize with focal adhesions, so that the concentration profile in figure 3.5 D relates to the profile of bound integrins b_b, indicated in blue in figure 3.4 (b2). The concentration profile in 3.5 H shows the distribution of actin, in both monomeric and filamentous states. Even though we model only F-actin explicitly, we compare H with the model prediction θ, see blue line in figure 3.4 (b1). Since this 'correspondence' is clearly incomplete, any interpretation arising from this particular comparison of experiment and theory should not be overstretched. Note also that in the averaged experimental profiles, the effect of the cell nucleus is clearly visible. Being situated at the cells rear, it decreases both actin and vinculin levels as one can see from the prominent blue/green spot within the otherwise mostly red cell circle in figure 3.5 D & H.

The cytoplasmic flow field in figure 3.5 B' has been recorded in lab coordinates, so that the highest amount of flow is situated at the cell's rear. The F-actin flow profile u as indicated by the black dotted line in figure 3.4 (b1), however, is displayed in cell-centric coordinate. By writing the F-actin velocity in the lab frame, $u_{\mathrm{lab}} = u_{\mathrm{plot}} + v$, we see that u_{lab} resembles the experimental situation quite precisely. Finally, the averaged traction forces from 3.5 F' mostly arise in the rear half of the cell. Note that in white regions of F' there was unfortunately not enough data to faithfully quantify traction. In any case, the traction analogue in the model cell f_u appears to match the general behavior, cf. the red line in figure 3.4 (b1).

Finally, we note that there are several other experimental data that exhibit the semi-quantitative features of the simulations presented here, for example (i) actin and myosin distribution in celloids, in both resting and migrating states [221, figure 2ac], (ii) actin velocity field [192, figure 1G], (iii) force distribution in *Dictyostelium discoideum* [55, figure 1(d)],

(iv) actin velocity field, traction forces and substratum interactions [78, figure 2], and (v) actin bundling, actin velocity field, myosin distribution [229, figure 1]. We take this as an indication and a-posteriori confirmation that the phenomenological constitutive force and stress laws introduced in sections 2.3, 3.3 are useful in compound fluid models and capable of describing whole cell motion.

3.7. The migration velocity of cells is sensitive to substratum adhesion

1. Modification of adhesion and friction model functions: In this section we investigate the influence of substratum adhesiveness on the distribution of focal adhesion integrins b_b and the generation of cellular traction forces. During focal adhesion formation, integrin binding clearly depends on the availability of substratum receptors such as fibronectin. For simplicity, we describe the arising effective substratum adhesiveness by the dimensionless number A_{dh}. Since both traction and friction ultimately arise from the substratum adhesiveness, effects on the migration velocity v of the cell are to be expected. Including the effect of substratum receptors leads to a linear dependence of the integrin reaction constants on the adhesiveness,

$$\alpha_{fs} = \alpha_{s0} \cdot A_{\mathrm{dh}}, \qquad \alpha_{ab} = \alpha_{s0} \cdot A_{\mathrm{dh}}, \tag{3.43}$$

with $\alpha_{s0} = 5\ \mathrm{min}^{-1}$ and typically $A_{\mathrm{dh}} \sim 3$, see also equations (3.6–3.9). At the same time, since the cell membrane friction is influenced by the molecular bonds towards the substrate, we suppose the proportionality

$$\phi_v = \phi_v^0 \cdot A_{\mathrm{dh}}, \tag{3.44}$$

for the cellular friction coefficient (3.39), whereby $\phi_v^0 = 6\ \mathrm{Pa} \cdot \mathrm{min}/\mu\mathrm{m}^2$.

2. The cellular adhesiveness-speed relation: In order to explore possible modifications in the migration machinery of the model cell, we put it on substrata of different adhesiveness A_{dh}, and measure the emerging steady-state speed together with the essential concentration and force profiles, see figure 3.6. The top left panel shows the resulting velocity-adhesiveness curve. Depending on substratum adhesiveness A_{dh}, the cell exhibits two distinct migration regimes. In the low adhesiveness regime, $A_{\mathrm{dh}} = 0 \ldots 3$, there is a quick adaption of the migration speed to the

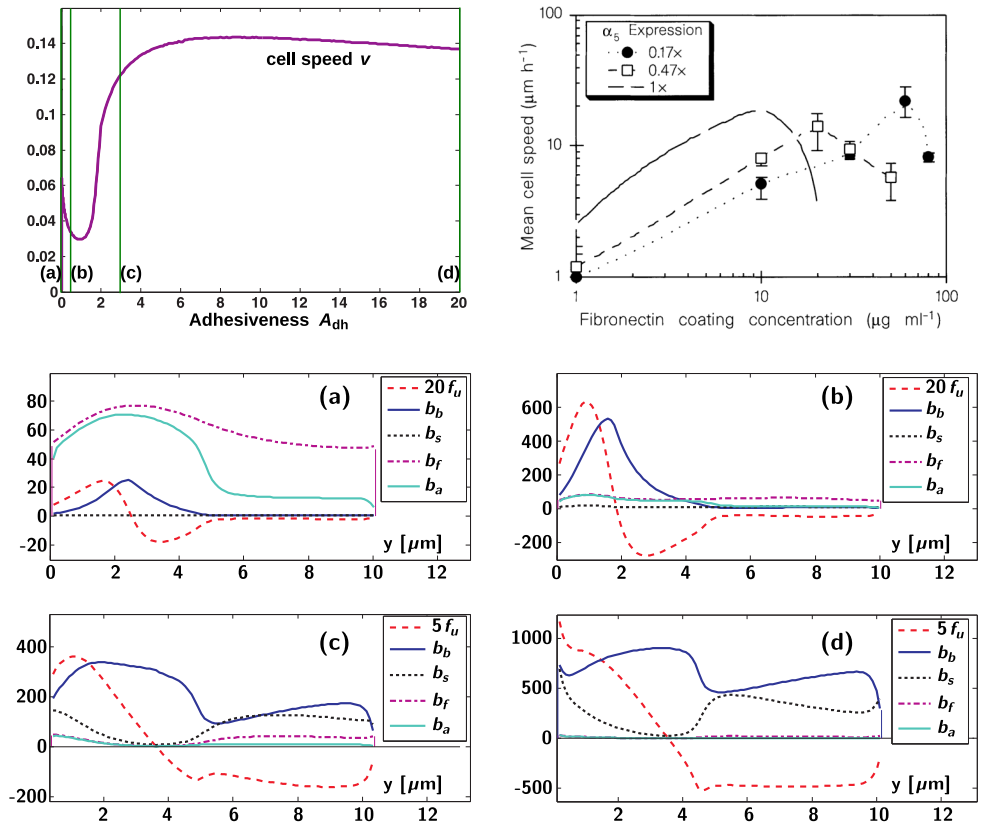

Figure 3.6.: The substratum adhesiveness A_{dh} influences the migration speed v of the model cell, see top left panel. For low substratum adhesiveness $A_{\mathrm{dh}} = 0 \ldots 3$, the cell is highly responsive to changes in A_{dh}. At higher levels of adhesiveness, there is a broad optimal range for the model cell's migration speed. Comparing with experiment, see top right panel, the model cell speed seems to capture the general behavior. The lower panels (a-d) show integrin and force profiles of the model cell at respective A_{dh}-values indicated in the top left panel. The top right plot containing experimental data is reproduced from [169, figure 1a], with kind permission by D.A. Lauffenburger.

substratum adhesiveness. In contrast, for higher values of A_{dh}, the speed of the model cell does not change much while it is fairly high in general. This points at the ability of the cell to adapt to various external conditions at seemingly optimal performance. Indeed, this adaption is also reflected in the traction force and integrin profiles from figure 3.6 (a–d), which characteristically vary according to the adhesiveness A_{dh} of the present substratum:

(a) $A_{\mathrm{dh}} \sim 0.01$: almost symmetric b_b and f_u distribution with flat force plateau at the front

(b) $A_{\mathrm{dh}} \sim 0.2$: start of integrin b_b accumulation at the rear reducing migration speed

(c) $A_{\mathrm{dh}} \sim 1 \ldots 3$: enriched b_b carpet at the front and sharp increase of disruptive forces at the rear

(d) $A_{\mathrm{dh}} \sim 20$: b_b accumulation at rear reducing migration speed v

Therefore, for $1 < A_{\mathrm{dh}} < 4$, the cell has a high sensitivity for responding to an increase of adhesiveness, while between $5 < A_{\mathrm{dh}} < 12$ a broad optimum in saturated migration speed occurs. This explains the polarization and haptotaxis of cells in spatial adhesion gradients, and reproduces adhesion and migration experiments on CHO B2 cells[4] [169, figure 1a].

Mechanistic understanding of cellular migration: In the light of the emerging concentration profiles in figures 3.4 (b1) & (b2) and 3.6 (a-d), a physical explanation for cell migration therefore is not "more adhesion" or "stronger force" at the front compared to the rear. Instead, the asymmetry in the polarized state leads to a wide front region with modest forward traction force, and a short rear region with strong opposing forces favoring FA rupture. This is how the self-organizing morphological features of crawling cells regulate the strength of motile force transduction.

[4] mutated Chinese hamster ovary cells

3.8. The cytoplasm flow model can be applied in a quasi two-dimensional geometry

1. Peripheral approximation and simulation domain: Here, we propose a modified version of the single cell motility model described in the preceding sections. Since that model was limited to one dimension, it is desirable to extend the theory so that two-dimensional shape and dynamics can be accounted for. At the same time, however, the need for additional simplifications arises. To this end we follow the general ideas laid out in the earlier efforts [200, 201, 218], while retaining the most essential quantities of the one-dimensional model from before.

The central idea to arrive at a quasi two-dimensional description is to go over to cell-centric coordinates, whereby the cell body center represents the co-moving origin. In figure 3.7, the cell body is indicated by the white line $R(\varphi)$. We then parameterize all field variables like actin and forces in terms of the polar angle φ, which constitutes the only considered spatial coordinate in the cell frame. In this way, the simulation domain is given by the unit circle. In order to quantify the shape of the cell, we introduce the local lamella width $L = L(t, \varphi)$ as additional field variable. It denotes the distance from the cell body to the exterior tip boundary in direction of φ at each time instant t, cf. figure 3.7. Concentrations like the one of actin $a = a(t, \varphi)$ are then assumed to be constant in the infinitesimal lamella segment $\big\{(r, \phi) \in \mathbb{R}^2 : R(\phi) \leq r \leq R(\phi) + L(t, \phi), \varphi - \mathrm{d}\varphi \leq \phi \leq \varphi + \mathrm{d}\varphi\big\}$ around φ. Alternatively, one could think of the average concentration of actin in that region. Importantly, since we are now employing cell-centric coordinates, we also measure the mass transport velocities relative to the moving cell center.

2. Peripheral mass balances: In order to set up the mass balance equation for the F-actin density $a(t, \varphi)$, we write the one-dimensional analogue of (2.1). Identifying $\rho_{\mathrm{f}} := a$, and introducing the modifications explained below, we obtain

$$\partial_t a + \partial_s\big(a u_a - D_a \partial_s a\big) = J''. \tag{3.45}$$

In the one-dimensional peripheral approximation, we employ the F-actin concentration $a = \theta / V_a$, where V_a indicates the volume of a single actin monomer. Moreover, we compute the derivatives involved in the transport terms on the surface of the cell body,

$$\partial_s := \frac{1}{R} \cdot \partial_\varphi, \tag{3.46}$$

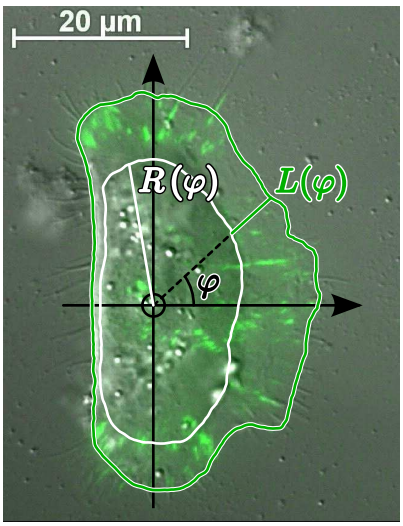

Figure 3.7.: Cell centric coordinates underlying the quasi two-dimensional migration model. In order to obtain a simple description, we attach a coordinate system to the center of the migrating cell, see black arrows, and parameterize all model variables over the unit circle as described by the polar angle φ. The curve of $L(\varphi)$ represents the outline of the cell as it spreads on the substratum, relative to the cell body $R(\varphi)$. The latter can be observed as the fan-like central region with bright white spots and almost no focal adhesions, and is indicated by the white line in the picture. In the micrograph, the focal adhesion sites are highlighted by a green fluorescence dye. The presented microscopic picture of a human epidermal keratinocyte is courtesy of Claudia Schäfer, Merkel group, Forschungszentrum Jülich [189, movie 05].

where we have assumed that the cell body is spherical and has a constant radius $R(\varphi) = \text{const.} =: R$. A certain amount of F-actin diffusion with constant D_a could arise from material transport not fully captured by the F-actin velocity u_a, which represents the tangential component of $\mathbf{u}$ from equation (2.1). For a more detailed explanation of the velocity u_a see the paragraph 3.8.4 on transport velocities below. The actin polymerization model function reads

$$J'' = \alpha_L L + \alpha_a b a - \delta_a a + \beta_a \xi_t. \tag{3.47}$$

F-actin assembly arises from the local cell extension L in the first summand with coefficient $\alpha_L > 0$. Adhesion-mediating integrins b recruit auto-catalyzing F-actin with the association constant α_a in the second summand, see below for details on the integrin concentration b. Moreover, filament disassembly is proportional to the amount of F-actin a, with the dissociation constant δ_a. The last term on the right-hand side induces small variations in the F-actin polymerization due to fluctuations in the environment, where ξ_t is a Gaussian random number with mean zero and variance one, and β_a the model parameter for the perturbation strength. The actual values of the parameters $D_a, \alpha_L, \alpha_a, \delta_a, \beta_a$ are all listed in table A.6. Previously, we have employed different representations of the polymerization function J'', cf. equations (2.1, 2.29). Though not directly needed in the present model formulation, the relations for conversion would be $J' = m_\mathrm{a} J'' = m_\mathrm{a} J / V_\mathrm{a}$, where m_a is the mass of a single actin monomer, and V_a its volume.

In this simplified model, we consider only one kind of integrin molecules involved in cellular adhesion, namely the bound ones $b \equiv b_b$, compare also figure 3.2. The corresponding mass balance for the concentration of bound integrin receptors b engaged in focal adhesions reads

$$\partial_t b + \partial_s\big(b u_b\big) = \alpha_b a d - \delta_b b \exp\big(f / f_b\big) - \delta_e b \big(v_\mathrm{tip}^\mathrm{out} + v_\mathrm{body}^\mathrm{out}\big). \tag{3.48}$$

Here, u_b denotes the transport velocity, see paragraph 3.8.4 for details. The first term on the right-hand side indicates that F-actin a facilitates the formation of integrin-mediated adhesions b. They assemble at sites where there are suitable substratum ligands $d = d(t, \varphi)$, see below for details. In this way, the reservoir function of the semi-bound integrins from figure 3.2 is included in the effective association rate constant α_b. The adhesions b disassemble with the rate δ_b, whereby the present tensile load $f := |\mathbf{f}(t, \varphi)|$ affects the kinetics in a Bell-type exponential factor [21]. The load $\mathbf{f}$ arises from the traction force of the cell and is defined below

in equation (3.57). The last term on the right-hand side includes passive effects of adhesion sites leaving the cell lamella domain in radial direction, where δ_e indicates the inverse characteristic length of effective radial egress. This type of transport occurs both at the lamella tip $L(\varphi)$ and at the cell body (cf. figure 3.7), with the respective velocities $v_{\text{tip}}^{\text{out}}, v_{\text{body}}^{\text{out}}$, whose definition is given in the following paragraph 3.8.3. The specific values for the parameters α_b, δ_b and δ_e are listed in table A.6.

The integrin kinetics above involve the adhesion ligand density d on the substratum, e.g. like fibronectin or collagen. In order to account for their variations, we consider their mass balance in an idealized manner,

$$\partial_t d + \partial_s\big(du_d\big) = -\alpha_b a d - \delta_e d\big(v_{\text{tip}}^{\text{out}} + v_{\text{body}}^{\text{out}}\big) + \alpha_d v_{\text{tip}}^{\text{in}} \zeta_t\big(d_0, \sigma_d\big), \quad (3.49)$$

where the velocities $u_d, v_{\text{tip}}^{\text{in}}, v_{\text{tip}}^{\text{out}}$, and $v_{\text{body}}^{\text{out}}$ are defined below. The first term on the right-hand side indicates that the substratum ligands d become occupied by integrin in focal adhesion sites b, see also equation (3.48). The ligands d can also leave the cell lamella domain in radial direction, which is represented by the second summand on the right hand side of the mass balance (3.49). The most important kinetic term is the last one. In the employed co-moving cell coordinate frame, new substratum ligands enter the cell lamella domain at the tip $R + L(t, \varphi)$. Thereby, the amount of entering ligands derives from the local lamella area increase, which is proportional to the tip growth velocity $v_{\text{tip}}^{\text{in}}$. Here we model the ligand density within the gained area by the stochastic variable $\zeta_t\big(d_0, \sigma_d\big) \geq 0$, which is assumed to be distributed according to the truncated positive Gaussian distribution with mean d_0 and standard deviation σ_d.[5] The coefficient α_d represents the effective radial ingress parameter for ligands entering from the lamella tip. Together with the values for α_b, δ_e, d_0 and σ_d, the ingress parameter α_d is is given in table A.6. An alternative and more complete adhesion model has been studied in [132], whereby the model cell crawls on a substrate with a check-board like Poissonian adhesion ligand density.

3. Passive radial transport velocities: In order to specify the transport velocities in equations (3.45, 3.48, 3.49), we introduce the radial and tangential unit vectors

$$\hat{\mathbf{e}}_r(\varphi) = \begin{pmatrix} \cos\varphi \\ \sin\varphi \end{pmatrix}, \qquad \hat{\mathbf{e}}_\varphi(\varphi) = \begin{pmatrix} -\sin\varphi \\ \cos\varphi \end{pmatrix}, \quad (3.50)$$

[5] This is implemented by drawing vectors of Gaussian random numbers $\zeta_t \in \mathcal{N}(d_0, \sigma_d)$ and replacing negative entries by zero.

defined for each angle φ in co-moving polar cell coordinates. Furthermore, let $\mathbf{v} = \mathbf{v}(t)$ denote the cellular migration velocity as defined in paragraph 3.8.5 below. Expressing $\mathbf{v}$ in terms of the local polar unit vectors (3.50) we have

$$v_r(t,\varphi) = \mathbf{v}(t) \cdot \hat{\mathbf{e}}_r(\varphi), \qquad v_\varphi(t,\varphi) = \mathbf{v}(t) \cdot \hat{\mathbf{e}}_\varphi(\varphi). \tag{3.51}$$

The relative radial lamella tip growth or local protrusion velocity at a certain position φ then reads

$$v_{\text{tip}}(t,\varphi) = v_r(t,\varphi) + \partial_t L(t,\varphi). \tag{3.52}$$

For the inward velocity $v_{\text{tip}}^{\text{in}}$ appearing in equation (3.49), we consider only forward tip growth and not shrinking,

$$v_{\text{tip}}^{\text{in}} = \big[v_{\text{tip}}(t,\varphi)\big]_{\geq 0}\,. \tag{3.53}$$

This is implemented by returning zero whence the expression in square brackets is negative. As already mentioned, the amount of incoming substratum ligands d is proportional to $v_{\text{tip}}^{\text{in}}$, because the local area gain at the lamella tip is proportional to the product $v_{\text{tip}}^{\text{in}} \cdot \mathrm{d}t$ at each time instant.

In a similar way, adhesion sites leave the cell domain at places where the lamella is retracting. The corresponding retraction velocity $v_{\text{tip}}^{\text{out}}$ is responsible for the loss of adhesion sites close to the tip,

$$-\,v_{\text{tip}}^{\text{out}}(t,\varphi) = \big[v_{\text{tip}}(t,\varphi)\big]_{\leq 0}\,. \tag{3.54}$$

where we consider cell shrinking by allowing for non-positive values only. Note that $v_{\text{tip}}^{\text{out}}$ is non-negative, cf. equations (3.48, 3.49).

When inspecting the micrograph in figure 3.7, on observes that there are only few green fluorescence spots of adhesion sites below the cell body as outlined by R in white. In order to take this observation into account, we suppose that the adhesions disassemble when they approach the cell body boundary. This could be triggered by specialized chemical agents close to or within the cell body. In human epidermal keratinocytes, tubulin is a possible candidate, because its location matches [231, figure 3.4], cf. also figure 1.6. Independent of the precise chemistry of their degradation pathway, we here assume that the adhesion sites vanish when they come into contact with the cell body. The relevant radial velocity of the cell body boundary with respect to the adhesion site is given by

$$v_{\text{body}}^{\text{out}}(t,\varphi) = \big[v_r(t,\varphi)\big]_{\geq 0}\,, \tag{3.55}$$

where we again pertain only non-negative values. In this way, adhesion sites approaching the cell body from the cell front in the direction of migration are removed from the pool at φ, see also equations (3.48, 3.49) and figure 3.7.

4. Passive tangential transport velocities: The peripheral mass balances from paragraph 3.8.2 describe transport and turnover of actin a, integrin receptors b and substratum ligands d. The corresponding transport velocities u_a, u_b, u_d redistribute the three species in φ-direction throughout the cell lamella. In order to keep this model as simple as possible, we suppose that the peripheral transport is purely passive and driven by drag effects arising from the cell being pulled over the substratum. Thus, as the cell proceeds, the stationary substratum underneath would be in transient contact with the cellular molecules, which would entail a certain amount of mutual sliding and result in an effective opposing drag. This is the essence of the molecular clutch mechanism described in paragraph 3.5.1, see also [156, section 3.4] for some experimental figures on the sliding of focal adhesion sites. In the basic description we develop here, we however take a short cut and have the velocity of the substratum with respect to the co-moving cell frame drive molecular transport, and not vice-versa. To this end we the assume the linear slip relations

$$\begin{aligned} u_a(t,\varphi) &= -\kappa_a v_\varphi(t,\varphi), & u_b(t,\varphi) &= -\kappa_b v_\varphi(t,\varphi), \\ & & u_d(t,\varphi) &= -\kappa_d v_\varphi(t,\varphi), \end{aligned} \tag{3.56}$$

expressing the molecular transport velocities u_a, u_b, u_d in terms of the local tangential projection of the substratum velocity $-v_\varphi$. The effective slip factors $\kappa_a < \kappa_b < \kappa_d \leq 1$ are model parameters, see table A.6.

Apart from considering φ as the only spatial variable, the equations (3.56) constitute the second major assumption in the peripheral approximation. Naturally, such a simplistic velocity model cannot fully capture the transport phenomena occurring in the cytoplasm or on the cell membrane. This is also the reason for including the diffusion term $\propto D_a$ in the F-actin mass balance (3.45), which provides for a certain smoothing property being essential for the model cell's stability and migration capability.

5. Cellular migration force: In paragraph 1.7.1, we have found that the key molecular players driving cellular locomotion are actin, myosin and integrin. In the one-dimensional migration model, we have seen how actin

retrograde flow, myosin induced contraction and integrin adhesion jointly create the cellular locomotion forces, cf. paragraph 3.7.3. Similar to the one-dimensional model equation (3.38), we assume that the locomotion force is proportional to the local integrin receptor density b. As additional modification, we account for actin a and the lamella width L in the local force density $\mathbf{f}$,

$$\mathbf{f}(t,\varphi) = f_{\mathrm{loc}} \cdot a(t,\varphi) b(t,\varphi) L(t,\varphi) \cdot \hat{\mathbf{e}}_r(\varphi). \tag{3.57}$$

We interpret the combination of aL as a measure for the contractility of the cell in the specific direction $\hat{\mathbf{e}}_r$, which would ultimately arise from the activity of myosin motors not explicitly resolved in the two-dimensional model. In this way, the lamella segment around φ imposes a force on the cell body pulling in centripetal direction $\hat{\mathbf{e}}_r$, where the pulling strength f_{loc} is a model parameter, see table A.6. The force integral over the unit circle then determines the total cellular locomotion,

$$\mathbf{F}_{\mathrm{loc}} = \int_{-\pi}^{\pi} \mathbf{f}(t,\varphi)\, \mathrm{d}\varphi. \tag{3.58}$$

Essential to the model is that the integrin dissociation term $\propto \delta_b$ in equation (3.48) involves the exponential of the local tensile density $|\mathbf{f}(t,\varphi)|$ defined here, otherwise the model cell seems to be incapable to migrate.

In a friction-dominated environment, the traction force $\mathbf{F}_{\mathrm{loc}}$ determines the velocity $\mathbf{v}$ of the cell body from the effective drag $\gamma_{\mathbf{v}}$ of the cell with the substratum,

$$\gamma_{\mathbf{v}} \mathbf{v} = \mathbf{F}_{\mathrm{loc}}. \tag{3.59}$$

For simplicity, we assume that $\gamma_{\mathbf{v}}$ is a constant model parameter, again see table A.6. Together with the force integral (3.58), equation (3.59) constitutes the cell-level force balance, in full analogy to (3.40) from the one-dimensional migration model.

6. Radial force balance at lamella tip: In order to close the description, we still need an equation for the evolution of the local lamella width $L(t,\varphi)$. To this end, we introduce the effective cellular curvature force $\widetilde{\tau} = \widetilde{\tau}(t,\varphi)$,

$$\tilde{\tau} = -\frac{\tau_0 a^2}{R+L} + \partial_s\big(\tau_0 a^2 \partial_s L\big) + \frac{p_0}{L}. \tag{3.60}$$

The first two summands derive from the uncompensated tension of the F-actin network $\tau_0 a^2$ close to the curved cell outline. The first term

resembles the contribution of a purely circular geometry with radius $R+L$, and the second term the deviations from that circle. The specific exponent in the model expression $\tau_0 a^2$ depends on the employed stress model for the actin filament network, see e.g. [69]. Other values are possible and typically range from 1 to 2, of which we choose the upper bound to facilitate shape deformations in our model cell. The overall tension of the actin network behind the lamella tip can be adjusted by prescribing the coefficient τ_0, see table A.6. Moreover, we evaluate the derivatives at the surface of the cell body for simplicity. This avoids further complications, as the derivatives would otherwise involve L. The last summand in equation (3.60) incorporates the pressure-like protrusion force p_0 initiating from the central cell body and propagating towards the cell periphery. Here we model the effective decrease of that force throughout the lamella by including the inverse local lamella width L. As a further simplifying approximation, we assume that $p_0/L \gg \tau_0 a^2/(R+L)$. The motivation for this approach is, that the actin network at the lamella tip is rather protrusive than tensile, which is consistent with the observation of stress softening in lammellipodia-like, reconstituted actin networks [47]. Under this approximation, we may write

$$\widetilde{\tau} \approx \tau = \partial_s\big(\tau_0 a^2 \partial_s L\big) + \frac{p_0}{L}. \tag{3.61}$$

Importantly, the choice of the p_0 and τ_0 parameters is consistent with the employed approximation, cf. table A.6.

Lamella protrusion and retraction derives from a force balance at the tip $L(t,\varphi)$. In the peripheral approximation and the employed co-moving cellular coordinate system, the involved forces are balanced in radial direction exclusively. The resulting scalar radial force balance for lamella protrusion and retraction is

$$\phi_0 a \partial_t L = \tau + p_b a b - \rho_0 a^2. \tag{3.62}$$

The left hand side represents the friction force that opposes the lamella deformation occurring with the radial velocity $\partial_t L$. This friction is assumed to be proportional to the local concentration of F-actin, because the viscosity of the cytosol can be neglected, see paragraph 2.3.2. The first term on the right-hand side is the effective cellular curvature force $\tau = \tau(t,\varphi)$ as described above. The second term on the right-hand side $\propto p_b$ represents enhanced lamella protrusion onto substratum adhesion sites b. Such a protrusion involves F-actin polymerization initiating from

the barbed ends of the filaments, which we here assume to be a linear function in a. Finally, the F-actin network is engaged in retrograde flow towards the cell center. This gives rise to retraction stresses at the lamella tip, which derive from the tension in the filament network. Consistent with the arguments for deriving τ, we suppose that the stress is proportional to the squared concentration of actin a^2. The model parameters ϕ_0, p_0, p_b and ρ_0 are constants and listed in appendix table A.6.

3.9. Simulations including the cell lamella exhibit cellular shape and trajectory characteristics

1. Dimensional considerations: In order to obtain meaningful data from our simulations, we have to clarify the units that are implied by the model equations in the preceding section. In paragraph 1.7, we have identified μm and min as the biologically relevant time- and length-scale of cellular migration. Moreover, the total traction force of cells has been estimated to be in the nN region [10, table 2]. Thus, the physical scales of the model are set.

For chemistry, we first observe that a is the volume concentration of actin monomers assembled in filaments. Here we measure this concentration in mM, i.e. milli-moles per liter. In this way, typical values of a in the model are close to the ones observed in the lamellipodia of mouse melanoma cells [129], cf. also table A.5. On the other hand, the integrin receptors b and substratum ligands d clearly represent area concentrations indicating the number of molecules per surface area. Unfortunately, there seem to be no quantitative experimental data on typical values for b and d. If one estimates the lateral extension of a single integrin to be approximately $2 \ldots 5$ nm, one concludes that there could be $40.000 \ldots 250.000$ molecules per μm^2 in maximal packing on a square lattice. With the values b, d as in table A.5, the suitable area concentration measure is approximately $10^6\, \mu\text{m}^{-2}$.

The resulting dimensions of the model variables are listed in table A.5, together with typical values obtained from the simulations described below.

2. Simulating the quasi two-dimensional model cell: For the in-silico simulation of migrating cells, we start by initializing the model variables a, b, d, L with constant values along the cell perimeter $\varphi \in [-\pi, \pi]$. We then solve the evolution equations (3.45, 3.48, 3.49, 3.62) in an explicit

Euler-Maruyama scheme [127], where we have to take into account the periodic boundary conditions $X(t, -\pi) = X(t, \pi)$ for all variables $X = a, b, d, L$. The locomotion force follows from (3.58) and the cell velocity $\mathbf{v}$ from (3.59), so that the cell position $\mathbf{x}$ is updated according to $\mathrm{d}\mathbf{x} = \mathbf{v}\mathrm{d}t$ in each time step. All parameter values involved in this numerical model are listed in table A.6. Part of one particular resulting trajectory of the migrating model cell is shown in figure 3.8, together with the instantaneous cell outline and the concentrations of actin and integrin.

3. Experimental reference data: For comparison with experiments we include some image analysis data from a migrating human epidermal keratinocyte. The phase-contrast micrograph presented in figure 3.8 is part of a movie taken by Christoph Möhl at the Institut für Zellbiologie [155]. From these raw data the outline of cell edge and body can be extracted by means of semi-automatized image processing tools that have been developed by Wolfgang Alt, Christoph Möhl and Carina Wollnik [231]. The central idea for image processing is same as for the simulation model: the local cell-centric coordinate system is a natural representation for the description of motility phenomena. Here we only briefly summarize the employed algorithm to reconstruct both cell body and tip outline.

The center of the migrating cell had already been quantified in earlier efforts. Therefore, the transformation in polar coordinates attached to this very cell center was straight forward. The resulting map of image brightness values in polar coordinates then formed the basis for further processing. The two outlines were then detected with the help of a stochastic chain or active contour algorithm [7, 141, 231]. To this end, a circle of interest was prescribed around the cell center to define relevant region within the micrograph. Next, the radial gradients in the polar brightness map were computed. Subsequently, an imaginary chain was placed on the polar picture, and moved according to "image forces" including chain stiffness, centripetal contraction and radial brightness gradients. With suitably chosen parameters, this chain is driven towards the cell (body) outline, where additional stochastic perturbations helped to overcome small obstacles due to dirt or other debris. Repeating the procedure, the two outlines were obtained for each frame in the movie. Cell body and edge outline are colored cyan and blue in figure 3.8, respectively, and comprise the data needed for the analysis below.

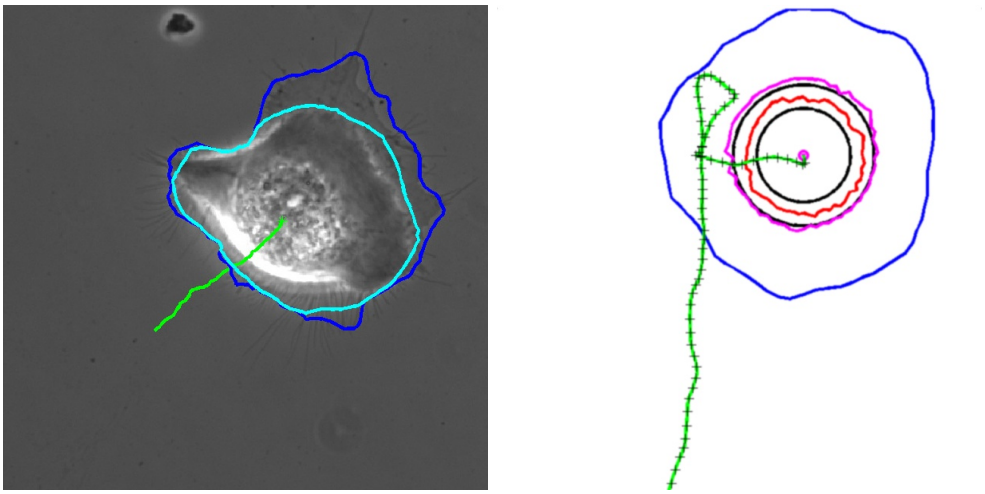

Figure 3.8.: Tracking of cell body and lamella outline of a migrating human epidermal keratinocyte (left) and a simulated model cell (right), both with the corresponding cell-center migration trajectory (green). In the simulation model we have assumed that the cell body has constant radius R as indicated by the innermost black circle in the right plot. The local lamella width L is indicated in blue, with the cell body circle as reference. Similarly, the concentration of actin a is drawn in red, with the same reference. Finally, the integrin adhesion sites b are indicated by the line in magenta, with respect to the outer black reference circle. Note that plotting the model cell in this compact figure involves additional rescaling of the values of a and b. For comparison, we present the analogous *in-vitro* experiment (left). Here, cell body (cyan) and lamella outline (blue) have been extracted by means of image analysis. The time-lapse phase-contrast micrographs have been taken by Christoph Möhl at the Institut für Zellbiologie, Universität Bonn. Subsequent image analysis was performed by Wolfgang Alt and Carina Wollnik.

4. Cell shape and trajectory: The full-length movie `s2d_simulation.avi`[6] of the simulated model cell exhibits several interesting quantitative features. As in figure 3.8, the lamella width L is represented by a blue line, F-actin a by a red line, adhering integrins b by a magenta line, and the cell center trajectory by a green one. After the initial start with evenly distributed molecular players, the lamella of the cell spreads in a symmetric manner for some 10 min. Next, the polar symmetry of the model cell breaks quite quickly due to the stochastic perturbation term in the actin polymerization, cf. equation 3.47. Approximately at $t \sim 14$ min, one can already see that the model cell starts to polarize, which coincides with a slow but steady increase in the cellular migration speed. Subsequently, the onsetting forward motion causes new adhesion ligands d to enter the cell domain from the tip, which gives a positive feedback on integrin b and thereby on actin a and lamella width L, as expected from equations (3.48, 3.45, 3.62). In this way, persistent migration emerges in a robust manner without the need for external guiding cues. In that sense, the essential guiding cue is the forward motion and protrusion of the model cell itself. Noteworthy, the cellular polarization seems to be most clearly visible in the integrin distribution.

Once a while, for example at $t \sim 30$ min, $t = 155$ min or $t \sim 200$ min, the model cell engages in rather sharp turns, whereby the apparent polarization tends to break down. However, protrusion continues so that the subsequent repolarization does not take very long. This exhibits the interplay between protrusion and persistent locomotion. The assembly of new adhesion sites induces an accelerated local protrusion, which pulls the cell in the corresponding direction. Thus, the shape dynamics of the model cell is decisive for the emerging directionally persistent trajectories.

5. Quantitative migration observables: In order to get a better understanding of the observed migration behavior of the model cell, we consider several quantities that serve as benchmarks for the ongoing cell motion and deformation. Apart from the cell's migration speed $|\mathbf{v}|$ and its lamella area

$$A_{\mathrm{Lam}}(t) = \frac{1}{2}\int_{-\pi}^{\pi} \left[L^2(t,\varphi) - R^2(t,\varphi)\right] \mathrm{d}\varphi, \tag{3.63}$$

we employ so-called directors that represent the instantaneous polarization of a certain cell characteristic like actin distribution. The director

[6] See supplementary material or `http://www.theobio.uni-bonn.de/people/mab/dsup`.

for a given quantity $X(\varphi)$ is given by

$$\mathbf{D}_X = \frac{\int_{-\pi}^{\pi} X \hat{\mathbf{e}}_r \, \mathrm{d}\varphi}{\int_{-\pi}^{\pi} X \, \mathrm{d}\varphi}, \tag{3.64}$$

and thus constitutes the orientation vector of X as averaged over the whole cell periphery. These directors can be defined for all model variables $X = a, b, d, L$, and have the property of being dimensionless with $|\mathbf{D}_X| \leq 1$.

In figure 3.9, we see the plots of mean cell speed $|\mathbf{v}|$ (green), lamella area A_{Lam} (blue), and the director strengths $|\mathbf{D}_L|, |\mathbf{D}_a|, |\mathbf{D}_b|$ for lamella width (black), actin (red) and integrin (magenta), respectively. Upon closer inspection one encounters characteristic time constants in these observables. For example, the integrin director seems to break down approximately every $15 \ldots 25$ min. Indeed, one can observe a sharp turn in the cell trajectory at $t \sim 200$ min, whence the integrin is evenly distributed around the cell. In the plots of figure 3.9, the lamella director $|\mathbf{D}_L|$ mostly seems to follow the actin director $|\mathbf{D}_a|$, unless there simultaneously occur rather dramatic evens in the integrin director $|\mathbf{D}_b|$. Similar effects are also exhibited by the cell migration speed and the lamella area, which will be discussed below.

Before that, however, we point out that the proposed directors and similar quantities are readily accessible to experimental measurements, although some require molecular staining by means of fluorescence. The main advantage of directors is that they provide for a cell-level description of subcellular detail. The molecular directors proposed here directly relate to the distribution of mechanically active units throughout the cell. We therefore suggest that such directors could serve as practical criteria to identify new phenotypes or mutants. For example, by looking at cell aspect ratio and actin variation along leading edge, the vast majority of observed keratocyte shapes could be predicted in a quantitative way [122]. As opposed to the common catalogization of genomics and proteomics, this emphasizes the importance of functional aspects as cornerstone of coherent biological model genesis.

6. Comparing correlation features in experiment and simulation: Here we take a closer look at the cell migration speed $|\mathbf{v}|$ and its possible relation with the lamella area A_{Lam}. To this end we consider the autocorrelation function

$$C_X(\tau) = \frac{\langle [X(t) - \mu_X] \cdot [X(t+\tau) - \mu_X] \rangle_t}{\sigma_X^2} \tag{3.65}$$

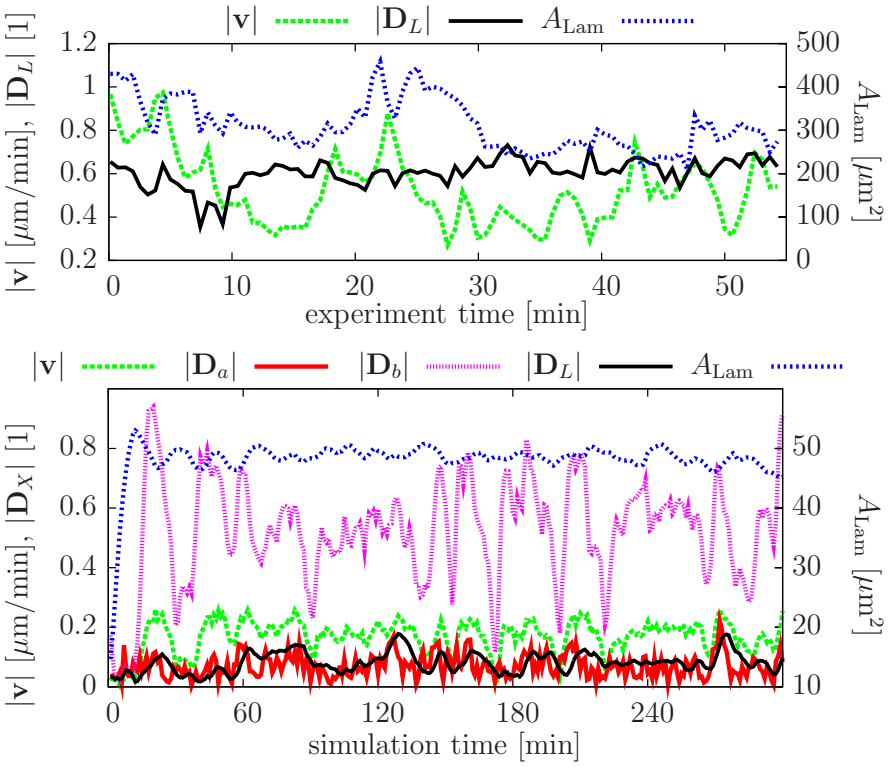

Figure 3.9.: Observables in the quasi two-dimensional cell migration experiment (top) and model (bottom). Here, we plot the time series of the cell speed $|\mathbf{v}|$ in green, the lamella director $|\mathbf{D}_L|$ in black, and the lamella area A_{Lam} in blue. In the simulation model, we additionally obtain the molecular directors of actin $|\mathbf{D}_a|$ (red) and integrin adhesions $|\mathbf{D}_b|$ (magenta). All directors are dimensionless, which is indicated by the symbol [1] for the respective units. In the model, the most prominent behavior is observed in the integrin director modulus $|\mathbf{D}_b|$, which is highly dynamic and varies almost over the whole possible range $0 \ldots 1$. Note that this director drops sharply before the model cell engages in turning movements, see e.g. at $t \sim 30, 155, 200$ min. Both model and experimental observables exhibit a seemingly regular quasi-periodic behavior. Further details are discussed in the text.

of a time-dependent quantity X, where $\langle\rangle_t$ indicates averaging over the time series, $\mu_X \equiv \langle X(t)\rangle_t$ the mean and $\sigma_X^2 \equiv \langle [X(t)-\mu_X]^2\rangle_t$ the squared standard deviation of X. The correlation coefficient $C_X(\tau)$ has the property of being $\in [-1,1]$. When it is close to $+1$, then – on average – $X(t)$ is similar to $X(t+\tau)$. Conversely, if $C_X(\tau)$ is around -1, $X(t)$ would be on average close to $-X(\tau)$. Finally, if $C_X(\tau)$ is close to zero, than there is no trend in either of the two aforementioned directions.

As can be seen in figure 3.10, the autocorrelation functions for the cell speed $X(t) = |\mathbf{v}(t)|$ has a pronounced minimum both in experiment and simulation. For the simulated cell, this reflects the properties of the green speed curve from figure 3.9, where the migration velocity increases and decreases in periods of approximately 25 min. Correspondingly, the correlation function exhibits a maximum for correlation times $\tau \sim 22 \ldots 28$ min. Consistent with this model prediction, a similar effect can also be observed in the experimental data. It is not surprising that these characteristic speed fluctuations are also reflected in the model cell's trajectory, cf. figure 3.8 and the movie. In particular, the black crosses on the green trajectory are evenly spaced in time, so that intermittent phases of decreased cell speed become visible by the proximity of these time checkmarks. Naturally, this effect is most pronounced close to the turning points in the trajectory. Thus, the autocorrelation function of the migration speed reflects the cell's tendency to reorient and additionally exhibits the inherent characteristic reorientation time-scale.

The autocorrelation functions (3.65) of the lamella area $X(t) = A_{\mathrm{Lam}}(t)$ exhibit the same general behavior, although the period times appear to be somewhat different, see figure 3.10 (bottom plot). In the experimental curve we observe a broad minimum from $\tau = 8 \ldots 13$ min, which however does not deviate significantly from the zero within the given confidence interval. There is also no clear subsequent maximum due to the limited observation time of the experiment. In contrast, there is a very pronounced trend and a very clear periodicity of $18 \ldots 19$ min for the model cell. Since the simulations can be run as long as desired, the confidence interval is very narrow as well. One might be tempted to extrapolate the period in the experiment to some 20 min, based on the position of the minimum at the red curve in figure 3.10 (bottom plot). However, the experimental data neither support nor contradict any such predictions.

Regardless of the precise periodicity, both experiment and model data point to the presence of certain persistence phenomena in migrating cells. Lamella area and cell speed are modulated in the sense that they increase and subsequently decrease in a repetitive manner, which hints

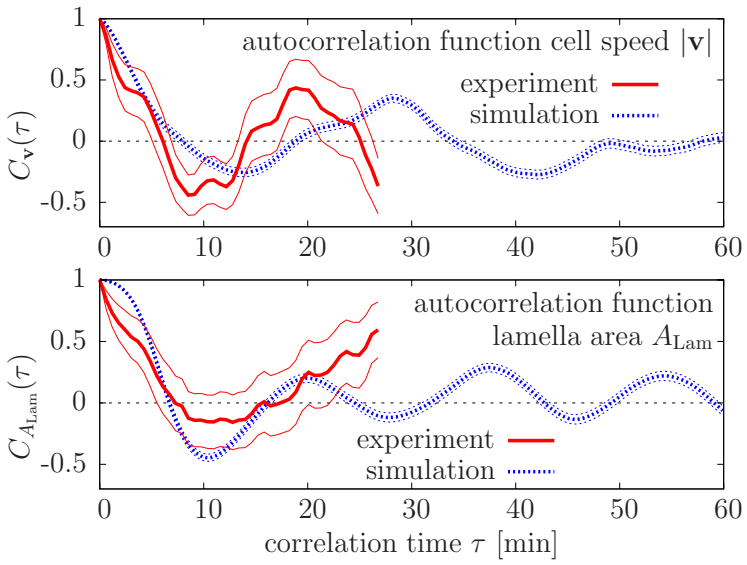

Figure 3.10.: Autocorrelation function of cell speed $|\mathbf{v}|$ (top) and lamella area (bottom) in experiment and model. The qualitative shapes of the experimental and simulation curves seem to coincide. The positions of minima and maxima of both speed autocorrelation functions (top) exhibit a certain periodicity, roughly 20 min for the experiment, and 27 min for the simulation model. A similar behavior can be observed in the lamella area autocorrelation function (bottom). There, the simulations show a very prominent periodicity of approximately 18 min. Due to the limited observation time, the experimental curve is less indicative. Note that the thin lines surrounding the autocorrelation curves indicate the 95% confidence interval.

towards specific adaptation properties in the underlying dynamical processes. Comparison of several cells from experiments shows that their modulation is universal, whereas the respective periodicity is not [210, figure 14 & 15]. In the well-controlled simulation model we do not have to expect ubiquitous variations across different individual cells, because the exact model behavior is naturally reproducible. It is therefore not surprising that both periodicity and modulation are robust for a given set of parameters. The degree of robustness can be tested by adjusting the stochastic perturbation β_a for actin, which does only barely affect the observed model dynamics of speed and lamella area, even when increased to quite high values.

Reviewing the plots from figure 3.10, it is remarkable that the area and speed autocorrelation functions look quite similar in a qualitative way. Thus one might suspect a relation or dependency between the two model observables. In order to test this hypothesis, we consider the cross-correlation function

$$C^{\times}_{XY}(\tau) = \frac{\langle [X(t) - \mu_X] \cdot [Y(t+\tau) - \mu_Y] \rangle_t}{\sigma_X \sigma_Y}, \tag{3.66}$$

where again μ_X denotes the mean of X over the whole time series and σ_X its standard deviation. This function probes the similarity of the two time series $X(t)$ and $Y(t+\tau)$, where τ represents the relative time lag.

The crosscorrelation function of cell speed $|\mathbf{v}| =: X$ versus lamella area $A_{\mathrm{Lam}} =: Y$ is plotted in figure 3.11. The data of experiment (red) and simulation (blue) exhibits a certain maximum close to $\tau = 0$, which seemingly implies that cell speed and lamella area are correlated, and the relative lag time is given by the position of the respective maximum. Yet the basis for the underlying data consists of only one single cell trajectory in both theory and experiment. Indeed, when comparing the experimental observation with [210, figure 19], one finds that other human epidermal keratinocytes behave markedly different. This individualism pervades also the simulation model. From the blue simulation curve in figure 3.11, one might be tempted to infer from the maximum plateau at $\tau \sim -7$ min, that the cell speed builds after the lamella area has increased. However, this feature is not robust and highly depends on the specific simulation, because the stochastic realizations of the two variables a, d differ for every run. Neither does fixing all other parameters and decreasing the stochastic perturbation lead to more conclusive results. In yet another cell migration model, there is also no clear trend whether the lamella area follows speed or vice versa [193, figures 12 &

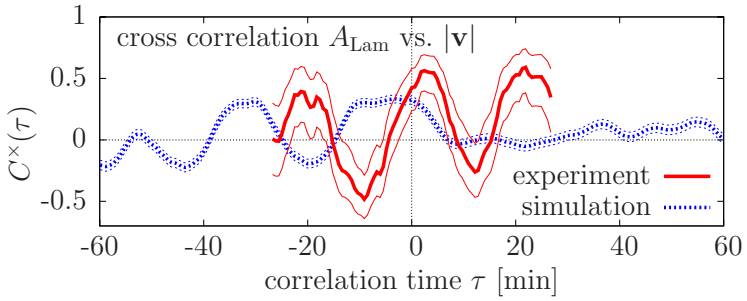

Figure 3.11.: Crosscorrelation function of speed and lamella area in experiment (red) and model (blue). The thin lines around the correlation plots represent the 95% confidence interval. As judged from the first maximum of the red experimental curve at $\tau \sim 3$ min, the lamella area seems to follow the cell speed with a small time lag. However, this phenomenon is not universal in human epidermal keratinocytes. The blue simulation curve also does not exhibit a clear trend. For further explanations see the text.

17].

The biological relevance of this question lies in the possibility to explain molecular interactions in a functional manner and particularly in terms of the whole-cell behavior. It is commonly perceived that the protrusion and retraction of the lamella constitutes a kind of cellular sensing, with an implicit assumption that the environment would thus be probed more efficiently. Consequently, one is lead to hypothesize that cellular reorientation would somehow be related with preceding protrusions. Since we could not make definite statements about this relation, it would be desirable to further refine the methodology of theoretical model and experimental data evaluation. In the worst case we could hope for finding that protrusion and subsequent migration are not related at all. In the best case we would quantify the precise relation so to make a prediction on the molecular pathways suitable to trigger the cellular reorientation. We emphasize, however, that such predictions are only possible by considering basic quantities such as cell and lamella size, area, orientation and relate them to the molecular distributions on the whole-cell level as summarized e.g. by the directors proposed above. Thus, to arrive at a modern biology of the cell, it is inevitable to consider quantitative spatio-temporal and kinetic features of molecular distributions.

4. Generalized Voronoi tessellations divide space into cellular compartments

Summary: In this chapter we propose a new method to construct Voronoi tessellations from generators of elliptic shape. The resulting set of Voronoi cells represents individual biological cells cooperating in small aggregates or proto-tissues.

The locus of the contact border between two Voronoi cells is given by an equality of mathematical norms. Each of these norms attributes a certain power to any point in space, and is associated with the generators adjacent to the contact border. Scaling the contact equation with a monotonic function gives an equivalent expression, so that the generators may be written in terms of matrices in homogeneous coordinates. These generator matrices describe ellipses of arbitrary size and orientation in the two-dimensional plane. Finding the shape of the contact border between two elliptic generators amounts to diagonalizing the so-called contact matrix. The entries of this matrix are coefficients of a quadratic form for a conic section. Non-degenerate contact matrices describe ellipses or hyperbolas, while degenerate contact matrices give rise to straight lines or parabolas. All these contact borders can be parameterized in polar coordinates. Using the polar ordering property of points on the contact border, we find an algorithm that constructs Voronoi tessellations from the elliptic generators.

4.1. Voronoi generators consisting of norm-functions give rise to curved cell-cell contacts

The following definitions involve the d-dimensional real vector space[1] $\mathbb{R}^d$, which is a particular example of a normed space. In principle one could give these definitions in the more general setting of normed spaces. However, this generalization is not useful for describing biological systems in the intended context. Let $\{i = 1, \ldots N\}$ be a set of indices with $N \in \mathbb{N}$ members.

[1]For an introductory text on vector spaces and linear algebra, see the particularly accessible textbook [25]. For reference purposes, [37] is quite versatile.

Definition 4.1.1 (Voronoi generator): Let $\|.\|_i$ be a norm on $\mathbb{R}^d$, and let the zero element of the normed space $\left(\mathbb{R}^d, \|.\|_i\right)$ be denoted by $\mathbf{x}_i$. Then the norm $\|.\|_i$ is called Voronoi generator.

Remark: The zero element $\mathbf{x}_i$ of the norm $\|.\|_i$ is defined by the expression $\|\mathbf{x}_i\|_i = 0$. In practice, $\mathbf{x}_i$ is supposed to coincide with the position of the cell center, for example as given by the center of cell body or nucleus.

Example 4.1.2: Consider the n-th power norm of the d-dimensional vector $\mathbf{x} := (x_1, \ldots, x_k, \ldots, x_d)$,

$$\|\mathbf{x}\|^{(n)} := \Big(\sum_{k=1}^{d} x_k^n\Big)^{1/n}. \tag{4.1}$$

The corresponding shifted expressions

$$\|\mathbf{x}\|_i := \|\mathbf{x} - \mathbf{x}_i\|^{(n)} \tag{4.2}$$

are also norms, whereby the normed spaces $\left(\mathbb{R}^d, \|.\|_i\right)$ have the zero-element $\mathbf{x}_i$.

Example 4.1.3: Let $\widetilde{\mathbb{F}} \in \mathbb{R}^{d\times d}$ be a d-dimensional, symmetric, positive definite matrix. With $\mathbf{x}$ as in the previous example, the expression

$$\|\mathbf{x}\|^{(\widetilde{\mathbb{F}})} = \left[\mathbf{x}^T \cdot \widetilde{\mathbb{F}} \cdot \mathbf{x}\right]^{1/2} \tag{4.3}$$

constitutes a norm. Allowing a separate $\widetilde{\mathbb{F}}_i$ for each i, and considering $\mathbf{x}$ relative to $\mathbf{x}_i$, we obtain the norms

$$\|\mathbf{x}\|_i := \|\mathbf{x} - \mathbf{x}_i\|^{(\widetilde{\mathbb{F}}_i)} \equiv \left[(\mathbf{x} - \mathbf{x}_i)^T \cdot \mathbb{F}_i \cdot (\mathbf{x} - \mathbf{x}_i)\right]^{1/2}, \tag{4.4}$$

where the corresponding normed space $\left(\mathbb{R}^d, \|.\|_i\right)$ again has its zero element at $\mathbf{x}_i$.

Definition 4.1.4 (Voronoi cell): Let $\left\{\|.\|_i : i = 1, \ldots, N\right\}$ be a set of Voronoi generators and $0 < d_{\max} \in \mathbb{R}$ a real number. Then

$$\mathcal{V}_i := \left\{\mathbf{x} \in \mathbb{R}^d : \|\mathbf{x}\|_i < \min\left[\|\mathbf{x}\|_j, d_{\max}\right] \ \forall j \neq i\right\} \tag{4.5}$$

is the Voronoi cell corresponding to the generator $\|.\|_i$.

Remark 4.1.5: This marks the central property of Voronoi tessellations. The set $\mathcal{V}_i$ consists of the "spatial" surrounding of $\mathbf{x}_i$. All points in $\mathcal{V}_i$ are – in this general sense – closer to $\mathbf{x}_i$ than to any other generator $\mathbf{x}_j$ with $i \neq j$.

Definition 4.1.6 (Contact border, neighbor pair): Let $\overline{\mathcal{V}_i}$ be the closure of Voronoi cell i, and let $i \neq j$. If the intersection

$$\Gamma_{ij} := \overline{\mathcal{V}_i} \cap \overline{\mathcal{V}_j} \neq \emptyset, \tag{4.6}$$

is non-empty, then i, j form a neighbor pair and Γ_{ij} is called the contact border. This neighbor relation is denoted by $i \sim j$.

Remark (Contact equation): From the definitions 4.1.4 and 4.1.6, we find that Γ_{ij} is embedded in a certain point set,

$$\Gamma_{ij} \subset \Big\{ \mathbf{x} \in \mathbb{R}^d : \|\mathbf{x}\|_i = \|\mathbf{x}\|_j \Big\}. \tag{4.7}$$

This set is described by the so-called contact equation, $\|\mathbf{x}\|_i = \|\mathbf{x}\|_j$, and represents a hyper-surface, which separates the two corresponding Voronoi cells.

Corollary 4.1.7 (Generalized Voronoi cell): Let $\mathcal{P} : \mathbb{R} \ni y \mapsto \mathcal{P}(y) \in \mathbb{R}$ be a scaling function of the form

$$\mathcal{P}\big(y\big) = q y^{\nu} + \mathcal{P}_0, \tag{4.8}$$

with the real constants $q \neq 0, \nu \neq 0, \mathcal{P}_0 \in \mathbb{R}$. The following definitions of a Voronoi cell $\mathcal{V}_i$ are equivalent:

1. $$\mathcal{V}_i = \Big\{ \mathbf{x} \in \mathbb{R}^d : \qquad \|\mathbf{x}\|_i < \min\Big[\|\mathbf{x}\|_j, d_{\max} \Big] \qquad \forall j \neq i \Big\}, \tag{4.9}$$

2. $\operatorname{sgn} q = \operatorname{sgn} \nu$:
$$\mathcal{V}_i = \Big\{ \mathbf{x} \in \mathbb{R}^d : \ \mathcal{P}\big(\|\mathbf{x}\|_i\big) < \min\Big[\mathcal{P}\big(\|\mathbf{x}\|_j\big), \mathcal{P}\big(d_{\max}\big) \Big] \ \ \forall j \neq i \Big\}, \tag{4.10}$$

3. $\operatorname{sgn} q \neq \operatorname{sgn} \nu$:
$$\mathcal{V}_i = \Big\{ \mathbf{x} \in \mathbb{R}^d : \ \mathcal{P}\big(\|\mathbf{x}\|_i\big) > \max\Big[\mathcal{P}\big(\|\mathbf{x}\|_j\big), \mathcal{P}\big(d_{\max}\big) \Big] \ \ \forall j \neq i \Big\}. \tag{4.11}$$

Proof: The result follows from equivalent reformulations of the inequality in equation (4.5). First we note that the shape of the contact border Γ_{ij} does not change when transforming both sides of the contact equation with the help of the scaling function $\mathcal{P}$. For the Voronoi cells not to change, however, the inequality in (4.5) has to be transformed simultaneously. The resulting expressions (4.9, 4.10, 4.11) depend on the monotonicity behavior of $\mathcal{P}$, which is determined by the sign function $\mathrm{sgn}(q \cdot \nu)$ of the involved constants q, ν.

Based on the corollary 4.1.7, we may extend our notion of Voronoi generators, so that the flexibility of the scaling function $\mathcal{P}$ can be exploited in the intended biological application.

Definition 4.1.8 (Generalized Voronoi generator): Let $\mathcal{P}(y) = qy^{\nu} + \mathcal{P}_0$ be a scaling function with real constants $q \neq 0, \nu \neq 0, \mathcal{P}_0 \in \mathbb{R}$. Define the abbreviations

$$\mathcal{P}_i(.) \equiv \mathcal{P}\big(\|.\|_i\big) \qquad\qquad \mathcal{P}_{\mathrm{ex}} \equiv \mathcal{P}\big(d_{\max}\big). \tag{4.12}$$

Then we call the scaled norm $\mathcal{P}_i(.)$ a generalized Voronoi generator, and $\mathcal{P}_{\mathrm{ex}}$ the extremal scaled norm.

Remark (Generalized contact equation, point power): With the preceding notion of generalized Voronoi generator, the embedding set of a contact border (4.7) is modified to

$$\Gamma_{ij} \subset \Big\{ \mathbf{x} \in \mathbb{R}^d : \mathcal{P}_i(\mathbf{x}) = \mathcal{P}_j(\mathbf{x}) \Big\}, \tag{4.13}$$

which now involves the generalized contact equation $\mathcal{P}_i(\mathbf{x}) = \mathcal{P}_j(\mathbf{x})$. In this sense, each generalized Voronoi generator $\mathcal{P}_i$ assigns to the point $\mathbf{x}$ a certain power $\mathcal{P}_i(\mathbf{x})$. Voronoi cells and contact equation therefore arise from the comparison of the point powers $\mathcal{P}_i(\mathbf{x}), \mathcal{P}_j(\mathbf{x})$, which also may be interpreted as distance notions, cf. also remark 4.1.5.

Definition 4.1.9 (Free margin): The free margin Γ_{i0} of a Voronoi cell $\mathcal{V}_i$ is the boundary set

$$\Gamma_{i0} := \partial \mathcal{V}_i \setminus \bigcup_{j \neq i} \Gamma_{ij}. \tag{4.14}$$

Remark: From definition 4.1.4, $d_{\max}$ determines the maximal extension of a Voronoi cell in directions where there is no other cell. Correspondingly,

the set Γ_{i0} is contained in $\{\mathbf{x} \in \mathbb{R}^d : \|\mathbf{x}\|_i = d_{\max}\}$. By corollary 4.1.7, this is equivalent to

$$\Gamma_{i0} \subset \{\mathbf{x} \in \mathbb{R}^d : \mathcal{P}_i(\mathbf{x}) = \mathcal{P}_{\text{ex}}\}, \tag{4.15}$$

meaning that the point power $\mathcal{P}_i(\mathbf{x})$ is constant on the free margin Γ_{i0}.

In the remaining part of this section, let $N \in \mathbb{N}$ indicate the number of present Voronoi generators.

Definition 4.1.10 (Voronoi tessellation): Let $\{\mathcal{P}_i(.) : i = 1, \ldots, N\}$ be a specific set of generalized Voronoi generators. The collection of all Voronoi cells

$$\bigcup_i \mathcal{V}_i \tag{4.16}$$

is called Voronoi tessellation.

Definition 4.1.11 (Voronoi diagram): Let $\{\mathcal{P}_i(.) : i = 1, \ldots, N\}$ be a specific set of generalized Voronoi generators. Then the graph of

$$\bigcup_{i \sim j} \Gamma_{ij} \quad \cup \quad \bigcup_i \Gamma_{i0} \tag{4.17}$$

is called Voronoi diagram.

Remark: In two spatial dimensions, the Voronoi tessellation covers space with its plastering mosaic tiles or cells, while the corresponding diagram refers to the emerging edges in between. However, in the rest of this thesis we do not insist on this peculiar distinction and consider Voronoi tessellation and Voronoi diagram as synonyms, regardless of the dimension of the underlying space.

Definition 4.1.12 (Delaunay triangulation): Let $\{\mathcal{P}_i(.) : i = 1, \ldots, N\}$ be a specific set of generators, and let $\{(i, j) : i \sim j\}$ be the set of neighbor pairs of the Voronoi tessellation. The graph of straight lines connecting the cell centers of all neighbor pairs (i, j) is called Delaunay triangulation.

Remark: As a historic note, Voronoi tessellations constructed from the Euclidean norm were described by Voronoi[2] in 1908 [223]. Delaunay triangulations were proposed by Delaunay[3] in 1934 [56].

[2]Russian name [228]: Георгий Феодосьевич Вороной
[3]Russian name [228]: Борис Николаевич Делоне

Example 4.1.13: Let the centers $\mathbf{x}_i \in \mathbb{R}^2$ for all $i = 1, \ldots, N$ and the generalized Voronoi generators $\mathcal{P}_i\big(\mathbf{x}\big) = \big(\mathbf{x} - \mathbf{x}_i\big)^2$. With $q = 1, \nu = 2, \mathcal{P}_0 = 0$ in equation (4.8), we see that the underlying norm $\|.\|_i$ is the Euclidean one, whereby the zero element is situated at $\mathbf{x}_i$, as usual. The generalized contact equation (4.13) reads

$$\mathcal{P}_i(\mathbf{x}) = \mathcal{P}_j(\mathbf{x}) \quad \Leftrightarrow \quad \|\mathbf{x}\|_i = \|\mathbf{x}\|_j \quad \Leftrightarrow \quad \|\mathbf{x} - \mathbf{x}_i\| = \|\mathbf{x} - \mathbf{x}_j\|, \tag{4.18}$$

where the equivalence to the ordinary contact equation 4.7 follows from corollary 4.1.7. In this two-dimensional setting, the set of all contact borders $\big\{\Gamma_{ij} : i \sim j\big\}$ (straight lines) and free margins $\big\{\Gamma_{i0} : \Gamma_{i0} \neq \emptyset\big\}$ (circular arcs) comprises the Voronoi diagram as sketched in figure 4.1 (left). The generator centers $\mathbf{x}_i$ are indicated by blue stars, which are situated within their surrounding Voronoi cell as delimited by the aforementioned Γ_{ij} and Γ_{i0}. The resulting Delaunay triangulation connects the centers $\mathbf{x}_i$ of neighboring cells by cyan lines. As a first generalization to these simple Euclidean generators, we have proposed a method to construct two-dimensional Voronoi tessellations from $\mathcal{P}_i(\mathbf{x}) = (\mathbf{x} - \mathbf{x}_i)^2/r_i^2$, with $r_i > 0$ a scalar weight representing the size of the cell [31]. It turned out, that the cell-cell contacts Γ_{ij} in general also comprise circular arcs, in addition to the free margins Γ_{i0}, see figure 4.1 (right).

In the following section we construct an anisotropic norm allowing for curved cell-cell contacts with varying curvature.

4.2. Homogeneous coordinates facilitate transformation operations on vectors

In the preceding section we have set up the formal definition of Voronoi tessellation in the vector space $\mathbb{R}^d$. However, in this section we employ the notion of homogeneous coordinates instead of considering the usual Cartesian vectors with d components.[4] Dating back to Möbius [149], homogeneous coordinates are heavily used in computer graphics, because they simplify and unify many operations on sets of points or vectors, see e.g. [102][5]. Most notably, translation and subsequent rotation can be

[4] Initially, I encountered the idea of homogeneous coordinates on `wikipedia.org` [228, fall 2010]. Subsequently, I have set up my own notions, which are presented in the rest of this section.

[5] Pierluigi Taddei, the author of [208], pointed me to the highly relevant article [102] by Kenneth J. Hill in August 2012, when the presented theory on elliptic Voronoi diagrams had already been completed.

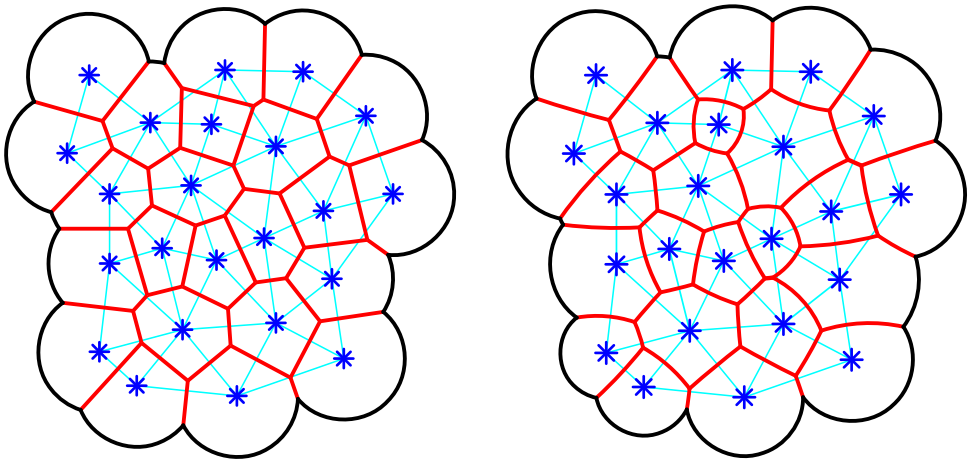

Figure 4.1.: Planar (left) and circular (right) Voronoi diagram differ in the shapes of their contact borders Γ_{ij} (red). The underlying centers $\mathbf{x}_i$ (blue stars) are the same in both diagrams. The generators in the planar Voronoi diagram consist of the Euclidean norm, centered at the center points $\mathbf{x}_i$. Weighting the Euclidean norm with different weights $r_i > 0$ for each center causes the Voronoi cells to exhibit varying sizes and shapes. In particular, the contacts are straight lines in the planar Voronoi diagram (left), whereas in the circular Voronoi diagram (right) they are spherical arcs. The free margins Γ_{i0} (black) close the cells towards the surrounding. The light cyan lines connect cell centers obeying the neighbor relation $i \sim j$, i.e. when the cells are adjacent to each other and thereby share a common cell boundary Γ_{ij}. In this way, the so-called Delaunay triangulation (cyan) is the geometric dual of the Voronoi tessellation (red).

represented by a product of two corresponding square matrices. This is also the main advantage of homogeneous coordinates to the modelling of cells in this thesis. For readers interested in a more formal development of homogeneous coordinates, we refer to mathematical texts on projective geometry, for example [51].

Definition 4.2.1 (Homogeneous coordinates): Let $\mathbf{x} = \big(x_1, \ldots, x_d\big) \in \mathbb{R}^d$, and let $\Lambda \neq 0$ be a length unit. The vector

$$\mathbf{x}_{\text{hom}} := \big(x_1/\Lambda, \ldots, x_d/\Lambda, 1\big) \qquad \in \mathbb{R}^{d+1} \tag{4.19}$$

is called homogeneous transform of $\mathbf{x}$. Its components $x_1, \ldots, x_d, 1$ are the homogeneous coordinates of $\mathbf{x}$.

Remark: In homogeneous coordinates, the position of a point is encoded in the ratios – and not the absolute values – of the vector components. Since we are dealing with cells and cell aggregates of finite extension, we do not need to take into account points at infinity, where Λ would be zero. Therefore, the transformation $\mathbf{x} \leftrightarrow \mathbf{x}_{\text{hom}}$ is bijective, i.e. an isomorphism. For convenience, we set $\Lambda := 1$.

Definition 4.2.2 (Translation matrix): Let $\mathbf{y} = \big(y_1, \ldots, y_d\big) \in \mathbb{R}^d$. Then

$$\mathbb{T} = \mathbb{T}\big(\mathbf{y}\big) := \begin{pmatrix} 1 & 0 & \ldots & 0 & y_1 \\ 0 & \ddots & \ddots & \vdots & \vdots \\ \vdots & \ddots & \ddots & 0 & \vdots \\ \vdots & & \ddots & 1 & y_d \\ 0 & \ldots & \ldots & 0 & 1 \end{pmatrix} \qquad \in \mathbb{R}^{(d+1)\times(d+1)} \tag{4.20}$$

is called d-dimensional homogeneous translation matrix.

Remark: The d-dimensional homogeneous translation matrix acts on the homogeneous transform $\mathbf{x}_{\text{hom}}$ of any d-dimensional vectors $\mathbf{x}$. Suppose $\mathbf{x} = \big(x_1, \ldots, x_d\big), \mathbf{y} = \big(y_1, \ldots, y_d\big) \in \mathbb{R}^d$. The operation

$$\widetilde{\mathbf{x}}_{\text{hom}} := \mathbb{T}\big(\mathbf{y}\big)\mathbf{x}_{\text{hom}} \tag{4.21}$$

displaces $\mathbf{x}$ by $\mathbf{y}$. This can be seen by assuming $\Lambda = 1$, inserting $\mathbf{x}_{\text{hom}}$ and computing the matrix product

$$\widetilde{\mathbf{x}}_h = \big(x_1 + y_1, \ldots, x_d + y_d, 1\big). \tag{4.22}$$

Definition 4.2.3 (Homogeneous rotation matrix): Let $\widetilde{\mathbb{D}} = \widetilde{\mathbb{D}}\big(\{\varphi_k\}\big)$ be the rotation matrix in d dimensions, with its angle parameters $\varphi_k \in \mathbb{R}\ \forall k = 1, \ldots, d(d-1)/2$. Then

$$\mathbb{D} = \mathbb{D}\big(\{\varphi\}\big) := \begin{pmatrix} \ddots & & \iddots & 0 \\ & \widetilde{\mathbb{D}}\big(\{\varphi_k\}\big) & & \vdots \\ \iddots & & \ddots & 0 \\ 0 & \ldots & 0 & 1 \end{pmatrix} \quad \in \mathbb{R}^{(d+1)\times(d+1)} \tag{4.23}$$

is called d-dimensional homogeneous rotation matrix.

With these notations at hand, we can conveniently define certain functions $\mathcal{P}_i$ as anisotropic generators of generalized Voronoi diagrams. As indicated before, each of these functions then encodes the approximate shape of a tissue cell in a sense that will become apparent in the following sections.

4.3. Matrices in homogeneous coordinates provide for anisotropic Voronoi generators

Definition 4.3.1 (Anisotropic generator matrix): Let $\mathbb{T}_i := \mathbb{T}\big(-\mathbf{x}_i\big)$ and $\mathbb{D}_i = \mathbb{D}\big(\{-\varphi_k^i\}\big)$ be d-dimensional homogeneous translation and rotation matrices, respectively. Furthermore, let the homogeneous axis matrix $\mathbb{F}_i := \mathrm{diag}\big(w_1^i, \ldots, w_d^i, -1\big)$, be diagonal with $w_j^i > 0$ for $j = 1, \ldots, d$. The anisotropic generator matrix $\mathbb{E}_i$ is then defined as

$$\mathbb{E}_i := \mathbb{T}_i^T \mathbb{D}_i^T \mathbb{F}_i \mathbb{D}_i \mathbb{T}_i \qquad \in \mathbb{R}^{(d+1)\times(d+1)}, \tag{4.24}$$

whereby superscript capital T indicates matrix transposition.

The parameters $\mathbf{x}_i$ describe center position, and $\big\{w_j^i\big\}$ the anisotropic axis weights of a specific Voronoi generator i. Its orientation is determined by the $d(d-1)/2$ angles $\{\varphi_k^i\}$ in the homogeneous rotation matrix $\mathbb{D}_i$. Again, the center position of a generator is supposed to coincide with the center of a model cell body or nucleus.

Definition 4.3.2 (Anisotropic Voronoi generator): The quadratic function

$$\mathcal{P}_i\big(\mathbf{x}\big) := \mathbf{x}_{\mathrm{hom}}^T \cdot \mathbb{E}_i \cdot \mathbf{x}_{\mathrm{hom}}. \tag{4.25}$$

is called anisotropic Voronoi generator.

Before exploring the formal properties of $\mathcal{P}_i$, and, in particular, whether it is of the form as required by definition 4.1.1, we consider a basic example, which provides also a kind of formal motivation for our approach.

Example: In $d = 2$ there is only the single angle parameter $\varphi_1^i \equiv \varphi_i$ in the homogeneous rotation matrix $\mathbb{D}_i$. Furthermore we identify $w_1^i \equiv 1/a_i^2, w_2^i \equiv 1/b_i^2$ in the homogeneous axis matrix $\mathbb{F}_i$, where a_i and b_i are positive real constants. Expansion of equation (4.25) leads to point powers being a quadratic form in the components x, y of $\mathbf{x}$,

$$\mathcal{P}_i\big(\mathbf{x}\big) = \frac{\big(\Delta x \cos\varphi_i + \Delta y \sin\varphi_i\big)^2}{a_i^2} + \frac{\big(-\Delta x \sin\varphi_i + \Delta y \cos\varphi_i\big)^2}{b_i^2} - 1, \tag{4.26}$$

with the abbreviations $\Delta x := x - x_i,\ \Delta y := y - y_i,\ \mathbf{x}_i = (x_i, y_i)$. Equating the right-hand side with a constant $C > -1$, one obtains the implicit definition of the graph of an ellipse. In the specific case of $x_i = y_i = \varphi_i = 0$, the point power $\mathcal{P}_i(\mathbf{x})$ simplifies to

$$\mathcal{P}_i(\mathbf{x}) = \frac{x^2}{a_i^2} + \frac{y^2}{b_i^2} - 1. \tag{4.27}$$

If we furthermore set $\mathcal{P}_i(\mathbf{x})$ equal to zero, we obtain an ellipse equation in its fundamental form, whereby the semi-axes a_i, b_i are aligned with the coordinate axes x, y,

$$\mathcal{P}_i\big(\mathbf{x}\big) = 0 \quad \Leftrightarrow \quad \frac{x^2}{a_i^2} + \frac{y^2}{b_i^2} = 1. \tag{4.28}$$

We interpret the emerging graph as the outline of the cell body, which surrounds the center of each cell, and encloses its nucleus.

Proposition 4.3.3: The expression $\mathbf{x}_{\text{hom}}^T \cdot \mathbb{E}_i \cdot \mathbf{x}_{\text{hom}}$ is a Voronoi generator, i.e. of the form $q\|\mathbf{x}\|^\nu + \mathcal{P}_0$.

Proof: Without loss of generality assume $\mathbb{E}_i = \mathbb{F}_i$ (otherwise use $\mathbb{T}_i, \mathbb{D}_i$ to transform both $\mathbb{E}_i$ and $\mathbf{x}$). Then we have

$$\mathcal{P}_i\big(\mathbf{x}\big) = \mathbf{x} \cdot \widetilde{\mathbb{F}}_i \cdot \mathbf{x} - 1, \qquad \text{with } \widetilde{\mathbb{F}}_i = \operatorname{diag}\big(w_1^{(i)}, \ldots, w_d^{(i)}\big), \tag{4.29}$$

where $\mathbf{x} = \big(x_1, \ldots, x_d\big)$. Note that $\widetilde{\mathbb{F}}_i \in \mathbb{R}^{d\times d}$ is the non-homogeneous axis matrix, without the additional "homogeneous" dimension. For convenience, we drop the generator index i for the rest of this proof. The

first summand in the preceding equation can be understood as a scalar product,

$$\mathbf{x} \cdot \widetilde{\mathbb{F}} \cdot \mathbf{y} = \sum_{k=1}^{d} w_k x_k y_k =: p\big(\mathbf{x}, \mathbf{y}\big), \tag{4.30}$$

because it is bilinear, symmetric and positive definite, since for all k : $w_k > 0$. Therefore, $\sqrt{p(\mathbf{x}, \mathbf{x})}$ is a norm, and we can identify $q = 1, \nu = 2, \mathcal{P}_0 = -1$. □

Remark: When employing Voronoi generators of the form (4.25), one can no longer express all norms that would have been possible according to definition 4.1.8. Instead, the attainable norms inherit the axis matrix $\widetilde{\mathbb{F}}_i$, which has to be positive definite for the norm property to hold. The resulting norms comprise quadratic forms in the components of the vector $\mathbf{x}$. In that sense, the previously given definition 4.1.8 of Voronoi generators is therefore more flexible. However, for the intended modeling aim of expressing the preferred shape function of biological cells as ellipses, the expression from equation (4.25) is sufficient.

In the following sections, we restrict our analysis to systems of two spatial dimensions. This approach does not only simplify the underlying equations, but it is also justifiable on biological grounds: all tissues ultimately arise from quasi two-dimensional epithelial structures during embryogenesis [77, 160], which partially carry over to the adult, e.g. in intestine and skin.

4.4. Circular Voronoi diagrams emerge from isotropic axis matrices

1. Isotropic axis weights: Let $\big\{\mathcal{P}_i : i = 1, \ldots, N\big\}$ be a set of N Voronoi generators, so that the resulting point powers $\big\{\mathcal{P}_i(\mathbf{x})\big\}$ are of the form (4.25). Furthermore, assume that the underlying axis weights $w_1^i, \ldots w_d^i$ in the axis matrices $\mathbb{F}_i$ from equation (4.24) coincide,

$$w_1^i = \ldots = w_d^i \equiv 1/r_i^2 \qquad \forall i = 1, \ldots, N, \tag{4.31}$$

where the r_i are positive real numbers. With the help of the additional assumption $(\mathbf{x}_i + \mathbf{x}_j)/2 = 0$ we have previously shown [31], that the

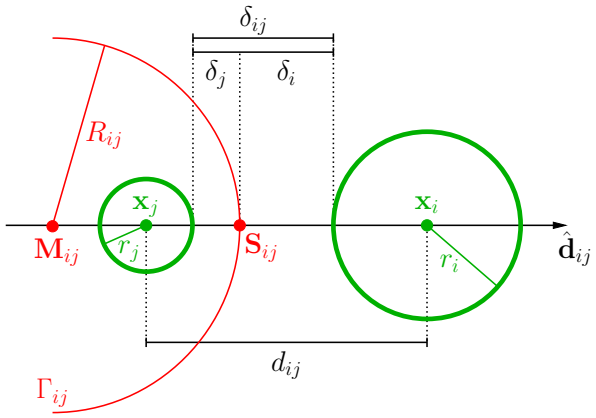

Figure 4.2.: Circular contact surface Γ_{ij} (red) with radius R_{ij} and centered at $\mathbf{M}_{ij}$ according to equation (4.33). Positions $\mathbf{x}_i, \mathbf{x}_j$ and weights r_i, r_j are indicated in green. The rest of the geometric items presented here will be explained in section 5.3.

generalized contact equation (4.13) can be rewritten to

$$\big(\mathbf{x} - \mathbf{M}_{ij}\big)^2 = R_{ij}^2, \quad \text{with} \tag{4.32}$$

$$\mathbf{M}_{ij} = -\frac{r_i^2 + r_j^2}{r_i^2 - r_j^2} \cdot \frac{\mathbf{x}_i - \mathbf{x}_j}{2}, \qquad R_{ij} = \frac{r_i r_j}{|r_i^2 - r_j^2|} |\mathbf{x}_i - \mathbf{x}_j|. \tag{4.33}$$

for $r_i \neq r_j$. Clearly, the preceding contact equation represents a sphere of radius R_{ij} centered at $\mathbf{M}_{ij}$, see figure 4.2.

Definition 4.4.1 (Circular Voronoi tessellation/diagram): A Voronoi tessellation constructed from the scaled norms (4.25) with isotropic weights such that $w_k^i \equiv 1/r_i^2$ holds $\forall k = 1, \ldots, d$ is called circular.

Remark: This method of constructing circular Voronoi tessellations in two dimensions is discussed as "quotient method" in [31, section 2.2]. Figure 4.1 displays an example of such a circular Voronoi diagram with 23 cells in the right panel.

Under the assumption of isotropic axis weights from equation (4.31), we can conveniently represent the information contained in a generator $\mathcal{P}_i$ by the mathematical ball $\mathcal{B}_{r_i}(\mathbf{x}_i)$, see the green circles in 4.2. In practice, this ball centered at $\mathbf{x}_i$ and with radius r_i could be fitted to the cell body

or nucleus. In terms of the point power $\mathcal{P}_i(\mathbf{x})$, we thus can express the cell body or nucleus by the set identity,

$$\mathcal{B}_{r_i}(\mathbf{x}_i) = \big\{\mathbf{x} \in \mathbb{R}^2 : \mathcal{P}_i(\mathbf{x}) \leq 0\big\}, \tag{4.34}$$

which provides for a clear-cut relation between formal description and the actual biological system. Importantly, the Voronoi generator balls $\mathcal{B}_{r_i}(\mathbf{x}_i)$ are readily accessible to experimental determination via image processing, see also section 5.2.

2. Planar cell-cell contacts: A notable special case in circular Voronoi diagrams is the occurrence of a planar contact boundary. This happens when the isotropic axis weights of two adjacent generators are equal, $r_i = r_j$. In this case, the two equations in (4.33) clearly degenerate and become undefined. However, under these circumstances, the contact equation $\mathcal{P}_i(\mathbf{x}) = \mathcal{P}_j(\mathbf{x})$ is still defined and yields

$$\Big(\mathbf{x} - \frac{\mathbf{x}_i + \mathbf{x}_j}{2}\Big) \cdot \big(\mathbf{x}_i - \mathbf{x}_j\big) = 0. \tag{4.35}$$

This represents a $(d-1)$-dimensional hyper-plane embedded in the d-dimensional space, which forms the perpendicular bisector of the straight line connecting the two centers $\mathbf{x}_i$ and $\mathbf{x}_j$. In this way, conventional Voronoi diagrams [105, 223] are contained in the generalized framework presented here.

In chapter 5, we show how to make use of spherical Voronoi tessellations in order to simulate the spatio-temporal dynamics of two-dimensional cell aggregates or proto-tissues. Before coming to numerics, however, we first explore how to construct Voronoi diagrams from general anisotropic generators of the form (4.25). Such diagrams are of novel type and have – to my knowledge – so far not been described elsewhere. There seems to be only one comparable approach [72–74], which employs another notion of point power, see also paragraph 4.9.4 for details.

4.5. The contact matrix can be diagonalized

Definition 4.5.1 (Contact matrix): Let $\mathcal{P}_i(\mathbf{x}) = \mathbf{x}_{\text{hom}}^T \cdot \mathbb{E}_i \cdot \mathbf{x}_{\text{hom}}$ and $\mathcal{P}_j(\mathbf{x}) = \mathbf{x}_{\text{hom}}^T \cdot \mathbb{E}_j \cdot \mathbf{x}_{\text{hom}}$ be two anisotropic Voronoi generators according to definitions 4.3.1 and 4.3.2. The matrix

$$\mathbb{E} := \mathbb{E}_i - \mathbb{E}_j \tag{4.36}$$

is called contact matrix of the two generators $\mathcal{P}_i, \mathcal{P}_j$.

Proposition 4.5.2 (Matrix contact equation): The contact equation (4.7) can be represented in matrix form

$$\mathbf{x}_{\text{hom}}^T \cdot \mathbb{E} \cdot \mathbf{x}_{\text{hom}} = 0, \tag{4.37}$$

with the contact matrix $\mathbb{E} \equiv \mathbb{E}_i - \mathbb{E}_j$.

Proof: The anisotropic generators $\mathcal{P}_i$ and $\mathcal{P}_j$ have the matrix representation (4.25), which we insert into the contact equation (4.7), namely $\mathcal{P}_i\big(\mathbf{x}\big) = \mathcal{P}_j\big(\mathbf{x}\big)$. We obtain the result by subtracting the right-hand side and factoring out $\mathbf{x}_{\text{hom}}^T$ and $\mathbf{x}_{\text{hom}}$.

Since the shape of the contact between two cells is determined by equation (4.37), it is worthwhile to study its properties in detail.

Corollary 4.5.3: The contact matrix $\mathbb{E}$ is symmetric.

Proof: By definition 4.3.1, $\mathbb{E}_i = \mathbb{T}^T(-\mathbf{x}_i)\mathbb{D}^T(-\varphi_i)\,\mathbb{F}_i\,\mathbb{D}(-\varphi_i)\mathbb{T}(-\mathbf{x}_i)$. In two dimensions, the translation matrix $\mathbb{T}(-\mathbf{x}_i)$ as defined in equation (4.20) contains the explicit vector components $(x_i, y_i) = \mathbf{x}_i$ of the cell center $\mathbf{x}_i$. Moreover, the homogeneous axis and rotation matrices are

$$\mathbb{F}_i := \begin{pmatrix} a_i^{-2} & 0 & 0 \\ 0 & b_i^{-2} & 0 \\ 0 & 0 & -1 \end{pmatrix}, \qquad \mathbb{D}\big(\varphi_i\big) := \begin{pmatrix} c_i & -s_i & 0 \\ s_i & c_i & 0 \\ 0 & 0 & 1 \end{pmatrix}, \tag{4.38}$$

respectively, with $c_i := \cos\varphi_i$ and $s_i := \sin\varphi_i$. Computing the product of the five matrices we obtain

$$\mathbb{E}_i = \begin{pmatrix} \alpha_i & \gamma_i & \kappa_i \\ \gamma_i & \beta_i & \lambda_i \\ \kappa_i & \lambda_i & \omega_i \end{pmatrix}, \quad \text{with} \quad \begin{aligned} \alpha_i &:= c_i^2 a_i^{-2} + s_i^2 b_i^{-2}, \\ \beta_i &:= s_i^2 a_i^{-2} + c_i^2 b_i^{-2}, \\ \gamma_i &:= c_i s_i \big(a_i^{-2} - b_i^{-2}\big), \\ \kappa_i &:= -\alpha_i x_i - \gamma_i y_i, \\ \lambda_i &:= -\gamma_i x_i - \beta_i y_i, \\ \omega_i &:= \alpha_i x_i^2 + 2\gamma_i x_i y_i + \beta_i y_i^2 - 1, \end{aligned} \tag{4.39}$$

Since the anisotropic generator matrix $\mathbb{E}_i$ is symmetric, also the contact matrix $\mathbb{E} = \mathbb{E}_i - \mathbb{E}_j$ is symmetric. □

Similar as for $\mathbb{E}_i$, we introduce the following short-hand notations for

the contact matrix,

$$\mathbb{E} = \mathbb{E}_i - \mathbb{E}_j := \begin{pmatrix} \alpha & \gamma & \kappa \\ \gamma & \beta & \lambda \\ \kappa & \lambda & \omega \end{pmatrix}, \quad \text{with} \quad \begin{aligned} \alpha &:= \alpha_i - \alpha_j, \\ \beta &:= \beta_i - \beta_j, \\ \gamma &:= \gamma_i - \gamma_j, \\ \kappa &:= \kappa_i - \kappa_j, \\ \lambda &:= \lambda_i - \lambda_j, \\ \omega &:= \omega_i - \omega_j. \end{aligned} \tag{4.40}$$

Clearly, the expression $\mathbf{x}_{\text{hom}} \cdot \mathbb{E} \cdot \mathbf{x}_{\text{hom}}$ from the contact equation is a quadratic form in the components x, y of $\mathbf{x}$. In general, such quadratic forms describe a conic section (or briefly, conic). In order to assess whether its graph is an ellipse, hyperbola, or other curve, one needs to find the eigenvalues of $\mathbb{E}$. One possibility to find them is diagonalizing the contact matrix $\mathbb{E}$. As an additional benefit, we may get some idea as to where the conic is located and how it is oriented in the two-dimensional plane.

Here we make an ansatz much alike the construction principle for $\mathbb{E}_i$ from definition 4.3.1. Consider the transformed contact matrix

$$\mathbb{E}' = \mathbb{D}^T\big(\phi\big)\mathbb{T}^T\big(\mathbf{x}_0\big)\,\mathbb{E}\,\mathbb{T}\big(\mathbf{x}_0\big)\mathbb{D}\big(\phi\big) =: \begin{pmatrix} \alpha' & \gamma' & \kappa' \\ \widetilde{\gamma}' & \beta' & \lambda' \\ \widetilde{\kappa}' & \widetilde{\lambda}' & \omega' \end{pmatrix}. \tag{4.41}$$

The specific coordinate system in which $\mathbb{E}'$ becomes diagonal has the origin at $\mathbf{x}_0 := \big(x_0, y_0\big)$. With the abbreviations $c \equiv \cos\phi, s \equiv \sin\phi$ we obtain

$$\begin{aligned} \alpha' &= \alpha c^2 + 2\gamma cs + \beta s^2, \\ \beta' &= \alpha s^2 - 2\gamma cs + \beta c^2, \\ \widetilde{\gamma}' = \gamma' &= -\big(\alpha - \beta\big)cs + \gamma\big(c^2 - s^2\big), \\ \widetilde{\kappa}' = \kappa' &= \quad c\big(\alpha x_0 + \gamma y_0 + \kappa\big) + \quad s\big(\gamma x_0 + \beta y_0 + \lambda\big), \\ \widetilde{\lambda}' = \lambda' &= -s\big(\alpha x_0 + \gamma y_0 + \kappa\big) + \quad c\big(\gamma x_0 + \beta y_0 + \lambda\big), \\ \omega' &= x_0\big(\alpha x_0 + \gamma y_0 + \kappa\big) + y_0\big(\gamma x_0 + \beta y_0 + \lambda\big) + \kappa x_0 + \lambda y_0 + \omega. \end{aligned} \tag{4.42}$$

This shows that $\mathbb{E}'$ is indeed symmetric. In order to diagonalize $\mathbb{E}'$, we have to find ϕ, x_0, y_0 such that $\gamma' = \kappa' = \lambda' = 0$. Once we know such ϕ, x_0, y_0, we have also found the actual center $\mathbf{x}_0$ and orientation ϕ of the contact border.

For the translation parts of $\mathbb{E}'$ to vanish, we set

$$\left.\begin{aligned}\kappa' &= 0\\ \lambda' &= 0\end{aligned}\right\} \Leftrightarrow \begin{cases}\alpha x_0 + \gamma y_0 = -\kappa\\ \gamma x_0 + \beta y_0 = -\lambda\end{cases} \tag{4.43}$$

Solvability of this linear system depends on the determinant of the two-dimensional part of the contact matrix,

$$\delta := \begin{vmatrix}\alpha & \gamma\\ \gamma & \beta\end{vmatrix} = \alpha\beta - \gamma^2. \tag{4.44}$$

With this short-hand notation, we solve the system (4.43) and thus we have proven the following

Proposition 4.5.4: The translation parts κ', λ' of the transformed contact matrix (4.42) vanish, iff[6]

$$\delta \neq 0 \quad \wedge \quad \mathbf{x}_0 = \frac{1}{\delta}\begin{pmatrix}\gamma\lambda - \beta\kappa\\ \gamma\kappa - \alpha\lambda\end{pmatrix}. \tag{4.45}$$

Remark: Using of (4.43) and (4.45), the last equation in (4.42) can be simplified to

$$\omega' = \omega + \kappa x_0 + \lambda y_0 = \omega - \frac{1}{\delta}\big(\alpha\lambda^2 - 2\gamma\lambda\kappa + \beta\kappa^2\big) \quad \text{iff } \delta \neq 0. \tag{4.46}$$

In order to complete the diagonalization of $\mathbb{E}'$, we investigate the implications of setting $\gamma' = 0$, however this requires several auxiliary constructs and additional notions. From the trigonometric relations $c = \big(e^{i\phi} + e^{-i\phi}\big)/2$ and $s = -i\big(e^{i\phi} - e^{-i\phi}\big)/2$ follows

$$cs = -\frac{i}{4}\big(e^{2i\phi} - e^{-2i\phi}\big), \qquad c^2 - s^2 = \frac{1}{2}\big(e^{2i\phi} + e^{-2i\phi}\big). \tag{4.47}$$

With these two identities we cast the γ'-equation from (4.42) into the form

$$4\gamma' = e^{2i\phi}\big[2\gamma + i(\alpha - \beta)\big] + e^{-2i\phi}\big[2\gamma - i(\alpha - \beta)\big]. \tag{4.48}$$

We observe that in the square brackets there appears the complex number $z := 2\gamma + i(\alpha - \beta)$ and its conjugate $z^* = 2\gamma - i(\alpha - \beta)$. Equivalently, one may use the polar representation of z,

$$\begin{aligned} z = re^{i\psi}, \qquad z^* = re^{-i\psi}, \quad &\text{with}\\ r^2 := 4\gamma^2 + (\alpha-\beta)^2, \qquad \sin\psi := \frac{\alpha-\beta}{r}, \quad &\cos\psi := \frac{2\gamma}{r}, \end{aligned} \tag{4.49}$$

[6] if and only if

where we employ the usual convention $r \geq 0$. Thus, for $r \neq 0$ the expression $4\gamma' = 0$ reads $e^{4i\phi} + e^{2i\psi} = 0$. In this way, we find with the help of $-1 = e^{i(2n+1)\pi}, n \in \mathbb{Z}$ the orientation

$$\phi = \frac{(2n+1)\pi}{4} - \frac{\psi}{2}, \qquad (\text{for } r \neq 0) \tag{4.50}$$

of the contact border in the plane. Without loss of generality it is sufficient to consider $n = -2, -1, 0, 1$. Moreover, in the equations (4.42) for α', β', γ', there appear only two-factor products of trigonometric functions $c = \cos\phi, s = \sin\phi$, namely c^2, s^2, cs. In order to express these products in terms of $(\alpha - \beta), \gamma, r$, we compute c and s from equation (4.50). They are both of the form

$$c, s = \pm\frac{\sqrt{2}}{2}\Big(\cos\frac{\psi}{2} \pm \sin\frac{\psi}{2}\Big), \tag{4.51}$$

where the actual signs depend on n. In this way, the products c^2, s^2, cs do only depend on $\sin\psi$ and $\cos\psi$. With the relations (4.49), we obtain

$$c^2 = \frac{1}{2}\Big(1 + [-1]^n\frac{\alpha-\beta}{r}\Big), \;\; s^2 = \frac{1}{2}\Big(1 - [-1]^n\frac{\alpha-\beta}{r}\Big), \;\; cs = \frac{1}{2}[-1]^n\frac{2\gamma}{r}, \tag{4.52}$$

Inserting these expressions into the first three equations of (4.42) yields

$$\begin{aligned} \alpha' &= \frac{1}{2}\big(\alpha + \beta + [-1]^n r\big), \\ \beta' &= \frac{1}{2}\big(\alpha + \beta - [-1]^n r\big), \qquad \text{with } n = -2, -1, 0, 1, \text{ and } r \neq 0, \end{aligned} \tag{4.53}$$

whereby γ' vanishes as expected. This completes the proof of:

Proposition 4.5.5: The two-dimensional rotation part γ' of the transformed contact matrix (4.42) vanishes, iff $r \neq 0 \wedge \phi = (2n+1)\pi/4 - \psi/2$.

Altogether, the transformed contact matrix is diagonal, namely $\mathbb{E}' = \mathrm{diag}\big(\alpha', \beta', \omega'\big)$, and all the other entries vanish. Based on this simple representation, we may explore special cases such as $\delta = 0$ or $r = 0$. Before that, however, we investigate under which conditions generator and contact matrices can be determined uniquely.

4.6. Generator and diagonalized contact matrices are unique

In the preceding sections we constructed Voronoi generators $\mathcal{P}_i(\mathbf{x}) = \mathbf{x}_{\text{hom}}^T \cdot \mathbb{E}_i \cdot \mathbf{x}_{\text{hom}}$ representing scaled norms. The identity $\mathcal{P}_i(\mathbf{x}) = 0$ describes the graph of an ellipse situated in the two-dimensional plane. Our initial premise was to construct Voronoi diagrams from certain properties of biological tissue cells. As a first approximation beyond the isotropic sphere, the shape of cell bodies (containing nucleus, organelles, etc.) can be represented by ellipses [231]. Now we ask for the corresponding generator matrix $\mathbb{E}_i$, given a cell body of idealized ellipsoid shape. Clearly, the center position of the cell body uniquely determines the position parameter $\mathbf{x}_i$ of $\mathbb{E}_i$. In contrast, there is some redundancy in the choice of the corresponding $\{a_i, b_i, \varphi_i\}$: First, a_i could be either major or minor half-axis of the ellipse. Next, for a fixed ratio of major and minor half-axes, four distinct angles $\varphi_i = \tilde{\varphi}_i + n\pi/2, n \in \mathbb{Z}$ align with the symmetry axes of the ellipse. Specifically, there are four parameter constellations of winding number zero[7] which all describe the same graph:

$$a_i > b_i \wedge \varphi_i = \pm\widetilde{\varphi}_i \qquad \text{and} \qquad a_i < b_i \wedge \varphi_i = \pm\widetilde{\varphi}_i^{\perp}. \tag{4.54}$$

Here, $\pm\widetilde{\varphi}_i^{\perp}$ indicate those two directions perpendicular to $\pm\widetilde{\varphi}_i \in [-\pi, \pi)$, which are also situated in the interval $[-\pi, \pi)$. In order to make the choice of $\{a_i, b_i, \varphi_i\}$ unique, we align φ_i with the major axis of the ellipse and impose the following two conditions:

$$a_i \geq b_i \quad \wedge \quad \varphi_i \in \Big[-\frac{\pi}{2}, \frac{\pi}{2}\Big). \tag{4.55}$$

In a similar manner, we can make the parameters $\{\alpha', \beta', \phi\}$ of the contact matrix $\mathbb{E}_i$ unique, if we require

$$\alpha' \leq \beta' \quad \wedge \quad \phi \in \Big[-\frac{\pi}{2}, \frac{\pi}{2}\Big), \tag{4.56}$$

cf. $\mathbb{F}_i$ in equation (4.38) and $\mathbb{E}'$ in equation (4.59). Specifically, if $r = 0$ then we have $\alpha' = \beta'$ from equation (4.49) and the graph of $\mathbf{x}_h \cdot \mathbb{E} \cdot \mathbf{x}_h = 0$ is circular. In this way, ϕ does not affect the shape of the contact graph.

With the help of the uniqueness criterion (4.56), we can slightly simplify the expressions (4.53). Enforcing $\alpha' \leq \beta'$ leads us to n being odd, so that

[7] Being of winding number zero means that the angle φ_i is situated within the interval $[-\pi, \pi)$.

way we obtain

$$\alpha' = \frac{1}{2}\Big(\alpha + \beta - r\Big), \qquad \beta' = \frac{1}{2}\Big(\alpha + \beta + r\Big). \tag{4.57}$$

Requiring the angle $\phi \in \big[-\pi/2, \pi/2\big)$ and considering only odd n leaves only one consistent choice for the signs of c, s from the identities in (4.52),

$$c = \frac{\sqrt{2}}{2}\sqrt{1 - \frac{\alpha - \beta}{r}}, \qquad \begin{cases} s = \dfrac{\sqrt{2}}{2}\sqrt{1 + \dfrac{\alpha - \beta}{r}}, & \text{for } \gamma \leq 0, \\ s = -\dfrac{\sqrt{2}}{2}\sqrt{1 + \dfrac{\alpha - \beta}{r}}, & \text{for } \gamma > 0, \end{cases} \tag{4.58}$$

where $r > 0$ has again been employed. We have thus proven the main result:

Theorem 4.6.1: Let $\mathbb{E}$ be a contact matrix of the form (4.40), with $\delta = \alpha\beta - \gamma^2 \neq 0$ and $r^2 = 4\gamma^2 + (\alpha - \beta)^2 > 0$. Then the transformed contact matrix $\mathbb{E}'$ in equation (4.41) is unique and diagonal,

$$\mathbb{E}' = \begin{pmatrix} \alpha' & 0 & 0 \\ 0 & \beta' & 0 \\ 0 & 0 & \omega' \end{pmatrix}, \quad \text{with} \quad \begin{aligned} \alpha' &= \frac{1}{2}\big(\alpha + \beta - r\big), \\ \beta' &= \frac{1}{2}\big(\alpha + \beta + r\big), \\ \omega' &= \omega - \frac{\alpha\lambda^2 - 2\gamma\lambda\kappa + \beta\kappa^2}{\delta}. \end{aligned} \tag{4.59}$$

Now we are in the position to study the properties of contact borders and the precise conditions under which a specific shape occurs. In the non-degenerate cases we have $\delta \neq 0 \wedge r > 0$, so that with $\operatorname{sgn}\alpha' = \operatorname{sgn}\beta' = -\operatorname{sgn}\omega'$, the contact border is an ellipse[8], whereas with $\operatorname{sgn}\alpha' \neq \operatorname{sgn}\beta'$ a hyperbola. Apart from these two simple cases, there are several degenerate contact surfaces which we treat in the following section.

4.7. There are several types of degenerate contact border surfaces

In the preceding sections we have found elliptic and hyperbolic contact borders by diagonalizing the contact matrix. There are several cases in which a complete diagonalization of the contact matrix is not possible:

[8] It remains elusive whether $\operatorname{sgn}\alpha' = \operatorname{sgn}\beta' = \operatorname{sgn}\omega'$ is actually possible.

1. $r^2 = 0 \;\Leftrightarrow\; \alpha = \beta \,\wedge\, \gamma = 0$, i.e. ψ and ϕ undefined, cf. (4.50)
2. $\delta = \alpha\beta - \gamma^2 = 0$, i.e. $\mathbf{x}_0 = \big(x_0, y_0\big)$ undefined, cf. (4.45)
   a) $\alpha = \beta = \gamma = 0$ (implies also case 1),
   b) $\alpha \neq 0 \,\wedge\, \beta = \gamma = 0$,
   c) $\beta \neq 0 \,\wedge\, \alpha = \gamma = 0$,
   d) $\gamma \neq 0 \,\wedge\, \alpha\beta = \gamma^2$.

Let us investigate what kind of contact border arises in these special cases.

1. Undefined contact orientation ϕ, circular contact: We have $r = 0$, i.e. $\alpha = \beta \,\wedge \gamma = 0$. First, assume $\alpha \neq 0$, so that also $\beta \neq 0$, otherwise refer to case 2a. Under these assumptions, $\delta = \alpha\beta - \gamma^2 = \alpha^2 > 0$. Next, we partially transform the contact matrix $\mathbb{E}$ according to equation (4.41), however without including the rotation $\mathbb{D}$. This is equivalent to formally setting $\phi = 0$, which yields the degenerate transformed contact matrix

$$\mathbb{E}' = \mathbb{T}^T\big(\mathbf{x}_0\big)\,\mathbb{E}\,\mathbb{T}\big(\mathbf{x}_0\big) = \begin{pmatrix} \alpha & 0 & 0 \\ 0 & \alpha & 0 \\ 0 & 0 & \omega' \end{pmatrix}. \tag{4.60}$$

Thereby, $\mathbb{E}'$ is written in coordinates centered at $\mathbf{x}_0$. Equations (4.45) and (4.46) remain valid, so that inserting $\delta = \alpha^2$ gives us the identities

$$\mathbf{x}_0 = -\frac{1}{\alpha}\begin{pmatrix} \kappa \\ \lambda \end{pmatrix}, \qquad\qquad \omega' = \omega - \frac{\kappa^2 + \lambda^2}{\alpha}. \tag{4.61}$$

Then, the quadratic form of the contact border reads

$$\big(\mathbf{x} - \mathbf{x}_0\big)^2 = \frac{\kappa^2 + \lambda^2}{\alpha^2} - \frac{\omega}{\alpha}. \tag{4.62}$$

The preceding equation represents – up to matters of sign on the right hand side – a sphere. Therefore, it remains to be shown that the right-hand side is ≥ 0. To this end, we investigate the premises $\alpha = \beta \,\wedge\, \gamma = 0$, together with the generator uniqueness criteria $a_i \geq b_i \geq 0$ and $\varphi_{i/j} \in \big[-\pi/2; \pi/2\big)$ (cf. section 4.6). We observe that there are two sub-cases,

1. $\varphi_i = \varphi_j \quad \rightsquigarrow \quad a_i^{-2} - b_i^{-2} = a_j^{-2} - b_j^{-2}$,
2. $\varphi_i \neq \varphi_j \quad \rightsquigarrow \quad a_i^{-2} = b_i^{-2} \,\wedge\, a_j^{-2} = b_j^{-2}$,

which also cover the situation with 'special' angles $\varphi_{i/j} = n\pi/4, n \in \mathbb{Z}$, whence $c_{i/j}^2 = s_{i/j}^2$.

In the first sub-case $\varphi_i = \varphi_j$, a longer but straight-forward calculation yields

$$\begin{aligned} \kappa^2 + \lambda^2 - \alpha\omega = \quad & \frac{1}{a_i^2 a_j^2}\Big(\quad c_i\big(x_i - x_j\big) + s_i\big(y_i - y_j\big)\Big)^2 \\ & + \frac{1}{b_i^2 b_j^2}\Big(-s_i\big(x_i - x_j\big) + c_i\big(y_i - y_j\big)\Big)^2 \geq 0, \end{aligned} \tag{4.63}$$

with the abbreviations $c_i \equiv \cos\varphi_i, s_i \equiv \sin\varphi_i$. In deriving this relation, we can use $\gamma_i = \gamma_j$ to symmetrize the γ-terms by setting $\gamma_i = \big(\gamma_i + \gamma_j\big)/2$, because $\gamma = 0$. Moreover, $\alpha^2 > 0$ by assumption, so that the right-hand side of equation (4.62) is indeed ≥ 0. In particular, equality holds iff $x_i = x_j \wedge y_i = y_j$, which we can exclude by requiring the generator centers to be not coinciding. Altogether, equation (4.62) represents a sphere under the premises $\alpha = \beta \neq 0 \ \wedge \ \gamma = 0 \ \wedge \ \varphi_i = \varphi_j \ \wedge \ \mathbf{x}_i \neq \mathbf{x}_j$.

In the second sub-case $\varphi_i \neq \varphi_j$, both generators represent spheres, $a_i = b_i =: r_i, a_j = b_j =: r_j$. Then the contact equation (4.62) again takes the form of a sphere,

$$\mathbf{x}_0 = \frac{r_j^2\mathbf{x}_i - r_i^2\mathbf{x}_j}{r_j^2 - r_i^2}, \qquad \frac{\kappa^2 + \lambda^2}{\alpha^2} - \frac{\omega}{\alpha} = \frac{r_i^2 r_j^2 (\mathbf{x}_i - \mathbf{x}_j)^2}{(r_i^2 - r_j^2)^2}. \tag{4.64}$$

The relation to equation (4.33) is as follows: First, we write the contact equation (4.62) in right-handed Cartesian coordinates centered at $\big(\mathbf{x}_i + \mathbf{x}_j\big)/2$, with the positive x-axis pointing towards $\mathbf{x}_j$. We observe that the form of $\mathbf{x}_0$ does not change under this transformation. Moreover, the y-component of both generator centers vanishes in these coordinates. Clearly, the x-component of both transformed $\mathbf{x}_i, \mathbf{x}_j$ are – up to the sign – equal to half the center distance $\big|\mathbf{x}_i - \mathbf{x}_j\big|/2$. In this way, centers $\mathbf{x}_i, \mathbf{x}_j$ and weights r_i, r_j can be disentangled and we see that the transformed $\mathbf{x}_0$ is identical to $\mathbf{M}_{ij}$ from equation (4.33).

2. Undefined contact center x_0, parabolic or flat contact border: We have $\delta = \alpha\beta - \gamma^2 = 0$. This happens, when the semi-axes of the two involved generator ellipses a_i, b_i, a_j, b_j obey certain ordering inequalities, see appendix A.3.1. Here we are interested in the specific form of the emerging contact equation $\mathbf{x}_{\mathrm{hom}}^T \cdot \mathbb{E} \cdot \mathbf{x}_{\mathrm{hom}} = 0$, which can be seen most directly when considering the aforementioned sub-cases:

2a, $\alpha = \beta = \gamma = 0$: The six individual identities $\alpha = \beta = \gamma = 0$ can be condensed into three,

$$\begin{aligned} \frac{1}{a_i^2} + \frac{1}{b_i^2} &= \frac{1}{a_j^2} + \frac{1}{b_j^2}, \\ \cos\bigl(2\varphi_i\bigr)\Bigl(\frac{1}{a_i^2} - \frac{1}{b_i^2}\Bigr) &= \cos\bigl(2\varphi_j\bigr)\Bigl(\frac{1}{a_j^2} - \frac{1}{b_j^2}\Bigr), \\ \sin\bigl(2\varphi_i\bigr)\Bigl(\frac{1}{a_i^2} - \frac{1}{b_i^2}\Bigr) &= \sin\bigl(2\varphi_j\bigr)\Bigl(\frac{1}{a_j^2} - \frac{1}{b_j^2}\Bigr). \end{aligned} \tag{4.65}$$

Squaring the last two equations and adding them yields $a_i^{-2} - b_i^{-2} = a_j^{-2} - b_j^{-2}$. Addition and subtraction to/from the first equation leads to $a_i = a_j \wedge b_i = b_j$, and we have

$$\text{ellipse-like generators:} \quad a_i = a_j, \quad b_i = b_j, \quad \varphi_i = \varphi_j, \tag{4.66}$$

meaning size and orientation of the generators are equal. If the generators are circles, the sin- and cos-equations of (4.65) hold for any φ_i, φ_j, because they vanish,

$$\text{circular generators:} \qquad a_i = b_i = a_j = b_j. \tag{4.67}$$

Recall the homogeneous coordinate vectors $\mathbf{x}_{\text{hom}} = (x, y, 1)$ as introduced in definition 4.2.1. The untransformed contact equation (4.37) reads

$$\mathbf{x}_{\text{hom}}^T \cdot \mathbb{E} \cdot \mathbf{x}_{\text{hom}} = \mathbf{x}_{\text{hom}}^T \cdot \begin{pmatrix} 0 & 0 & \kappa \\ 0 & 0 & \lambda \\ \kappa & \lambda & \omega \end{pmatrix} \cdot \mathbf{x}_{\text{hom}} = 2\kappa x + 2\lambda y + \omega = 0. \tag{4.68}$$

This clearly represents a straight line. There are two possibilities,

$$\begin{aligned} \lambda \neq 0: &\qquad y = -\frac{\kappa}{\lambda} x - \frac{\omega}{2\lambda}, \\ \lambda = 0, \kappa \neq 0: &\qquad x = -\frac{\omega}{2\kappa}. \end{aligned} \tag{4.69}$$

Both κ and λ cannot vanish at the same time, because this would imply $\mathbf{x}_i = \mathbf{x}_j$, which we again exclude by requiring $|\mathbf{x}_i - \mathbf{x}_j| > 0$, i.e. the centers of two distinct cells may not coincide.

2b, $\alpha \neq 0 \ \wedge \ \beta = \gamma = 0$: In contrast to sub-case 2a above, the three identities $\beta = \gamma = 0$ do not lead to expressions of similar simplicity.

However, we still can use $\beta_i = \beta_j$ and $\gamma_i = \gamma_j$, while $\gamma = \beta$ gives no new information. The untransformed contact equation (4.37) is

$$\mathbf{x}_{\text{hom}}^T \cdot \mathbb{E} \cdot \mathbf{x}_{\text{hom}} = \mathbf{x}_{\text{hom}}^T \cdot \begin{pmatrix} \alpha & 0 & \kappa \\ 0 & 0 & \lambda \\ \kappa & \lambda & \omega \end{pmatrix} \cdot \mathbf{x}_{\text{hom}} = \alpha x^2 + 2\kappa x + 2\lambda y + \omega = 0. \tag{4.70}$$

If λ does not vanish, this identity represents a parabola,

$$\lambda \neq 0: \qquad y = -\frac{\alpha}{2\lambda} x\Big(x + \frac{2\kappa}{\alpha}\Big) - \frac{\omega}{2\lambda}. \tag{4.71}$$

Otherwise, for $\lambda = 0$, we end up with a quadratic equation for x. Solvability in the real numbers $\mathbb{R}$ depends on the discriminant $\kappa^2 - \omega\alpha$, which happens to be one of the two other sub-determinants of the contact matrix $\mathbb{E}$, besides δ. Appendix A.3.2 shows that with $\beta = \gamma = \lambda = 0$, the discriminant $\kappa^2 - \omega\alpha \geq 0$, whereby equality arises when $y_i = y_j$. In this way we may write

$$\lambda = 0: \qquad x = -\frac{\kappa}{\alpha} \pm \frac{1}{\alpha}\sqrt{\kappa^2 - \omega\alpha}, \tag{4.72}$$

representing two straight lines, both parallel to the y-axis. This perhaps puzzling situation can be understood in terms of a degenerate underlying cone, which has its vertex at infinity. The "cone" thus appears as a cylinder. The "conic section" of two parallel lines from above is then obtained by intersecting the cylinder with a plane parallel to the polar symmetry axis.

2c, $\beta \neq 0 \ \wedge \ \alpha = \gamma = 0$: This case is conceptually similar to 2b. The untransformed contact equation (4.37) is

$$\mathbf{x}_{\text{hom}}^T \cdot \mathbb{E} \cdot \mathbf{x}_{\text{hom}} = \mathbf{x}_{\text{hom}}^T \cdot \begin{pmatrix} 0 & 0 & \kappa \\ 0 & \beta & \lambda \\ \kappa & \lambda & \omega \end{pmatrix} \cdot \mathbf{x}_{\text{hom}} = \beta y^2 + 2\lambda y + 2\kappa x + \omega = 0. \tag{4.73}$$

If $\kappa = 0$, the discriminant $\lambda^2 - \omega\beta \geq 0$, see appendix paragraph A.3.2. Thus, we arrive at

$$\kappa \neq 0: \qquad x = -\frac{\beta}{2\kappa} y\Big(y + \frac{2\lambda}{\beta}\Big) - \frac{\omega}{2\kappa}, \tag{4.74}$$

$$\kappa = 0: \qquad y = -\frac{\lambda}{\beta} \pm \frac{1}{\beta}\sqrt{\lambda^2 - \omega\beta}, \tag{4.75}$$

which again represents parabola and straight lines.

2d, $\gamma \neq 0 \ \wedge \alpha\beta = \gamma^2$: The two-dimensional part of the contact matrix can be rotated by the uniquely determined angle ϕ from equation (4.58), which leads to

$$\mathbb{E}' = \begin{pmatrix} \alpha' & 0 & \kappa' \\ 0 & \beta' & \lambda' \\ \kappa' & \lambda' & \omega' \end{pmatrix}, \quad \text{with} \quad \begin{aligned} \alpha' &= \big(\alpha + \beta - r\big)/2, \\ \beta' &= \big(\alpha + \beta + r\big)/2, \\ \kappa' &= \ \ \kappa\cos\phi + \lambda\sin\phi, \\ \lambda' &= -\kappa\sin\phi + \lambda\cos\phi, \\ \omega' &= \omega. \end{aligned} \tag{4.76}$$

Here, the matrix entries follow from equations (4.42), by formally setting $x_0 = y_0 = 0$. Alternatively one can construct $\mathbb{E}'$ without translation, $\mathbb{E}' = \mathbb{D}^T(\phi)\,\mathbb{E}\,\mathbb{D}(\phi)$, which leads to the same result.

By equation (4.49), the helper radius is given by $r^2 = 4\gamma^2 + (\alpha-\beta)^2$. Since we have $\gamma^2 = \alpha\beta$ in this case, we obtain

$$r^2 = \big(\alpha+\beta\big)^2, \quad \text{i.e.} \quad \begin{aligned} \alpha' &= \big(\alpha + \beta - |\alpha+\beta|\big)/2, \\ \beta' &= \big(\alpha + \beta + |\alpha+\beta|\big)/2. \end{aligned} \tag{4.77}$$

Depending on the sign of $\alpha + \beta$, either α' or β' will vanish, while the other will be equal to $\alpha + \beta$. Note that due to $\delta = \alpha\beta - \gamma^2 = 0$, the sign of α and β will coincide. Altogether, for any $\mathbb{E}$ with $\delta = 0$ there exists a unique coordinate system tilted by $-\phi$, so that the transformed $\mathbb{E}'$ attains the representation (4.76) with (4.77). In these coordinates, the contact equation attains the form of either case 2b or 2c, and these previous results can be readily applied. The shape of the contact border is therefore either a parabola or two parallel straight lines, possibly in superposition.

4.8. How to construct Voronoi diagrams from elliptic generators?

In the previous two sections we have discovered various possible shapes for the contact border between two Voronoi cells. All these shapes may arise from the contact equation (4.37). As an overviewing summary we recapitulate all different types of contact shapes together with precise conditions when they do occur, see table 4.1. A specific realization of a Voronoi diagram constructed from elliptic generators is presented in figure 4.3. For the sake of brevity, we shall call such a diagram "elliptic Voronoi

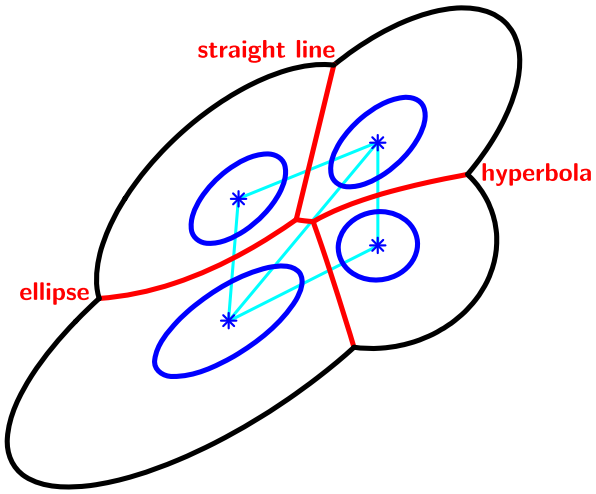

Figure 4.3.: Voronoi diagram of four elliptic generators. The centers of the generators are indicated by stars, and their elliptic contours arising from $\mathcal{P}_i(\mathbf{x}) = \mathbf{x}_{\mathrm{hom}} \cdot \mathbb{E}_i \cdot \mathbf{x}_{\mathrm{hom}} = 0$ are drawn in blue. The emerging Voronoi diagram consists of cell-pair contact borders Γ_{ij} (red) and free margins Γ_{i0} (black). The corresponding Delaunay triangulation is indicated in thin cyan lines connecting the generator centers. The two uppermost cells share common size $a_i = a_j \wedge b_i = b_j$ and orientation $\varphi_i = \varphi_j$, so that the contact matrix degenerates, $\alpha = \beta = \gamma = 0$. Therefore, the corresponding contact border is a straight line. Other common contact shapes are ellipse and hyperbola. Both unlabeled contact borders (bottom and center red line) are also hyperbola segments.

#	δ	r^2	α, β, γ	section	shape
0a	$-$	$+$		4.6	hyperbola
0b	$+$	$+$		4.6	ellipse
1	$+$	0		4.7.1	circle
2a	0	0	$\alpha = \beta = \gamma = 0$	4.7.2a	single straight line
2b	0	$+$	$\beta = \gamma = 0$	4.7.2b	$\lambda \neq 0$ parabola; $\lambda = 0$ two parallel straight lines
2c	0	$+$	$\alpha = \gamma = 0$	4.7.2c	$\kappa \neq 0$ parabola; $\kappa = 0$ two parallel straight lines
2d	0	$+$	$\alpha\beta = \gamma^2$	4.7.2d	cf. 2b or 2c

Table 4.1.: Different types of emerging contact border shapes under various conditions for the contact determinant $\delta = \alpha\beta - \gamma^2$, the helper radius $r^2 = (\alpha - \beta)^2 + 4\gamma^2$, and the coefficients α, β, γ. Note that the non-trivial zero of r^2 in case 1 implies $\delta > 0$, otherwise see 2a. For 2d it has been shown that it either maps to 2b or 2c. Possible contact shapes then are parabola or a pair of parallel straight lines.

diagram" in the rest of this thesis. We now come to the algorithm how to numerically construct such a diagram. After the detailed explanation of each algorithm step 1–7 as given below, the involved key variables like indices and arrays are briefly summarized at the end of each paragraph.[9]

1. Ordering property of the contact border: It is clear that both the circular and the elliptic contact border from table 4.1 can be conveniently parameterized in polar coordinates. The resulting expression $R = R(\theta)$ is explicit, in contrast to the implicit contact equation (4.37). Using the same polar ansatz, also hyperbolas, straight lines and parabolas can be written as $R(\theta)$. All these polar expressions are given in appendix A.5. With the help of this parameterization one can devise the following ordering property for points $\mathbf{x}_1, \mathbf{x}_2 \in \Gamma_{ij}$:

$$\mathbf{x}_1 < \mathbf{x}_2 \quad \Leftrightarrow \quad \theta(\mathbf{x}_1) < \theta(\mathbf{x}_2) \qquad \text{for } \theta \in [-\pi, \pi). \tag{4.78}$$

[9]The following paragraphs explain the accompanying prototype routine `mwvoro.m` for circular generators. The presented algorithm however is general in the sense that it is also capable to construct elliptic Voronoi tessellations. See `http://www.theobio.uni-bonn.de/people/mab/dsup`for the supplementary material including `mwvoro.m`.

As discussed below, this ordering property is essential to identify the correct contact borders.

2. Construction of candidate contact borders: The general equation parameterizing a superset of each contact border Γ_{ij} is given by (4.37). We compute the involved matrix $\mathbb{E} = \mathbb{E}_i - \mathbb{E}_j$ for all the generator pairs (i, j) with $j > i$, where $i, j \in \{1, \ldots, N\}$ are cell indices. The resulting set of matrices is stored in the array `EE`, which is indexed by the pair index m.[10] Additionally, we set up a mapping array `p2c`, which contains the paired cell numbers (i, j) as indexed by the corresponding pair index $m \rightsquigarrow (i, j)$. Conversely, the cell's membership in pair m is recorded in the mapping array `c2p`, indexed by the cell number. In principle, the computational cost of this step is quadratic in the number of generators N, because usually the "exterior" Voronoi cells of a specific diagram are unbounded. However, in definition 4.1.4 we made an additional assumption, which could be exploited to consider fewer generator pairs. Clearly, the maximal extension of a Voronoi cell is bounded by extremal scaled norm $\mathcal{P}(d_{\max}) \equiv \mathcal{P}_{\text{ex}}$, cf. equations (4.9–4.11). For example, the black surrounding lines in figure 4.3 indicate the emerging exterior boundary delimiting the Voronoi cells. Given a set of generalized generators $\{\mathcal{P}_i\}$, one can therefore derive a maximal generator distance, beyond which no contact border is possible. This property can be used to divide the simulation space into boxes, where only generator pairs in the same or in two adjacent boxes need to be considered. This approach is also useful to distribute the computation to multiple processor cores and is sometimes called "linked-cell" algorithm [92, chapter 3].

indices:	cell numbers i, j, candidate cell pair number m
arrays:	mapping pair-to-cell `p2c` and cell-to-pair `c2p`, contact matrices `EE`

3. Construction of candidate vertices: A vertex is the intersection of three contact borders. It arises from a triple consisting of three pairs formed by three generators. In the case when four or more contact borders intersect in one common point, we merely obtain several distinct triples. Contact border intersections between two general conical sections ($\equiv$ conics) can be computed according to [102, 208]. To find vertex

[10] The array `EE` in this description corresponds to the pair-to-sphere array `p2s` in the accompanying prototype implementation `mwvoro.m`.

candidates, we iterate over cell pairs m and $m' > m$. If these two pairs share a common cell, we have identified a triple and acquire the third pair index m'' from the cell-to-pair mapping array `c2p`. In a subroutine we mutually intersect the three candidate contact borders and keep those intersection points that occur three times. A possible safety check for such a potential vertex with position $\mathbf{v}$ is whether the norm function $[\mathcal{P}_i(\mathbf{v})]^{1/2}$ values are – up to numerical fluctuations – identical for all three generators i of the triple. Additionally, we impose that $\mathcal{P}_i(\mathbf{v}) \leq \mathcal{P}_{\mathrm{ex}}$, because otherwise the vertex will be outside of the Voronoi cell. Having identified these triple's vertex candidates, we store their position in the `VV` array, indexed by their respective vertex candidate number n.[11] Subsequently, we associate contact border and potential vertex by means of the mapping array `p2v`, containing all vertex candidate numbers n of the pair as indexed by m. For bookkeeping purposes we also create the pair-to-triple `p2t` and triple-to-cell `t2c` mapping arrays.

index:	vertex candidate number n
arrays:	mapping pair-to-vertex `p2v`, pair-to-triple `p2t`, triple-to-cell `t2c`, vertex candidate positions `VV`

4. Injection of free margin and connection vertices: For each candidate contact border m, we gather all vertices in the vertex candidate array `VCL`.[12] For each vertex we record position $\mathbf{v} \equiv (v_x, v_y)$ and squared norm $\mathcal{P}_i(\mathbf{v})$ with respect to any/all the surrounding generator centers $\{\mathbf{x}_i\}$. All this information can be obtained from `p2v`, `VV` and `EE`. Such a vertex is said to be "ordinary" and of type 1, which is also recorded. In addition to these "ordinary" vertices, we have to consider two kinds of special vertices.

First, we need to account for the limited size of the Voronoi cells under construction. Therefore we include in `VCL` so-called "margin" vertices. They arise from the intersection of the free margin supersets, $\mathcal{P}_i(\mathbf{x}) = \mathcal{P}_{\mathrm{ex}} = \mathcal{P}_j(\mathbf{x})$, cf. definition 4.1.9.[13] Up to four such margin vertices may

[11] The array `VV` in this description corresponds to the vertex-to-vertex array `v2v` in the accompanying prototype implementation `mwvoro.m`.

[12] The equivalent in the prototype implementation is `vcl`, which contains slightly more information. This information is not strictly needed to construct the Voronoi tessellation, and therefore was omitted in the present description of the algorithm.

[13] These margin vertices are termed "wertex" in the accompanying prototype implementation `mwvoro.m`.

arise, which are designated the type 0. As before, squared norm $\mathcal{P}_{\text{ex}}$ and vertex position is also stored in `VCL`.

In order to correctly identify the Voronoi contact borders, we still need another type of special vertices called "connection" vertices.[14] Since the angle parameter $\theta \in [-\pi, \pi)$ is discontinuous at the cut $\theta = \pm\pi$, we have to work around the resulting continuation problem. By inserting a pair of connection vertices at the θ-discontinuity, the unit circle can be connected, see also step 6 below. These connection vertices are of type 2, and are also recorded in `VCL`.

array: vertex candidate array `VCL`

5. Vertex erosion and sorting: This is the central step in the algorithm. Previously, in step 4, we have constructed the vertex candidate array `VCL` for each candidate contact boundary m. To decide whether a vertex is part of the contact border, we have to check that its squared norm $\mathcal{P}_i(\mathbf{v}) = \mathcal{P}_j(\mathbf{v})$ with respect to the pair generators i, j is less than $\mathcal{P}_k(\mathbf{v})$ for all surrounding generators k. The index set $\{k\}$ is stored in the common neighbor candidates vector `cnbc`, which is constructed from `p2t` and `t2c` by finding all generators that participate in a triple with pair m. For each candidate vertex in `VCL`, we iterate over the generators k in `cnbc`. If $\mathcal{P}_i(\mathbf{v}) > \mathcal{P}_k(\mathbf{v})$ for some vertex candidate, then it is ignored. The remaining vertices are then part of the contact border m, and subsequently transfered into the vertex array `vl`. When adding vertices to `vl`, we additionally record their orientation

$$\theta(\mathbf{v}) = \operatorname{atan}(\mathbf{v} - \mathbf{x}_0) \tag{4.79}$$

with respect to the contact border center $\mathbf{x}_0$. Here, atan denotes the arc tangent function with vector argument that uniquely determines $\theta \in [-\pi, \pi)$.

In principle, the number of vertices in `vl` has to be even, because each line segment is delimited precisely by two points. However, when four or more cells share a common vertex, this vertex appears two or more times in `vl`. Therefore, before sorting, only vertices of unique position are retained in `vl`, where an exception is made only for the connection vertices. Then we sort `vl` according to increasing $\theta(\mathbf{v})$. The resulting sorted vertex array `svl` starts with the connection vertex at $\theta = -\pi$ and ends with the connection vertex at $\theta = \pi$, unless they have been removed during erosion.

[14] Connection vertices are termed "uertices" in `mwvoro.m`.

array: sorted vertex array `svl`

6. Connecting vertices to full contact borders: Now we can use the essential contact border ordering property introduced in step 1 above. In general, the contact border Γ_{ij} consists of one or more non-touching contact arcs. If the first vertex in `svl` is a connection vertex, it has to be situated on a contact arc, because it was kept during the erosion step. Otherwise, it has been removed so that the first non-connection vertex initiates an arc. Thus, in any case the first vertex in `svl` will initiate an arc. Correspondingly, we iterate over pairs of consecutive vertices and connect them by contact arc segments in alternating fashion like a check board. When arriving at the last vertex, we take into account the possibility that the first/last vertex in `svl` may be a connection vertex. In this case, we remove the connection vertices so that the two arcs adjacent to $\theta = \pm\pi$ are united. Each of the obtained contact arcs is then stored in the array `AA`, indexed by the arc number p.[15] Specifically, we store the index of the corresponding cell contact border matrix in `EE`, and the θ-parameters for the start and stop vertex. Moreover, we record the involved vertex positions and types. For bookkeeping purposes, we also introduce a cell-to-arc mapping array `c2a`. The candidate pair m fulfills the neighbor relation $i \sim j$ if there exists a corresponding contact border arc. This neighbor property is recorded in the neighbor array `nd`, indexed by cell number i and containing the indices of neighboring cells j.

index: arc number p

arrays: neighbor arc array `AA`, cell-to-arc mapping array `c2a`, neighbor array `nd`

7. Closing free margins of Voronoi cells: The idea to close the free margins of the Voronoi cells towards the surrounding is similar as for step 6. Since each free margin arc is situated on an ellipse given by $\mathcal{P}_i(\mathbf{x}) = \mathcal{P}_{\mathrm{ex}}$, the ordering property described in step 1 applies here as well. For each cell i we first collect all margin vertices from the contact borders involving i, as recorded in `c2a` and `AA`. For each of these vertices we then determine the angular orientation φ with respect to the cell center

[15] The array `AA` is the analogue of `a2a` in the prototype implementation `mwvoro.m`. Minor differences in the data structure of `AA` and `a2a` are owed to the generality of the algorithm described here, which is capable of constructing Voronoi tessellations from elliptical, and not only spherical generators.

$\mathbf{x}_i$. In order to ensure connectivity at $\varphi = \pm\pi$, we inject an additional pair of connecting vertices, which we erode over the already defined neighbors j of i, as recorded in `nd`. After sorting the obtained vertex list according to their angular position φ, we can connect consecutive vertices, so that the resulting arcs form a checked pattern. For each of these arcs we gather the generator index i, and the involved φ-parameters in the free arc array `FF`, indexed by arc number q.[16]

index: margin arc index q

array: margin arc array `FF`

Taking together the steps 1–7 we have shown the second result:

Theorem 4.8.1: The algorithm described above constructs a Voronoi diagram from generalized anisotropic generators.

Remark: The Voronoi tessellation has been introduced in definition 4.1.10, and the generalized anisotropic generator in definition 4.3.2. The corresponding Delaunay triangulation according to definition 4.1.12 follows from the set of constructed Voronoi neighbor relations $\{i \sim j\}$.

Remark: The notion of cell is of utmost importance in biology. Therefore it is indispensable for the intended modelling aim to extract explicit cellular entities from the computed Voronoi diagram. This purpose is achieved by the `c2a` and `nd` data structures, which enable the modeler to directly address a specific cell's boundary and its direct neighbors.

4.9. Comparing generalized Voronoi tessellation methods

Before coming to the comparison of several types of Voronoi diagrams, we recapitulate the critical steps in the construction of the formal theory proposed here. In section 4.1 we have started from Voronoi generators comprising of norms $\|.\|_i$, whereby the zero element of the associated normed (vector) space $\left(\mathbb{R}^d, \|.\|_i\right)$ represents the center $\mathbf{x}_i$ of cell body or nucleus. We then constructed equivalent formulations of the Voronoi cell by scaling the norms $\|.\|_i =: y$ with the scaling function $\mathcal{P}(y) = qy^\nu +$

[16] Again, there are slight differences in the data structure of `FF` with respect to the analogue `f2f` in the prototype implementation `mworo.m`.

$\mathcal{P}_0$, leading to Voronoi generators $\mathcal{P}_i$ in terms of scaled norms, $\mathcal{P}_i(\mathbf{x}) \equiv \mathcal{P}\big(\|\mathbf{x}\|_i\big)$. The scaled norms $\mathcal{P}_i(\mathbf{x})$ represent the power of the point $\mathbf{x}$ with respect to the generator $\mathcal{P}_i$. Comparing point powers of individual generators leads to the equation contact $\mathcal{P}_i(\mathbf{x}) = \mathcal{P}_j(\mathbf{x})$, which forms the basis of constructing the Voronoi diagram, cf. equation (4.13). In order to be able to write this contact equation as a simple product of the form $\mathbf{x}_{\text{hom}}^T \cdot (\mathbb{E}_i - \mathbb{E}_j) \cdot \mathbf{x}_{\text{hom}} = 0$, we then introduced homogeneous coordinates $\mathbf{x}_{\text{hom}}$ in section 4.2. They allowed to understand both translations and rotations in terms of matrix products. In particular, this formulation involved generator norms $\|.\|_i$ in terms of the positive definite axis matrix $\widetilde{\mathbb{F}}_i$, namely $\|.\|_i = (\mathbf{x}^T \cdot \widetilde{\mathbb{F}}_i \cdot \mathbf{x})^{1/2}$. We additionally assumed that the $\widetilde{\mathbb{F}}_i$ are diagonal, with strictly positive matrix elements called axis weights. This means that all norms involved in the proposed Voronoi tessellation method are elliptic, even though the initial formulation from section 4.1 accommodates for arbitrary norms in $\mathbb{R}^d$. In any case, we denote by $\|.\|$ without superscript the Euclidean norm. Note also that in this section we compare only two-dimensional Voronoi diagrams, even though there are generalizations of some of the presented generator formulas to higher spatial dimensions.

1. Polar generator symmetry: From the definition (4.3.2) of anisotropic Voronoi generators $\mathcal{P}_i$, we can derive an equivalent formulation for the point power $\mathcal{P}_i(\mathbf{x})$, see appendix section A.4. The resulting expression

$$\mathcal{P}_i(\mathbf{x}) = \frac{\|\mathbf{x} - \mathbf{x}_i\|}{r_i(\varphi_{\mathbf{x}}^i)}, \tag{4.80}$$

relies on the inherent polar symmetry, where $r_i(\varphi_{\mathbf{x}}^i)$ denotes the polar parameterization of an ellipse, cf. equation (A.31), possibly with non-zero orientational tilt. Importantly, the angle $\varphi_{\mathbf{x}}^i = \text{atan}(\mathbf{x} - \mathbf{x}_i)$ depends on the relative position of the point $\mathbf{x}$ with respect to the generator center $\mathbf{x}_i$. see figure 4.4 (blue). In particular, the point power (4.80) represents the Euclidean norm of $\mathbf{x} - \mathbf{x}_i$, divided by the weighting extension r_i of the generator ellipse in the direction of $\mathbf{x} - \mathbf{x}_i$, again see figure 4.4 (blue). Anisotropic Voronoi generators as described in this thesis have the favorable property that their diagram does not change when scaling all $\mathcal{P}_i$ with a common factor, or – equivalently – adjusting q in the scaling function $\mathcal{P}$ from equation (4.8). We emphasize that the particular representation (4.80) of the point powers $\mathcal{P}_i(\mathbf{x})$ yields an implicit expression for the contact equation $\mathcal{P}_i(\mathbf{x}) = \mathcal{P}_j(\mathbf{x})$ which is not well-suited to further

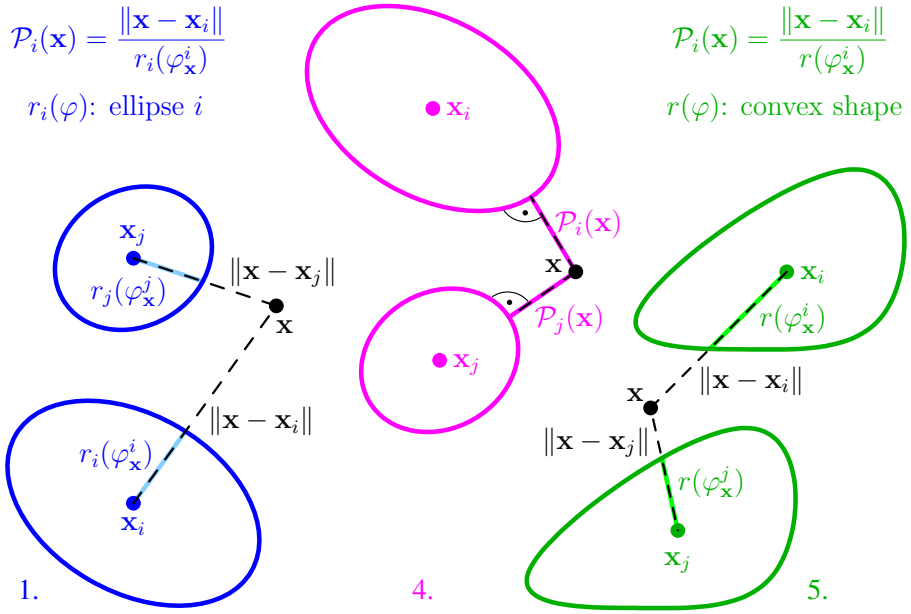

Figure 4.4.: Voronoi generators $\mathcal{P}_i$ attribute to each point $\mathbf{x}$ in the plane a certain power $\mathcal{P}_i(\mathbf{x})$, which is usually some function of the distance of $\mathbf{x}$ from the generator. Here, we compare generators which can be described by convex shape functions $r_i(\varphi)$ in polar coordinates with respect to the generator center $\mathbf{x}_i$. In this thesis, we have developed point powers as in 1 (blue), whereby we prescribe ellipses centered at $\mathbf{x}_i$ and with radius function r_i as Voronoi generators. For finding the power $\mathcal{P}_i(\mathbf{x})$ of the point $\mathbf{x}$, we divide the Euclidean norm $\|\mathbf{x}-\mathbf{x}_i\|$ by the local ellipse radius $r_i(\varphi^i_{\mathbf{x}})$ in the relative direction of the point $\mathbf{x}$. This idea is also used in method 5 (green), however the weighting radius $r(\varphi^j_{\mathbf{x}})$ is the same for all generators, and it may represent a single but arbitrary convex shape [143]. Although based on ellipses as well, method 4 (magenta) developed by Emiris and coworkers [73] is different. There, the point power $\mathcal{P}_i(\mathbf{x})$ is the shortest distance to the surface of the ellipse surface of the Voronoi generator. For further explanations of the methods 1, 4 and 5, see the respective paragraphs 4.9.1, 4.9.4 and 4.9.5 in the text.

analysis. However, equation (4.80) is still useful to compare the Voronoi tessellation described in this work with other approaches.

2. Circular Voronoi diagrams: Setting $r_i = \text{const.}$ in equation (4.80), we obtain the point power

$$\mathcal{P}_i(\mathbf{x}) = \frac{\|\mathbf{x} - \mathbf{x}_i\|}{r_i}. \tag{4.81}$$

as generalized Voronoi generator. Such generators lead to the conventional multiplicatively weighted Voronoi diagram by Aurenhammer and Edelsbrunner [16], which is discussed as "quotient method" in our work [31]. The equivalent representation of the generator (4.81) in terms of homogeneous matrices has already been derived in section 4.4. As can be seen from equation (4.81), such a diagram is based on the Euclidean norm weighted by r_i, with the scaling function $\mathcal{P}$ coefficients from equation (4.8) being $q = 1, \nu = 2, \mathcal{P}_0 = -1$. In the multiplicatively weighted Voronoi diagram the generators can also be represented as circles of radius r_i centered at $\mathbf{x}_i$, and the resulting contact borders are either circles or straight lines. We therefore refer to such a diagram as circular. Specifically, the circular generators (4.81) are special cases of the elliptic ones from the preceding paragraph, with the simplification of $r_i(\varphi^i_{\mathbf{x}}) = r_i$ being constant and independent of $\varphi^i_{\mathbf{x}}$. Aurenhammer and Edelsbrunner have shown that the optimal time to construct a circular Voronoi diagram is $\mathcal{O}(N^2)$, i.e. quadratic in the number of generators N [16]. To achieve this optimality, the authors map the two-dimensional plane on a two-sphere embedded in three dimensions. This is a way to introduce the projective plane and thereby the homogeneous coordinates used in this thesis. However, whether and in which way the cell complex described in [16] can be mapped to the concepts described here is less obvious.

3. Increasing functions of the Euclidean norm: Ash and Bolker have worked on the question whether a given tessellation is Voronoi and, if so, what are the underlying generators [14]. For the point power $\mathcal{P}_i(\mathbf{x})$ they write the expression

$$\mathcal{P}_i(\mathbf{x}) = f\big(\|\mathbf{x} - \mathbf{x}_i\|\big) + w_i. \tag{4.82}$$

The function f is increasing in the Euclidean norm $\|.\|$, and the additive weights w_i may be different for each generator. If $w_i < 0$ and $f = \|\mathbf{x} - \mathbf{x}_i\|$, the resulting contact borders are straight lines and the emerging Voronoi

diagram is often called "power diagram". This special case is discussed as "difference method" in [31], where it turned out that the partition of space between two neighboring cell bodies exhibits a biologically undesirable monotonicity behavior in the w_i. For $w_i > 0$ and $f = \|\mathbf{x}-\mathbf{x}_i\|$, the contact borders are hyperbolic arcs or straight lines. Another possible choice for f involves the distance constructed from a quadratic form with the help of a two-dimensional matrix $\widetilde{\mathbb{F}}$ [15, section 3.1.5], cf. also example 4.1.3. For comparison, the anisotropic generator expression (4.80) sets $w_i := w \equiv$ const. in (4.82), while generalizing the matrix $\widetilde{\mathbb{F}}$ in f to prescribe $\widetilde{\mathbb{F}}_i$ independently for each generator, see section 4.3. Finally, by taking the logarithm of the circular generator function (4.81), one finds that it is also of the form (4.82). Therefore, the anisotropic generators (4.80) proposed in this thesis generalize the expressions (4.81) and certain versions of (4.82). In this way, the expression (4.80) establishes a formal connection between Voronoi diagrams with hyperbolic and circular contact borders, and closes the formalism to allow for all kinds of conic section type contact shapes.

4. Voronoi diagram of ellipses: Another type of Voronoi diagrams has been been developed by Emiris and coworkers [72–74], and is called a "Voronoi diagram of ellipses". The employed point power $\mathcal{P}_i(\mathbf{x})$ constitutes the Euclidean distance of $\mathbf{x}$ from the surface of the ellipse i, see figure 4.4 (magenta). The resulting contact equation $\mathcal{P}_i(\mathbf{x}) = \mathcal{P}_j(\mathbf{x})$ is computationally quite demanding, because it involves the solution of degree-184 polynomial equations [74]. Remarkably, the Voronoi diagram constructed in such a way changes when scaling the generator ellipses with a common factor.

5. Polar weighting functions: Klein and Ma have prescribed $r(\varphi^i_{\mathbf{x}})$ as the same polar weighting function for all generators [17, 143],

$$\mathcal{P}_i(\mathbf{x}) = \frac{\|\mathbf{x}-\mathbf{x}_i\|}{r(\varphi^i_{\mathbf{x}})}, \tag{4.83}$$

see figure 4.4 (green). This technique shares some similarity with the one proposed in this thesis. The main difference is that there is only one single global shape template r for all $\mathcal{P}_i$. The shape of the resulting Voronoi cells then depends on the particular choice of r. Interestingly, in Voronoi diagrams constructed from (4.83), the symmetry property $\mathbf{x} \leftrightarrow \mathbf{x}_i$ of the anisotropic Voronoi generators (4.80) is not required [143]. This allows

for generator shapes which are not point symmetric with respect to their center.

6. Abstract Voronoi diagrams: Yet another approach is the framework of "abstract Voronoi diagrams" as proposed by Klein and coworkers [125, 126]. For each pair of generators (i, j) there is a unique contact border given by an arbitrary curve with a stereographic projection that contains the north pole of the projective sphere. Thus, it is required that the contact borders extend to infinity, and curves such as circles and ellipses are not allowed. Conversely, hyperbolas, straight lines and parabolas can be described by the abstract Voronoi diagram framework.

7. Partial Delaunay property, clustering and parallel computing: The extension of a Voronoi cell $\mathcal{V}_i$ from definition 4.1.4 is bounded by the maximal generalized distance $d_{\max}$ of a point $\mathbf{x}$ from the generator center $\mathbf{x}_i$. In the definition 4.1.7 of a generalized Voronoi cell, the value $\mathcal{P}_{\text{ex}} = \mathcal{P}(d_{\max})$ indicates the resulting extremal value attainable by the point power $\mathcal{P}_i(\mathbf{x})$. This $\mathcal{P}_{\text{ex}}$-bound manifests itself in definition 4.1.9, which means that the cells have a so-called free margin arc in directions void of a sufficiently close neighbor cell. Thus, the tessellation arising from a given set of anisotropic generators does not span the whole plane. Instead, it is confined to a limited region, which surrounds the generator centers $\{\mathbf{x}_i\}$. Therefore, the hull of the emerging Delaunay triangulation is not necessarily convex. In this sense, the Voronoi tessellation put forward here has only a partial Delaunay property. However, completing the Delaunay triangulation for a given finite Voronoi diagram is straight forward. We merely have to increase the maximal cell extension $d_{\max} \rightsquigarrow \mathcal{P}_{\text{ex}}$, so that the cells at the margin become aware of one another. In order to construct the corresponding infinite Voronoi tessellation, and thereby the convex Delaunay hull, we have to consider only those generators that previously have been situated at the margin. Indeed, the remaining interior Voronoi cells have already neighbors and extend only up to points with power within the initial $\mathcal{P}_{\text{ex}}$ bound.

The proposed property of finite Voronoi tessellations could be exploited in several ways. Obviously, for a given $\mathcal{P}_{\text{ex}}$, there can be several clusters of cells which are internally connected via neighbor relation chains of the type $i \sim j \sim \ldots \sim k$. The outer limit of such a cluster is naturally given by the free margins. Limiting the maximal $\mathcal{P}_i(\mathbf{x})$ for a point $\mathbf{x}$ by $\mathcal{P}_{\text{ex}}$ thus provides for a facility to detect clusters of Voronoi cells.

Similarly, one could start to construct a Voronoi tessellation of many generators by initially choosing $d_{\max}$ fairly small. As pointed out earlier, only those generator pairs need to be considered that are sufficiently close. Assuming the coefficients $q = 1, \nu = 1, \mathcal{P}_0 = 0$ in the scaling function $\mathcal{P}$ from equation (4.8), the plane can be subdivided into boxes of size $\mathcal{P}_{\text{ex}} \cdot \max_i a_i$, where a_i denotes the major half-axis of the generator ellipses. Neighbor pairs can only form between generators in adjacent boxes, so that this initial stage of the Voronoi construction can be easily computed in parallel. Then, $\mathcal{P}_{\text{ex}}$ can be successively increased and new pairs would only arise between some of the formerly marginal cells. Once the minimal stretched minor half-axis $\mathcal{P}_{\text{ex}} \cdot \min_i b_i$ exceeds $\max_{i \neq j} |\mathbf{x}_i - \mathbf{x}_j|$, all generators become aware of one another. Thus one obtains the "infinite" Delaunay triangulation, i.e. those neighbor relations that would arise from a Voronoi tessellation without any $\mathcal{P}_{\text{ex}}$ bound.

In summary, we have found a mathematical method to divide space into closed, contacting regions. In the following chapter we apply this method to quantitatively describe the motion within biological cell aggregates.

5. Coupling intracellular stress and cell-cell adhesion determines cooperative cell motion in tissue monolayers

Summary: In this chapter we combine results from the preceding chapters to arrive at a simulation model suited to describe motion in mesenchymal cell aggregates or epithelial tissues. First, we survey earlier models of multi-cellular aggregates and outline a selection of their findings. Next, we analyze *in-vitro* micrographs in order to investigate whether planar or spherical Voronoi tessellation is the more appropriate cell shape model. Then we construct cellular interaction and locomotion forces based on the cell outline geometry as obtained from the Voronoi tessellation. Here, cadherin and integrin densities are assumed to be constant on the surface of each model cell but different across the tissue. An explicit distance dependence of the emerging force density hinders tissue collapse by providing for an idealized contact inhibition mechanism. With the help of simulations of the resulting model tissue we find:

1. For a given set of Voronoi generators, there are several quasi-stable topological arrangements. The multiple inherent relaxation time scales seem to indicate that the model tissue behaves like a structural glass.

2. Starlike Voronoi cells enhance the cohesion stability of the whole aggregate. The starlikeness property can be enforced a priori by allowing only for moderate variation in the sizes of the model cells.

3. Since the tissue geometry is reduced to the two-dimensional plane, cell sorting can only be partially recapitulated in our simulations. This limitation can be understood in terms of incompletely permeating strands of non-mixing cells.

4. Convergent tissue extension as occurring during embryo development is driven by anisotropic cell-cell interactions. Here we impose a small force anisotropy in the interactions of the inner cells for a limited time. Surprisingly, the resulting shape deformation of the whole tissue is large, global and persistent.

5.1. There are several types of multi-cell tissue models

The fundamental compartment of life is the cell [195], which separates the interior metabolism from the exterior environment [9]. This separation is essential for gene expression and biomolecular reaction, because both processes require a located and confined vessel providing for a well-controlled micro-environment. In order to describe the large-scale organization of tissue from the underlying cell compartments, we therefore need a mathematical formalism that is able to partition space into well-defined and distinct regions. If we can uniquely identify the mathematical regions with corresponding biological cells, such a formalism would allow us to obtain a detailed description of the organizational principles of tissue formation, which would be directly inferred from individual cell properties. Indeed, there are several frameworks suited to perform such a task, with different emphasis, advantages, but also shortcomings.

1. Vertex dynamics: The first important class of collective motility models describes cells as shape-changing polygonal objects given by a set of vertices. In two spatial dimensions a vertex is located at the junction of three (or more) cells, and in three dimensions it is located at that of four or more cells. Usually, one prescribes force balances at these node or vertex points, and the motion of the cells is calculated accordingly.

- Sulsky and coworkers derive the force balances from a surface energy minimizing variational principle [205].
- Weliky and Oster consider force balances at polygon nodes by incorporation of internal pressures and surface tensions [226, 227].
- Honda and coworkers take a similar approach by starting from a three-dimensional Voronoi tessellation [106].
- Brodland and coworkers reproduce the morphogenetic movement of whole embryos by carefully measuring the involved forces *in vivo* and implementing them in their simulations [48, 49, 111]. In earlier work they investigate the influence of directed mitosis on the emerging cell shapes and the resulting stresses in the tissue [36].
- Jülicher and coworkers describe the dynamics of developing tissues such as the *Drosophila* wing disk [1]. They write an essentially elastic potential-like work function, which determines the forces onto the vertices at the cellular junctions [197].

Models using vertex dynamics naturally implement tensile forces on the cell boundaries. Friction automatically dominates the resulting mechanical system, because the forces are imposed on massless vertices instead of the center of gravity of the cells [106]. On the other hand, topological rearrangements lead to the disappearance of vertices, which is usually implemented by imposing a lower threshold on the distance of two vertices on a particular edge. Energy changes arising from topological rearrangements therefore might not be fully accounted for.

2. Contact boundary dynamics: The broad class of cellular Potts type models relies on the minimization of surface energy arising from homo- and heterotypic cell-cell adhesion contacts. The involved stochastic Monte-Carlo update procedure locally and gradually shifts the position of cell-cell boundaries.

- The Cellular Potts model was pioneered by Glazier and Graner [90]. Originally it appeared as a multi-spin generalization of the Ising model in statistical physics. The simulation domain is a square or cubic lattice, where each cell occupies several lattice sites, usually approximately 40. Importantly, the model cells are identified by the spin number of their underlying lattice sites. They are only connected in a certain dynamical regime of the Monte-Carlo update, where the level of stochastic fluctuations is not too high. Since its initial proposal, the cellular Potts model has been extended [167] and integrated into a freely available simulation framework [114]. Therefore it appears to be quite popular [120, 146, 219].

- Czirok and coworkers enhance the cellular Potts model and implement anisotropy in the adhesiveness of the cells. In this way, they successfully reproduce the formation of blood vessels [207].

As already mentioned, the boundary dynamics method of the Cellular Potts model relies on stochastic Monte-Carlo update rules. While usually each component of the underlying Cellular Potts Hamiltonian function has a straight forward interpretation in terms of biological terms like cell protrusiveness or persistence, the relation of the Monte-Carlo update to measurable physical force balances is less obvious. Despite of this limitation, cellular Potts models perform exceptionally well in cell sorting simulations.

3. Center dynamics: Another popular approach represents cells as individual particles of finite extension. In contrast to cellular automata on a lattice, these particles may attain arbitrary positions in continuous space. In general, the common feature of this class of models is that the translation dynamics acts on the cell centers exclusively.

- Drasdo and coworkers mainly model the growth kinetics of tissue-cell populations [71, 82]. In their Monte-Carlo approach, the cell center positions are stochastically updated depending on the change in pair interaction energies. The simulation domain is partitioned into polygonal cells by constructing a Voronoi tessellation. Recently, they established a mapping between the cellular expansion kinetics in two and three dimensions [181].

- Similarly, Schaller and Meyer-Hermann obtain polyhedral cells from a three-dimensional Voronoi diagram [191]. However, their method accounts for different sizes of the elastic cells. In a Langevin approach, the cellular motility is governed by both stochastic perturbations and chemical adhesion forces. This leads to the prediction of tissue internalization instability induced by cell transmembrane receptor dynamics [26, 148]. Moreover, Beyer and Meyer-Hermann could conceive the formation of the primary lymphoid follicle within their framework of Delaunay object dynamics [27].

- Palsson and Othmer describe biological cells as deformable ellipsoids with viscoelastic deformation forces. By employing locomotion forces due to taxis and cell-cell interaction forces, they obtain results on individual and collective movement of *Dictyostelium discoideum* [172] and the sorting of its prestalk and prespore cells [171].

The specific construction principle for cell-cell contacts fully determines the tissue geometry, which generally forms the basis of the dynamical force balances in center-based tissue models. The latter have, however, difficulties in cell sorting, as fluctuations in the cell boundaries are not represented correctly. It is noteworthy that the earliest descriptions of cell aggregates in terms of Voronoi tessellation date back to Honda [105]. Moreover, the tissue model described in this thesis falls into this category, see also [31].

5.2. Confluent monolayers and epithelial tissues can be described by circular Voronoi tessellations

1. Shapes of biological cells in mesenchyma and epithelia: In chapter 4 we developed a method that divides space into compartments resembling distinct model cells. While it has been shown that the general method is consistent and does the envisioned job for the model, it is not yet clear whether its application as formal description of two-dimensional biological tissues is appropriate.

Two-dimensional cell motility ranges from single cells moving independently to almost epithelial sheets undergoing collective and directed migration. The intermediate regime is usually referred to as epithelial-mesenchymal transition, see e.g. [214]. Thereby the cells loosen their contacts to engage in relatively fast migration, for example towards a wound. By the late 1970s, Hisao Honda had already shown that planar Voronoi diagrams (figure 4.1 left) generally describe the cell morphology observed highly polarized and densely packed epithelial sheets quite accurately [105]. However, in these diagrams the resulting cell-cell contacts are all represented by straight lines being flat without curvature. Also, there is no explicit provision for cells of different sizes.

Certainly, however, both cell size and cell-cell contact shape have some influence on cell functions, such as the formation and stabilization of mutual adhesion, especially in the mesenchymal state between collective epithelial resting and the independent migration of isolated cells. The generalized Voronoi method from chapter 4 is in principle capable to account for curved cell-cell contact shapes. It is therefore worthwhile to check whether certain Voronoi shape models accurately resemble a given confluent monolayer of biological cells close to the epithelial-mesenchymal transition.

2. Aggregates of Zebrafish ectodermal cells: Both outline and nucleus features of quasi two-dimensional cell aggregates can be extracted in a particularly easy manner, if suitable fluorescence dyes are employed to highlight regions of interest. In [145, figure 1A], Schoetz and coworkers have stained membranes and nuclei of Zebrafish ectoderm cells in blue and green, respectively, see figure 5.1 bottom.

For the purpose of computer-assisted image processing, we use the command line tool `pdfimages` to extract [145, figure 1] from the `pdf`-file of the article. Subsequently, we crop the figure to contain only the panel

A, and split the resulting micrograph into red, green and blue channels for further use. In order to segment the cell nuclei, we create a blurred version B_b of the original blue channel O_b by employing a Gaussian filter with 50 pixels radius. Next, we subtract the blurred nuclei micrograph from the original one, $D_b = O_b - B_b$. If the brightness of a pixel in D_b exceeds the threshold value of 0.23 times the brightness in B_b, then we assign the corresponding pixel a value of 1, and otherwise set it to 0. The resulting boolean picture $Z_b = (D_b > 0.23 B_b)$ is then smoothed by five dilation and five subsequent erosion steps with a boolean and approximately circular stencil of 5 pixels in diameter. As a result, we obtain several white pixel aggregates with very sharp boundaries, indicated as white rings in figure 5.1 top left. These aggregates are then identified with the help of a self-written clustering routine of Hoshen-Kopelman type [109][1]. It uniquely assigns a number to each of the found pixel clusters, and gathers all pixels of a specific cell's nucleus so that they can be collectively addressed by their respective nucleus number. Importantly, we ignore clusters consisting of only one single pixel.

The cell-cell contacts can be extracted from the green channel of the micrograph, in a procedure similar to the one for the nuclei described above. Thereby, the blurred picture B_g is created from the original O_g by employing a Gaussian filter of 15 pixels radius. Then, the relative difference is computed by $D_g = (O_g - B_g)/B_g$, renormalized to $D'_g = D_g/(\max D_g)$ and converted to boolean by thresholding, namely $Z_g = (D'_g > 0.39)$ for each pixel, see figure 5.1 top right. No further dilation or erosion steps need to be performed, because these boolean membrane images merely serve as a synthetic benchmark for quantifying the accuracy of certain kinds of Voronoi tessellations.

To this end, we consider the two specific types of tessellations from example 4.1.13, both based on the Euclidean norm: (i) the circular diagram with isotropic weighted point powers $\mathcal{P}_i(\mathbf{x}) = \|\mathbf{x} - \mathbf{x}_i\|/r_i$, and (ii) the planar diagram without explicit generator weights, $\mathcal{P}_i(\mathbf{x}) = \|\mathbf{x} - \mathbf{x}_i\|$. First, we compute the centers $\mathbf{x}_i$ of the generators from the center of mass of the cell nuclei, and choose the weights r_i such that the total pixel area of the nucleus coincides with the area of a circle with radius r_i. In this way, the resulting Voronoi generator balls $\mathcal{B}_{r_i}(\mathbf{x}_i)$ resemble the size and position of the cell nuclei quite closely. With the help of the routine

[1] Alternatively, one can employ the `bwlabel()` function of GNU Octave `http://www.octave.org`. In computer science, the Hoshen-Kopelman procedure is apparently also known as union find, see `http://www.ocf.berkeley.edu/~fricke/projects/hoshenkopelman/hoshenkopelman.html` (accessed September 18, 2012).

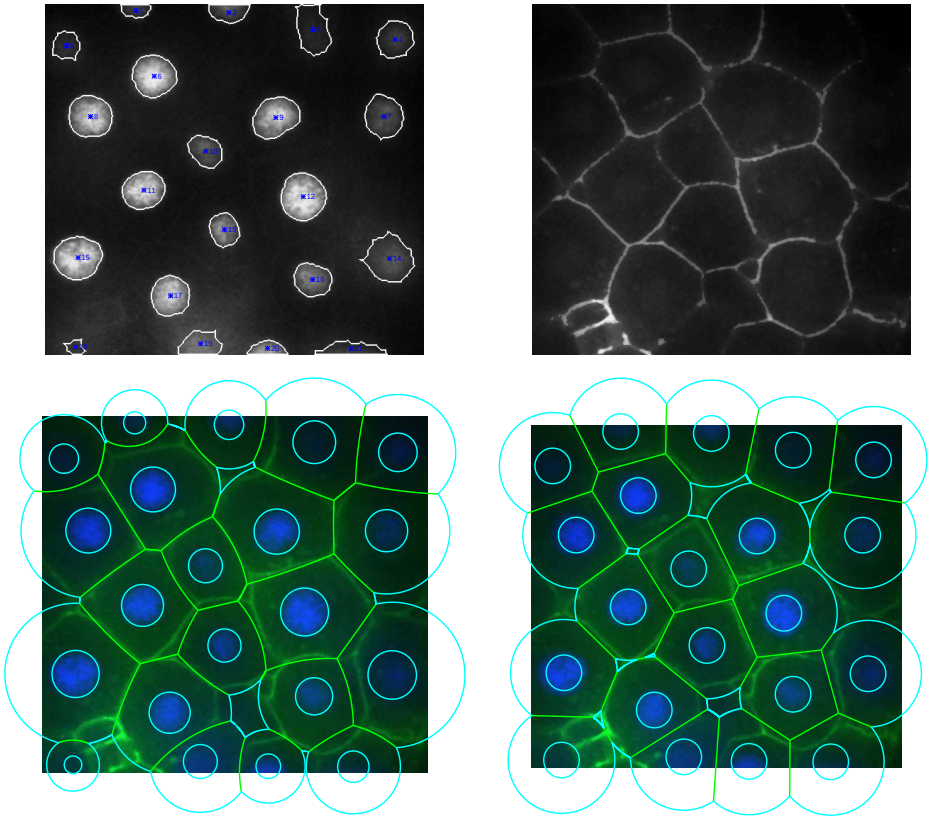

Figure 5.1.: Comparing monolayer of Zebrafish ectoderm cells with related Voronoi diagram. The top row of panels represents the overlay of extracted cell characteristics and the original intensity profiles, whereby objects found from image analysis are artificially highlighted. As described in the text, both cell nuclei (left) and membranes (right) can be extracted from fluorescence data in the individual channels of the original micrograph [145, figure 1A]. The shown Voronoi tessellations then can be constructed from size and position data of the nuclei. In the lower row, panels show the original micrograph in overlay with (i) a circular Voronoi diagram (left), and (ii) an ordinary Voronoi diagram with planar cell-cell contacts (right). The original fluorescence picture is extracted from [145], with kind permission by Eva-Maria Schötz.

`mwvoro.m`[2] implementing the algorithm from section 4.8, we construct the Voronoi diagrams (i) & (ii), see figure 5.1. Moreover, we render the resulting cell-cell contact borders into the two boolean images V_{planar} and V_{circular}, respectively. For (ii), an identical radius is assigned to all nucleus balls $\{\mathcal{B}_{r_i}(\mathbf{x}_i)\}$, so that we obtain an ordinary Voronoi diagram from example 4.1.13. In order to quantify how well the tessellations describe the actual tissue, we define the relative match $\mathcal{M}$ as ratio,

$$\mathcal{M} := \frac{\#\text{ matching Voronoi contact border pixels}}{\text{total }\#\text{ membrane pixels}}, \tag{5.1}$$

which is computed from boolean template Z_g and Voronoi images $V_{\text{planar}}, V_{\text{circular}}$. All results of the image analysis are summarized in figure 5.1, together with an overlay of the Voronoi diagrams on top of the original micrograph. As turns out, the relative match is (i) $\mathcal{M}_{\text{circular}} = 4.6\%$ for the circular and (ii) $\mathcal{M}_{\text{planar}} = 2.9\%$ for the ordinary planar Voronoi diagram. Moreover, the circles generally seem to resemble the qualitative features of the observed cell outline curves more closely.

The relatively low values of $\mathcal{M}$ arise from the incomplete segmentation of the cell membranes and from rendering of the Voronoi contact borders as thin lines. The significance of $\mathcal{M}$ is however not affected since the situation is the same for both types of Voronoi tessellations, and because we are mostly interested in their mutual comparison. Thus, although the quality measure $\mathcal{M}$ is simplistic and certainly could be improved, we take its values as an indication that circular Voronoi diagrams are to be preferred when describing quasi two-dimensional cell aggregates.

3. Quail embryo endocardial cells: In order to further inquiry on the accuracy of the two Voronoi tessellation methods, we apply the image segmentation described above also to micrographs of endocardial cells extracted from a quail embryo, see figure 5.2. Here, only the nuclei are available in a separate fluorescence channel. However, the phase contrast images taken simultaneously are also suitable for extracting data on the cell-cell contacts. In particular, cells in the bulk seem to be surrounded by a fairly bright halo, which is prominent enough to be taken as indication for the membrane situated between two distinct cells.

As before, we identify the nuclei from the fluorescence channel O_f. Here, the Gaussian filter for creating the blurred image B_f has a radius

[2]See electronic supplementary material, section A.7, or `http://www.theobio.uni-bonn.de/people/mab/dsup`.

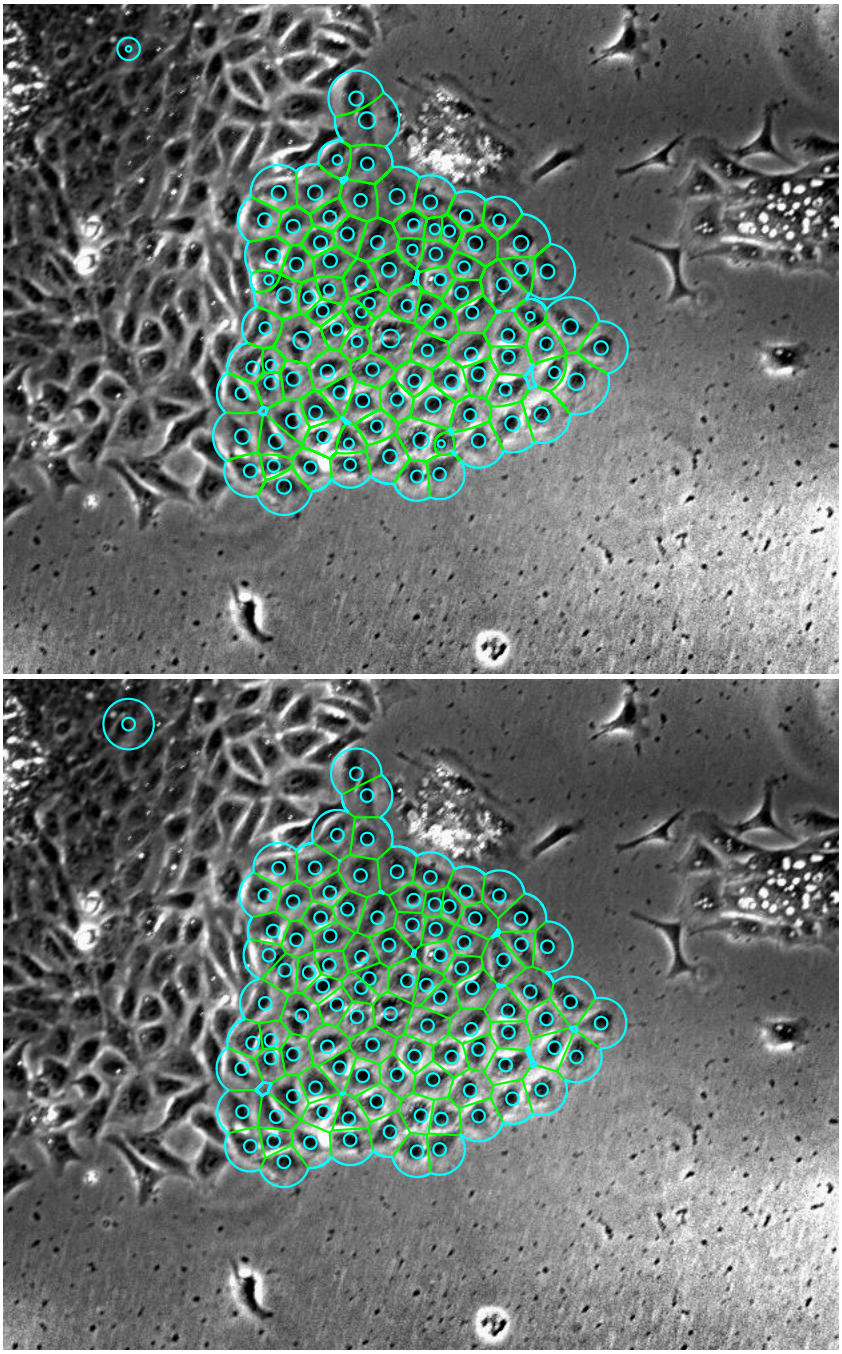

Figure 5.2.: Comparison of circular and planar Voronoi diagram constructed from the nuclei of quail embryonic endocardial cells in a confluent monolayer. The original micrograph is courtesy of Andras Czirok.

of 25 pixels, and the difference picture is $D_f = O_f - B_f$. Thresholding according to $Z_f = (D_f{>}1.8B_f)$ creates the Boolean version Z_f, and only one single dilation/erosion step is performed with a small cross-like stencil of diameter 3. In the resulting boolean image Z'_f, we neglect clusters of less than 12 pixels in size. Segmentation of the cell-cell contacts works as described for the Zebrafish cells above, with Gaussian radius of 5 pixels and the cell-cell contact brightness threshold of 0.29.

Figure 5.2 shows phase contrast and circular (top) versus planar (bottom) Voronoi diagram in overlay. For cells with smaller nuclei, the differences in Voronoi cell shape are quite pronounced. In the figure, one can also observe dividing cells near the big cell in the center of the monolayer. Apparently, the fluorescent area associated with the nucleus appears to split into two equal parts. This interesting feature is exhibited only in the first image, because only the circular Voronoi diagram takes into account the varying sizes of the cell nuclei. While the relative matches $\mathcal{M}_{\text{circular}} = 13.7\%$ versus $\mathcal{M}_{\text{planar}} = 13.3\%$ give no clear indication, the observed cellular shape variations clearly favor the circular Voronoi tessellation over the planar one. In the following sections, we therefore model cell aggregates by circular Voronoi tessellations exclusively.

5.3. Cell pairs interact via cadherin mediated adhesion[3]

1. Geometry of a cell pair and starlikeness: In order to define meaningful pair interaction forces, we first explore the geometric properties of a single cell pair comprising the circular Voronoi tessellation from section 4.4. As before, the cell bodies are represented by mathematical balls $\mathcal{B}_{r_i}(\mathbf{x}_i), \mathcal{B}_{r_j}(\mathbf{x}_j)$ from equation (4.34) and drawn green in figure 5.3. The maximal possible extension of a Voronoi cell can be represented as ball,

$$\mathcal{B}_{R_{i0}}(\mathbf{x}_i) = \{\mathbf{x} \in \mathbb{R}^2 : \mathcal{P}_i(\mathbf{x}) \leq \mathcal{P}_{\text{ex}}\} \supset \mathcal{V}_i, \tag{5.2}$$

which follows from the defining relation (4.10) of a Voronoi cell $\mathcal{V}_i$. Correspondingly, a free cell without contact to another would comprise the open version of the the so-called free ball $\mathcal{B}_{R_{i0}}(\mathbf{x}_i)$. Setting $q = 1, \nu = 2, \mathcal{P}_0 = 0$ in the scaling function (4.8), and thereby dropping the matrix notation

[3]Most paragraphs of this section appeared in [31], as indicated in separate footnotes. The article [31] was jointly written by M.B., Amit Kumar Tyagi, Jan-Ulrich Kreft and Wolfgang Alt.

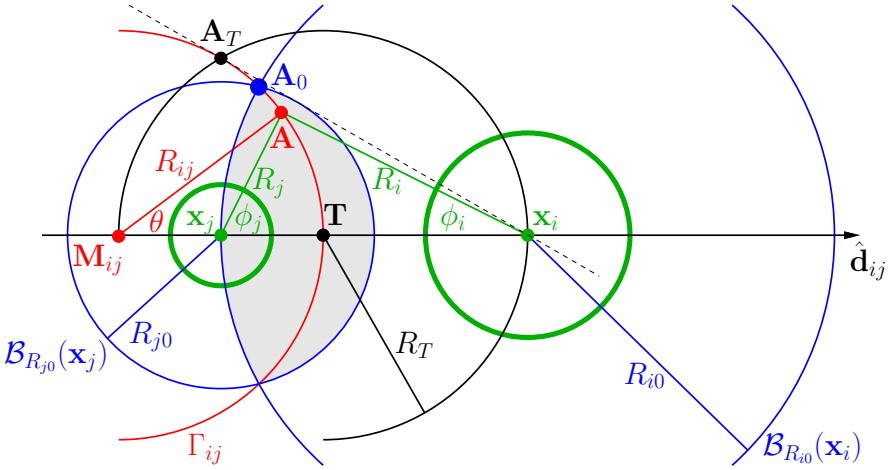

Figure 5.3.: Contact geometry of a pair of two circular Voronoi cells. The properties of their generators $\mathcal{P}_i, \mathcal{P}_j$ are represented by the two cell body balls $\mathcal{B}_{r_i}(\mathbf{x}_i), \mathcal{B}_{r_j}(\mathbf{x}_j)$ (green circles), cf. equation (4.34). On the other hand, the maximal extension of the corresponding Voronoi cells $\mathcal{V}_i, \mathcal{V}_i$ is limited by the extremal scaled norm $\mathcal{P}_{\text{ex}}$, see equation (5.2). It gives rise to the so-called free balls $\mathcal{B}_{R_{i0}}(\mathbf{x}_i), \mathcal{B}_{R_{j0}}(\mathbf{x}_j)$ (blue outer circles), which represent the occupied domains of the Voronoi cells $\mathcal{V}_i, \mathcal{V}_j$ in isolation. The latter can only be neighbors $i \sim j$ if the shaded region $\mathcal{B}_{R_{i0}}(\mathbf{x}_i) \cap \mathcal{B}_{R_{j0}}(\mathbf{x}_j)$ is non-empty. Otherwise, there would be no contact border Γ_{ij} (red), because it would be situated in the void between the distant cells. For proposition 5.3.1, we additionally need several geometric quantities. The point $\mathbf{A}$ (red dot) on the contact circle (red line) with radius R_{ij} is parameterized by the polar angle θ with respect to the contact center $\mathbf{M}_{ij}$. The corresponding angles as viewed from the cell centers $\mathbf{x}_i, \mathbf{x}_j$ are ϕ_i, ϕ_j, and R_i, R_j are the distances of $\mathbf{A}$ from $\mathbf{x}_i, \mathbf{x}_j$. The circle through $\mathbf{M}_{ij}$ and $\mathbf{x}_i$ (black) has its center at $\mathbf{T}$ (center black dot), and intersects Γ_{ij} (red) at the $\mathbf{A}_T$ (top black dot). The point $\mathbf{A}_0$ (blue dot) marks the intersection of the circles associated with the free balls $\mathcal{B}_{R_{i0}}(\mathbf{x}_i)$ and $\mathcal{B}_{R_{j0}}(\mathbf{x}_j)$. Finally, the coordinate system has been aligned with the cell center connection $\mathbf{x}_i - \mathbf{x}_j$, which defines the unit vector $\hat{\mathbf{d}}_{ij}$.

(4.25) of the generator $\mathcal{P}_i$, we have

$$\mathcal{P}_i(\mathbf{x}) = \left\|\mathbf{x} - \mathbf{x}_i\right\|_i^2 \equiv \frac{(\mathbf{x} - \mathbf{x}_i)^2}{r_i^2}. \tag{5.3}$$

In this way, the relation of free cell radius R_{i0} defined by (5.2) and body radius r_i is

$$R_{i0} = r_i \cdot \sqrt{\mathcal{P}_{\text{ex}}}, \qquad \text{with} \quad \mathcal{P}_{\text{ex}} > 1. \tag{5.4}$$

The later inequality condition is a consequence of the model requirement that a Voronoi cell should have at least some space around the central cell body region $\mathcal{B}_{r_i}(\mathbf{x}_i)$. According to equation (4.15) we also have

$$\Gamma_{i0} \subset \left\{\mathbf{x} \in \mathbb{R}^2 : \ \|\mathbf{x} - \mathbf{x}_i\| = R_{i0}\right\} \tag{5.5}$$

for the free margin Γ_{i0} of the Voronoi cell $\mathcal{V}_i$.

With these notions at hand, we take a closer look at geometrical properties of the contact surface Γ_{ij} between two adjacent cells as in figure 5.3. From this figure and the formulae (4.33) defining the circular contact border Γ_{ij}, it becomes apparent that the larger cell may not always be starlike. Recall the definition of starlikeness with respect to the center $\mathbf{x}_i$: $\forall \mathbf{x} \in \mathcal{V}_i$ also the line segment $\overline{\mathbf{x}_i\mathbf{x}} \subset \mathcal{V}_i$. Not being starlike is – however – an unusual property of biological cells. While exceptions to this rule naturally do exist, they usually have a rather extreme architecture, like e.g. neurons with multiple dendritic extensions and a long axon. Since non-starlike cells also deviate from earlier tissue models [71,105,191,205], we investigate under which circumstances Voronoi cells of circular generators remain starlike.[4]

In figure 5.3, the straight line connecting $\mathbf{x}_i$ and $\mathbf{A}_T$ is a tangent to Γ_{ij}. Thus it is clear from the geometry that both $\mathcal{V}_i$ and $\mathcal{V}_j$ are star-like domains with respect to $\mathbf{x}_i, \mathbf{x}_j$, if and only if their corresponding free balls $\mathcal{B}_{R_{i0}}(\mathbf{x}_i), \mathcal{B}_{R_{j0}}(\mathbf{x}_j)$ do not extend beyond the point $\mathbf{A}_T$. Before we proceed, we introduce the cell size homogeneity quotient

$$Q = \min_{i,j} \frac{r_i + r_j}{|r_i - r_j|} = \frac{r_{\max} + r_{\min}}{r_{\max} - r_{\min}}, \tag{5.6}$$

where $r_{\min} = \min_i r_i$, $r_{\max} = \max_i r_i$, and the last equality in (5.6) follows from monotonicity arguments. Therefore, $Q = Q(\{r_i : i = 1 \dots N\})$ is a measure of the uniformity of cell sizes within a tissue, with $Q \to \infty$ for almost equal r_i and $Q \approx 1$ for $r_{\max} \gg r_{\min}$.

[4]The remainder of this paragraph appeared in slightly modified form as part of [31, section 2.2]. M.B. performed the presented research and wrote that part of the paper.

Proposition 5.3.1 (Starlike cells): For a circular Voronoi tessellation, the resulting cells $\mathcal{V}_i$ are starlike with respect to $\mathbf{x}_i$, if the maximal $\mathcal{P}$-distance $\mathcal{P}_{\text{ex}}$ fulfills the homogeneity constraint

$$1 < \mathcal{P}_{\text{ex}} \leq Q. \tag{5.7}$$

Proof: Consider the figure 5.3. From fundamental trigonometric relations follows the angle

$$\phi_j^T := \angle(\mathbf{T}, \mathbf{x}_j, \mathbf{A}_T) = \frac{\pi}{2}, \tag{5.8}$$

and the geometric similarity of the triangles $\triangle(\mathbf{M}_{ij}, \mathbf{x}_i, \mathbf{A}_T), \triangle(\mathbf{x}_i, \mathbf{A}_T, \mathbf{x}_j)$. Let $d_{ij} := \|\mathbf{x}_i - \mathbf{x}_j\|$ denote the distance between the two cell centers. With $r_j < r_i$, we have for the point $\mathbf{A} = \mathbf{A}_T$

$$\cos\theta_T = \frac{r_j}{r_i} \tag{5.9}$$

$$R_{jT} = \frac{r_j}{\sqrt{|r_i^2 - r_j^2|}} \cdot d_{ij}, \qquad R_{iT} = \frac{r_i}{\sqrt{|r_i^2 - r_j^2|}} \cdot d_{ij}, \tag{5.10}$$

where the angle θ_T corresponds to the θ-parameterization of $\mathbf{A}_T$ on Γ_{ij} and the radii R_{iT}, R_{jT} connect $\mathbf{A}_T$ and $\mathbf{x}_i, \mathbf{x}_j$, respectively. With the equations in (5.10), the maximal distances of a point $\mathbf{A}$ on Γ_{ij} from the two cell centers have been identified. Starlikeness of $\mathcal{V}_i$ is equivalent to the condition $R_{i0}^2 \leq R_{iT}^2$ with $R_{i0}^2 = \mathcal{P}_{\text{ex}} r_i^2$, thus $\mathcal{P}_{\text{ex}} \leq (\mathbf{x}_i - \mathbf{x}_j)^2 / |r_i^2 - r_j^2|$, which can be fulfilled by requiring $\mathcal{P}_{\text{ex}} \leq Q$, since we have $(r_i + r_j)^2 \leq (\mathbf{x}_i - \mathbf{x}_j)^2$, i.e. non-overlapping generator balls for all i, j. With the inequality condition in (5.4) the assertion follows. □

In particular, starlikeness prohibits engulfment of one cell by the other, so that $\mathcal{B}_{R_{i0}}(\mathbf{x}_i)$ may not contain $\mathcal{B}_{R_{j0}}(\mathbf{x}_j)$ completely for $r_i > r_j$. Note that within sufficiently large tissues, the smallest and biggest cell will usually not be in contact, which relaxes inequality (5.7) into the condition:

$$1 < \mathcal{P}_{\text{ex}} \leq \min_{\text{neighbors } i,j} \frac{r_i + r_j}{|r_i - r_j|} =: Q_{\text{nb}}, \tag{5.11}$$

where Q_{nb} indicates the cell size homogeneity over all neighbor pairs.

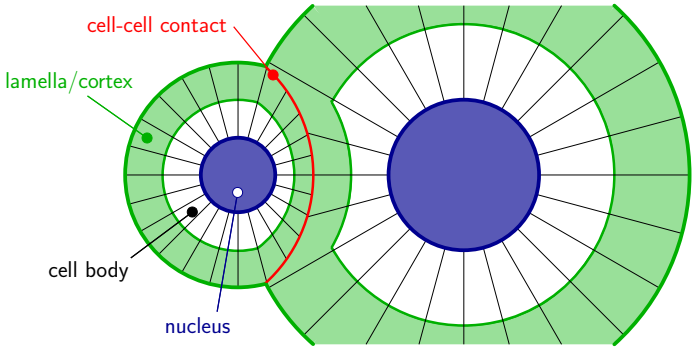

Figure 5.4.: Scheme of interacting cell pair with the biologically motivated functional units nucleus (dark blue), cell body (white), and lamella/cortex (green). The interplay of intracellular cytoplasm dynamics and external substratum adhesion beneath the lamella leads to cellular locomotion. In addition, the mutual transcellular adhesion is mediated by links bridging the cytoskeleton of both cells via dedicated junctions at the cell-cell contact (red), which is influenced by the underlying density of pairing filaments (black), see text for details.

2. Structural components of cell-cell adhesions[5]: The cytoskeleton with its network of filaments often features bundled structures, which are commonly visible as so-called stress fibers. They emanate from the cell body or nucleus in radial direction and often reach out towards the cell border, cf. the red and green lines in figure 1.4. According to [68], filamentous actin at cell cell contacts attaches to transmembrane complexes called adherens junctions. The latter are made from e.g. catenins on the cytosolic side and cadherins at the exterior of the cell, cf. also section 1.6. By connecting neighboring cells, these structures stiffen and strengthen the tissue coherence.

Inspired by this observation, it is assumed that the interaction force between two cell bodies is transduced by radial filament structures extending towards the cell boundaries. Thereby, the filaments of one cell connect to those of the other and form pairs along the contact border Γ_{ij}, see figure 5.4. However, these cell-cell junctions are not fixed and undergo dissociation, diffusion, and renewed association. Motivated by protein (e.g. cadherin) diffusion properties in membranes [85], this pro-

[5] A slightly modified form of this paragraph appeared in [31, section 3.1]. M.B. performed the presented research and wrote that part of the paper.

cess is considered to be fast (seconds) compared to the slower time scale (several minutes) of cell deformation and translocation. In this way, pair formation of cross-attachments between filament bundles from both cell bodies can be regarded as a pseudo-stationary stochastic process [76]. In order to compute the interaction force between two cells, one needs a suitable expression for the density of pairing filaments $\rho(\theta)$ at the border of the cells i, j.

3. Filament pair density at cell-cell contacts[6]: Consider the cell pair as illustrated in figures 5.3 and 5.4, with cell body radii $r_i > r_j$, and all geometric quantities as before. Starting from the surface of the cell bodies $\mathcal{B}_{r_i}(\mathbf{x}_i)$ and $\mathcal{B}_{r_j}(\mathbf{x}_j)$, filaments extend in radial direction under angles $\phi_i(\theta)$ and $\phi_j(\theta)$, respectively, to eventually meet at $\mathbf{A}(\theta)$ on the contact border Γ_{ij}. The density of the radial filaments is assumed to be constant on the surface of each cell body, and given by a universal value $\tilde{\rho} > 0$, which represents the active structures of the cytoskeleton and thereby the capability for cellular contraction and spreading forces. In order to construct the pairing density of filaments $\rho(\theta)$, we need to establish a mapping of the single densities $\tilde{\rho}$ from the cell body surfaces onto the contact border Γ_{ij}. Denoting the mapped densities by $\rho_i(\theta), \rho_j(\theta)$ we find

$$\rho_i(\theta) R_{ij} \mathrm{d}\theta = \tilde{\rho} r_i \mathrm{d}\phi_i, \qquad \rho_j(\theta) R_{ij} \mathrm{d}\theta = \tilde{\rho} r_j \mathrm{d}\phi_j. \tag{5.12}$$

by equating corresponding surface elements. For a point $\mathbf{A}(\theta) \in \Gamma_{ij}$, we have

$$R_{ij} \sin\theta = R_i \sin\phi_i = R_j \sin\phi_j, \tag{5.13}$$

$$R_{ij} \cos\theta = |\mathbf{x}_j - \mathbf{M}_{ij}| + R_j \cos\phi_j. \tag{5.14}$$

With the help of equation (5.3), the defining condition for the contact border in equation (4.13) can be written as

$$R_j = \eta R_i \qquad \text{with } \eta = \frac{r_j}{r_i} < 1. \tag{5.15}$$

Thus, from equation (5.13) we obtain the relation

$$\sin\phi_i = \eta \cdot \sin\phi_j \tag{5.16}$$

[6] A longer version of this paragraph appeared in [31, section 3.2]. M.B. and Amit Kumar Tyagi performed the presented research, and M.B. wrote that part of the paper.

between the two angles $\phi_i(\theta)$ and $\phi_j(\theta)$. Differentiation of (5.16) with respect to θ yields the proportionality

$$\frac{\mathrm{d}\phi_i}{\mathrm{d}\theta} = \eta \cdot \frac{\cos\phi_j}{\cos\phi_i} \cdot \frac{\mathrm{d}\phi_j}{\mathrm{d}\theta} = \frac{\eta}{\kappa_\eta(\phi_j)} \cdot \frac{\mathrm{d}\phi_j}{\mathrm{d}\theta}, \tag{5.17}$$

where $\kappa_\eta(\phi_j) = \sqrt{1 + (1-\eta^2) \cdot \tan^2\phi_j}$. Moreover, by solving equation (5.13) for R_j in terms of R_{ij}, inserting it into equation (5.14), and using the relations (4.33) we get an explicit expression for $\tan\phi_j$ in terms of θ,

$$\tan\phi_j = \frac{\sin\theta}{\cos\theta - \eta}. \tag{5.18}$$

This expression holds for all $|\theta| < \theta_T$ or equivalently $|\phi_j| < \pi/2$, see equations (5.8, 5.9). Finally, by differentiation of equation (5.18) with respect to θ we obtain

$$\frac{\mathrm{d}\phi_j}{\mathrm{d}\theta} = \frac{\tan\phi_j}{1+\tan^2\phi_j} \cdot \Big(\tan\phi_j + \frac{1}{\tan\theta}\Big) = \frac{1-\eta\cos\theta}{1-2\eta\cos\theta+\eta^2} > 0. \tag{5.19}$$

Let us now assume that the pairing density function $\rho(\theta)$ depends on $\rho_i(\theta)$ and $\rho_j(\theta)$, is even in θ, maximal at $\theta = 0$, and strictly monotonically decreasing for increasing $|\theta|$. In [31, section 3.2], two exemplary models to specify such a density function $\rho(\theta)$ are discussed. Here, we prefer the so-called mean density pairing involving the geometric mean,

$$\rho(\theta) = \sqrt{\rho_i(\theta) \cdot \rho_j(\theta)} = \tilde{\rho} \cdot \frac{r_j}{R_{ij} \cdot \sqrt{\kappa_\eta(\phi_j)}} \cdot \frac{\mathrm{d}\phi_j}{\mathrm{d}\theta}. \tag{5.20}$$

It describes the steady-state of short-term stochastic filament association provided that each filament from either of the neighboring cells has some probability to randomly engage in some junction on Γ_{ij}.

4. Pair interaction force[7]: Consider two adjacent neighbor cells $i \sim j$ with their cell-cell center distance being $d_{ij} = \|\mathbf{x}_i - \mathbf{x}_j\|$. This axis connecting the cell center defines the horizontal direction of the pair-local coordinate system in figure 5.3, and is denoted by the unit vector $\hat{\mathbf{d}}_{ij}$. The orthogonal direction is given by the vertical unit vector $\hat{\mathbf{d}}_{ij}^{\perp}$ with

[7] A slightly modified version of this paragraph appeared in [31, section 3.3]. Wolfgang Alt and M.B. jointly performed the presented research and wrote that part of the paper.

the property $\hat{\mathbf{d}}_{ij} \cdot \hat{\mathbf{d}}_{ij}^{\perp} = 0$ and facing upwards in figure 5.3. The cell body distance corresponding to d_{ij} is $\delta_{ij} := d_{ij} - r_i - r_j$ and relative partition of the space in between is denoted by $\delta_{ij} = \delta_i + \delta_j$, cf. figure 4.2. Let the cells be situated in such a manner that they are barely touching each other, so that any further increase in δ_{ij} would cause them to dissociate. Then, $d_{ij} = R_{i0} + R_{j0}$, and by equation (5.4) we have for the limiting rupture distance $\delta_{ij}^{\mathrm{rup}}$ of the cell bodies

$$\delta_{ij}^{\mathrm{rup}} = \big(\sqrt{\mathcal{P}_{\mathrm{ex}}} - 1\big)(r_i + r_j) =: \delta_{i0} + \delta_{j0}, \tag{5.21}$$

where $\delta_{i0} := R_{i0} - r_i, \delta_{j0} := R_{j0} - r_j$ quantify the partition of $\delta_{ij} = \delta_{ij}^{\mathrm{rup}}$ at rupture. Then according to the assumptions in the two preceding paragraphs, any paired couple of actin fibers meeting at an adherens junction in the contact boundary Γ_{ij} develops a certain positive stress between the two cell bodies. As in the model function (3.20) for single cell migration, this stress depends on the mean volume fraction q_0 of the contractile cytoskeletal network[8], which before touching was equal in both contacting lamellae of width δ_{i0}, δ_{j0}, respectively. If now δ_{ij} further decreases, then both lamellae will be compressed by the equal factor $\delta_i/\delta_{i0} = \delta_j/\delta_{j0} = \delta_{ij}/\delta_{ij}^{\mathrm{rup}} < 1$. as a consequence of the Voronoi partition laws (4.10, 4.15). Thus, we can make the following two assumptions: first, the mean volume fraction in both lamellae increases to the same value q satisfying the inverse relation

$$\frac{q}{q_0} = \frac{\delta_{ij}^{\mathrm{rup}}}{\delta_{ij}}. \tag{5.22}$$

Second, any paired actin fibers develop the same stress between their adherens junction and the corresponding cell body, with a strength f that, for simplicity, depends only on the common cytoskeletal volume fraction q, i.e. $f = f(q)$. Yet the cytoskeletal network consists not only of cross-linked actin-myosin filaments but also of more or less flexible microtubuli and intermediate filaments [128, 196, 211]. Therefore, the stress function $f(q)$ has to decrease to (large) negative values for increasing $q \to q_{\max} = 1$, which would also resemble a certain amount of contact inhibition between cells in close contact. Here we chose the simple, thermodynamically compatible strictly decreasing model function

$$f(q) = f_{\mathrm{int}}\Big(\ln(1-q) - \ln q - \ln z_c\Big), \tag{5.23}$$

[8] In order to avoid notational clashes, the cytoskeletal volume fraction is denoted by the letter q in this multi-cell model and not by θ as in chapter 3.

where the coefficient f_{int} is a model parameter. The corresponding generalized free energy $\mathcal{F}$ is convex and satisfies

$$\mathcal{F}(1-q) = (1-q)\big(f(q) - f_{\text{int}}\big) \tag{5.24}$$

for $0 < q < 1$ (cf. [4]), where the positive constant $z_c < (1-q_0)/q_0$ determines the critical volume fraction $q_c = 1/(1+z_c) > q_0$ such that $f(q_c) = 0$. Applying transformation (5.22) we finally obtain an actin fiber stress function that depends only on the relative cell body distance $\Delta_{ij} = \delta_{ij}/\delta_{ij}^{\text{rup}} < 1$, namely

$$f(\Delta_{ij}) = f_{\text{int}} \cdot \ln\Big(\frac{\Delta_{ij} - \Delta_{\min}}{\Delta_{\text{crit}} - \Delta_{\min}}\Big), \tag{5.25}$$

where $0 < \Delta_{\min} = q_0 < q_0(1+z_c) = \Delta_{\text{crit}} < 1$.

The derivation of this cellular interaction model relies on several simplifying assumptions. First, the stress arises from filaments emanating from the two cell bodies $\mathcal{B}_{r_i}(\mathbf{x}_i)$, $\mathcal{B}_{r_j}(\mathbf{x}_j)$, and engaging in an adherens junction at Γ_{ij}. Second, the stress in the filament pair is completely determined by the coupling of effective adhesion strength f_{int} and the local cytoskeleton state q. According to equation (5.22), this state is attained in the lamellae near the horizontal cell-cell connection axis along $\hat{\mathbf{d}}_{ij}$, see figures 5.3 and 5.4. Finally, within this pair-coordinate frame, the respective filament orientations are $\hat{\mathbf{R}}_i = (-\cos\phi_i,\ \sin\phi_i)$ and $\hat{\mathbf{R}}_j = (\cos\phi_j,\ \sin\phi_j)$, so that the corresponding adherens junction at Γ_{ij} experiences two force vectors $\mathbf{f}_i = -f(\Delta_{ij}) \cdot \hat{\mathbf{R}}_i$ and $\mathbf{f}_j = -f(\Delta_{ij}) \cdot \hat{\mathbf{R}}_j$ with opposing horizontal components. However, their resultant vector $\mathbf{f}_i + \mathbf{f}_j$ generally does not vanish (except for $\phi_i = \phi_j = 0$). It has a negative vertical component $(\mathbf{f}_i + \mathbf{f}_j) \cdot \hat{\mathbf{d}}_{ij}^{\perp} = -f(\Delta_{ij}) \cdot (\sin\phi_i + \sin\phi_j)$, which could pull the adherens junction towards the cell-cell connection line along the contact boundary Γ_{ij}.

Therefore, some counterforces due to substrate adhesion via e.g. integrin [79, 98] or frictional drag have to be supposed in order to guarantee the assumed pseudo-stationary equilibrium condition for Γ_{ij}. Using the simplifying decomposition in horizontal and vertical components, we arrive at the following model expression for the force $\mathbf{f}_{ij}$ applied by a single filament pair onto the cell body center $\mathbf{x}_j$:

$$\begin{aligned} \mathbf{f}_{ij} &= \frac{1}{2}\Big((\mathbf{f}_i - \mathbf{f}_j) \cdot \hat{\mathbf{d}}_{ij},\ \ \alpha(\mathbf{f}_i + \mathbf{f}_j) \cdot \hat{\mathbf{d}}_{ij}^{\perp}\Big) \\ &= \frac{f(\Delta_{ij})}{2}\Big((\cos\phi_i + \cos\phi_j)\hat{\mathbf{d}}_{ij} + \alpha(\sin\phi_i + \sin\phi_j)\hat{\mathbf{d}}_{ij}^{\perp}\Big), \end{aligned} \tag{5.26}$$

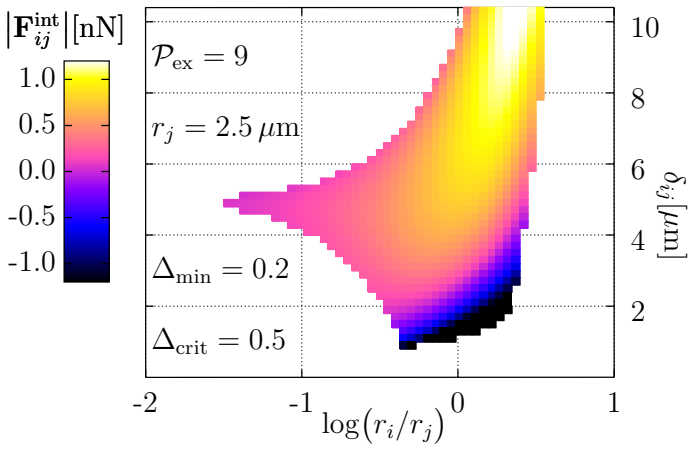

Figure 5.5.: Dependence of the in-tissue cellular interaction force $|\mathbf{F}_{ij}^{\text{int}}|$ on the cell body distance δ_{ij} and the ratio r_i/r_j of their generator radii. In the empty regions of the plot, $\mathbf{F}_{ij}^{\text{int}}$ is not defined, because there the two cells are not in contact.

where $\alpha \geq 0$ is an additional adhesion or friction parameter, representing the cooperative traction activity of the cell pair in the vertical direction. By relying on the pairing filament density $\rho(\theta)$ from paragraph 5.3.3, we obtain an integral expression for the total pair interaction force applied by cell i onto cell j:

$$\mathbf{F}_{ij}^{\text{int}} = R_{ij} \int_{\Gamma_{ij}} \mathrm{d}\theta \; \rho(\theta) \cdot \mathbf{f}_{ij}(\theta) \tag{5.27}$$

where the trigonometric relations between ϕ_i, ϕ_j and the parameterization angle θ have to be extracted from equations (5.16, 5.17). The emerging cell pair interaction force $\mathbf{F}_{ij}^{\text{int}}$ is shown in figures 5.5 and 5.6. A natural and maximal cut-off distance for the force is given by the finiteness of the Voronoi tessellation, whereby neighboring is only possible for sufficiently small cell center distances $\delta_{ij} < \delta_{ij}^{\text{rup}} + r_i + r_j$, i.e. $\mathcal{B}_{R_{i0}}(\mathbf{x}_i) \cap \mathcal{B}_{R_{j0}}(\mathbf{x}_j) \neq \emptyset$. Once two previously isolated cells come close enough for contact, there is a strong tendency to attach, which facilitates multicellular tissue formation. As one can see from figure 5.6 (a), the interaction force is attractive until the cell distance δ_{ij} reaches $\delta_{ij}^{\text{crit}} = \Delta_{\text{crit}} \cdot \delta_{ij}^{\text{rup}}$, where $\mathbf{F}_{ij}^{\text{int}}$ vanishes. Finally, if δ_{ij} drops below $\delta_{ij}^{\text{crit}}$, $\mathbf{F}_{ij}^{\text{int}}$ becomes repulsive and therefore hinders tissue collapse at distances approaching $\delta_{ij}^{\text{min}} = \Delta_{\text{min}} \cdot \delta_{ij}^{\text{rup}}$, which resembles the contact-mediated inhibition of collectively migrating cells.

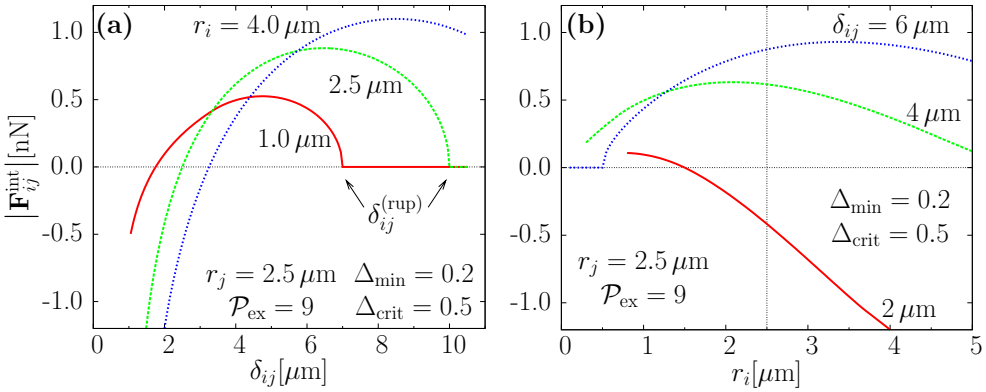

Figure 5.6.: Dependence of the in-tissue cellular interaction force $|\mathbf{F}_{ij}^{\mathrm{int}}|$ on (a) the cell body distance δ_{ij} and (b) the cell body radius r_i. In each plot we show three distinct curves corresponding to the indicated parameter values of r_i and δ_{ij}, respectively.

Note that with the relative cell body distances $\Delta_{ij} > \Delta_{\min}$, the lower bound from inequality (5.11) on the homogeneity of cell radii due to fixed $\sqrt{\mathcal{P}_{\mathrm{ex}}}$ can be relaxed to

$$1 < \frac{\mathcal{P}_{\mathrm{ex}}}{\left(\Delta_{\min}(\sqrt{\mathcal{P}_{\mathrm{ex}}} - 1) + 1\right)^2} \leq Q_{\mathrm{nb}}. \tag{5.28}$$

Correspondingly, $\mathcal{P}_{\mathrm{ex}}$ can be increased for given cell size homogeneity Q or neighbor size homogeneity Q_{nb}, cf. equations (5.6, 5.11). For example, the constraint (5.28) yields $Q_{\mathrm{nb}} = 6.25$ for $\sqrt{\mathcal{P}_{\mathrm{ex}}} = 3$, or $r_{\min} \geq 0.73 \cdot r_{\max}$ for each cell pair. In fact, the actual distances Δ_{ij} in a tissue will be larger than $\Delta_{\min}$, effectively relaxing (5.28) even further.

5.Locomotion force at the free boundary[9]: In addition to the dynamics induced by pair interaction forces, cells at the tissue margin may migrate into open space. The locomotion force causing such a migration is due to lamellipodial protrusion and retraction, which is unhindered only at the free cell boundary Γ_{i0}. In a similar manner as before, we assume that this locomotion or free boundary force onto the cell body $\mathcal{B}_{r_i}(\mathbf{x}_i)$ is determined by connecting radial filament bundles as indicated

[9] A slightly modified version of this paragraph appeared in [31, section 3.4]. Wolfgang Alt and M.B. jointly performed the presented research, and M.B. wrote that part of the paper.

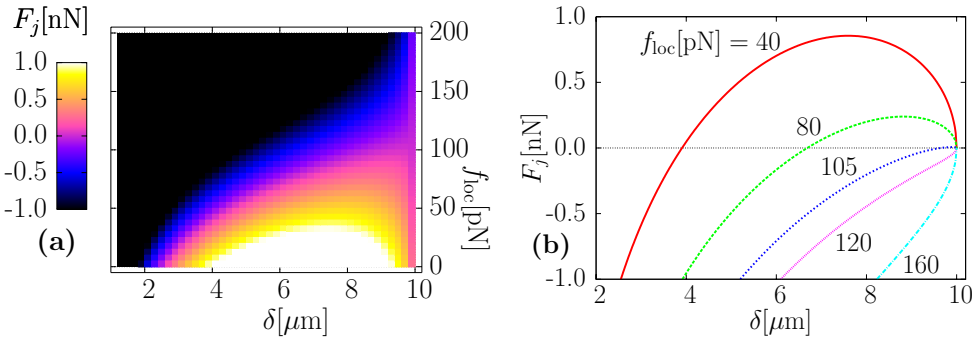

Figure 5.7.: Force balancing in an isolated cell pair. The deterministic force $F_j = |\mathbf{F}_{ij}^{\rm int} + \mathbf{F}_j^{\rm loc}|$ acts on the cell center $\mathbf{x}_j$. Parameters are $f_{\rm int} = 60\,$pN, $\alpha = 1$, $r_i = 3.0$, $r_j = 2.0$, $\tilde{\rho} = 6.6/\mu$m, $\Delta_{\rm min} = 0.2$, $\Delta_{\rm crit} = 0.5$.

in figure 5.4. The filament density of cell i along its free boundary Γ_{i0} is given by

$$\rho_{i0} = \frac{\tilde{\rho} r_i}{R_{i0}} = \frac{\tilde{\rho}}{\sqrt{\mathcal{P}_{\rm ex}}}, \tag{5.29}$$

and thus independent of r_i. In this way, the locomotion force of a cell i reads as

$$\mathbf{F}_i^{\rm loc} = f_{\rm loc} \int_{\Gamma_{i0}} \mathrm{d}s_i \; \rho_{i0} \hat{\mathbf{R}}_{i0}(\phi_i), \tag{5.30}$$

with arc length $s_i = R_{i0}\phi_i$, the radial unit vector $\hat{\mathbf{R}}_{i0}(\phi_i) = (\cos\phi_i, \sin\phi_i)$ and the locomotion strength parameter $f_{\rm loc}$, see table 5.1 below. We remark that this expression for the locomotion force is in full analogy to equations (3.57, 3.58) from the peripheral cell migration model, except that the free boundary Γ_{i0} does not occupy the full cell perimeter. The resultant force $F_j = |\mathbf{F}_{ij}^{\rm int} + \mathbf{F}_j^{\rm loc}|$ for a cell j interacting with another cell i in a pair including locomotion is shown in figure 5.7. Apparently, there is a stable contact equilibrium in F_j for lower values of the locomotion strength $f_{\rm loc} \leq 105$ pN.

In order to heuristically account for ubiquitous perturbations due to lamellipodial fluctuations or possible signals, we additionally implement stochastic force increments at the tissue margin

$$\mathrm{d}\mathbf{F}_i^{\rm st} = b_{\rm st} \int_{\Gamma_{i0}} \mathrm{d}\mathbf{B}_{t,s_i}. \tag{5.31}$$

Here we assume a uniform and isotropic vector noise $\mathbf{B}_{t,s_i}$ defining a spatio-temporal Brownian sheet in arc length and time coordinates with

independent Gaussian increments satisfying $\mathrm{Var}\big(\mathrm{d}\mathbf{B}_{ts_i}\big) = \mathrm{d}s_i \cdot \mathrm{d}t$. The strength of the stochastic force is determined by the the parameter b_{st}, again see table 5.1 below. For each time t, stochastic integration results in a simple weighted Gaussian noise term with random increments $\mathrm{d}\mathbf{W}_t$

$$\mathrm{d}\mathbf{F}_i^{\mathrm{st}} = b_{\mathrm{st}}\sqrt{|\Gamma_{i0}|}\mathrm{d}\mathbf{W}_t \mathrel{\widehat{=}} b_{\mathrm{st}}\sqrt{\frac{|\Gamma_{i0}|\mathrm{d}t}{2}}\boldsymbol{\xi}_t, \tag{5.32}$$

where $\boldsymbol{\xi}_t$ is a vector of Gaussian random numbers, which is chosen independently for every time step in a corresponding numerical realization of the stochastic process.

6. Drag forces[10]: Apart from interaction and free boundary forces, the cell is subject to drag forces $\mathbf{F}_i^{\mathrm{drag}}$ slowing down its movement. Such drag forces are generally functions of the cell body velocity $\dot{\mathbf{x}}_i = \mathbf{v}_i$. As in paragraph 3.8.5, we assume the simplest dependency of a linear force-velocity relation

$$\mathbf{F}_i^{\mathrm{drag}} = -\gamma_i \mathbf{v}_i, \tag{5.33}$$

with drag coefficient $\gamma_i = \gamma(r_i)$. Arising from friction with the substratum, γ_i could depend on the area of the cell body, e.g. $\gamma(r_i) \propto r_i^2$, however, for simplicity, here we take $\gamma_i = \tilde{\gamma}$ independent of cell body sizes.

7. Dynamics of cell movement[11]: The previously described, active and anisotropic forces $\mathbf{F}_{ij}^{\mathrm{int}}, \mathbf{F}_i^{\mathrm{loc}}$ arise from the actin filament network and cooperative adhesions, act onto the cell center $\mathbf{x}_i$, and thereby cause the cell to translocate. Thereby, the friction from equation (5.33) is considered to be dominating and inertia terms are neglected [83,106,191], so that the emerging deterministic overdamped Newtonian equations of motion read as

$$\mathbf{F}_i + \mathbf{F}_i^{\mathrm{drag}} = 0, \qquad \text{with} \qquad \mathbf{F}_i = \mathbf{F}_i^{\mathrm{loc}} + \sum_{j\,\mathrm{neighbor}} \mathbf{F}_{ji}^{\mathrm{int}}. \tag{5.34}$$

However, any change of the translocation direction as well as adjustment of speed to the pseudo-steady state as given by the previous equation

[10] In slightly modified from, this paragraph appeared in [31, section 3.4]. Wolfgang Alt and M.B. jointly performed the presented research, and M.B. wrote that part of the paper.

[11] A slightly modified version of this paragraph appeared in [31, section 3.4]. Wolfgang Alt and M.B. jointly performed the presented research, and M.B. wrote that part of the paper.

(5.34) requires some (mean) time T_i for restructuring and reinforcing the anisotropic actin network. The simplest way to model this adjustment process involves a linear stochastic filter of first order for the velocity [13]. Together with equation (5.31) this results in the stochastic differential equation (SDE) system

$$\mathrm{d}\mathbf{v}_i = \frac{1}{T_i}\left(\frac{\mathbf{F}_i}{\gamma_i} - \mathbf{v}_i\right)\mathrm{d}t + b_{\mathrm{st}}^{(i)}\sqrt{|\Gamma_{i0}|}\mathrm{d}\mathbf{W}_t, \qquad \mathrm{d}\mathbf{x}_i = \mathbf{v}_i\mathrm{d}t, \quad (5.35)$$

with $b_{\mathrm{st}}^{(i)} = b_{\mathrm{st}}/\gamma_i$. Similarly as the friction γ_i, also the mean adjustment time T_i could be cell dependent, however here we restrict ourselves to the case of cells with a single activity time scale $\forall i : T_i = T$ for all cells.

For each time t, the forces (5.27, 5.30, 5.32, 5.33) can be computed explicitly from the Voronoi tessellation of the generating cell bodies $\{\mathcal{B}_{r_i}(\mathbf{x}_i) : i = 1 \dots N\}$ using a spatial discretization of $\{\Gamma_{ij}\}$ in the parameterizing angle θ. Next, the velocities $\{\mathbf{v}_i\}$ and positions $\{\mathbf{x}_i\}$ of the cell centers are updated according to both equations (5.35) in an explicit Euler-Maruyama step [127]. Finally, the Voronoi tessellation is recomputed from the updated cell bodies $\{\mathcal{B}_{r_i}(\mathbf{x}_i)\}$.

Higher order stochastic integration schemes were not applied, since such procedures require the distribution of both forces and perturbations onto the powers of a Taylor expansion. In general, the involved derivatives of cell-cell contacts $\{\Gamma_{ij}\}$ and cell margins $\{\Gamma_{i0}\}$ cannot be computed easily *a priori*. Particularly, the change of a contact Γ_{ij} may depend on the behavior of several distinct nearby cells $k \neq i, j$. Altogether, here we use the versatile basic method for integrating the equations of motion, because it is applicable regardless of the structure of the underlying SDE system.

8. Dimensional considerations[12]: Before coming to simulations of model tissues, we further study the cellular equations of motion (5.35). Since both time (seconds) and length scale (microns) of cell motility processes are well known, the only remaining free scaling figure is the magnitude of cell forces. In accordance to [10], we assume that a typical bundle of several actin filaments can exert a force of approximately 10 pN. A single cell can, with the overall filament density parameter $\tilde{\rho}$ and the force prefactors $f_{\mathrm{loc}}, f_{\mathrm{int}}$ as in table 5.1, reach an effective traction of $\mathcal{O}(1000\,\mathrm{pN})$ from a force as given by equation (5.27). The drag coefficient $\tilde{\gamma}$ then naturally

[12] A slightly modified version of this paragraph has been published in [31, section 5]. M.B. performed the presented research and wrote that part of the paper.

Symbol	Meaning	Value	Units
$\sqrt{\mathcal{P}_{\text{ex}}}$	Relative maximal cell extension	3	dimensionless
r_i	Cell body radii	$0.9 \dots 2.0$	μm
T	Cytoskeletal reorganization time	120	s
$\tilde{\rho}$	Filament bundle density on cell body	9.55	$1/\mu$m
f_{loc}	Strength of cellular locomotion force	$10 \dots 20$	pN
f_{int}	Strength of cellular interaction force	60	pN
α	Cooperative vertical traction coefficient	$0 \dots 0.17$	dimensionless
Δ_{min}	Relative minimal cell pair distance	0.1	dimensionless
Δ_{crit}	Relative critical cell pair distance	$0.2 \dots 0.7$	dimensionless
$b_{\text{st}} \cdot \mathcal{P}_{\text{ex}}^{-1/4}$	Strength of stochastic migration force	8.31	pN $/\sqrt{\mu\text{m} \cdot \text{s}}$
$\tilde{\gamma}$	Cellular friction constant	$2.5 \cdot 10^4$	pN $\cdot$ s $/ \mu$m
dt	Numerical time step	2	s

Table 5.1.: Model parameter values as employed in this chapter 5, unless indicated otherwise. As explained in the text, $\mathcal{P}_{\text{ex}}$ determines the relative size of the lamella region around the cell body $\mathcal{B}_{r_i}(\mathbf{x}_i)$. The scaled interaction distances $\Delta_{\text{min}}, \Delta_{\text{crit}}$ are defined in equation (5.25) and determine the sign and scaling of the cell pair interaction force $\mathbf{F}_{ij}^{\text{int}}$. The relative strength of the vertical component of $\mathbf{F}_{ij}^{\text{int}}$ in equation (5.26) is given by α. Finally, the stochastic perturbation parameter b_{st} in equation (5.32) contains a factor $(\mathcal{P}_{\text{ex}})^{-1/4}$ in order to obtain the same amount of perturbation for cells with equal body radii r_i. Since we look for robust features in the simulations, b_{st} was chosen fairly high.

follows from experimentally observed cell velocities [79, 155, 234]. These and all the other model parameters used in this chapter are summarized in table 5.1, together with a brief description of their meaning. Unless indicated otherwise, we here employ the default parameter set from table 5.1.

5.4. Small cell groups exhibit several topological arrangements[13]

1. Emergence of tissue shape and multiple stable states: Consider a simple proto-tissue of seven cells as shown in figure 5.8 'start'. Using the

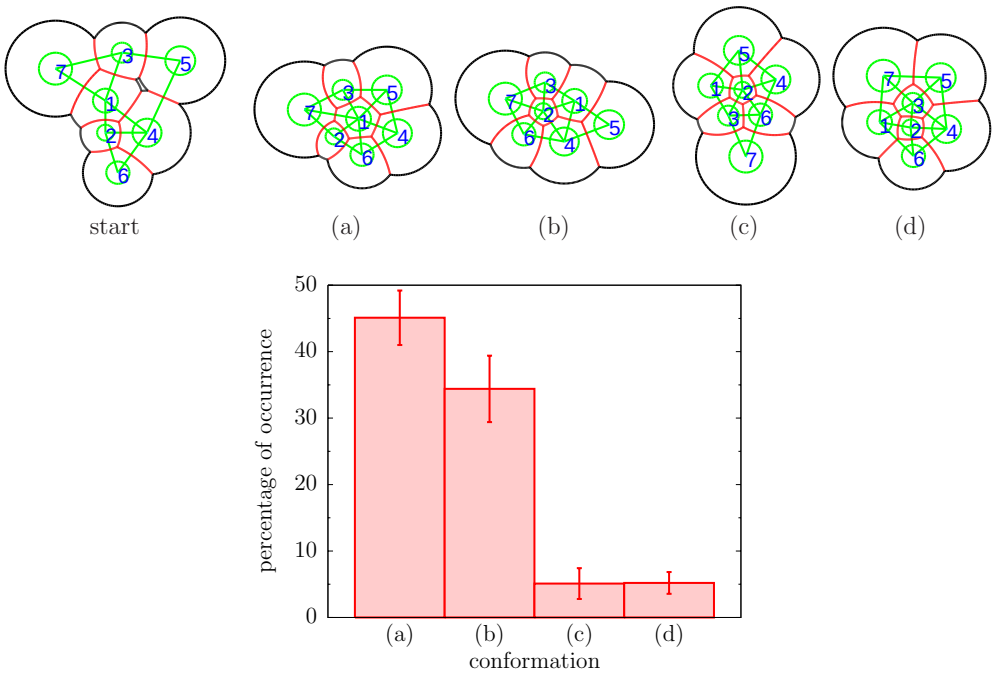

Figure 5.8.: Different tissue conformations (a–d) evolving from the configuration 'start' after a simulation time of 8 h; here $r_{\max} = 2.0\,\mu$m (cell 7), $r_{\min} = 1.0\,\mu$m (cell 2), and parameters $f_{\text{loc}} = 20\,$pN, $\alpha = 0$, $\Delta_{\text{crit}} = 0.25$. The percentage of occurrence of a particular conformation then was computed, and the error bars were obtained by a simple bootstrap method. Other features are further explained in the text.

parameters $f_{\text{loc}} = 20\,\text{pN}, \alpha = 0, \Delta_{\text{crit}} = 0.25$, a series of 1000 simulations has been performed. After a simulation time of 8 h, the emerging tissue conformations as distinguished by Delaunay network topology have been recorded. In the course of these 8 h, significant changes appear within the

[13] A slightly modified version of this section has been published in [31, section 5.1], which was jointly written by M.B., Amit Kumar Tyagi, Jan-Ulrich Kreft, and Wolfgang Alt. M.B. performed the presented research and wrote that part of the paper.

tissue, and apparently several equilibrium conformations emerge. For the four most prevalent cellular arrangements the percentage of occurrence is displayed in figure 5.8. One observes two rather globular shapes (a), (d), where either the big cell 1 or the two small cells $2, 3$ are engulfed by the others, respectively. Furthermore, there are two quite elongated shapes (b), (c), where only the single small cell 2 is completely surrounded by other cells. Being distinguished by topology, (b) and (c) are in fact quite close in shape, despite of their rotational variation.

2. Quantifying tissue shape and its fluctuations: From the high occurrence of the topological conformations (a), (b) one might conclude that these two conformations are the most stable ones. Thus, and to clarify the interrelations between the conformations (a–d), we investigate (a) and (b) in longer simulations. To this end, by starting from the configurations (a) and (b) (see figure 5.8), both tissues have been evolved for 40 additional hours of simulation time. In order to characterize the shape of tissue with respect to global and elongated shape, here we observe tissue size, i.e. the maximum diameter, and tissue circularity

$$\Omega = \frac{2\sqrt{\pi A_{\text{tiss}}}}{\sum_i |\Gamma_{i0}|} \leq 1, \tag{5.36}$$

where A_{tiss} is the total area of the tissue. Note that in connected tissues $\Omega = 1$ would be attained for a purely circular globe. In figure 5.9, we plot the full time series of size and circularity for the two tissues from 5.8 (a) & (b). After approximately 8 h, the time series for (a $\widehat{=}$ blue) & (b $\widehat{=}$ red) exhibit clearly different conformations. While the circularity Ω is only slightly different in the two cases, the tissue size is clearly higher for the elongated conformation (b). Apart from stochastic fluctuations and an initial equilibration phase for $t < 1\,\text{h}$, both observables attain a constant value for time series (a). In contrast, for time series (b) there appear distinct states between $t \sim 2.5\,\text{h}$ and $t \sim 24\,\text{h}$. Indeed these observations are reflected by the actual evolution of the tissue. While the topology of the tissue does not change after $t = 2\,\text{h}$ for time series (a) (`mova.avi`[14]), tissue (b) (`movb.avi`) goes through several different conformational states. At $t = 13.5\,\text{h}$ it attains the same topology as conformation (c), identifying (c) as a transient state (`movc.avi`). Afterwards, approximately at $t \sim 18.5\,\text{h}$, cell 7 establishes contact with cells

[14]All electronic supplementary material is available from `http://www.theobio.uni-bonn.de/people/mab/dsup`.

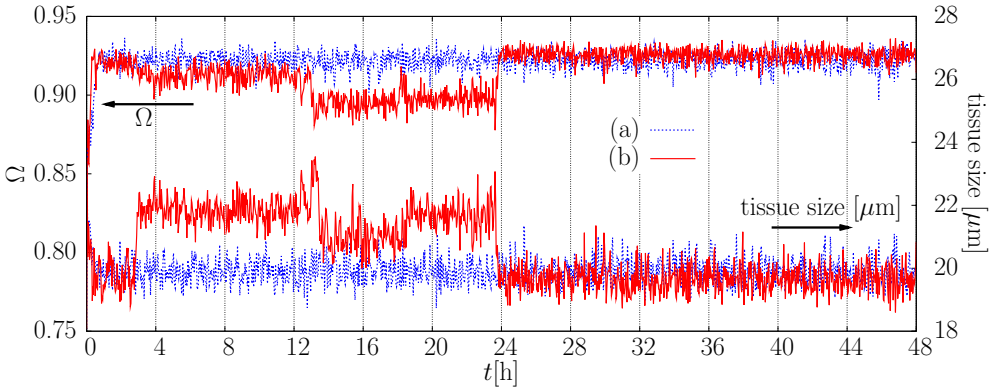

Figure 5.9.: Two time series (blue, red) for the tissue in figure 5.8 'start'. After 8 h the two distinct topological conformations from figure 5.8(a) (blue) and 5.8(b) (red) have emerged. These topological conformations are characterized by distinct tissue size (right axis) and circularity Ω (left axis). While (a) is apparently a stable topological conformation that does not change even for strong stochastic perturbations, (b) relaxes into a topological conformation of globular shape via several intermediate steps, see supplementary `mova.avi` & `movb.avi`.

1 and 3, so that the tissue shape is similar to (c). Finally, shortly before $t = 24\,\mathrm{h}$, the tissue reaches its final conformation similar to (d) except for the order of the marginal cells. Conformation (d) emerges in a similar manner as (a), however instead of cells $1, 5$ initially cells $3, 4$ form a neighbor pair, quickly leading to the stable final arrangement in less than 0.5 h (`movd.avi`). Moreover, the time series of conformation (b) in figure 5.9 suggests, that during $t = 0.5 \ldots 3\,\mathrm{h}$ the tissue already attains a shape of similar compactness and stability as in figure 5.8(a). Nevertheless, the Delaunay mesh (green lines) is not convex there (`movb.avi`), which explains this surprising instability.

3. Shape deformation barriers and tissue stability: It appears, that the stability of a tissue is related to its globular shape. This is not a surprise, since the stochastic forces in equation (5.30) are defined only on free cell boundaries Γ_{i0}, and therefore act only on marginal cells. Thus, by minimizing the total extension of all Γ_{i0}, maximal circularity minimizes stochastic perturbations, which enhances the stability of the tissue.

Additionally, for a tissue to change its topology, its cells have to over-

come barriers as imposed by the other cells. For example, cell 3 has to displace cell 1 in `movb.avi` at $t \approx 3\,\mathrm{h}$ in order to make contact with 2. Depending on the particular configuration, the severity of these barriers might range from prohibitive to practically non-existent. Influenced by the strength of the stochastic interactions, these barriers then determine the time scale of further relaxation to equilibrium. In this sense, the notion of equilibrium is directly related to an inherent time scale. According to the previous evolution of the tissue, there may be several stable topological conformations for a given time scale.

5.5. Tissue stability is favored by starlike cell geometries[15]

1. Effects of maximal cell extension and critical distance: In order to explore the ramifications of piecewise spherical cells within our model framework, we study the influence of $\mathcal{P}_{\mathrm{ex}}$ and Δ_{crit} on tissue formation. To this end, a simulation has been performed starting from an exemplary configuration as in figure 4.1 (right) with $\Delta_{\mathrm{crit}} = 0.3, \sqrt{\mathcal{P}_{\mathrm{ex}}} = 3, \alpha = 0.17$ and $f_{\mathrm{loc}} = 10\,\mathrm{pN}$. After 8 h, either Δ_{crit} or $\sqrt{\mathcal{P}_{\mathrm{ex}}}$ was modified to a nearby parameter position as indicated in figure 5.10, and the simulation was continued for another 8 h. This procedure was repeated until the whole panel in 5.10 was filled with the final tissue configurations.

For fixed $\{r_i\}$, $\sqrt{\mathcal{P}_{\mathrm{ex}}}$ defines the free cell radius R_{i0} in units of r_i, and Δ_{crit} presets the equilibrium cell-cell body distance in units of $\delta_{ij}^{\mathrm{rup}}$, see equations (5.4, 5.25, 5.21). In this way, both parameters jointly determine the emerging tissue size. In figure 5.10, the corresponding overall tissue extension increases from left to right and from top to bottom. Furthermore, for given Δ_{crit}, tissues with higher $\sqrt{\mathcal{P}_{\mathrm{ex}}}$ exhibit a rather compact, almost quadratic shape. We speculate that this is due to spontaneous formation of distinct protrusions arising from stochastic perturbations and leading to an increase of locomotion at the corners. In contrast, tissues with lower $\sqrt{\mathcal{P}_{\mathrm{ex}}}$ feature more irregular margins. Similarly, for given $\sqrt{\mathcal{P}_{\mathrm{ex}}}$, larger values of Δ_{crit} yield more irregularity, most pronounced directly before dissociation of the tissue.

[15] A slightly modified version of this section has been published in [31, section 5.2], which was jointly written by M.B., Amit Kumar Tyagi, Jan-Ulrich Kreft, and Wolfgang Alt. M.B. performed the presented research and wrote that part of the paper.

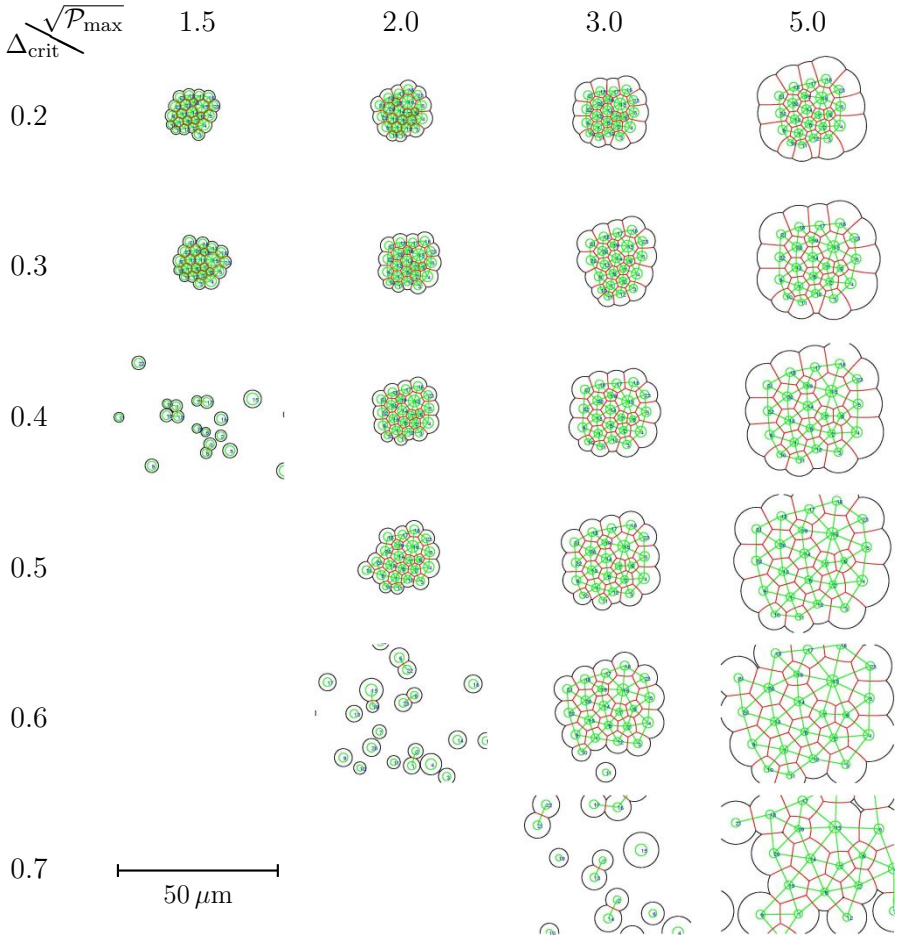

Figure 5.10.: Stability of tissue for various values of the parameters $\sqrt{\mathcal{P}_{\mathrm{ex}}}$ and Δ_{crit}, where $f_{\mathrm{loc}} = 10\,\mathrm{pN}$, and $\alpha = 0.17$. When increased, both parameters $\sqrt{\mathcal{P}_{\mathrm{ex}}}, \Delta_{\mathrm{crit}}$ lead to an increased tissue size. For sufficiently large Δ_{crit}, the tissue eventually dissociates. The extremal cell body radii are $r_{\mathrm{min}} = 0.9\,\mu\mathrm{m}$ and $r_{\mathrm{max}} = 1.7\,\mu\mathrm{m}$ in all simulations presented in this figure.

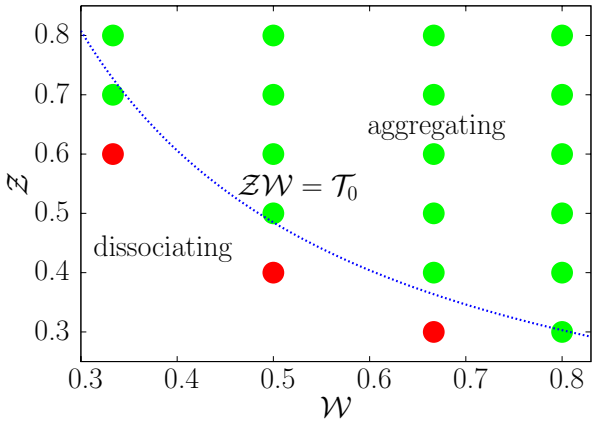

Figure 5.11.: Tissue aggregation and dissociation depending on the relative lamella width $\mathcal{W}$ and the dimensionless cell overlap $\mathcal{Z}$. The line $\mathcal{Z} \cdot \mathcal{W} = \mathcal{T}_0 \approx 0.24 \pm 3\%$ separates associating from dissociating tissues and was determined from a linear regression against $\mathcal{Z} = \mathcal{T}_0/\mathcal{W}$. See also the explanations in the text.

2. Cell overlap and tissue coherence threshold: Apparently, for sustaining the aggregation of the tissue, the interaction forces are sufficiently strong only if there is enough space for the adaptation of neighboring cell lamellae. This space serves as a cushion for accommodating near-range repulsion from multiple neighbor cells and at the same time poses a resistance to stochastic perturbations by mid-range neighbor cell attraction, cf. also figure 5.7. Otherwise the tissue dissociates, leading to isolated cells exclusively driven by stochastic perturbations. In order to quantify these findings, consider the relative lamella width $\mathcal{W}$ and the dimensionless cell overlap $\mathcal{Z}$ defined by

$$\mathcal{W} = \frac{\sqrt{\mathcal{P}_{\text{ex}}} - 1}{\sqrt{\mathcal{P}_{\text{ex}}}} < 1, \qquad \mathcal{Z} = 1 - \Delta_{\text{crit}} < 1. \tag{5.37}$$

Since $\mathcal{W}$ relates only to $\sqrt{\mathcal{P}_{\text{ex}}}$ and $\mathcal{Z}$ only to Δ_{crit}, we can reconstitute the panel from figure 5.10 in terms of $\mathcal{W}$ and Δ_{crit}. The result is shown in figure 5.11, where dissociating tissues are indicated by red dots, and aggregating tissues by green ones. Next, we fit the function $\mathcal{Z}(\mathcal{W}) = \mathcal{T}_0/\mathcal{W}$ to the lower-most green dots, whereby $\mathcal{T}_0$ is the fitting parameter. On the resulting blue line in figure 5.11, the product $\mathcal{Z} \cdot \mathcal{W}$ attains the constant value $\mathcal{T}_0 \approx 0.24$, and aggregating tissues are located above – but

not below – the fitted line. Thus, $\mathcal{T}_0$ can be identified as a threshold value guaranteeing tissue coherence under the condition

$$\mathcal{Z} \cdot \mathcal{W} \geq \mathcal{T}_0. \tag{5.38}$$

The specific value of $\mathcal{T}_0$ eventually depends on the other dynamical tissue parameters from table 5.1. The presence of the coherence threshold $\mathcal{T}_0$ confirms that for tissue aggregation to occur, there has to be enough space for the formation of cellular lamellae. This means that the relative lamella width $\mathcal{W}$ and thereby the maximal cell extension parameter $\sqrt{\mathcal{P}_{\text{ex}}}$ have to be sufficiently large.

3. Starlike cells and coherent tissues: On the other hand, we have established this result under the tissue homogeneity condition (5.11), guaranteeing starlikeness of cells, which can now be rewritten as

$$\mathcal{Z}_{\max} \cdot \mathcal{W} = 1 - \frac{1}{Q_{\text{nb}}}, \tag{5.39}$$

with $\mathcal{Z}_{\max} := 1 - \Delta_{\min}$ defining the maximal dimensionless overlap. Since $\mathcal{W} < 1$ by construction, inequality (5.38) always holds with (5.39) for very high cell size homogeneities $Q_{\text{nb}} \geq 1/\Delta_{\min}$. However, for lower Q_{nb} there is an upper bound on $\mathcal{W}$ restricting the available lamella space. If, in addition, starlikeness of cells is enforced for all possible neighborhood constellations, then Q_{nb} has to be replaced by Q, see equation (5.7). In this way the relations (5.38) and (5.39) lead to the sufficient condition for tissue coherence

$$\frac{\mathcal{T}_0}{1 - \Delta_{\text{crit}}} \leq \mathcal{W} = 1 - \frac{1}{\sqrt{\mathcal{P}_{\text{ex}}}} \leq \frac{2}{(1 - \Delta_{\min})(1 + r_{\max}/r_{\min})}. \tag{5.40}$$

From these estimates we conclude that the formation of connected tissue aggregates is guaranteed within a certain finite range of the free cell size parameter $\sqrt{\mathcal{P}_{\text{ex}}}$. The precise range of $\sqrt{\mathcal{P}_{\text{ex}}}$ depends on the model force parameters ($\Delta_{\min}$, Δ_{crit}, f_{int}, α, f_{loc}, b_{st}) and the extremal cell body radii $r_{\min}$ and $r_{\max}$. Within the limits of inequality (5.40), the lamellae regions are wide enough to perform the necessary deformations by adapting to the surrounding neighbors through shape changes. Thus, nature's freedom in developing aggregating tissues may be constrained by a tradeoff between the relative size of cells with respect to their bodies ($\sqrt{\mathcal{P}_{\text{ex}}}$) and the cell size heterogeneity ($1/Q$).

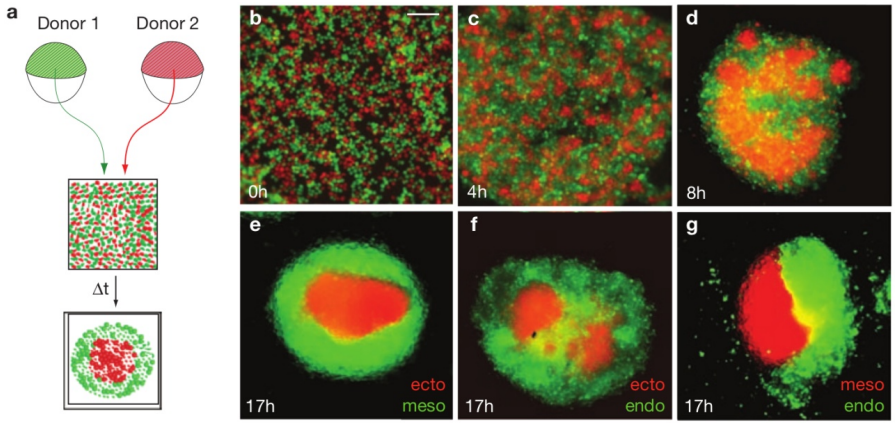

Figure 5.12.: Experimental cell sorting assay with Zebrafish cells. The cells are stained by injecting fluorescence molecules in the one-cell stage of the embryo. Subsequently, progenitor cells for a specific dermal layer of each donor embryo are extracted and subsequently mixed (a). After several hours the cells start to demix (b–d) and sort out in prominent domains. Depending on the combination of endoderm, mesoderm or ectoderm cells, different sorting patterns emerge (e–g). This figure is reprinted from [130, figure 3], with kind permission by Carl-Philip Heisenberg.

5.6. Two-dimensional cell sorting cannot be fully reproduced in cell-center based tissue models

1. Self-sorting of embryonic cells: In the early development of amphibia, between the so-called gastrula and late neurula stages, the embryo is organized in three layers of cells called the endoderm, mesoderm and ectoderm [77,160]. Most parts of the ectoderm will form the exterior skin. The mesoderm will become muscle and connective tissue. The fate of the endoderm is to form the digestive system and possibly other inner organs, see e.g. [77,160].

When embryonic cells from the three dermal layers are extracted and subsequently brought in contact *in-vitro*, they adhere to one another, even if they come from different species [217]. Moreover, they arrange in a way that recapitulates the order as present in the original embryo, which is usually referred to as cell sorting [77,91]. One example of such a cell sorting assay is shown in figure 5.12. Early and very extensive studies

in the 1950s lead Townes and Holtfreter to suggest an "emergence of a selectivity of cell adhesion" [217, p. 115] as an explanation of the observed cellular arrangement patterns.

Based on this idea, Steinberg developed his theory of "differential adhesion" in the 1960s [198, 199]. Thereby, the demixing of cells is explained from their microscopic molecular adhesion properties, whence the cells would adhere to one another just like molecules in a fluid. Adhesion would occur in a differential manner according to the mutual binding energies of the involved molecules or cells. For the same molecular reason, one can observe the spontaneous demixing of oil and water in the salad bowl. Despite of the obvious appeal of this simple argument, only few years later it was pointed out that cell sorting might not be fully explained by differential adhesion [96]. The main arguments were that cells are active, i.e. thermodynamically open systems and not passive molecules. Also, the cells might engage in non-local interactions extending far beyond the molecular range. Finally, there are highly localized adhesion zones like desmosomes, which would seem to contradict the necessity for maximizing the contact area [96]. The subsequent fruitful debate on the intricacies of cell sorting lead to the suggestion of various sorting mechanisms and is still in progress.

Approaching the problem with modern experimental techniques gave rise to the conclusion that differential adhesion would not suffice to explain cell sorting [130]. These measurements were performed by means of atomic force microscopy, and involved the selective knock-down of cadherin and myosin. Apparently, the by now well appreciated cortical tension arising from acto-myosin needs to be accounted for to explain the observed cell sorting behavior [130]. As usual in science, this study lead to puzzling new questions. In particular, it could not be explained why the ectoderm cells would sort to the interior of aggregates *in-vitro* [91]. It is therefore worthwhile to further inquire the problem in fully controlled *in-silico* environments.

2. Modifications of model forces and their interpretation: Within the tissue model presented in this thesis, there are several possible hooks to influence specific characteristics of individual cells. Here, we consider three behavior parameters that affect the tissue-scale dynamics by allowing for differential cell properties in the force balances.

Based on the classical idea that cell sorting arises from differential cell-cell adhesion, and according to the arguments from section 1.7, we assign

to each model cell i its cadherin expression level c_i. This dimensionless number affects the interaction force from equation (5.27), and represents the amount of expressed cadherin receptors on the cell membrane. Recall that the cellular interaction force derives from the stress exerted by cytoskeletal filament bundles meeting on the contact surface Γ_{ij} with the mutual pairing density ρ. Generalizing the purely filament-driven interaction, we include also the cadherin expression level,

$$\mathbf{F}_{ij}^{\mathrm{int}} = R_{ij} \int_{\Gamma_{ij}} \mathrm{d}\theta \; c_{ij} \, \rho(\theta) \cdot \mathbf{f}_{ij}(\theta) \tag{5.41}$$

where the adhesion density $c_{ij} = \sqrt{c_i \cdot c_j}$ results from the joint cooperation of the cell pair $i \sim j$. In this way, the intracellular stresses are coupled to trans-cellular adhesion sites.

In order to additionally incorporate differential adhesion towards the extracellular matrix, we include the cellular integrin expression level b_i in the locomotion forces from equation (5.30), again as dimensionless number. As before, locomotion occurs at the free margin arcs Γ_{i0} forming the exterior tissue boundary,

$$\mathbf{F}_{i}^{\mathrm{loc}} = f_{\mathrm{loc}} \int_{\Gamma_{i0}} \mathrm{d}s_i \; b_i \rho_{i0} \hat{\mathbf{R}}_{i0}(\phi_i), \tag{5.42}$$

There, the joint action of lamella-like structures and the cell's capability to engage in integrin adhesions would create a net pulling force directed outwards. Higher values of b_i will therefore bias the cellular positioning towards the free margin of the tissue with fewer surrounding neighbors.

Another factor that might influence the cellular sorting behavior is their sensitivity to external cues. In this model, no such cues are considered explicitly. However, stochastic perturbations provide for a related function in that they directly inject fluctuations in the force-generating migration machinery. A possible interpretation for a strong fluctuation is that the cell would receive a dedicated though unspecified migratory signal. In the stochastic force from equation (5.31), the fluctuations arise from the free cell boundary Γ_{i0} exclusively. As an additional model refinement, we here also include stochastic forces originating from the cell-cell contact borders Γ_{ij},

$$\begin{aligned} \mathrm{d}\mathbf{F}_{i}^{\mathrm{st}} &= b_{\mathrm{st}} q_i \mathrm{d}\mathbf{W}_{t}^{(i)}, \\ \mathrm{d}\mathbf{W}_{t}^{(i)} &= \kappa_\Gamma \cdot \int_{\Gamma_{i0}} \mathrm{d}\mathbf{B}_{t,s_i} + (1-\kappa_\Gamma) \cdot \sum_{j:j\sim i} \int_{\Gamma_{ij}} \mathrm{d}\mathbf{B}_{t,s_{ij}} \end{aligned} \tag{5.43}$$

The overall strength of stochastic perturbation is regulated by the b_{st} parameter. Moreover, $\kappa_\Gamma \in [0,1]$ describes the relative importance of perturbation signals from free cell margin Γ_{i0} and the pair contacts Γ_{ij}. Finally, the per-cell sensitivity to external fluctuations in the environment is quantified by the dimensionless number q_i, which we shall call protrusiveness.

3. Sorting in two-dimensional Voronoi models: In the computer simulations presented in this section, the model tissue contains two distinct cell types with differential properties:

(i) blue cells strongly adhere to one another, $c_i^{\mathrm{blue}} = 3.0$, while exhibiting only weak locomotion at the tissue margin, $b_i^{\mathrm{blue}} = 0.2$,

(ii) green cells have a decreased ability for adhesion, $c_j^{\mathrm{green}} = 1.0$, and exert high locomotion forces at their free boundary, $b_j^{\mathrm{green}} = 2.0$.

Apart from the following non-differential parameters, there are no further modifications with respect to the values used in the preceding sections and table 5.1. In this section we employ

- $\Delta_{\mathrm{min}} = 0.02, \Delta_{\mathrm{crit}} = 0.4$, to achieve a broad repulsive region in the interaction force,
- $\alpha = 0.66$, so that there is a high degree of neighbor cooperativity in the vertical component of the interaction force,
- $\kappa_\Gamma = 0.45$, $q_i^{\mathrm{blue}} = q_j^{\mathrm{green}} = 1.0$, so that the stochastic perturbations are the same for both cell types.

The interaction ranges $\Delta_{\mathrm{min}}, \Delta_{\mathrm{crit}}$ facilitate the cellular rearrangements within the tissue, because then the slope of the resulting force at the equilibrium point $\mathbf{F}_{ij}^{\mathrm{int}} = 0$ becomes fairly flat, cf. figure 5.6. The locomotion strength was $f_{\mathrm{loc}} = 10$ pN. Moreover, according to the κ_Γ parameter, the majority of perturbations arises from the interior cell-cell contact borders. The simple assumption of uniform protrusivity q_i is justified because earlier trial simulations have revealed that there is no significant influence on the observed sorting behavior (data not shown).

Here we start each simulation with a tissue as depicted in figure 5.13 at $t = 0$, whereby the cell radii $r_i = 1.08 \ldots 1.78$ are fairly uniform. Already after two hours we observe that the blue and more adherent cells have gathered in the interior to form a characteristic strand throughout the

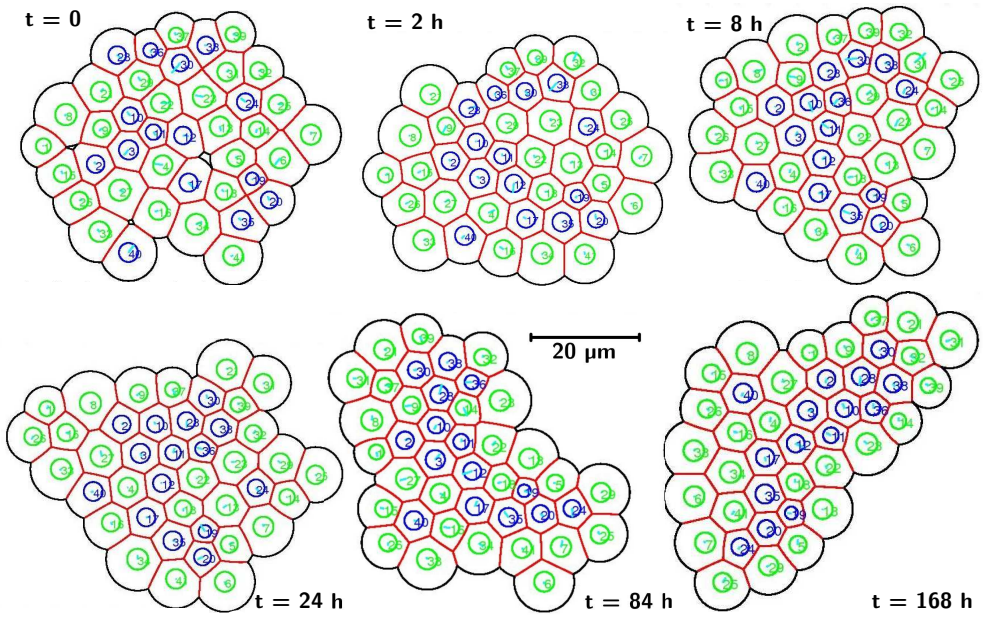

Figure 5.13.: Cell sorting and strand formation in two-dimensional aggregates. According to the expression level of cadherin and integrin proteins, the blue cells are strongly adherent, whereas the green cells do only weakly attach to one another. Additionally, the latter are capable of sustaining relatively high traction forces at the tissue margin, in contrast to the blue ones. As can be observed from the second panel $t = 2$ h, strands of blue cells quickly assemble in the tissue bulk. However, sorting remains incomplete, even after the model tissue has evolved for one week, $t = 168$ h. Remarkably, the central strand of the blue cells seems to determine the overall tissue shape.

tissue. After that, and during the typical time-scale of few days set by *in-vitro* experiments, no major changes arise. Sometimes, the blue cell strands locally break up, though the general structure is rather persistent. Inspecting the accompanying movie `mov_sort.avi`[16], one observes that the formation of new contacts between blue cells is hindered by intermediate and usually big green cells. Trying various combinations of differential c_i, b_i, q_i (data not shown) and changing the other model parameters within biologically reasonable bounds (not shown) did not result in quicker or more complete cell sorting. Differential protrusiveness $q_i^{\text{green}} > q_j^{\text{blue}}$ enhances the mobility of the green cells, but otherwise does not affect the aforementioned observation. In contrast, differential integrin expression $b_i^{\text{green}} > b_j^{\text{blue}}$ seems to facilitate sorting until strand formation, for given amounts of differential cadherin expression.

A similar phenomenon was already observed in the small aggregates from section 5.4. There, the steric interactions between individual cells have posed effective barriers against otherwise favorable rearrangements. For given amounts of stochastic perturbation, these barriers set a characteristic time-scale to the further topological relaxation of the tissue. Indeed, when continuing to evolve a model tissue for a very long simulation time of up to half a year, one can observe that the cells do sort out as expected. Thereby, the blue cells form a globular tissue core, and the green cells gather in an exterior ring (data not shown). Apparently, the employed cellular interaction model exhibits intermittent barriers between meta-stable tissue states that are unphysical in the sense that these barriers cannot be overcome in the expected time frame of at most two days.

In the spirit of Harris [96], we could consider differential cellular surface contraction or cortical tension. Unfortunately, such tensile forces would be situated within the cell-cell contacts of the model. For a valid implementation, we would need to impose the force balances at the vertices, and not at the cell centers as required by the Voronoi description. One might also be tempted to blame the discrepancy in sorting time on model parameter uncertainties. Indeed, since their estimation is rather crude and the underlying measured data exhibits quite some variation, we have to expect at least some error accumulation due to the employed parameter values. However, even taking into account these possible error sources, being off by two orders of magnitude does not appear to be reasonable.

[16] See `http://www.theobio.uni-bonn.de/people/mab/dsup`.

In the context of pattern formation, the observed strand formation nevertheless constitutes an interesting phenomenon, because the tissue shape appears to follow the central strand. Since the interior cells are highly adhesive, they gather the exterior green ones in their neighborhood, without breaking the central strand cohesion. For further details on pattern formation and several related mechanisms, see [144].

4. New theoretical and experimental insights: In vertex-based models, the sorting of cells can surprisingly be recapitulated in three – but not in two – spatial dimensions (G. Wayne Brodland, private communication; cf. also [111]). In particular, due to the additional freedom in the third dimension, after strand formation there still is the possibility of forming contacts with nearby cells of the same kind. One can understand this mechanism by thinking of two connected chain links of different kinds of cells. In this scenario, even though one cell of the blue kind would be surrounded by green cells from almost all sides, the freedom of the third dimension enables the blue cell to make new contacts with other adjacent blue ones. In contrast, in two dimensions the strands are quite stable objects, because new contacts to the other side of the strand cannot be made. More formally, the disentangling of the presorted cellular strands occurs through a Plateau-Rayleigh or dripping-faucet instability in three dimensions [111]. In two dimensions, such a breakup of the presorted chains naturally works against sorting.

This provides for a fundamental explanation why cell sorting takes so long when simulated in two dimensions. Moreover, the occurrence of the problem in both Voronoi and vertex tissue models seems to indicate that the specific nature of the involved forces is not critical. In fact, since center and vertex based geometries are dual to one another, so is the structure of their accessible model forces. This rises the question why cellular Potts type models are able to reproduce sorting even in two dimensions [90]. The reason lies in their dynamical properties. As in the original proposal by Steinberg [198], cellular Potts models are formulated in terms of surface energies, which do not directly give rise to force balances. Instead, tissue evolution is driven by the energy-centric and stochastic Monte-Carlo update rule, causing the cells to perpetually deform. The resulting fairly strong fluctuations enable the strands to quickly disentangle so that the additional effect of the Plateau-Rayleigh instability is not needed.

In a recent report, Steinberg and coworkers propose a theory that ex-

plains the apparent tissue surface tension from underlying cellular properties [145]. In their theory, they find that the ratio of cell-cell adhesion and intracellular cortical tension determines the overall surface tension of a group of specific tissue cells. Moreover, there occurs an intermediate transitional regime between sorting driven by cortical tension and sorting driven by cell-cell adhesion. Remarkably, several of these theoretical predictions could also be confirmed in accompanying experiments [145], and generally agree with aforementioned AFM measurements [130]. These results suggest a modified interpretation for "adhesion energy" or "surface contraction" as proposed in the pioneering works [96, 198]. Both could be understood in terms of the total group surface tension divided by the number of individual cells.

Even though the *in-silico* studies presented here were not conclusive, we gain several insights from our undertaking. First, modeling efforts of reduced dimensionality entail fundamental inherent limits. However, the full explanation of the slow sorting in two dimensions revealed detailed mechanistic predictions on the condensation kinetics of presorted cellular domains in three dimensions. Second, cell sorting can be influenced by the cellular adhesion, cortical tension and possibly other differential properties or combinations thereof. This points at a certain modularity and failure tolerance in the mechano-active cellular components or proteomics.

5.7. Convergent tissue extension is driven by anisotropic cell-cell interactions

1. The early development of Drosophila: The fruit fly *Drosophila malanogaster* plays a very special role in developmental biology. It was the first species at which certain events during morphogenesis could be traced back to the underlying genetic regulation circuitry [163], which was awarded the Nobel Price in Physiology or Medicine in 1995. After the initial fertilization of the egg, the first 12-13 division rounds occur in a synchronous manner, whereby all nuclei share one common *syncytium* or cytoplasm, see e.g. [121]. After the subsequent formation of separating cell membranes, the three dermal layers of endoderm, mesoderm and ectoderm form in so-called invagination processes, cf. [77,160]. When the ecto- and mesoderm have been formed, a particular movement pattern occurs at the ectoderm on the surface of the embryo. Thereby, the so-called germband converges in lateral direction, while it simultaneously expands

along the anterior-posterior body axis. The common understanding of this behavior relies on the collective action of the involved cells, which are said to intercalate, i.e. squeeze in between one another towards the anterior-posterior axis [77, section "Convergence and extension"]. The mechanisms that give rise to the observed intercalation, however, remain under debate.

For example, laser ablation experiments have revealed a certain anisotropy in the distribution of the cortical actin tension, which is sufficient to drive the elongation of the germband [183]. Estimating the cortical tension from the observed rupture velocities, one is lead to conclude that the bond tensions differ by a factor of approximately 2 [183, figure 6f'], depending on their direction with respect to the anterior-posterior body axis. On the other hand, precise monitoring of cellular elongation versus intercalation and tissue expansion lead to the suggestion that the observed ectodermal cell shape changes would be mostly a passive response to the invagination movement of the underlying mesoderm [40]. We therefore recapitulate the elongation movement in terms of the proposed Voronoi tissue model and see what we can learn from this paradigmatic biological model system.

2. Modifications to the individual cell locomotion forces: Inspired by the correlation features of single cell migration trajectories from section 3.9, we write a new expression as a substitute for the locomotion and stochastic forces from equations (5.42) and (5.43). In order to devise a sufficiently versatile structure, we first attribute to each cell i a certain polarity vector $\mathbf{p}_i = \mathbf{p}_i(t)$. This phenomenological and dimensionless quantity describes the instantaneous and in-plane polarization state of the cellular cytoskeleton, and is computed according to

$$\mathrm{d}\mathbf{p}_i = \frac{1}{T_{\mathrm{pol}}} \cdot \left(\frac{\mathbf{v}_i}{v_{\mathrm{pol}}} - \mathbf{p}_i \right) \cdot \mathrm{d}t - \delta_{\mathbf{p}} \widehat{\mathbf{p}}_i \cdot \mathrm{d}t + \alpha_{\mathbf{p}} q_i \mathrm{d}\mathbf{W}_t^{(i)}. \tag{5.44}$$

The first contribution to $\mathrm{d}\mathbf{p}_i$ represents a linear filter of first order, in full analogy to the previous velocity update rule (5.35). This filter causes the polarity vector $\mathbf{p}_i$ to adapt to the normalized cell migration velocity $\mathbf{v}_i / v_{\mathrm{pol}}$, with an effective time lag of T_{pol}, representing the average cellular reorientation time. From the cell speed autocorrelation plots from figure 3.10, we would expect the cellular reorientation time to be approximately 20 min. However, we here take the relatively low value $T_{\mathrm{pol}} \approx 10$ min in order to facilitate the cellular reorientation in highly dynamic embryonic

tissues. For a list of the employed model parameters see table A.9. The second term on the right-hand side of equation (5.44) implies that the polarity decreases by a constant amount in each time step, however only when $\mathbf{p}_i$ is still large enough. The parameter $\delta_{\mathbf{p}}$ indicates the rate of polarity degradation, and $\widehat{\mathbf{p}}_i$ the unit vector in direction of $\mathbf{p}_i$. Finally, the last summand in (5.44) provides for an autonomous build-up of polarity due to cellular guiding cues, which we however do not consider explicitly in the model. Instead, we write the stochastic terms $\mathbf{W}_t^{(i)}$ from equation (5.43), with the dimensionless protrusivity number q_i. The overall strength of the cellular perturbation is therefore regulated by the rate $\alpha_{\mathbf{p}}^2$, again see table A.9.

With the polarity vector $\mathbf{p}_i$ as defined above, the so-called polarity force

$$\mathbf{F}_i^{\mathrm{pol}} = f_{\mathrm{pol}} b_i \tilde{\rho}_i r_i \mathbf{p}_i \tag{5.45}$$

comprises a combined stochastic and locomotion force for each cell. Here, the force-generating polar filament density $\tilde{\rho}_i$ is a specific cell property, with the total number of filaments in a cell being $\tilde{\rho}_i \cdot r_i$. Finally, the dimensionless number b_i indicates the effective integrin expression level, and f_{pol} the strength of the polarity force.

If a single model cell is subjected to the polarity force (5.45) and the drag force (5.33) with a cellular friction coefficient

$$\gamma_i = \gamma_{\mathrm{drag}} b_i \mathcal{P}_{\mathrm{ex}} r_i^2 \pi, \tag{5.46}$$

one obtains the persistent migration trajectories as discussed earlier in section 3.9. Here, γ_{drag} is the characteristic friction force per cell area. In figure 5.14, we plot the resulting autocorrelation function of the migration speed of the model cell with polarity force. The overall features of the corresponding experimental red curve in figure 3.10 are quite similar. We therefore conclude that the polarity force $\mathbf{F}_i^{\mathrm{pol}}$ is capable of reproducing the most essential properties of isolated cellular migration trajectories. For the collective motion in tissues, we postulate that the cell's in-plane polarity $\mathbf{p}_i$ essentially carries over, albeit in a less insisting manner. In particular, the less prominent individualism effectively would result in decreased perturbation and force parameters $\alpha_{\mathbf{p}}, f_{\mathrm{pol}}$. For the specific values employed in both figure 5.14 and the simulations described below, see table A.9.

3. Anisotropic interaction force: It has been shown in experiments that during the elongation of the germband of Drosophila, the involved

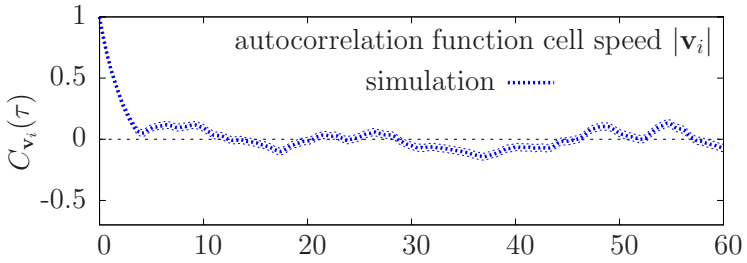

Figure 5.14.: Autocorrelation function of cell migration speed arising from the polarity force from equation (5.45). The underlying single-cell trajectories exhibit the piecewise persistent structure found in in section 3.9. Note that the 95 % confidence interval around the autocorrelation curve is only barely visible because of its relative smallness.

cells intercalate by exerting anisotropic tension throughout their actin cortex underneath the adhesion belt [183]. In a quantitative tissue model it would therefore be natural to assume that the tension within the cell-cell contact depends on its orientation. However, in contrast to vertex-based models, this cannot be directly implemented in center-based Voronoi models. Instead, we have to devise an interaction force that would encompass the in-tissue effect of anisotropic cellular cortex contractions. To this end we think of an idealized model cell being of rectangular box-like shape and filled with fluid. If we were to squeeze the cell box at its two opposite shorter faces, incompressibility of the interior fluid would cause the box to elongate in lateral direction perpendicular to the squeezing. Correspondingly, enhanced contractions at opposite cell-cell contacts would drive the directed elongation of a single cell in the tissue. Thus we can model the anisotropic cortical tension by designating a specific direction in which the cells prefer to arrange with enhanced mutual spacing.

Accordingly, the interaction force (5.27), and in particular its distance-dependent contribution (5.25), namely

$$f(\Delta_{ij}) = f_{\text{int}} \cdot \ln\Big(\frac{\Delta_{ij} - \Delta_{\text{min}}}{\Delta_{\text{crit}} - \Delta_{\text{min}}}\Big) \tag{5.47}$$

has to be modified in a cell-dependent fashion. The equilibrium distance of two adjacent cells $i \sim j$ is given by the parameter Δ_{crit}. Here we consider two distinct types of model cells: (i) the blue (and also the black) cells are under anisotropic cortical tension, and (ii) the green cells are

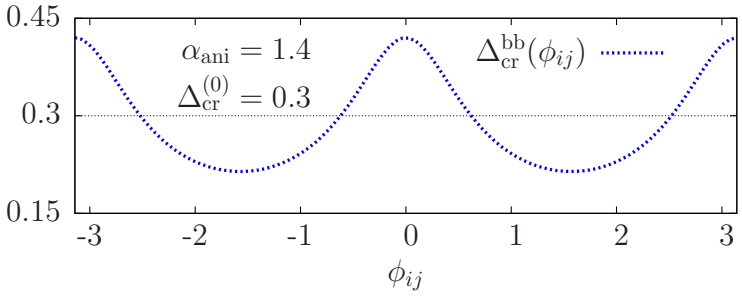

Figure 5.15.: The anisotropic cortical tension present in Drosophila cells during germband elongation cannot be directly implemented in center-based Voronoi tissue models. However, as a phenomenological substitute one can prescribe anisotropic equilibrium distances between neighbor cells. Here we plot this equilibrium distance $\Delta_{\text{crit}}^{\text{bb}}$ between two such cells. If the cell-center connection vector $\mathbf{x}_i - \mathbf{x}_j$ is parallel to the x-axis, then the neighbor bond angle $\phi_{ij} = \text{atan}(\mathbf{x}_i - \mathbf{x}_j) = -\pi, 0, \pi$, where $\Delta_{\text{crit}}^{\text{bb}}$ attains its maxima. Conversely, its minima are located at $\phi_{ij} = -\pi/2, \pi/2$, where $\mathbf{x}_i - \mathbf{x}_j$ is parallel to the y-axis.

under isotropic cortical tension. For the anisotropic ones, Δ_{crit} should be higher in x-direction than in y-direction. To account for the directionality, we introduce the angle $\phi_{ij} \equiv \text{atan}(\mathbf{x}_i - \mathbf{x}_j)$ indicating the direction of the connecting line between the cell centers $\mathbf{x}_i - \mathbf{x}_j$. We thus end up with three different constellations for the preferred cell-cell equilibrium distance,

$$\text{green–green:} \qquad \Delta_{\text{crit}}^{\text{gg}} = \Delta_{\text{crit}}^{(0)} \equiv 0.3, \tag{5.48}$$

$$\text{blue–blue:} \qquad \Delta_{\text{crit}}^{\text{bb}} = \frac{\Delta_{\text{crit}}^{(0)}}{\sqrt{\alpha_{\text{ani}}^2 (\cos\phi_{ij})^2 + (\sin\phi_{ij})^2/\alpha_{\text{ani}}^2}}, \tag{5.49}$$

$$\text{blue–green:} \qquad \Delta_{\text{crit}}^{\text{bg}} = \frac{1}{2}\big(\Delta_{\text{crit}}^{\text{bb}} + \Delta_{\text{crit}}^{\text{gg}}\big). \tag{5.50}$$

The expression for $\Delta_{\text{crit}}^{\text{bb}}$ involves the anisotropy parameter α_{ani}. Its effect is shown in figure 5.15, where we have chosen $\alpha_{\text{ani}} = 1.4$ in such a way that the maximum of $\Delta_{\text{crit}}^{\text{bb}}$ is approximately two times its minimum.

4. Additional cell-cell friction forces: When adjacent cells within an aggregate move with respect to one another, we certainly have to expect a certain response to the perceived mutual sliding. In principle, such a

response could arise from various underlying molecular interaction signals. Within the present model there are, however, only two relevant players, namely the cadherin cell-cell adhesion molecules and the F-actin cytoskeleton providing for intracellular adhesion anchoring. The most basic modeling expression involving the mutual cell sliding is proportional to the difference of cell velocities $\mathbf{v}_i - \mathbf{v}_j$,

$$\mathbf{F}_{ij}^{\mathrm{vis}} = \gamma_{ij}^{\mathrm{vis}}(\mathbf{v}_j - \mathbf{v}_i), \tag{5.51}$$

with respect to each of the topological neighbors $j \sim i$ from the Voronoi tessellation. The sign of the velocity difference $\mathbf{v}_j - \mathbf{v}_i$ is such that the velocity $\mathbf{v}_i$ of cell i tends to adjust to its surrounding spatial neighbor cells. Thus, if the cell i were passive in all other regards, due to $\mathbf{F}_{ij}^{\mathrm{vis}}$ it would still be partially dragged along by its neighbors. Here we assume that this velocity adaptation is driven by a force-induced cross-talk between the adjacent cells. Therefore, the effective pair-drag $\gamma_{ij}^{\mathrm{vis}}$ derives from the filament and adhesion densities along the contact border Γ_{ij},

$$\gamma_{ij}^{\mathrm{vis}} = \gamma_0^{\mathrm{vis}} \cdot R_{ij} \int_{\Gamma_{ij}} \mathrm{d}\theta \; \rho(\theta) c_{ij}, \tag{5.52}$$

see figure 4.2 for the contact radius R_{ij}. The model parameter γ_0^{vis} regulates the overall strength of the viscous cell-cell friction, see table A.9. The integral on the right-hand side of equation (5.52) corresponds to the one from the cellular interaction force (5.41). Specifically, we again integrate the product filament pairing density $\rho(\theta)$ and the cadherin adhesion density $c_{ij} = \sqrt{c_i \cdot c_j}$, cf. equations (5.20) and (5.41), respectively. At this stage one could raise the question how cell-cell adhesions might be robust while there is apparently a non-zero strain rate $\mathbf{v}_i - \mathbf{v}_j$ perpetually tearing on the underlying chemical bonds. However, if the formation and dissociation of these bonds were fast as compared to the related cellular migration processes, then the transient amount of adhesions would enter the cell-cell friction in a temporally averaged manner, which is fully compatible with the expression in (5.52). Indeed, this line of arguments is based on the very idea behind the whole-cell traction clutch from paragraph 3.5.1, or behind the fluidity of the cytoskeleton, cf. paragraph 1.7.2. Thus, the proposed pair-drag model is the minimal consistent extension of the assumptions made in the preceding cellular migration models.

5. Equations of motion and their numerical integration: First we define the active forces $\mathbf{F}_i$ acting on each cell i as the sum of polarity and

interaction forces,

$$\mathbf{F}_i = \mathbf{F}_i^{\text{pol}} + \sum_{j:j\sim i} \mathbf{F}_{ji}^{\text{int}}. \tag{5.53}$$

In principle, all these active forces should be balanced by the the friction forces in a whole-cell force equilibrium,

$$\mathbf{F}_i + \mathbf{F}_i^{\text{drag}} + \sum_{j:j\sim i} \mathbf{F}_{ij}^{\text{vis}} = 0. \tag{5.54}$$

This equation has to be solved for the cell velocity $\mathbf{v}_i \equiv (v_i^x, v_i^y)$. However, the sum in the last term involves also several of the neighbor velocities $\mathbf{v}_j$, which have to be computed simultaneously. Therefore, we gather all velocity components in one single combined vector $\mathbf{V}_{\text{tiss}} = (\ldots, v_i^x, v_i^y, \ldots, v_j^x, v_j^y, \ldots)$ and write the drag $\mathbf{F}_i^{\text{drag}}$ and friction forces $\mathbf{F}_{ij}^{\text{vis}}$ with the help of the large matrix

$$\mathbb{G}_{\text{tiss}} = (g_{ij}) \quad \text{with} \quad \begin{cases} g_{ij} = \gamma_i & \text{for } i = j, \\ g_{ij} = \gamma_{ij}^{\text{vis}} & \text{for } i \sim j, \\ g_{ij} = 0 & \text{otherwise,} \end{cases} \tag{5.55}$$

where γ_i and γ_{ij}^{vis} have been defined in equations (5.46) and (5.52), respectively. With the help of the force vector $\mathbf{F}_{\text{tiss}} = (\ldots, F_i^x, F_i^y, \ldots F_j^x, F_j^y, \ldots)$ built from the components $\mathbf{F}_i \equiv (F_i^x, F_i^y)$, we can embed the force equilibrium (5.54) in the linear system of equations

$$\mathbb{G}_{\text{tiss}} \cdot \mathbf{V}_{\text{tiss}} = \mathbf{F}_{\text{tiss}}. \tag{5.56}$$

This system of equations describes the force equilibria (5.54) of all tissue cells simultaneously. In each time-step we therefore invert[17] the global drag matrix $\mathbb{G}_{\text{tiss}}$ and apply its inverse to $\mathbf{F}_{\text{tiss}}$, which then yields the desired velocities.

6. Cellular anisotropy drives topological cell rearrangements: We start the tissue simulation from a cellular arrangement close to the first panel in figure 5.16, see supplementary material[18] for the precise constellation at $t = 0$. Subsequently, the model cells move according to

[17]Such a kind of matrix inversion can be conveniently implemented by the left-division operator of the open-source simulation software `GNU octave`, `http://www.octave.org`.

[18]The electronic supplementary material is available from `http://www.theobio.uni-bonn.de/people/mab/dsup`.

the equations (5.56) without anisotropy $\alpha_{\text{ani}} = 1.0$. The other parameters are given in table A.9. After the tissue has settled, we activate the anisotropy at the simulation time of $t = 8$ h. To this end we set $\alpha_{\text{ani}} = 1.4$, which models the cells' anisotropic cortical tension and prescribes direction-dependent equilibrium distances Δ_{crit} for the pair interaction force. Specifically, we have $\Delta^{\text{bb}}_{\text{crit}}|_{\text{horizontal}} \approx 2\Delta^{\text{bb}}_{\text{crit}}|_{\text{vertical}}$ for the interior blue and black cells, see figure 5.15. At $t = 24$ h, we then reset $\alpha_{\text{ani}} = 1.0$ and continue the simulation for another 24 h, especially to see whether the apparent tissue deformation is permanent.

In the accompanying movie `mov_elo.avi` we observe that the polarity force causes small but persistent motions throughout the model tissue. This inherent mobility of the cells facilitates the possibility for topological neighbor changes, even though the tissue as a whole is robust and remains connected. Indeed, already at $t = 1$ h the small cell 39 on the right margin of the tissue connects with cell 8. Moreover, the cell-cell friction force (5.52) also plays an important role in the overall tissue motion. If one reduces the cell-cell friction coefficient γ_0^{vis}, there seem to occur even less topological neighbor changes (data not shown). This can be conceptualized if one presumes that the rearrangements require the joint persistent motion of several adjacent cells.

In figure 5.16, we observe the development of the elongated tissue from its initially rather round appearance. In the panels at $t = 10$ h, $t = 15$ h and $t = 20$ h, whence the blue and black cells interact in the same anisotropic manner, we observe several cells of partially quadratic shape at the core of the tissue. This is a prominent signature for a topological neighbor change being in progress. For example, at $t = 10$ h, the big blue cells 6 & 37 are about to form a neighbor connection, cf. also the panel at $t = 15$ h. In order to form this specific connection, the two cells 6 & 37 have to squeeze the intermediate black cells 22 & 23[19] apart. The whole process of squeezing and reconnecting is one example of cell intercalation.

The effect of repeated intercalations on the whole tissue is quite dramatic. In the first panel of figure 5.16 at $t = 5$ h, the blue and black cells are ordered in clear horizontal stripes. At the late stages of the simulation, e.g. at $t = 30$h, the blue cells have intercalated the black ones and the interior tissue core has clearly extended in horizontal direction. Now the skeptic might point to the interaction anisotropy from equation (5.49), which states that the interior cells prefer to elongate. To clarify

[19]The black cell 28 is situated close to the green cells in the north-west corner of the central group of blue/black cells.

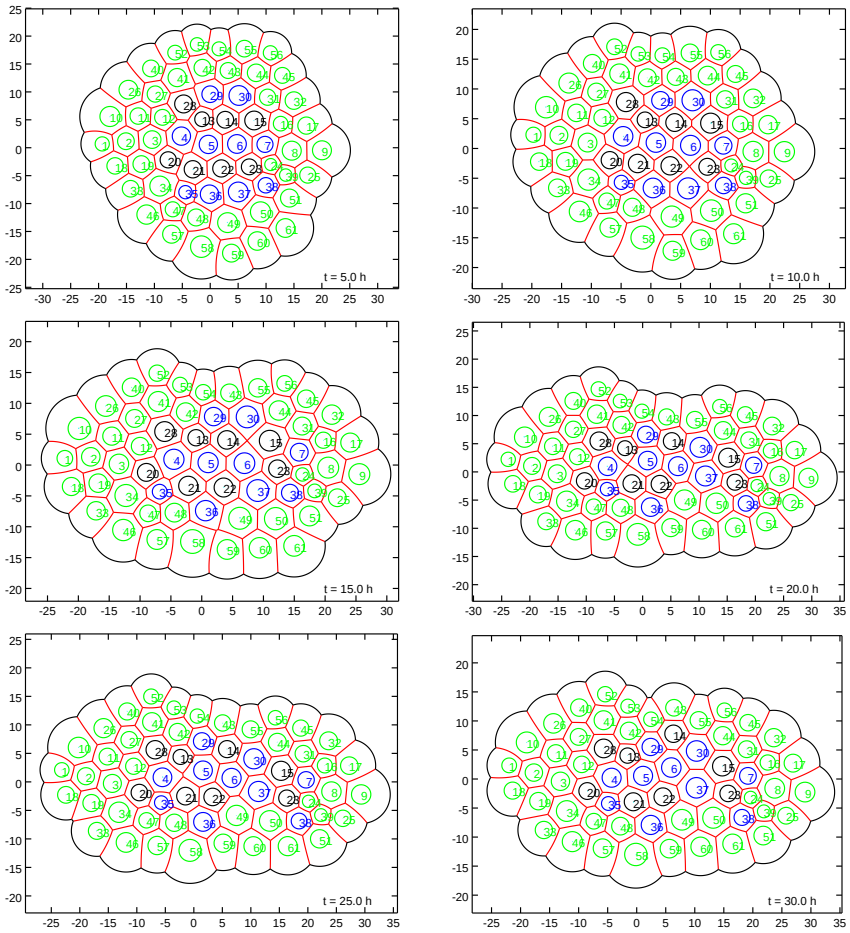

Figure 5.16.: Evolution of intercalating tissue cells driven by anisotropic cell-cell interaction forces. While the inner cells (blue, black) do not seem to elongate, the tissue as a whole performs a prominent stretch in horizontal direction. This is due to the topological rearrangement of the inner cells, which is driven by vertical pairs of cells squeezing in between two horizontal ones. This phenomenon is generally known as cell intercalation. The inner cells (blue, black) have anisotropic interaction forces to their neighbors for times $t = 8\,\mathrm{h} \ldots 20\,\mathrm{h}$, whereas the outer cells (green) have isotropic interaction forces for all times. Note that the unit length in the plots slightly varies in time.

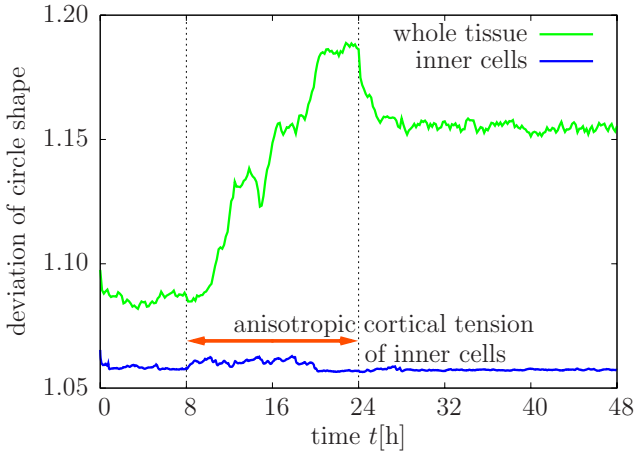

Figure 5.17.: Shape factor quantifying deviation of circularity for inner cells (blue line) and whole tissue (green line). The anisotropic equilibrium distance for the cell-cell interaction force was activated for times $t = 8\,\mathrm{h} \ldots 20\,\mathrm{h}$ (red arrow), and affected only the inner blue and black cells.

this question, we introduce the normalized perimeter-area ratio

$$P_A = \frac{\text{perimeter}}{2\sqrt{\text{area} \cdot \pi}} \geq 1, \tag{5.57}$$

as a measure to quantify shapes and in particular "elongatedness". Since the shape factor P_A is a purely geometric quantity, it is equally valid for the whole tissue or individual cells. It has the specific property of $P_A = 1$ for exactly circular shapes. Any deviation such as an elongation in a particular direction leads to increased P_A-values.[20]

Having established the shape measure P_A, we are able to decide whether the tissue elongation can be attributed to the anisotropic interactions of the inner blue and black cells. Plotting the time-course of their average P_A-value – see figure 5.17 – we find that they in fact remain quite spherical, even during the phase of anisotropic interaction forces. In contrast, the P_A-value of the whole tissue – including green, blue and black cells – increases much further, even in a relative sense. Indeed, in figure 5.16 we see that the tissue bulk elongates by almost 30% during the anisotropic interaction phase. Thus we conclude that the tissue elongation is mostly driven by the directed intercalation of the inner cells.

[20] P_A is also the reciprocal value of the "circularity" Ω defined in equation (5.36).

Within the Voronoi tissue simulations, the effect of elongation driven by intercalation is of remarkable robustness. In the examplary simulation from figure 5.16, only the inner cells could contribute to the directed intercalation. If one extends the anisotropic interaction to all cells in the tissue, it elongates even faster and further (data not shown). However, even few anisotropic cells at the core of the tissue seem suffice for a net elongation of the tissue. Moreover, after the anisotropy has ceased, the tissue remains in its elongated state, at least for another 24 h. The newly found topological cell arrangement apparently is favorable enough so to persist and withstand the ordinary in-tissue fluctuations. Clearly, such a robustness is helpful for ensuring the correct succession of embryogenetic events.

7. Cause, effect and biological redundancy: In this section, we have built our model on the assumption of an anisotropic cortical tension that would drive the cell intercalation and subsequent germband elongation in *Drosophila*. From the simulations we arrive at the conclusion, that a certain interaction anisotropy is sufficient to drive elongation, which matches the findings in [183]. Moreover, since the cortical tensions in the ectoderm apparently are anisotropic [183], it is natural – though not compellable – to assume that it is their purpose to drive the cell intercalation.

However, there might also be other mechanisms that contribute to the observed intercalation and/or elongation effect. With the help of the classical notion of strain[21] [29], the relative contributions of cell intercalation and deformation to elongation could be quantified [40]. In intercalation-defective mutants (so-called *Krüppel*), the cells initially compensate by means of enhanced cellular deformation, whereas in mutants without mesoderm (*twist*), the ectodermal germband elongation is reduced [40]. Based on these fascinating observations, the authors of [40] therefore suggest that the ectodermal shape changes would comprise a passive reponse to the mesoderm invagination.

If this is indeed the case, then the causation chain would point in the opposite direction. The invagination of the mesoderm constitutes a coordinated motion towards the anterior-posterior body axis. Since the ectoderm is situated on top of the mesoderm, the movement of the latter would deform the cells of the former, leading to intercalation and therefore elongation. What, then, causes the cortical tension in the ectoderm cells

[21] Another possible name would be deformation.

to be anisotropic? From the present data we cannot make any definite decision. Indeed, the ectoderm intercalation could be (partly) responsible for the mesoderm invagination as well. Without further measurements, one could speculate that for the sake of developmental robustness, both mesoderm and ectoderm would cooperate in mutually ensuring the processes of invagination and intercalation. In any case, this calls for a a better understanding of the interactions between mesoderm and ectoderm.

6. Mechanical and functional principles of cellular motion

1. Persistence and polarization: One important aspect of two-dimensional cellular migration trajectories is their persistence, as e.g. quantified in the experiments described in section 3.9. The key feature is that a migrating cell undergoes successive phases of polarization and depolarization, with relatively fast but also intermittently stalling locomotion. Such a persistence is advantageous because it comprises an optimized search strategy when signals are lacking or weak, see e.g. [67].

Apart from the migration speed, there are also morphological and molecular polarization markers, in particular the lamella outline shape or the localization of the actin polymerization front. In principle, however, there could be an asymmetry in the distribution of any molecule that is somehow involved in the migration machinery, including integrin and myosin. The directors introduced in section 3.9 provide for a quantitative description of these asymmetries, both for molecular distributions and cell shape characteristics.

If one considers the cell to be a dynamical system involving chemical reactions, force generating processes and mutual feedback, then one has to expect that persistence arises from the system's inherent time constants. By extracting persistence times from aforementioned directors, one obtains quantitative figures that directly describe the kinetics and transport dynamics of the underlying molecular pathways on the whole-cell level. Thus, directors provide for a prominent landmark to validate or falsify quantitative models of biological cells. Accordingly, the parameter space of the two-dimensional migration model could be restrained by reproducing several persistence features determined from experiments, cf. section 3.9. Similarly, one could employ the directors for quantifying genotypic or phenotypic characteristics.

2. Modularity and robustness: It has been argued in chapter 1, that the modular combination of relatively few mechanisms would cause diversity in cellular migration behavior. Such a modularity arises naturally when multi-functional units like biomolecules are integrated in a

compound system. In the context of cell migration, both extracellular integrin adhesions and intracellular F-actin network jointly cooperate to generate locomotion forces. Thereby, actin plays two apparently antagonistic roles, as it may enhance both assembly and disassembly of integrin adhesions by imposing a suitable tensile load, see paragraph 1.6.6. This Janus-faced behavior of actin is also implemented in the two single-cell migration models from chapter 3.

Functionally, this a mechanism is a very elegant solution for the cytoplasm to inhere its two fundamental dynamical modes, cf. figure 1.6 A & B. In the symmetric mode the forces balance around the cell periphery, whereby adhesion assembly and disassembly occur simultaneously in all directions. In contrast, in the asymmetric and migrating mode, adhesion assembly occurs mostly at the lamella front, whereas disassembly dominates at the cell rear, due to localized actin contractions inducing rupture. In both modes, however, the feedback of actin on integrin adhesions has the tendency to maintain the respective morphological organization.

Other modular cell properties are exhibited in sorting assays as discussed in section 5.6. Cellular sorting may be driven by differential cell-cell adhesion, surface contraction, or a combination thereof. Thus, various sorting patterns can be achieved by merely adjusting the cellular level of contraction and adhesion. At the same time, such a modularity gives rise to graceful failure recovery and robustness, which is particularly important during the early development of the embryo.

These two examples emphasize how functional diversity arises from few underlying modular constituents. This is one motivation for constructing synthetic models of biological systems, because the quantification of functional principles helps to identify common patterns and modular building blocks.

3. Scales and separation: At several instances in this work, the argument of scale-separation was invoked to neglect one particular model contribution over another. This principle is ubiquitous in physics, as it helps to design well-controllable assays or to simplify mathematical intricacies of a theory. For the proposed cell models, the basic argument was that the chemical reaction time-scale is much faster than the cellular migration time-scale, see e.g. paragraphs 1.6.2 & 3.5.1, and sections 2.2 & 2.5. Correspondingly, the cytoplasm was treated as a two-component, incompressible fluid mixture of filamentous F-actin and aqueous solvent, much like a dynamic, internally condensing sponge.

With the help of the same argument, the adhesions of a cell were considered to exhibit a certain slip, meaning that their bonds connect only transiently to the cytoskeleton and/or the substrate. It is important not to picture biological bonds as overly rigid entities. Indeed, the bond energy is typically only slightly above the thermal fluctuation energy, see e.g. [177].

Finally, in expressing the single cell migration models with the help of continuum equations, also a spatial scale separation argument has been invoked, see paragraph 2.5.2. Clearly, one cannot describe all the molecules comprising a cell in full detail. Instead, one averages over tiny boxes containing thousands of molecules, and subsequently deals with the emerging averaged densities.

4. Geometry and shape: There are two classics on the quantification and conceptualization of biological shape, written by D'Arcy Thompson [215] and Harry Blum [30]. Since large parts of this thesis deal with the geometric properties of cell aggregates, it is worthwhile to draw a connection from those seminal works to the proposed Voronoi tessellation.

The contact border between two adjacent model cells can be constructed in various ways, though it is desirable to employ a simple rule that would conform to the biological requirements. To this end, D'Arcy Thompson develops the soap-bubble principle, see figure 6.1 top panel. Adjacent soap bubbles have the property that any three contour lines meet at angles of 120 degrees. Each of the bubbles inherits a certain pressure, and the contour radii of curvature adapt accordingly. Comparing with circular Voronoi cells from section 4.4, it appears that the soap bubble centers are fairly close. Indeed, the distance between the Voronoi cell centers can be arbitrary, without being influenced by the body radii (fat lines in bottom right panel of figure 6.1). This additional freedom in the Voronoi pair is also the reason why its outer cell boundaries do not exhibit the 120 degree rule.

Harry Blum developed a whole geometry based on the primitives of point and growth. When a point grows for some time, it becomes a disc. Forming so-called ligatures from two discs, one obtains a pattern that is remarkably close to a pair of circular Voronoi cells, see figure 6.1 central panel, and compare e.g. figure 5.4 or the outer lines of the bottom right panel in 6.1. However, the drawback of the ligature principle is that the cell-cell contact is comprised of two straight line segments.

Surprisingly, the concept of growth is also useful for constructing a

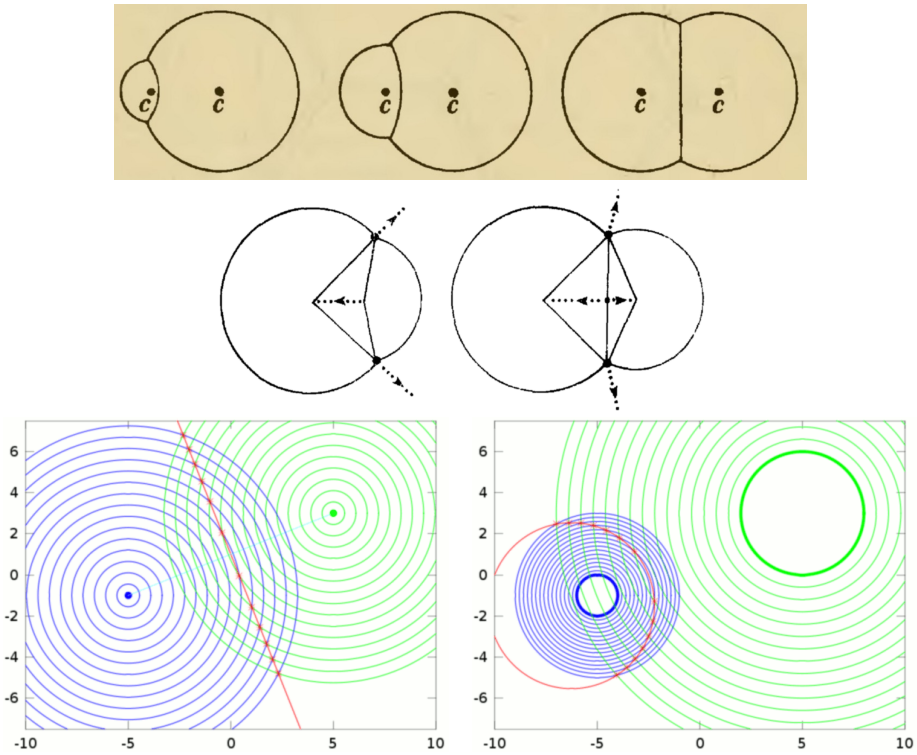

Figure 6.1.: Shape geometry concepts for a cell pair. In the top panel, there are three soap bubble "cell" pairs, whereby the centers are rather close and the angles at the marginal triple junction are 120 degrees each (reprinted from D'Arcy Thompson's book [215, figure 157]). In the central panel, the so-called ligature is built from two overlapping discs, where the interior triangles follow from so-called sym-axes (reprinted from Harry Blum's article [30, figure 32]). The two bottom panels show how the contact border between (red) two Voronoi cells emerges from the growth of the two adjacent generators (blue, green). Different rules for the speed of growth give rise to different contact borders. In the left bottom panel there appears a straight line contact, whereas in the right bottom panel a circular contact, cf. also figure 4.1.

Voronoi tessellation. Depending on the growth process of the two adjacent cells, several different contact shapes may arise. In the elliptical Voronoi tessellation developed in chapter 4, there appear ellipses, circles, hyperbolas, parabolas, and straight lines as possible contact shapes. Thus, most of the basic geometric items suggested in [30, page 279] can be naturally obtained from the proposed Voronoi tessellation.

5. Problems and ideas: Based on the results of this work, there several starting points for furthergoing research.

The regulation pathways affecting force-bearing players in various kinds of cells seem to share some similarities, possibly because important protein structure motifs being evolutionary conserved [168]. In any case, by quantitatively studying the functional aspect of force generation and transduction, regulative similarities could be exhibited in order to pinpoint modular pathway components. Molecular directors according to paragraph 3.9.5 provide for suitable whole-cell measures, which however require targeted fluorescence staining.

One specific pathway centers around the epidermal growth factor, which triggers the epithelial-mesenchymal transition (EMT) [214]. During EMT, cells leave the tissue bulk and subsequently migrate autonomously. From the modeler's view one expects a full continuum of cell states ranging from embedded epithelial to isolated and autonomous. Importantly, the EMT has been implicated in wound healing and cancer. Therefore, the force machinery of cells undergoing EMT should be studied, in particular with respect to cooperative motion patterns, see e.g. figure 1.5. A necessary ingredient to faithfully model EMT are polarized cells of anisotropic shape according to chapter 4.

During wound healing, embryo development and tumor expansion, cells divide while remaining in more or less dense contact. At some point, however, growth usually stops and the tissue enters the homeostatic state, whereby cell division is balanced by apoptosis [182]. This raises two questions. First, how is the transition to the homeostatic state initiated, and second, how does the transformation to a functional but otherwise passive homeostatic tissue take place. To represent the cellular deformations during cell cycle and mitosis, one again needs anisotropic model cells, see chapter 4.

The force generation mechanism of a single crawling cell has been investigated in section 3.7. The next step towards understanding tissue forces would therefore be to extend the single-cell system and include a

single neighbor cell. The full problem involves the cytoplasm dynamics of both adjacent cells, which can be written in terms of a dissipation functional $J[u, \partial u, p]$ of the F-actin velocity u and the pressure p, see chapter 2 and [5]. As an additional complication one has to consider the motion of the free boundary between the cells. This involves cell-cell adhesion, cortex tension and curvature, all of which has to be incorporated in a joint variational principle with the cytoplasm functional. The boundary conditions from section 3.4 would serve as guideline for the envisioned free boundary evolution.

A. Appendix

A.1. Estimating the characteristic dimensions of cytoplasm flow

At room temperature, the viscosity of the aqueous solvent phase is approximately that of water $\eta_\mathrm{w} \approx 10^{-3}\,\mathrm{Pa}\cdot\mathrm{s} = 10^{-3}\,\mathrm{pN}\cdot\mathrm{s}/\mu\mathrm{m}^2$. Typical physiological concentrations of dissolved proteins are expected to increase this value by a factor of approximately 1.5 [202, table I]. In contrast, the overall cell viscosity of neutrophils has been measured to be $\eta_\mathrm{cell} \sim 100\,\mathrm{Pa}\cdot\mathrm{s}$ in micropipette aspiration experiments [104]. Therefore we suspect the cytoskeleton to be mostly responsible for the observed whole-cell viscosity. Indeed, by comparing experiments on the ingression of neutrophils into micropipettes with corresponding simulation data, possible values of the actin network viscosity have been narrowed down to $\eta_\mathrm{f} \approx 300\ldots600\ \mathrm{Pa}\cdot\mathrm{s}$ [101]. In fact, these numbers are the extremal values with which qualitative and semi-quantitative features of the time-velocity ingression curve could be recovered. Altogether, we conclude that the viscosity in the aqueous solvent phase θ_w can be neglected over the viscosity in the actin network θ_g. In the light of $\eta_\mathrm{f}/\eta_\mathrm{w} \gtrsim 10^5$, this is a conservative assumption to make, because it still would hold if either of our estimated viscosities were off by two orders of magnitude.

In fish keratocytes, which are known to crawl very fast, the upper limit of the F-actin retrograde flow velocity is approximately $0.25\,\mu\mathrm{m/s}$ [78, 192, 229, 233]. In the same cell type, the transport velocity of G-actin embedded in the solvent has been determined indirectly, being up to $0.7\,\mu\mathrm{m/s}$ [123, page 1221 and figure 3e]. Unfortunately, experimental data on other cell types are not as widely available. However, these numbers still provide a reasonable estimate, because it is expected that the flow velocity in fast cells is fast as compared to cells crawling more slowly. Moreover, an upper bound to flow velocity will give us an upper-bound estimate for the Reynolds number, which we aim to put forward here.

Typical diameters of cells range from few to several tens of μm [2, chapter 22], whereby possible exceptions like neurons have a rather extreme architecture. Therefore, the characteristic length-scale is $1\,\mu\mathrm{m}$, because

streaming varies in the cells' interior. Finally, the overall mass density of single cells is fairly close to $1.1\,\mathrm{mg}/\mu\mathrm{l} = 1.1\,\mathrm{pg}/\mu\mathrm{m}^3$ [39, 93]. Taking all these numbers together, we obtain the Reynolds numbers

$$\text{F-actin network phase:} \qquad \mathrm{Re_g} \sim 10^{-12}, \tag{A.1}$$

$$\text{aqueous solvent phase:} \qquad \mathrm{Re_w} \sim 10^{-6}. \tag{A.2}$$

A.2. Polymerization pressure and viscosity for the one-dimensional model cell

The relations described in this appendix are all defined only on the boundary Γ of the model cell, i.e. $y = y_1, y_2$. In the boundary pressure balances (3.27, 3.28) there appears the polymerization pressure,

$$P_{\mathrm{poly}}\big(\theta, m_b, V\big) = P_{\mathrm{clamp}}(\theta) + P_{\mathrm{ratchet}}(\theta) - \eta_\Gamma\big(\theta, m_b\big)V. \tag{A.3}$$

1. Intermediate actin volume fractions: The dependence on θ involves several intermediate players. Let θ_B denote the fraction of membrane-bound filaments, with

$$2\theta_B(\theta) = \theta_A + \theta + \frac{K^2}{\theta} - \sqrt{\big(\theta_A - \theta\big)^2 + \frac{2(\theta_A+\theta)K^2}{\theta} + \frac{K^4}{\theta^2}}, \tag{A.4}$$

see [6, section 4.2.2]. Here, the model parameter $\theta_A = 0.0625$ denotes the effective volume fraction of available membrane proteins for actin binding. Their binding process is self-enhanced, e.g. due to clustering or cooperativity, whereby the effective dissociation constant $K = 0.198$ is also a model parameter. With θ_B from equation (A.4), the volume fraction of the remaining free filaments not bound to the membrane is therefore

$$\text{free filaments:} \qquad \theta_F(\theta) = \theta - \theta_B(\theta). \tag{A.5}$$

Filament branching involves only barbed or plus ends of the filaments, which are oriented roughly in direction of the cell membrane. Their volume fraction is modeled by the so-called Monod kinetics [20, section 4.3] in the free filaments θ_F,

$$\text{barbed} \equiv \text{'+' filament ends:} \qquad \theta_+(\theta) = \alpha_{\mathrm{Arp}} \cdot \frac{\theta_F(\theta)}{\theta_\beta + \theta_F(\theta)}. \tag{A.6}$$

Here, the prefactor $\alpha_{\mathrm{Arp}} = \alpha^0_{\mathrm{Arp}} \cdot [\mathrm{Arp2/3}]$ is proportional to the concentration of the Arp2/3 branching agent, and θ_β is the half saturation volume fraction as introduced in (3.18).

2. Clamp-motor and Brownian ratchet pressure: The polymerization pressure arising from the Brownian ratchet mechanism is assumed to be proportional to the volume fraction of the barbed ends,

$$P_{\text{ratchet}}(\theta) = \pi_{\text{ratchet}} \cdot \theta_+(\theta). \tag{A.7}$$

Moreover, the clamp-motor polymerization pressure is a linear function of the clamped actin filaments θ_c at the tip,

$$P_{\text{clamp}} = \pi_{\text{clamp}} \cdot \theta_c(\theta) \equiv \pi_{\text{clamp}} \cdot \frac{\theta_B(\theta)}{10}, \tag{A.8}$$

where it was assumed that one tenth of the bound filaments at the membrane are actually clamped within motors.

3. Viscous polymerization resistance: The viscosity resisting F-actin polymerization at the tip is a linear function in the bound myosin motors m_b and the fraction of membrane-bound filaments θ_B,

$$\eta_\Gamma = \big(\eta_0^\Gamma + \eta_m^\Gamma m_b\big)\theta_B(\theta), \tag{A.9}$$

where $\eta_0^\Gamma = 0.09\ \text{Pa} \cdot \text{min}/\mu\text{m}$, and $\eta_m^\Gamma = 4.05\ \text{Pa} \cdot \text{min}/(\mu\text{m} \cdot \mu\text{M})$.

A.3. Some formulae regarding the transformed contact matrix

1. The two-dimensional contact matrix determinant $\delta = \alpha\beta - \gamma^2$: In equation 4.44, the two-dimensional contact matrix determinant was defined as $\delta = \alpha\beta - \gamma^2$. Moreover, according to equations (4.39) and (4.40), we have

$$\begin{aligned}
\alpha &= \alpha_i - \alpha_j = \frac{c_i^2}{a_i^2} + \frac{s_i^2}{b_i^2} - \frac{c_j^2}{a_j^2} - \frac{s_j^2}{b_j^2}, \\
\beta &= \beta_i - \beta_j = \frac{s_i^2}{a_i^2} + \frac{c_i^2}{b_i^2} - \frac{s_j^2}{a_j^2} - \frac{c_j^2}{b_j^2}, \\
\gamma &= \gamma_i - \gamma_j = c_i s_i\Big(\frac{1}{a_i^2} - \frac{1}{b_i^2}\Big) - c_j s_j\Big(\frac{1}{a_j^2} - \frac{1}{b_j^2}\Big),
\end{aligned} \tag{A.10}$$

with the usual abbreviations $c_i \equiv \cos\varphi_i$ and $s_i \equiv \sin\varphi_i$ for all i. Inserting into δ, and factoring out products in a, b, one obtains

$$\begin{aligned}\delta = \frac{1}{a_i^2 b_i^2} + \frac{1}{a_j^2 b_j^2} - \Big(c_i c_j + s_i s_j\Big)^2 \Big(\frac{1}{a_i^2 b_j^2} + \frac{1}{a_j^2 b_i^2}\Big) \\ - \Big(c_i s_j - c_j s_i\Big)^2 \Big(\frac{1}{a_i^2 a_j^2} + \frac{1}{b_i^2 b_j^2}\Big),\end{aligned} \tag{A.11}$$

whereby the pure fourth-order terms drop out. For convenience, we may bring the factors a, b to the left-hand side. Finally, the trigonometric functions can be further simplified, and we end up with

$$\begin{aligned}a_i^2 b_i^2 a_j^2 b_j^2 \delta = \quad & \cos^2\big(\varphi_i - \varphi_j\big)\big(a_i^2 - a_j^2\big)\big(b_i^2 - b_j^2\big) \\ & + \sin^2\big(\varphi_i - \varphi_j\big)\big(a_i^2 - b_j^2\big)\big(b_i^2 - a_j^2\big).\end{aligned} \tag{A.12}$$

Inspecting the right-hand side, one can enumerate the cases when $\delta = 0$, since by assumption the generator ellipse semi-axes are positive, $a_i > 0 \wedge b_i > 0 \; \forall i$. All these possibilities for $\delta = 0$ are summarized in table A.1. The most prominent case of $\delta = 0$ is, when any three of the involved generator axes a_i, b_i, a_j, b_j are equal. Then, both summands in equation (A.12) vanish separately, independent of the angle difference $\Delta\varphi \equiv \varphi_i - \varphi_j$, cf. cases 11., 13., and 15. in the table. The other cases $\delta = 0$, namely 5., 7., 8., 10., and 14., involve a specific relation between the orientation of the two generators φ_i and φ_j. This also happens in case 2., $\delta \gtreqless 0$, where we expect a transition from elliptic ($\delta > 0$) to hyperbolic ($\delta < 0$) contact surfaces.

Indeed, setting $\delta = 0$ in equation (A.11), and employing $c_i c_j + s_i s_j = \cos\big(\varphi_i - \varphi_j\big)$, $c_i s_j - s_i c_j = \sin\big(\varphi_i - \varphi_j\big)$, we find

$$\cos^2\big(\varphi_i - \varphi_j\big) = \frac{\big(a_i^2 - b_j^2\big)\big(a_j^2 - b_i^2\big)}{\big(a_i^2 - b_i^2\big)\big(a_j^2 - b_j^2\big)}. \tag{A.13}$$

For this equation to have a valid solution $\Delta\varphi := \varphi_i - \varphi_j$, the right-hand side has to be $\in [0, 1]$. Suppose now $a_i > a_j > b_i > b_j$ as in case 2. of table A.1. Splitting the expressions $\big(a_i^2 - b_j^2\big)$ and $\big(a_j^2 - b_j^2\big)$ at $b_i^2 \in \big(b_j^2, a_j^2\big)$, one finds for the right-hand side in equation (A.13)

$$\begin{aligned}\text{numerator} &= \big(a_i^2 - b_i^2\big)\big(a_j^2 - b_i^2\big) + \big(b_i^2 - b_j^2\big)\big(a_j^2 - b_j^2\big), \\ \text{denominator} &= \big(a_i^2 - b_i^2\big)\big(a_j^2 - b_i^2\big) + \big(b_i^2 - b_j^2\big)\big(a_i^2 - b_j^2\big).\end{aligned} \tag{A.14}$$

Clearly, the ratio is < 1, since $a_i > a_j$. Moreover, we see from equation (A.13) that this ratio is > 0, since by assumption all brakets are positive.

#	Ellipse axis order	$\mathcal{C}, \mathcal{S}$	δ	Comment
1.	$a_i > b_i > a_j > b_j$	+,+	> 0	
2.	$a_i > a_j > b_i > b_j$	+,−	$\gtrless 0$	for specifics on $\delta = 0$ see text
3.	$a_i > a_j > b_j > b_i$	−,−	< 0	
4.	$a_i > b_i > a_j = b_j$	+,+	> 0	
5.	$a_i > b_i = a_j > b_j$	+,0	≥ 0	$\delta = 0$ iff $\varphi_i - \varphi_j = (2n+1)\pi/2$
6.	$a_i = b_i > a_j > b_j$	+,+	> 0	
7.	$a_i > a_j > b_i = b_j$	0,−	≤ 0	$\delta = 0$ iff $\varphi_i - \varphi_j = n\pi$
8.	$a_i = a_j > b_i > b_j$	0,−	≤ 0	$\delta = 0$ iff $\varphi_i - \varphi_j = n\pi$
9.	$a_i > a_j = b_j > b_i$	−,−	< 0	
10.	$a_i = a_j > b_j > b_i$	+,+	> 0	$\delta = 0$ iff $\varphi_i - \varphi_j = n\pi$
11.	$a_i > b_i = a_j = b_j$	0,0	$= 0$	
12.	$a_i = b_i > a_j = b_j$	+,+	> 0	
13.	$a_i = b_i = a_j > b_j$	0,0	$= 0$	
14.	$a_i = a_j > b_i = b_j$	0,−	≤ 0	$\delta = 0$ iff $\varphi_i - \varphi_j = n\pi$
15.	$a_i = a_j = b_j > b_i$	0,0	$= 0$	
16.	$a_i = b_i = a_j = b_j$	0,0	$= 0$	

Table A.1.: Possible constellations of generator ellipses and corresponding sign of the determinant $\delta = \alpha\beta - \gamma^2$. Here, $\mathcal{C} := \operatorname{sgn}\left(a_i^2 - a_j^2\right) \cdot \operatorname{sgn}\left(b_i^2 - b_j^2\right), \mathcal{S} := \operatorname{sgn}\left(a_i^2 - b_j^2\right) \cdot \operatorname{sgn}\left(b_i^2 - a_j^2\right)$, i.e. $\mathcal{C}$ indicates the sign of the coefficient at $\cos^2\left(\varphi_i - \varphi_j\right)$, whereas $\mathcal{S}$ the one at $\sin^2\left(\varphi_i - \varphi_j\right)$. Upon interchanging i, j in the "axis order" column, the behavior in the other columns remains valid. In principle, $\delta > 0$ will lead to elliptic contact surfaces, whereas $\delta < 0$ gives rise to hyperbolic ones. In the degenerate cases $\delta = 0$, several types of contact surfaces may occur, which are all discussed in section 4.8.

Therefore, $\forall a_i > a_j > b_i > b_j \; \exists \; \Delta\varphi : \delta = 0$. For the identity (A.13) to hold, there are four distinct $\Delta\varphi \in \big[-\pi, \pi\big)$. These four angle differences divide the unit circle into four regions, where the contact surface alternates from elliptic to hyperbolic in a checked pattern. Specifically, we have

$$\cos^2\big(\varphi_i - \varphi_j\big) \gtreqless \frac{\big(a_i^2 - b_j^2\big)\big(a_j^2 - b_i^2\big)}{\big(a_i^2 - b_i^2\big)\big(a_j^2 - b_j^2\big)} \quad \leftrightsquigarrow \quad \begin{cases} \text{ellipse}, \\ \text{degenerate}, \\ \text{hyperbola}, \end{cases} \tag{A.15}$$

for $a_i > a_j > b_i > b_j$ and $a_j > a_i > b_j > b_i$. Notably, this relation holds also for the second case, i.e. when $a_j > a_i$. The only difference in the derivation of the result is, that the aforementioned interval splitting has to be performed at b_j.

2. Other sub-determinants of the contact matrix: Apart from δ discussed in the previous section, the contact matrix $\mathbb{E}$ has two other sub-determinants,

$$\delta^{(\kappa)} := \alpha\omega - \kappa^2, \qquad \delta^{(\lambda)} := \beta\omega - \lambda^2, \tag{A.16}$$

where α, β are defined as in the equations A.10. Moreover, by equations (4.39) and (4.40), the translation coefficients κ, λ and the scaling factor ω depend on the positions $\big(x_i, y_i\big), \big(x_j, y_j\big)$ of the generators,

$$\begin{aligned} \kappa &= -\alpha_i x_i - \gamma_i y_i + \alpha_j x_j + \gamma_j y_j, \\ \lambda &= -\gamma_i x_i - \beta_i y_i + \gamma_j x_j + \beta_j y_j, \\ \omega &= \alpha_i x_i^2 + 2\gamma_i x_i y_i + \beta_i y_i^2 - \alpha_j x_j^2 - 2\gamma_j x_j y_j - \beta_j y_j^2, \end{aligned} \tag{A.17}$$

with γ defined in A.10. Inserting these relations into (A.16) and factoring out $x_i - x_j$, $y_i - y_j$, one finds the two identities

$$\begin{aligned} -\delta^{(\kappa)} &= \alpha_i\alpha_j\big(x_i - x_j\big)^2 + 2\big(\alpha_j\gamma_i y_i - \alpha_i\gamma_j y_j\big)\big(x_i - x_j\big) \\ &\qquad + \big(\gamma_i y_i - \gamma_j y_j\big)^2 - \big[\alpha_i - \alpha_j\big]\big(\beta_i y_i^2 - \beta_j y_j^2\big) \\ -\delta^{(\lambda)} &= \beta_i\beta_j\big(y_i - y_j\big)^2 + 2\big(\beta_j\gamma_i x_i - \beta_i\gamma_j x_j\big)\big(y_i - y_j\big) \\ &\qquad + \big(\gamma_i x_i - \gamma_j x_j\big)^2 - \big[\beta_i - \beta_j\big]\big(\alpha_i x_i^2 - \alpha_j x_j^2\big). \end{aligned} \tag{A.18}$$

Under the premises of the special cases 2b and 2c from section 4.7, the two rightmost terms in both preceding equations (A.18) can be treated

jointly,

$$\begin{aligned} &\text{2b, } \beta=\gamma=\lambda=0: \quad 2()() - []() = \gamma_i\big(\alpha_i+\alpha_j\big)\big(x_i-x_j\big)\big(y_i-y_j\big), \\ &\text{2c, } \alpha=\gamma=\kappa=0: \quad 2()() - []() = \gamma_i\big(\beta_i+\beta_j\big)\big(x_i-x_j\big)\big(y_i-y_j\big). \end{aligned} \tag{A.19}$$

In this way, both $-\delta^{(\kappa)}$ and $-\delta^{(\lambda)}$ are ≥ 0 when $\gamma_i = \gamma_j = 0$, since $\forall i : \alpha_i, \beta_i > 0$ by construction, see equation (4.39).

Let us now turn to the more general case $\gamma_i = \gamma_j \neq 0$. To this end, we first compute the two-dimensional determinant of the generator matrix $\mathbb{E}_i$ from equation (4.39),

$$\delta_i := \alpha_i\beta_i - \gamma_i^2 = \frac{1}{a_i^2 b_i^2} > 0. \tag{A.20}$$

With the help of these short-hand notations, (A.19) can be rewritten to

$$\begin{aligned} &\text{2b, } \beta=\gamma=\lambda=0: \quad -\delta^{(\kappa)} = \frac{2\delta_i\delta_j}{\gamma_i^2+\gamma_j^2}\big(y_i-y_j\big)^2 \geq 0, \\ &\text{2c, } \alpha=\gamma=\kappa=0: \quad -\delta^{(\lambda)} = \frac{2\delta_i\delta_j}{\gamma_i^2+\gamma_j^2}\big(x_i-x_j\big)^2 \geq 0, \end{aligned} \tag{A.21}$$

which holds for $\gamma_i = \gamma_j \neq 0$ (otherwise see above).

3. The third Eigenvalue ω' of the transformed contact matrix: According to equation (4.59), we have

$$\delta\omega' = \delta\omega - \alpha\lambda^2 + 2\gamma\kappa\lambda - \beta\kappa^2. \tag{A.22}$$

Again, α, β, γ are δ are as in equations A.10. Now we separately compute the four summands of $\delta\omega'$ on the right-hand side of equation (A.22), and factor out powers and products of x, y. Once we have all these terms, we gather them in ten groups, namely the pure ones $x_i^2, x_j^2, x_ix_j; y_i^2, y_j^2, y_iy_j$ and the mixed ones $x_iy_i, x_jy_j, x_iy_j, x_jy_i$. As turns out, the latter have one single prefactor in common. Similarly, the former split into two subgroups x and y. In this way, differences in x, y separate and we obtain

$$\begin{aligned} \delta\omega' = \quad & \big(\alpha_i\delta_j - \alpha_j\delta_i\big)\big(x_i-x_j\big)^2 + \big(\beta_i\delta_j - \beta_j\delta_i\big)\big(y_i-y_j\big)^2 \\ & + 2\,\big(\gamma_i\delta_j - \gamma_j\delta_i\big)\big(x_i-x_j\big)\big(y_i-y_j\big) \end{aligned} \tag{A.23}$$

Even though of similar form, the coefficients cannot be molded together,

$$\begin{aligned}
\alpha_i\delta_j - \alpha_j\delta_i =& \frac{b_i^2c_i^2 + a_i^2s_i^2 - b_j^2c_j^2 - a_j^2s_j^2}{a_i^2b_i^2a_j^2b_j^2},\\
\beta_i\delta_j - \beta_j\delta_i =& \frac{b_i^2s_i^2 + a_i^2c_i^2 - b_j^2s_j^2 - a_j^2c_j^2}{a_i^2b_i^2a_j^2b_j^2},\\
\gamma_i\delta_j - \gamma_j\delta_i =& \frac{c_is_i(b_i^2 - a_i^2) - c_js_j(b_j^2 - a_j^2)}{a_i^2b_i^2a_j^2b_j^2},
\end{aligned} \tag{A.24}$$

because this would break the difference structure of the x, y factors. However, with the help of equations (A.24) we can construct an alternate representation,

$$\begin{aligned}
&a_i^2a_j^2b_i^2b_j^2\delta\omega' = \\
&\quad a_i^2\Big(-s_i\big[x_i - x_j\big] + c_i\big[y_i - y_j\big]\Big)^2 - a_j^2\Big(-s_j\big[x_i - x_j\big] + c_j\big[y_i - y_j\big]\Big)^2\\
&+ b_i^2\Big(\quad c_i\big[x_i - x_j\big] + s_i\big[y_i - y_j\big]\Big)^2 - b_j^2\Big(\quad c_j\big[x_i - x_j\big] + s_j\big[y_i - y_j\big]\Big)^2,
\end{aligned} \tag{A.25}$$

again separating the i and j terms.

A.4. Polar representation of anisotropic Voronoi generators

Consider a two-dimensional Voronoi generator according to definition 4.1.1 with the elliptic norm

$$\|\mathbf{x}\|_i = \sqrt{\frac{x^2}{a_i^2} + \frac{y^2}{b_i^2}}, \tag{A.26}$$

where $\mathbf{x} \equiv (x, y)$. For convenience, we have written $\|\mathbf{x}\|_i$ in its diagonal coordinate system, in which the generator center $\mathbf{x}_i$ coincides with the origin, and the longer semi-axis a_i of the generator ellipse aligns with the positive x-axis. As we have shown in corollary 4.1.7 and proposition 4.3.3, the elliptic norm generator from equation (A.26) has an equivalent representation in terms of homogeneous matrices as in definition 4.3.2.

The ellipse graph of the norm generator (A.26) is given by the identity

$$\|\mathbf{x}\|_i = 1. \tag{A.27}$$

Next, we scale the norm $\|\mathbf{x}\|_i =: z$ with the function $\mathcal{P}(z) = qz^\nu + \mathcal{P}_0$ from equation (4.8), whereby we employ the simplest possible coefficients $q = 1, \nu = 1, \mathcal{P}_0 = 0$. In this way we obtain a generalized Voronoi generator according to definition 4.1.8,

$$\mathcal{P}_i(\mathbf{x}) = \sqrt{\frac{x^2}{a_i^2} + \frac{y^2}{b_i^2}}, \tag{A.28}$$

where we have employed the abbreviation (4.12), namely $\mathcal{P}_i(\mathbf{x}) \equiv \mathcal{P}\big(\|\mathbf{x}\|_i\big)$. Next, we express $\mathbf{x}$ in polar coordinates,

$$x := R_\mathbf{x} \cos\varphi^i_\mathbf{x}, \qquad y := R_\mathbf{x} \sin\varphi^i_\mathbf{x}, \tag{A.29}$$

where the superscript i indicates that the polar angle $\varphi^i_\mathbf{x}$ for the point $\mathbf{x}$ has its apex at the generator center $\mathbf{x}_i$. Inserting the polar form of $\mathbf{x}$ into equation (A.28), we find that the scaled norm $\mathcal{P}_i$ is a product of two factors,

$$\mathcal{P}_i\big(R_\mathbf{x}, \varphi^i_\mathbf{x}\big) = R\left[\frac{\cos^2(\varphi^i_\mathbf{x})}{a_i^2} + \frac{\sin^2(\varphi^i_\mathbf{x})}{b_i^2}\right]^{1/2} \tag{A.30}$$

whereby the first factor involves only the $R_\mathbf{x}$- and the second only the $\varphi^i_\mathbf{x}$-coordinate of $\mathbf{x}$. The latter factor in square brackets constitutes the polar representation of equation (A.27) for the ellipse graph underlying the present generator. Indeed, by transforming the (A.27) with the scaling function $\mathcal{P}$, and making the polar ansatz $x = r_i \cos\varphi^i, y = r_i \sin\varphi^i$, we arrive at

$$\frac{1}{r_i(\varphi^i)} = \left[\frac{\cos^2(\varphi^i)}{a_i^2} + \frac{\sin^2(\varphi^i)}{b_i^2}\right]^{1/2}. \tag{A.31}$$

Identifying $\varphi^i \equiv \varphi^i_\mathbf{x}$, the polar generalized Voronoi generator from equation (A.30) becomes a ratio of radii. Moreover, the radius $R_\mathbf{x}$ of the point $\mathbf{x}$ can be written as Euclidean norm $\|\mathbf{x}\|$, which follows from the polar ansatz in equation (A.29). In more general coordinates, where $\mathbf{x}_i \neq 0$, this norm becomes $\|\mathbf{x} - \mathbf{x}_i\|$. Altogether we have found

$$\mathcal{P}_i(\mathbf{x}) = \frac{\|\mathbf{x} - \mathbf{x}_i\|}{r_i(\varphi^i_\mathbf{x})}, \tag{A.32}$$

where the $\mathbf{x}$ dependence in the radius r_i is implicitly encoded in the polar angle $\varphi^i_\mathbf{x}$ of the point $\mathbf{x}$ with respect to the generator center $\mathbf{x}_i$. Thus, the point power $\mathcal{P}_i(\mathbf{x})$ of the elliptic Voronoi generator $\mathcal{P}_i$ represents the Euclidean distance $\|\mathbf{x} - \mathbf{x}_i\|$ being directionally weighted by the angle-dependent ellipse radius $r_i(\varphi^i_\mathbf{x})$.

A.5. Contact surface parameterizations in polar coordinates

This appendix builds on the results in sections 4.6 and 4.7, where the shape of the contact border is investigated for several distinct cases, namely 0ab (ellipse, hyperbola), 1 (circle), 2a (single straight line) and 2b–d (parabola or two parallel straight lines).

Ellipse, hyperbola, circle, cases 0ab & 1: The graph of an ellipse centered at the coordinate origin and with semi-axes $a \geq b$ aligned on the x– and y–axis, respectively, is described by the quadratic form

$$\frac{x^2}{a^2} + \frac{y^2}{b^2} = 1. \tag{A.33}$$

Inserting $x := R(\theta)\cos\theta, y := R(\theta)\sin\theta$ and eliminating the sin-function yields

$$R^2(\theta) = \frac{b^2}{1 - \varepsilon^2 \cos^2\theta}, \tag{A.34}$$

where $\varepsilon^2 := 1 - b^2/a^2 < 1$ denotes the excentricity.[1] On the other hand, the contact equation (4.37) in its diagonal form (4.59) reads

$$\alpha' x^2 + \beta' y^2 + \omega' = 0 \tag{A.35}$$

Comparing the identity (A.34) with the corresponding expression derived from (A.35), we find

$$a^2 = -\frac{\omega'}{\alpha'}, \qquad b^2 = -\frac{\omega'}{\beta'}, \qquad \varepsilon^2 = 1 - \frac{\alpha'}{\beta'}. \tag{A.36}$$

Center $\mathbf{x}_0 = (x_0, y_0)$ and orientation ϕ of this contact ellipse were already determined during contact matrix diagonalization, cf. equations (4.45, 4.58), where ϕ is unique since both $\cos\phi$ and $\sin\phi$ are known. Altogether, we obtain an explicit parameterization of the contact border,

$$\begin{aligned} x = x_0 + R(\theta)\cos\theta, \qquad & y = y_0 + R(\theta)\sin\theta, \\ R^2(\theta) = -\frac{\omega'}{\beta' - (\beta' - \alpha')\cos^2(\theta - \phi)}. & \end{aligned} \tag{A.37}$$

[1] Note that the coordinate origin coincides with the center of the ellipse. This representation is different from the commonly used description centered at one focus of the ellipse, where we have $R = a(1 - \varepsilon^2)/(1 + \varepsilon\cos\tilde{\theta})$.

with $\theta \in [-\pi, \pi)$. Below we argue that this parameterization is general and holds for elliptic, circular and hyperbolic contact shapes.

If the right-hand side of the R-equation were positive for all θ, then the graph $\{x(\theta), y(\theta)\}$ would describe an ellipse. Recall the uniqueness conditions (4.56), namely $\alpha' \leq \beta' \wedge \phi \in [-\pi/2, \pi/2)$. Thus, the following three coefficient constellations may arise:

(i) $\alpha' < \beta' < 0$,

(ii) $\alpha' < 0 < \beta'$,

(iii) $0 < \alpha' < \beta'$.

Inspecting the diagonal contact equation (A.35), it becomes apparent that only (i) and (iii) are suitable for the contact surface to be elliptic. The sign of the homogeneous scaling coefficient ω' then has to behave accordingly[2], i.e. $\omega' > 0$ for (i) and $\omega' < 0$ for (iii). If $\omega' = 0$, then the determinant $\delta = 0$, and the contact is a degenerate one (see below). In case of (ii), the graph $\{x, y\}$ arising from the implicit equation A.35 will be a hyperbola regardless of the sign of ω', because then $\operatorname{sgn}\alpha' \neq \operatorname{sgn}\beta'$. Since we did not use any specific properties of the coefficients α', β', ω' in deriving the parameterization (A.37), it can also be employed to explicitly describe the graph of a hyperbola. Importantly, only those θ need to be considered where the imaginary part of $R(\theta)$ vanishes. There are four angles θ where R becomes infinite, which coincide with the two asymptotes of the hyperbola. In summary, all non-degenerate contact borders are covered by aforementioned parameterization.

Parabola, cases 2b–d: For degenerate contact borders of parabola shape, the contact equation (4.37) has the from

$$2\mathrm{bd}, \lambda' \neq 0: \quad y' = -\frac{\alpha'}{2\lambda'} x' \Big(x' + \frac{2\kappa'}{\alpha'} \Big) - \frac{\omega'}{2\lambda'}, \tag{A.38}$$

$$2\mathrm{cd}, \kappa' \neq 0: \quad x' = -\frac{\beta'}{2\kappa'} y' \Big(y' + \frac{2\lambda'}{\beta'} \Big) - \frac{\omega'}{2\kappa'}, \tag{A.39}$$

cf. equations (4.71, 4.74). In the pure cases 2b & 2c, the variables do not involve any transformation, $x \equiv x', y \equiv y', \alpha' \equiv \alpha, \beta' \equiv \beta, \ldots$. In

[2]Currently, it is not clear whether this follows from the assumed premises $\delta > 0 \wedge r^2 > 0 \wedge \operatorname{sgn}\alpha' = \operatorname{sgn}\beta'$. Therefore this should be explicitely checked in a numerical implementation.

contrast, in the case 2d, the contact matrix has been rotated, see relations (4.76), which is indicated by the primes. In order to arrive at the simplest representation for $R(\theta)$, we first choose the coordinate center,

$$2\text{bd}, \lambda' \neq 0: \quad \mathbf{x}_0 = \Big(-\frac{\kappa'}{\alpha'}, \frac{\kappa'^2 - \alpha'\omega'}{2\alpha'\lambda'} - \frac{\lambda'}{2\alpha'}\Big), \tag{A.40}$$

$$2\text{cd}, \kappa' \neq 0: \quad \mathbf{x}_0 = \Big(\frac{\lambda'^2 - \beta'\omega'}{2\beta'\kappa'} - \frac{\kappa'}{2\beta'}, -\frac{\lambda'}{\beta'}\Big). \tag{A.41}$$

Rewriting equations (A.38, A.39) in the coordinates $(x'', y'') \equiv \mathbf{x}'' := \mathbf{x}' - \mathbf{x}_0$, and inserting $x'' := R(\theta)\cos\theta, y'' := R(\theta)\sin(\theta)$, one finds that the discriminant of the quadratic equation in R vanishes. Note that here the contact matrix coefficients $\alpha', \beta', \ldots$ are not changed by this translation. Thus we obtain the following expressions for the polar radius

$$2\text{bd}, \lambda' \neq 0: \qquad R(\theta) = \frac{\lambda'}{\alpha'} \cdot \frac{-\sin\theta \pm 1}{\cos^2\theta}, \tag{A.42}$$

$$2\text{cd}, \kappa' \neq 0: \qquad R(\theta) = \frac{\kappa'}{\beta'} \cdot \frac{-\cos\theta \pm 1}{\sin^2\theta}. \tag{A.43}$$

In particular, $\theta \in [-\pi, \pi)$, and both signs describe the same graph. Conventionally, however, one requires $R > 0$ which rules out one of the signs in the numerator, depending on the sign of the respective prefactor λ'/α' or κ'/β'. The polar contact border parameterization therefore is

$$x' = x_0 + R(\theta)\cos\theta, \qquad y' = y_0 + R(\theta)\sin\theta, \tag{A.44}$$

for the cases 2bc. In the case 2d, the described set of points has to be rotated by the angle $-\phi$ as indicated in (4.58). Finally, there is one angle θ_0 where R becomes infinite. This angle indicates the direction of the opening of the parabola.

Straight lines, cases 2a–d: In case of 2a we have $\alpha = \beta = \gamma = 0$, and the contact border is given by the linear relation

$$2\text{a}, \lambda \neq 0: \qquad y = -\frac{\kappa}{\lambda}x - \frac{\omega}{2\lambda}, \tag{A.45}$$

cf. (4.69). Inserting $x := R(\theta)\cos\theta, y := R(\theta)\sin\theta$, we obtain

$$2\text{a}, \forall\lambda: \quad R(\theta) = -\frac{\omega}{2\lambda\sin\theta + 2\kappa\cos\theta}. \tag{A.46}$$

This expression also holds for $\lambda = 0$, because then we have $x = -\omega/2/\kappa$, whence the λ–term in the denominator drops out. In this case, only those θ need to be considered where $R(\theta) > 0$, because the other, unconventional scenario $R(\theta) < 0$ describes the same straight line.

For 2b–d, we again employ primed quantities to indicate the rotation involved in 2d, whereas for 2bc primed and unprimed quantities coincide. The corresponding contact equations describe a parallel pair of straight lines,

$$2\text{bd}, \lambda' = 0: \quad x' = -\frac{\kappa'}{\alpha'} \pm \frac{1}{\alpha'}\sqrt{\kappa'^2 - \omega'\alpha'}, \tag{A.47}$$

$$2\text{cd}, \kappa' = 0: \quad y' = -\frac{\lambda'}{\beta'} \pm \frac{1}{\beta'}\sqrt{\lambda'^2 - \omega'\beta'}. \tag{A.48}$$

Fixing the center of the coordinate system to $\mathbf{x}_0 = (-\kappa'/\alpha', 0)$ (2bd) or $\mathbf{x}_0 = (0, -\lambda'/\beta')$ (2cd) yields for the polar radii

$$2\text{bd}, \lambda' = 0: \quad R(\theta) = \pm\frac{1}{\alpha' \cos\theta}\sqrt{\kappa'^2 - \omega'\alpha'}, \tag{A.49}$$

$$2\text{cd}, \kappa' = 0: \quad R(\theta) = \pm\frac{1}{\beta' \sin\theta}\sqrt{\lambda'^2 - \omega'\beta'}. \tag{A.50}$$

Each of these expressions describes both parallel lines simultaneously, where the correct sign has to be chosen in a θ-dependent manner from $R > 0$. Again, the resulting polar parameterizations of the contact border are

$$x' = x_0 + R(\theta)\cos\theta, \qquad y' = y_0 + R(\theta)\sin\theta, \tag{A.51}$$

where an additional rotation by $-\phi$ has to be performed for 2d, according to the relations (4.58, 4.76). There are two angles $\theta_0, \theta_0 + \pi$ where $R(\theta)$ becomes infinite. These angles indicate the direction of the described pair of straight lines.

A.6. Model parameters and selected mathematical symbols

One-dimensional cell migration model, sections 3.1–3.7:

Symbol	Meaning	Value	Units
λ	Length of model cell (fragment)	10	μm
θ_g	Volume fraction of G-actin	0.0375	dimensionless
α_B	Amount of F-actin polymerization at plus ends	$5.57 \cdot 10^5$	dimensionless
δ_B	Amount of F-actin depolymerization at plus ends	258	dimensionless
ω	F-actin capping rate	1250	1/min
δ_a	F-actin disassembly rate	0.2	1/min
ε	Amount of F-actin nucleation	0.75	dimensionless
[Arp2/3]	Concentration of activated Arp2/3 complexes	10	μM
ν_0	Amount induced nucleation by Arp2/3	60	$1/\mu$M
θ_β	Half-saturation concentration for nucleation	0.00375	dimensionless
η_0	Viscosity coefficient of the F-actin network phase	0.625	Pa $\cdot$ min
ψ_0	Contractile stress per bound myosin-II	$1.04 \cdot 10^4$	Pa $\cdot /\mu$M
σ_0	Strength of the swelling pressure	$8 \cdot 10^5$	Pa
ϕ_{ph}	Drag coefficient between network and solvent	2	Pa $\cdot$ min/μm^2
$\overline{\kappa}_\Gamma$	Tip curvature weight factor for membrane tension	0.5	dimensionless
τ_0	Minimal cellular membrane tension	25	Pa
ϕ_u	Friction per actin-substrate bound integrin	0.02	Pa $\cdot$ min
ϕ_v	Additional friction associated to the cell body	18	Pa $\cdot$ min/μm^2
D_m	Diffusion coefficient for free myosin-II	0.5	μm^2/min
α_m	F-actin binding rate of myosin-II	400	1/min
δ_{m0}	Dissociation rate of bound myosin-II	3	1/min
θ_m	Optimal F-actin for myosin-II binding	0.025	dimensionless
D_f	Diffusion coefficient for free integrin	0.5	μm^2/min
α_{fa}^0	Free integrin binding rate to F-actin	$1.2 \cdot 10^4$	1/min
δ_{af}	Dissociation rate for F-actin bound integrin	5	1/min
α_{fs}	Free integrin binding rate to substrate	15	1/min
δ_{sf}	Dissociation rate for substrate bound integrin	5	1/min
α_{sb}^0	F-actin binding rate for substrate bound integrin	$1.2 \cdot 10^4$	1/min
δ_{bs}^0	FA dissociation of the F-actin link	0.1	1/min
ρ_{bs}	Exponential FA-rupture coefficient substrate link	11.7	μm/Pa
α_{ab}	Substrate binding rate for F-actin bound integrin	15	1/min
δ_{ba}^0	FA dissociation rate of the substrate link	0.1	1/min
ρ_{ba}	Exponential FA-rupture coefficient F-actin link	11.7	μm/Pa
A_{dh}	Effective substratum adhesiveness coefficient	3	dimensionless

Table A.2.: Parameter values in the one-dimensional cell migration model from sections 3.1–3.7, unless indicated otherwise.

Symbol	Meaning	Units
$\theta(t,y)$	Volume fraction of F-actin	dimensionless
$\mathbf{u}(t,y)$	F-actin velocity	μm/min
$p(t,y)$	Effective two-phase flow pressure	Pa
$\tau(t,y)$	Dorsal membrane tension induced effective pressure	Pa
$\dot{y}_1 \equiv \dot{y}_2 \equiv$	Protrusion / retraction speed at cell ends	μm/min
$v(t)$	Migration velocity of model cell	μm/min
V	Relative inward F-actin velocity at boundary	μm/min
ν_Γ	Outer normal of the free boundary $\Gamma(t)$	dimensionless
$m_f(t,y)$	Concentration of free myosin-II	μM
$m_b(t,y)$	Concentration of F-actin bound myosin-II	μM
$b_f(t,y)$	Concentration of free integrin	$1/\mu\text{m}^2$
$b_a(t,y)$	Concentration of actin bound integrin	$1/\mu\text{m}^2$
$b_s(t,y)$	Concentration of substrate bound integrin	$1/\mu\text{m}^2$
$b_b(t,y)$	Concentration of substrate and actin bound integrin	$1/\mu\text{m}^2$

Table A.3.: Variables in the one-dimensional cell migration model from sections 3.1–3.7.

Symbol	Meaning	Units
$J(\theta)$	F-actin net polymerization rate	1/min
$\psi(\theta, m_b)$	Contractile stress	Pa
$\sigma(\theta)$	Swelling pressure	Pa
$S(\theta, m_b)$	Effective cytoplasmic stress	Pa
$\eta(\theta)$	Viscosity of F-actin phase	Pa $\cdot$ min
$\beta_n(\theta)$	F-actin branching rate at tip	dimensionless
$\nu([\text{Arp2/3}])$	Stimulated F-actin branching coefficient at tip	dimensionless
f_u	Active frictional clutch force at focal adhesions	Pa/μm
f_v	Passive frictional force at dorsal membrane	Pa/μm
P_{poly}	Total polymerization pressure	Pa
P_{clamp}	Clamp-motor polymerization pressure	Pa
P_{ratchet}	Brownian ratchet polymerization pressure	Pa
$\eta_\Gamma(m_b)$	Effective F-actin shear viscosity at tip	Pa $\cdot$ min/μm
$\theta_+(\theta)$	F-actin barbed/plus end volume fraction at tip	dimensionless

Table A.4.: Model functions for one-dimensional cell migration as employed in sections 3.1–3.7.

Two-dimensional cell migration model, sections 3.8–3.9:

Symbol	Meaning	Values	Units
$a(t,\varphi)$	Concentration of F-actin	$0.3 \ldots 0.8$	mM
$b(t,\varphi)$	Area concentration of adhering integrin	$0 \ldots 0.03$	$10^6/\mu\text{m}^2$
$d(t,\varphi)$	Area concentration of substratum ligands	$0 \ldots 0.2$	$10^6/\mu\text{m}^3$
$L(t,\varphi)$	Local lamella width	$2 \ldots 5$	μm
$\mathbf{v}(t)$	Migration velocity of model cell	$0 \ldots 0.3$	μm/min

Table A.5.: Variables in the two-dimensional cell migration model from sections 3.8–3.9.

Symbol	Meaning	Value	Units
C_A	Area concentration		$10^6/\mu\text{m}^2$
$\text{d}t$	Numerical time step increment	0.01	min
R	Cell body radius	2	μm
$\gamma_\mathbf{v}$	Effective cellular friction coefficient	25	nN·min/μm
f_loc	Strength of locomotion force	17	nN/μm/mM/C_A
κ_a	Slip factor for actin transport velocity	0.3	dimensionless
α_L	Actin assembly rate per lamella extension	0.04	mM/min/μm
α_a	Integrin stimulated F-actin autocatalysis	0.016	1/min/C_A
δ_a	F-actin depolymerization rate	0.30	1/min
β_a	F-actin polymerization perturbation strength	0.14	mM/min$^{1/2}$
D_a	Diffusion coefficient for F-actin	0.04	μm^2/min
α_b	Adhesion assembly stimulated by F-actin	1.8	1/min/mM
δ_e	Adhesion loss due to radial transport	1	1/μm
δ_b	Adhesion disassembly rate	0.2	1/min
f_b	Characteristic adhesion rupture force	0.2	nN
κ_b	Slip factor for integrin transport velocity	0.7	dimensionless
d_0	Effective amount of substratum receptors	0.1	dimensionless
σ_d	Substratum receptor variation	0.05	dimensionless
α_d	Substratum receptor gain factor	0.03	C_A/μm
κ_d	Slip factor for substratum velocity	1.0	dimensionless
ϕ_0	Amount of tip protrusion friction	1.5	nN·min/mM/μm
τ_0	Effective cellular surface tension	0.04	nN·μm/mM^2
p_0	Protrusion pressure from cell body	1.2	nN·μm
p_b	Protrusion induced by adhesions	0.3	nN/mM/C_A
ρ_0	Retrograde F-actin flow contraction	1.2	nN/mM^2

Table A.6.: Values of model parameters from sections 3.8–3.9, unless indicated otherwise.

Symbol	Meaning	Units
$J''(a,b,L)$	F-actin net polymerization rate	mM/min
$u_a(\mathbf{v})$	F-actin transport velocity	μm/min
$u_b(\mathbf{v})$	Integrin transport velocity	μm/min
$u_d(\mathbf{v})$	Effective substratum receptor transport velocity	μm/min
$v_{\text{tip}}^{\text{in}}(\mathbf{v})$	Velocity of incoming receptors at cell tip	μm/min
$v_{\text{tip}}^{\text{out}}(\mathbf{v})$	Velocity of leaving receptors at cell tip	μm/min
$v_{\text{body}}^{\text{out}}(\mathbf{v})$	Velocity of leaving receptors at cell body	μm/min
$\tau(a,L)$	Effective curvature force at the cell outline	mN/μm
$\mathbf{f}(a,b,L)$	Local cellular locomotion force	mN/μm
$\mathbf{F}_{\text{loc}}(\mathbf{f})$	Total cellular locomotion force	mN

Table A.7.: Model functions for two-dimensional cell migration as employed in sections 3.8–3.9.

Cell tissue model, chapter 5:

Symbol	Meaning	Value	Units
$\sqrt{\mathcal{P}_{\text{ex}}}$	Relative maximal cell extension	3	dimensionless
r_i	Cell body radii	$0.9 \dots 2.0$	μm
T	Cytoskeletal reorganization time	120	s
$\tilde{\rho}$	Filament bundle density on cell body	9.55	$1/\mu$m
f_{loc}	Strength of cellular locomotion force	$10 \dots 20$	pN
f_{int}	Strength of cellular interaction force	60	pN
α	Cooperative vertical traction coefficient	$0 \dots 0.17$	dimensionless
$\Delta_{\min}$	Relative minimal cell pair distance	0.1	dimensionless
Δ_{crit}	Relative critical cell pair distance	$0.2 \dots 0.7$	dimensionless
$b_{\text{st}} \cdot \mathcal{P}_{\text{ex}}^{-1/4}$	Strength of stochastic migration force	8.31	pN $/\sqrt{\mu\text{m} \cdot \text{s}}$
$\tilde{\gamma}$	Cellular friction constant	$2.5 \cdot 10^4$	pN $\cdot$ s / μm
$\mathrm{d}t$	Numerical time step	2	s

Table A.8.: Values of model parameters from chapter 5, unless indicated otherwise. These values have been derived from the dimensional estimates in paragraph 5.3.8. This table is a duplicate of 5.1, and repeated here for reference.

Symbol	Meaning	Value	Units
r_i	Cell body radii	$1.08 \ldots 1.93$	μm
$\tilde{\rho}_i$	Force generating filament density	$7.02 \ldots 9.13$	$1/\mu$m
b_i	Effective integrin expression level	1.0	dimensionless
c_i	Effective cadherin expression level	1.0	dimensionless
q_i	Perturbation response, protrusivity	1.0	dimensionless
f_{int}	Strength of interaction force	60	pN
α	Cooperative vertical traction coefficient	0.0	dimensionless
$\Delta_{\min}$	Minimal normalized cell-cell distance	0.1	dimensionless
$\Delta_{\text{crit}}^{(0)}$	Critical normalized cell-cell distance	0.3	dimensionless
α_{ani}	Anisotropy parameter for $\Delta_{\text{crit}}^{\text{bb}}$	1.0 & 1.4	dimensionless
f_{pol}	Strength of polarity force	2.5	pN
T_{pol}	Polarity reorientation time	600	s
v_{pol}	Characteristic polarity adaptation velocity	1.0	μm/s
$\delta_{\mathbf{p}}$	Polarity decrease rate	$8.3 \cdot 10^{-4}$	1/s
$\alpha_{\mathbf{p}}$	Stochastic polarity increase	0.03	$1/\sqrt{\text{s}}$
γ_{drag}	Friction coefficient per free cell area	1326.3	$\text{pN} \cdot \text{s}/\mu\text{m}^3$
γ_0^{vis}	Viscous cell-cell friction coefficient	200	$\text{pN} \cdot \text{s}/\mu\text{m}$
$\mathrm{d}t$	Numerical time step	2	s

Table A.9.: Parameter values introduced in section 5.7 in addition to the ones from table A.8. The values presented here are defaults and employed only unless indicated otherwise in the respective sections.

A.7. Accompanying electronic supplementary material

This thesis is accompanied by several files of electronic supplementary material. This material can also be obtained from `http://www.theobio.uni-bonn.de/people/mab/dsup`.

Single cell migration – section 3.9:

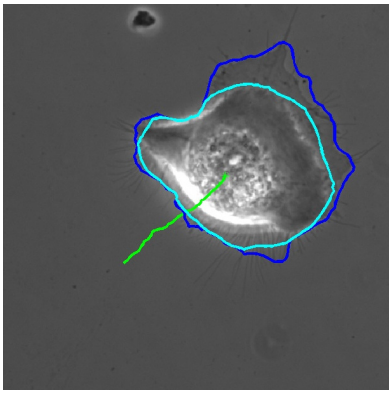

`s2d_experiment.avi`

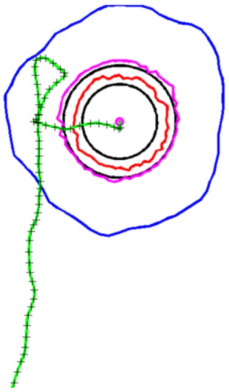

`s2d_simulation.avi`

Voronoi algorithm – section 4.8: The zip-file `mwvoro.zip` contains the Octave code (Matlab-compatible) to construct circular Voronoi diagrams, licensed under the two-clause BSD open-source license. The program files are extensively commented.

Voronoi tissue topology – section 5.4

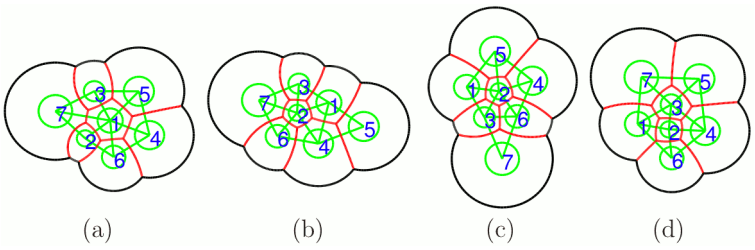

(a) (b) (c) (d)

`mova.avi` `movb.avi` `movc.avi` `movd.avi`

Cell sorting model – section 5.6

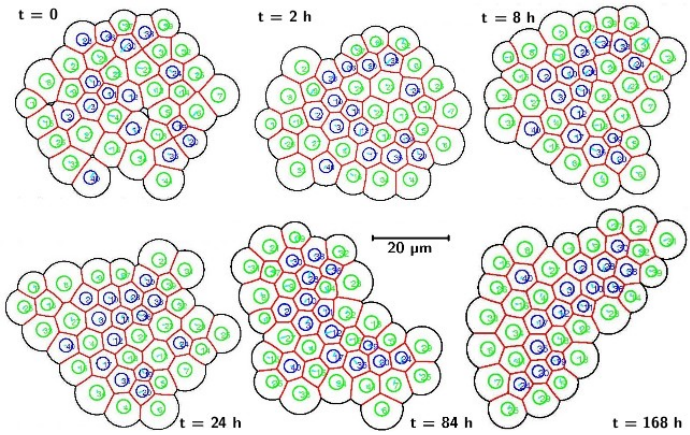

mov_sort.avi

Germband elongation model – section 5.7

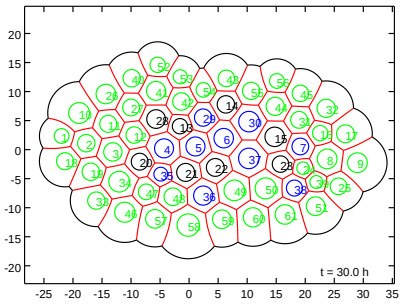

mov_elo.avi

List of Figures

List of Tables

Bibliography

[1] B. Aigouy, R. Farhadifar, D. B. Staple, A. Sagner, J.-C. Röper, F. Jülicher, and S. Eaton. Cell flow reorients the axis of planar polarity in the wing epithelium of Drosophila. *Cell*, 142:773, 2010.

[2] B. Alberts, A. Johnson, J. Lewis, M. Raff, K. Roberts, and P. Walter. *Molecular Biology of the Cell*. Garland Science, 4th edition, 2002.

[3] A. Y. Alexandrova, K. Arnold, S. Schaub, J. M. Vasiliev, J.-J. Meister, A. D. Bershadsky, and A. B. Verkhovsky. Comparative dynamics of retrograde actin flow and focal adhesions. *PLoS ONE*, 3:e3234, 2008.

[4] H. W. Alt and W. Alt. Phase boundary dynamics: transition between ordered and disordered lipid monolaùers. *Interfaces and Free Boundaries*, 11:1, 2009.

[5] W. Alt. Nonlinear hyperbolic systems of generalized Navier-Stokes type for interactive motion in biology. In S. Hildebrandt and H. Karcher, editors, *Geometric Analysis and Nonlinear Partial Differential Equations*, pages 431–461. Springer, 2003.

[6] W. Alt, M. Bock, and C. Möhl. Coupling of cytoplasm and adhesion dynamics determines cell polarization and locomotion. In A. Chauvière, L. Preziosi, and C. Verdier, editors, *Cell Mechanics: From Single Scale-Based Models to Multiscale Modeling*, pages 86–125. Chapman & Hall / CRC, 2010. Preprint `http://arxiv.org/abs/0907.5078`.

[7] W. Alt, O. Brosteanu, B. Hinz, and H.-W. Kaiser. Patterns of spontaneous motility in videomicrographs of human epidermal keratinocytes (HEK). *Biochemistry and Cell Biology*, 73:441, 1995.

[8] W. Alt and M. Dembo. Cytoplasm dynamics and cell motion: two-phase flow models. *Mathematical Biosciences*, 156:207, 1999.

[9] W. Alt, U. Eibach, V. Herzog, S. Schleim, and G. Schütz. *Lebensentstehung und künstliches Leben*. Die Graue Edition, 2010.

[10] R. Ananthakrishnan and A. Ehrlicher. The forces behind cell movement. *International Journal of Biological Sciences*, 3:303, 2007.

[11] Y. Aratyn-Schaus and M. L. Gardel. Transient frictional slip between integrin and the ECM in focal adhesions under myosin II tension. *Current Biology*, 20:1145, 2010.

[12] S. Archer, D. W. Wylie, L. S. Harris, J. W. Schulenberg, T. R. Lewis, M. R. Bell, R. K. Kullnig, and A. Arnold. l-(indolylalkyl)-4-arryr-piperazmes: a new class of tranquillizers. *Journal of the American Chemical Society*, 84:1306, 1962.

[13] L. Arnold. *Stochastische Differentialgleichungen: Theorie und Anwendung*. R. Oldenbourg Verlag, 1973.

[14] P. F. Ash and E. D. Bolker. Generalized Dirichlet tessellations. *Geometrica Dedicata*, 20:209, 1986.

[15] F. Aurenhammer. Voronoi diagrams – a survey of a fundamental geometric data structure. *ACM Computing Surveys*, 23:345, 1991.

[16] F. Aurenhammer and H. Edelsbrunner. An optimal algorithm for constructing the weighted Voronoi diagram in the plane. *Pattern Recognition*, 17:251, 1984.

[17] F. Aurenhammer and R. Klein. Voronoi diagrams. In J.-R. Sack and J. Urrutia, editors, *Handbook of Computational Geometry*, pages 201–290. North Holland, 1999.

[18] N. Q. Balaban, U. S. Schwarz, D. Riveline, P. Goichberg, G. Tzur, I. Sabanay, D. Mahalu, S. Safran, A. Bershadsky, L. Addadi, and B. Geiger. Force and focal adhesion assembly: a close relationship studied using elastic micropatterned substrates. *Nature*, 3:466, 2001.

[19] I. Banga and A. Szent-Györgyi. Preparation and properties of myosin A and B. *Studies from the Institute of Medical Chemistry, University Szeged*, 1:5, 1942.

[20] D. A. Beard and H. Qian. *Chemical Biophysics – Quantitative Analysis of Cellular Systems*. Cambridge University Press, 2008.

[21] G. I. Bell. Models for the specific adhesion of cells to cells. *Science*, 200:618, 1978.

[22] M. Ben Amar, C. Chatelain, and P. Ciarletta. Contour instabilities in early tumor growth models. *Physical Review Letters*, 106:148101, 2011.

[23] T. Betz, D. Koch, D. Lim, and J. A. Käs. Stochastic actin polymerization and steady retrograde flow determine growth cone advancement. *Biophysical Journal*, 96:5130, 2009.

[24] T. Betz, D. Koch, Y.-B. Lu, K. Franze, and J. A. Käs. Growth cones as soft and weak force generators. *Proceedings of the National Academy of Sciences of the United States of America*, 108:13420, 2011.

[25] A. Beutelspacher. *Lineare Algebra – Eine Einführung in die Wissenschaft der Vektoren, Abbildungen und Matrizen*. Vieweg, 2001.

[26] T. Beyer and M. Meyer-Hermann. Cell transmembrane receptors determine tissue pattern stability. *Physical Review Letters*, 101:148102, 2008.

[27] T. Beyer and M. Meyer-Hermann. Multiscale modeling of cell mechanics and tissue organization. *IEEE Engineering in Medicine and Biology*, 28:38, 2009.

[28] I. B. Bischofs, S. S. Schmidt, and U. S. Schwarz. Effect of adhesion geometry and rigidity on cellular force distributions. *Physical Review Letters*, 103:048101, 2009.

[29] G. B. Blanchard, A. J. Kabla, N. L. Schultz, L. C. Butler, B. Sanson, N. Gorfinkiel, L. Mahadevan, and R. J. Adams. Tissue tectonics: morphogenetic strain rates, cell shape and intercalation. *Nature Methods*, 6:1327, 2009.

[30] H. Blum. Biological shape and visual science (part 1). *Journal of Theoretical Biology*, 38:205, 1973.

[31] M. Bock, A. K. Tyagi, J.-U. Kreft, and W. Alt. Generalized Voronoi tessellation as a model of two-dimensional cell tissue dynamics. *Bulletin of Mathematical Biology*, 72:1696, 2010. Preprint `http://arxiv.org/abs/0901.4469`.

[32] M. Bock and C. Wollnik. How do biological cells move? *European Communications in Mathematical and Theoretical Biology*, 14:54–69, Oct. 2011. Special issue on occasion of the 25th anniversary of Wolfgang Alt's Theoretical Biology group at the University of Bonn, edited by Martin Bock and Markus P. Knappitsch.

[33] N. Borghi, M. Lowndes, V. Maruthamuthu, M. L. Gardel, and W. J. Nelson. Regulation of cell motile behavior by crosstalk between cadherin- and integrin-mediated adhesions. *Proceedings of the National Academy of Sciences of the United States of America*, 107:13324, 2010.

[34] S. L. Brenner and E. D. Korn. Substoichiometric concentrations of cytochalasin D inhibit actin polymerization. *Journal of Biological Chemistry*, 254:9982, 1979.

[35] J. Brevier, D. Montero, T. Svitkina, and D. Riveline. The asymmetric self-assembly mechanism of adherens junctions: a cellular push-pull unit. *Physical Biology*, 5:016005, 2008.

[36] G. W. Brodland and J. H. Veldhuis. Computer simulations of mitosis and interdependencies between mitosis orientation, cell shape and epithelia reshaping. *Journal of Biomechanics*, 35:673, 2002.

[37] I. N. Bronstein, K. A. Semendjajew, G. Musiol, and H. Mühlig. *Taschenbuch der Mathematik*. Harri Deutsch, 4. Auflage, 1999.

[38] C. M. Brown, B. Hebert, D. L. Kolin, J. Zareno, L. Whitmore, A. R. Horwitz, and P. W. Wiseman. Probing the integrin-actin linkage using high-resolution protein velocity mapping. *Journal of Cell Science*, 119:5204, 2006.

[39] A. K. Bryan, A. Goranov, A. Amon, and S. R. Manalis. Measurement of mass, density, and volume during the cell cycle of yeast. *Proceedings of the National Academy of Sciences of the United States of America*, 107:999, 2010.

[40] L. C. Butler, G. B. Blanchard, A. J. Kabla, N. J. Lawrence, D. P. Welchman, L. Mahadevan, R. J. Adams, and B. Sanson. Cell shape changes indicate a role for extrinsic tensile forces in Drosophila germ-band extension. *Nature Cell Biology*, 11:859, 2009.

[41] Y. Cai, O. Rossier, N. C. Gauthier, N. Biais, M.-A. Fardin, X. Zhang, L. W. Miller, B. Ladoux, V. W. Cornish, and M. P. Sheetz. Cytoskeletal coherence requires myosin-IIA contractility. *Journal of Cell Science*, 123:413, 2010.

[42] A. C. Callan-Jones and F. Jülicher. Hydrodynamics of active permeating gels. *New Journal of Physics*, 13:093027, 2011.

[43] H. B. Callen. *Thermodynamics and Introduction to Thermostatistics*. Wiley, 2nd edition, 1985.

[44] M. Chalfie, Y. Tu, G. Euskirchen, W. W. Ward, and D. C. Prasher. Green fluorescent protein as a marker for gene expression. *Science*, 263:802, 1994.

[45] C. E. Chan and D. J. Odde. Traction dynamics of filopodia on compliant substrates. *Science*, 322:1687, 2008.

[46] C. Chatelain, T. Balois, P. Ciarletta, and M. Ben Amar. Emergence of microstructural patterns in skin cancer: a phase separation analysis in a binary mixture. *New Journal of Physics*, 13:115013, 2011.

[47] O. Chaudhuri, S. H. Parekh, and D. A. Fletcher. Reversible stress softening of actin networks. *Nature*, 445:295, 2007.

[48] H. H. Chen and G. W. Brodland. Cell-level finite element studies of viscous cells in planar aggregates. *Journal of Biomedical Engineering*, 122:394, 2000.

[49] X. Chen and G. W. Brodland. Multi-scale finite element modeling allows the mechanics of amphibian neurulation to be elucidated. *Physical Biology*, 5:015003, 2008.

[50] N. G. Cogan and R. D. Guy. Multiphase flow models of biogels from crawling cells to bacterial biofilms. *HFSP Journal*, 4:11, 2010.

[51] H. S. M. Coxeter. *Projective Geometry*. Springer, 2003. Reprint of the 2nd edition from 1973.

[52] L. P. Cramer. Forming the cell rear first: breaking cell symmetry to trigger directed cell migration. *Nature Cell Biology*, 12:628, 2010.

[53] H. Darcy. *Les fontaines publiques de la ville de Dijon.* Paris, 1856. Available online from the Bibliotéque nationale de France, `http://gallica.bnf.fr/ark:/12148/bpt6k624312`.

[54] S. R. DeGroot and P. Mazur. *Non-Equilibrium Thermodynamics.* Dover, 1984.

[55] H. Delanoë-Ayari, S. Iwaya, Y. T. Maeda, J. Inose, C. Rivière, M. Sano, and J.-P. Rieu. Changes in the magnitude and distribution of forces at different Dictyostelium developmental stages. *Cell Motility and the Cytoskeleton*, 65:314, 2008.

[56] B. Delaunay. Sur la sphère vide. A la mémoire de Georges Voronoï. *Bulletin de l'Academie des Sciences de l'URSS*, 1934(6):793–800, 1934. Russian journal name: Известия Академии наук СССР. VII серия. Отделение математических и естественных наук, available online from `http://www.mathnet.ru/php/archive.phtml?wshow=paper&jrnid=im&paperid=4937&option_lang=rus` (accessed October 22, 2012).

[57] M. Dembo. The mechanics of motility in dissociated cytoplasm. *Biophysical Journal*, 50:1165, 1986.

[58] M. Dembo. Field theories of the cytoplasm. *Comments Theoretical Biology*, 1:159, 1989.

[59] M. Dembo. Mechanics and control of the cytoskeleton in amoeba proteus. *Biophysical Journal*, 55:1053, 1989.

[60] M. Dembo. On free boundary proplems and amoeboid motion. In N. Akkas, editor, *Biomechanics of Active Movement and Division of Cells*, volume 84 of *NATO ASI Series H*, pages 231–283. Springer, 1994.

[61] M. Dembo and F. Harlow. Cell motion, contractile networks and the physics of interpenetrating reactive flow. *Biophysical Journal*, 50:109, 1986.

[62] M. Dembo, F. H. Harlow, and W. Alt. The biophysics of cell surface motility. In C. DeLisi, F. W. Wiegel, and A. S. Perelson, editors, *Cell Surface Dynamics: Concepts and Models*, pages 495–542. Marcel Dekker, New York, 1982.

[63] M. Dembo and Y.-L. Wang. Stresses at the cell-to-substrate interface during locomotion of fibroblasts. *Biophysical Journal*, 76:2307, 1999.

[64] `http://dict.leo.org`. Web dictionary English ↔ German, accessed 2007–2012. Used as language reference and for translation purposes. Any specific technical terms have been veryfied from independent resources such as textbooks or journal articles, each of which are separately listed in the present bibliography.

[65] R. B. Dickinson. Models for actin polymerization motors. *Journal of Mathematical Biology*, 58:81, 2009.

[66] R. B. Dickinson, L. Caro, and D. L. Purich. Force generation by cytoskeletal filament end-tracking proteins. *Biophysical Journal*, 87:2838, 2004.

[67] P. Dieterich, R. Klages, R. Preuss, and A. Schwab. Anomalous dynamics of cell migration. *Proceedings of the National Academy of Sciences of the United States of America*, 105:459, 2008.

[68] G. J. Doherty and H. T. McMahon. Mediation, modulation, and consequences of membrane-cytoskeleton interactions. *Annual Reviews of Biophysics*, 37:65, 2008.

[69] M. Doi and S. F. Edwards. *The Theory of Polymer Dynamics*. Oxford University Press, 1986.

[70] M. Doi and A. Onuki. Dynamic coupling between stress and composition in polymer solutions and blends. *Journal de Physique II*, 2:1631, 1992.

[71] D. Drasdo, R. Kree, and J. S. McCaskill. Monte Carlo approach to tissue-cell populations. *Physical Review E*, 52:6635, 1995.

[72] I. Z. Emiris, E. P. Tsigaridas, and G. M. Tzoumas. The predicates for the Voronoi diagram of ellipses. In *Proceedings of the twenty-second annual symposium on Computational Geometry*, SCG '06, pages 227–236. ACM, 2006.

[73] I. Z. Emiris, E. P. Tsigaridas, and G. M. Tzoumas. Exact Delaunay graph of smooth convex pseudo-circles: general predicates, and implementation for ellipses. In *2009 SIAM/ACM Joint Conference on*

Geometric and Physical Modeling, SPM '09, pages 211–222. ACM, 2009.

[74] I. Z. Emiris, E. P. Tsigaridas, and G. M. Tzoumas. Voronoi diagram of ellipses in CGAL. `http://cgi.di.uoa.gr/~geotz/bib/papers/EmTsTz-EWCG08-VorEll.pdf` (2008), accessed September 10, 2012.

[75] M. Enculescu, M. Sabouri-Ghomi, G. Danuser, and M. Falcke. Modeling of protrusion phenotypes driven by the actin-membrane interaction. *Biophysical Journal*, 98:1571, 2010.

[76] E. Evans and K. Ritchie. Dynamic strength of molecular adhesion bonds. *Biophysical Journal*, 72:1541, 1997.

[77] G. Forgacs and S. A. Newman. *Biological Phyics of the Developing Embryo*. Cambridge University Press, 2005.

[78] M. F. Fournier, R. Sauser, D. Ambrosi, J.-J. Meister, and A. B. Verkhovsky. Force transmission in migrating cells. *Journal of Cell Biology*, 188:287, 2010.

[79] P. Friedl, K. S. Zänker, and E.-B. Bröcker. Cell migration strategies in 3-D extracellular matrix: Differences in morphology, cell matrix interactions, and integrin function. *Microscopy Research and Technique*, 43:369, 1998.

[80] C. G. Galbraith and M. P. Sheetz. A micromachined device provides a new bend on fibroblast traction forces. *Proceedings of the National Academy of Sciences of the United States of America*, 94:9114, 1997.

[81] C. G. Galbraith, K. M. Yamada, and M. P. Sheetz. The relationship between force and focal complex development. *Journal of Cell Biology*, 159:695, 2002.

[82] J. Galle, G. Aust, G. Schaller, T. Beyer, and D. Drasdo. Individual cell-based models of the spatial-temporal organization of multicellular systems – achievements and limitations. *Cytometry Part A*, 69:704, 2006.

[83] J. Galle, M. Loeffler, and D. Drasdo. Modeling the effect of deregulated proliferation and apoptosis on the growth dynamics of epithelial cell populations in vitro. *Biophysical Journal*, 88:62, 2005.

[84] W. J. Gallin, G. M. Edelman, and B. A. Cunningham. Characterization of L-CAM, a major cell adhesion molecule from embryonic liver cells. *Proceedings of the National Academy of Sciences of the United States of America*, 80:1038, 1983.

[85] Y. Gambin, R. Lopez-Esparza, E. Sierecki, N. S. Gov, M. Genest, R. S. Hodges, and W. Urbach. Lateral mobility of proteins in liquid membranes revisited. *Proceedings of the National Academy of Sciences of the United States of America*, 102:2098, 2006.

[86] M. L. Gardel, B. Sabass, L. Ji, G. Danuser, U. S. Schwarz, and C. M. Waterman. Traction stress in focal adhesions correlates biphasically with actin retrograde flow speed. *Journal of Cell Biology*, 183:999, 2008.

[87] M. L. Gardel, I. C. Schneider, Y. Aratyn-Schaus, and C. M. Waterman. Mechanical integration of actin and adhesion dynamics in cell migration. *Annual Review of Cell and Developmental Biology*, 26:315, 2010.

[88] `http://www.gnuplot.info`. Plotting tools, versions 4.0, 4.2, and 4.4, 2007–2012. Most of the presented plots have been created with Gnuplot.

[89] G. Giannone, B. J. Dubin-Thaler, O. Rossier, Y. Cai, O. Chaga, G. Jiang, W. Beaver, H.-G. Döbereiner, Y. Freund, G. Borisy, and M. P. Sheetz. Lamellipodial actin mechanically links myosin activity with adhesion-site formation. *Cell*, 128:561, 2007.

[90] J. A. Glazier and F. Graner. Simulation of the differential adhesion driven rearrangement of biological cells. *Physical Review E*, 47:2128, 1992.

[91] J. B. A. Green. Sophistications of cell sorting. *Nature Cell Biology*, 10:375, 2008.

[92] M. Griebel, S. Knapek, G. Zumbusch, and A. Caglar. *Numerische Simulation in der Molekül̈dynamik*. Springer, 2004.

[93] W. H. Grover, A. K. Bryan, M. Diez-Silva, S. Suresh, J. M. Higgins, and S. R. Manalis. Measuring single-cell density. *Proceedings of the National Academy of Sciences of the United States of America*, 108:10992, 2011.

[94] J. M. Halbleib and W. J. Nelson. Cadherins in development: cell adhesion, sorting, and tissue morphogenesis. *Genes & Development*, 20:3199, 2006.

[95] W. D. Halliburton. On muscle plasma. *Journal of Physiology*, 8:133, 1887.

[96] A. K. Harris. Is cell sorting caused by differences in the work of intercellular adhesion? A critique of the Steinberg hypothesis. *Journal of Theoretical Biology*, 061:267, 1976.

[97] A. K. Harris, P. Wild, and D. Stopak. Silicone rubber substrata: a new wrinkle in the study of cell locomotion. *Science*, 208:177, 1980.

[98] Y. Hegerfeldt, M. Tusch, E.-B. Bröcker, and P. Friedl. Collective cell movement in primary melanoma explants: Plasticity of cell-cell interaction, β-integrin function, and migration strategies. *Cancer Research*, 62:2125, 2002.

[99] M. Herant and M. Dembo. Form and function in cell motility: From fibroblasts to keratocytes. *Biophysical Journal*, 98:1408, 2010.

[100] M. Herant, V. Heinrich, and M. Dembo. Mechanics of neutrophil phagocytosis: experiments and quantitative models. *Journal of Cell Science*, 119:1903, 2006.

[101] M. Herant, W. A. Marganski, and M. Dembo. The mechanics of neutrophils: Synthetic modeling of three experiments. *Biophysical Journal*, 84:3389, 2003.

[102] K. J. Hill. Matrix-based ellipse geometry. In A. W. Paeth, editor, *Graphics Gems V*, pages 72–77. Academic Press, 1995.

[103] B. Hinz, W. Alt, C. Johnen, V. Herzog, and H.-W. Kaiser. Quantifying lamella dynamics of cultured cells by SACED, a new computer-assistet motion analysis. *Experimental Cell Research*, 251:234, 1999.

[104] R. M. Hochmuth. Micropipette aspiration of living cells. *Journal of Biomechanics*, 33:15, 2000.

[105] H. Honda. Description of cellular patterns by dirichlet domains: The two-dimensional case. *Journal of Theoretical Biology*, 072:523, 1978.

[106] H. Honda, M. Tanemura, and T. Nagai. A three-dimensional vertex dynamics cell model of space filling polyhedra simulating cell behavior in a cell aggregate. *Journal of Theoretical Biology*, 226:439, 2004.

[107] S. Hong, R. B. Troyanovsky, and S. M. Troyanovsky. Spontaneous assembly and active disassembly balance adherens junction homeostasis. *Proceedings of the National Academy of Sciences of the United States of America*, 107:3528, 2010.

[108] R. Hooke. *Micrographia – Some Physiological Descriptions of Minute Bodies Made by Magnifying Glasses with Observations and Inquiries Thereupon.* Royal Society of London, 1665. Available online from `http://www.gutenberg.org/files/15491/15491-h/15491-h.htm`.

[109] J. Hoshen and R. Kopelman. Percolation and cluster distribution. I. cluster multiple labeling technique and critical concentration algorithm. *Physical Review B*, 14:3438, 1976.

[110] P. Hotulainen and P. Lappalainen. Stress fibers are generated by two distinct actin assembly mechanisms in motile cells. *Journal of Cell Biology*, 173:383, 2006.

[111] M. S. Hutson, G. W. Brodland, J. Yang, and D. Viens. Cell sorting in three dimensions: Topology, fluctuations, and fluidlike instabilities. *Physical Review Letters*, 101:148105, 2008.

[112] R. O. Hynes. Integrins: a family of cell surface receptors. *Cell*, 48:549, 1987.

[113] R. O. Hynes. Integrins: Bidirectional, allosteric signaling machines. *Cell*, 110:673, 2002.

[114] J. A. Izaguirre, R. Chaturvedi, C. Huang, T. Cickovski, J. Coffland, G. Thomas, G. Forgacs, M. Alber, G. Hentschel, S. A. Newman, and J. A. Glazier. Compucell, a multi-model framework for simulation of morphogenesis. *Bioinformatics*, 20:1129, 2004.

[115] I. Jahn, editor. *Geschichte der Biologie.* Nikol Verlag, 3rd edition, 2004.

[116] A. Jilkine and L. Edelstein-Keshet. A comparison of mathematical models for polarization of single eukaryotic cells in response to guided cues. *PLoS Computational Biology*, 7:e1001121, 2011.

[117] J. F. Joanny, F. Jülicher, K. Kruse, and J. Prost. Hydrodynamic theory for multi-component active polar gels. *New Journal of Physics*, 9:422, 2007.

[118] J.-F. Joanny and J. Prost. Active gels as a description of the actin-myosin cytoskeleton. *HFSP Journal*, 3:94, 2009.

[119] F. H. Johnson, O. Shimomura, Y. Saiga, L. C. Gershman, G. T. Reynolds, and J. R. Waters. Quantum efficiency of cypridina luminescence, with a note on that of aequorea. *Journal of Cellular and Comparative Physiology*, 60:85, 1962.

[120] J. Käfer, T. Hayashi, A. F. M. Marée, R. W. Carthew, and F. Graner. Cell adhesion and cortex contractility determine cell patterning in the Drosophila retina. *Proceedings of the National Academy of Sciences of the United States of America*, 104:18549, 2007.

[121] T. Kanesaki, C. M. Edwards, U. S. Schwarz, and J. Grosshans. Dynamic ordering of nuclei in syncytial embryos: a quantitative analysis of the role of cytoskeletal networks. *Integrative Biology*, 3:1112, 2011.

[122] K. Keren, Z. Pincus, G. M. Allen, E. L. Barnhart, G. Marriott, A. Mogilner, and J. A. Theriot. Mechanism of shape determination in motile cells. *Nature*, 453:475, 2008.

[123] K. Keren, P. T. Yam, A. Kinkhabwala, A. Mogilner, and J. A. Theriot. Intracellular fluid flow in rapidly moving cells. *Nature Cell Biology*, 11:1219, 2009.

[124] G. Kirfel, A. Rigort, B. Borm, C. Schulte, and V. Herzog. Structural and compositional analysis of the keratinocyte migration track. *Cell Motility and the Cytoskeleton*, 55:1, 2003.

[125] R. Klein. Abstract Voronoi diagrams and their applications. In H. Noltemeier, editor, *Proceedings Workshop on Computational Geometry and its Applications*, volume 333 of Lecture Notes in Computer Science, page 148. Springer, 1988.

[126] R. Klein, E. Langetepe, and Z. Nilforoushan. Abstract Voronoi diagrams revisited. *Computational Geometry*, 42:885, 2009.

[127] P. E. Kloeden and E. Platen. *Numerical Solution of Stochastic Differential Equations*. Springer, 1999.

[128] S. A. Koestler, S. Auinger, M. Vinzenz, K. Rottner, and J. V. Small. Differentially oriented populations of actin filaments generated in lamellipodia collaborate in pushing and pausing at the cell front. *Nature Cell Biology*, 10:306, 2008.

[129] S. A. Koestler, K. Rottner, F. Lai, J. Block, M. Vinzenz, and J. V. Small. F- and G-actin concentrations in lamellipodia of moving cells. *PLoS ONE*, 4:e4810, 2009.

[130] M. Krieg, Y. Arboleda-Estudillo, P.-H. Puech, J. Käfer, F. Graner, D. J. Müller, and C.-P. Heisenberg. Tensile forces govern germ-layer organization in zebrafish. *Nature Cell Biology*, 10:429, 2008.

[131] H. Krobath, B. Rozycki, R. Lipowsky, and T. R. Weikl. Binding cooperativity of membrane adhesion receptors. *Soft Matter*, 5:3354, 2009.

[132] S. Krokowski. *Simulation der Migration von Keratinozyten mit Fokus auf die Adhäsionskinetik*. Bachelor thesis, Universität Bonn, 2011.

[133] K. Kruse, J. F. Joanny, F. Jülicher, J. Prost, and K. Sekimoto. Generic theory of active polar gels: a paradigm for cytoskeletal dynamics. *European Physical Journal E*, 16:5, 2005.

[134] W. Kühne. Myosin, seine Darstellung, Eigenschaften, Umwandlung in Syntonin und Rückbildung aus demselben. *Journal of Physiology*, 8:133, 1864.

[135] E. Kuusela and W. Alt. Continuum model of cell adhesion and migration. *Journal of Mathematical Biology*, 58:135, 2009.

[136] I. R. Kuznetsov, M. Herant, and M. Dembo. Analysis of actin FLAP dynamics in the leading lamella. *PLoS ONE*, 5:e10082, 2010.

[137] L. D. Landau and E. M. Lifshitz. *Fluid Dynamics*, volume 6 of *Course of Theoretical Physics*. Butterworth Heinemann, 2nd edition, 1987.

[138] D. A. Lauffenburger and A. F. Horwitz. Cell migration: A physically integrated molecular process. *Cell*, 84:359, 1996.

[139] D. Leckband. Beyond structure: mechanism and dynamics of intercellular adhesion. *Biochemical Society Transactions*, 36:213, 2008.

[140] J. Lee, M. Lenord, T. N. Oliver, A. Ishihara, and K. Jacobson. Traction forces generated by locomoting keratinocytes. *Journal of Cell Biology*, 127:1957, 1994.

[141] F. Leymarie and M. D. Levine. Tracking deformable objects in the plane using an active contour model. *IEEE Transactions on Pattern Analysis and Machine Intelligence*, 15:617, 1993.

[142] T. Libotte, H.-W. Kaiser, W. Alt, and T. Bretschneider. Polarity, protrusion-retraction dynamics and their interplay during keratinocyte cell migration. *Experimental Cell Research*, 270:129, 2001.

[143] L. Ma. *Bisectors and Voronoi Diagrams for Convex Distance Functions*. PhD thesis, FernUniversität Hagen, 2000.

[144] P. K. Maini and H. G. Othmer, editors. *Mathematical Models for Biological Pattern Formation*. Springer, 2001.

[145] M. L. Manning, R. A. Foty, M. S. Steinberg, and E.-M. Schoetz. Coaction of intercellular adhesion and cortical tension specifies tissue surface tension. *Proceedings of the National Academy of Sciences of the United States of America*, 107:12517, 2010.

[146] P. Marmottant, A. Mgharbel, J. Käfer, B. Audren, J.-P. Rieu, J.-C. Vial, B. van der Sanden, A. F. M. Marée, F. Graner, and H. Delanoë-Ayari. The role of fluctuations and stress on the effective viscosity of cell aggregates. *Proceedings of the National Academy of Sciences of the United States of America*, 106:17271, 2009.

[147] R. Merkel. Force spectroscopy on single passive biomolecules and single biomolecular bonds. *Physics Reports*, 346:343, 2001.

[148] M. Meyer-Hermann. Delaunay-object dynamics: Cell mechanics with a 3D kinetic and dynamic weighted Delaunay-triangulation. In S. Schnell, P. K. Maini, S. A. Newman, and T. J. Newman, editors, *Multiscale Modeling of Developmental Systems*, pages 373–399. Elsevier, 2008.

[149] A. F. Möbius. *Der barycentrische Calcul*. Verlag von Johann Ambrosius Bart., Leipzig, 1827. Available online from the Bayerische Staatsbibliothek, `http://opacplus.bsb-muenchen.de/search?oclcno=166123133`.

[150] A. Mogilner. Mathematics of cell motility: have we got its number? *Journal of Mathematical Biology*, 58:105, 2009.

[151] A. Mogilner and L. Edelstein-Keshet. Regulation of actin dynamics in rapidly moving cells: A quantitative analysis. *Biophysical Journal*, 83:1237, 2002.

[152] A. Mogilner and G. Oster. Cell motility driven by actin polymerization. *Biophysical Journal*, 71:3030, 1996.

[153] A. Mogilner and G. Oster. The physics of lamellipodial protrusion. *European Biophysics Journal*, 25:47, 1996.

[154] A. Mogilner and G. Oster. Force generation by actin polymerization II: The elastic ratchet and tethered filaments. *Biophysical Journal*, 84:1591, 2003.

[155] C. Möhl. *Modellierung von Adhäsions- und Cytoskelett-Dynamik in Lamellipodien migratorischer Zellen*. Diploma thesis, Universität Bonn, 2005.

[156] C. Möhl. *Untersuchungen zur Adhäsionsdynamik migrierender Keratinozyten*. Doctoral thesis, Universität Bonn and Forschungszentrum Jülich, 2009. Available online from `http://nbn-resolving.de/urn:nbn:de:hbz:5N-18944`.

[157] C. Möhl, N. Kirchgeßner, C. Schäfer, B. Hoffmann, and R. Merkel. Quantitative mapping of averaged focal adhesion dynamics in migrating cells by shape normalization. *Journal of Cell Science*, 125:155, 2011.

[158] C. Möhl, N. Kirchgeßner, C. Schäfer, K. Küpper, S. Born, G. Diez, W. H. Goldmann, R. Merkel, and B. Hoffmann. Becoming stable and strong: The interplay between vinculin exchange dynamics and adhesion strength during adhesion site maturation. *Cell Motility and the Cytoskeleton*, 66:350, 2009.

[159] D. J. Montell. Morphogenetic cell movements: Diversity from modular mechanical properties. *Science*, 322:1502, 2008.

[160] W. A. Müller and M. Hassel. *Entwicklungsbiologie und Reproduktionsbiologie*. Springer, 2012.

[161] M. Muskat. The flow of fluids through porous media. *Journal of Applied Physics*, 8:274, 1937.

[162] W. Norris and P. G. M. Wallace. Oxypertine (Integrin): a study of its use in premedication. *British Journal of Anaesthesia*, 45:1222, 1973.

[163] C. Nüsslein-Volhard and E. Wieschaus. Mutations affecting segment number and polarity in Drosophila. *Nature*, 287:795, 1980.

[164] `http://www.octave.org`. Simulation language, versions 2.9, 3.0, and 3.2, 2007–2012. Most of the presented simulations have been implemented in Octave.

[165] L. Onsager. Reciprocal relations in irreversible processes I. *Physical Review*, 37:405, 1931.

[166] L. Onsager. Reciprocal relations in irreversible processes II. *Physical Review*, 38:2265, 1931.

[167] N. B. Ouchi, J. A. Glazier, J.-P. Rieu, A. Upadhyaya, and Y. Sawada. Improving the realism of the cellular Potts model in simulations of biological cells. *Physica A*, 329:451, 2003.

[168] S. B. Padrick and M. K. Rosen. Physical mechanisms of signal integration by WASP family proteins. *Annual Reviews of Biochemistry*, 79:707, 2010.

[169] S. P. Palacek, J. C. Loftus, M. H. Ginsberg, D. A. Lauffenburger, and A. F. Horwitz. Integrin-ligand binding properties govern cell migration speed through cell-substratum adhesiveness. *Nature*, 385:537, 1997.

[170] S. P. Palecek, A. F. Horwitz, and D. A. Lauffenburger. Kinetic model for integrin-mediated adhesion release during cell migration. *Annals of Biomedical Engineering*, 27:219, 1999.

[171] E. Palsson. A 3-D model used to explore how cell adhesion and stiffness affect cell sorting and movement in multicellular systems. *Journal of Theoretical Biology*, 254:1, 2008.

[172] E. Palsson and H. G. Othmer. A model for individual and collective cell movement in dictyostelium discoideum. *Proceedings of the National Academy of Sciences of the United States of America*, 97:10448, 2000.

[173] R. Pankov, Y. Endo, S. Even-Ram, M. Araki, K. Clark, E. Cukierman, K. Matsumoto, and K. M. Yamada. A Rac switch regulates random versus directional persistent cell migration. *Journal of Cell Biology*, 170:793, 2005.

[174] R. J. Pelham and Y.-L. Wang. Cell locomotion and focal adhesions are regulated by substrate flexibility. *Proceedings of the National Academy of Sciences of the United States of America*, 94:13661, 1997.

[175] A. E. Pelling and M. A. Horton. An historical perspective on cell mechanics. *Pflügers Archiv – European Journal of Physiologoy*, 456:3, 2008.

[176] S. V. Perry. When was actin first extracted from muscle? *Journal of Muscle Research and Cell Motility*, 24:597, 2003.

[177] R. Philips, J. Kondev, J. Theriot, and N. Orme. *Physical biology of the cell*. Garland Science, 2008.

[178] E. Pokorná, P. W. Jordan, C. H. O'Neill, D. Zicha, C. S. Gilbert, and P. Veselý. Actin cytoskeleton and motility in rat sarcoma cell populations with different metastatic potential. *Cell Motility and the Cytoskeleton*, 28:25, 1994.

[179] T. D. Pollard and G. G. Borisy. Cellular motility driven by assembly and disassembly of actin filaments. *Cell*, 112:453, 2003.

[180] E. Puklin-Faucher and M. P. Sheetz. The mechanical integrin cycle. *Journal of Cell Science*, 122:179, 2009.

[181] M. Radszuweit, M. Block, J. G. Hengstler, E. Schöll, and D. Drasdo. Comparing the growth kinetics of cell populations in two and three dimensions. *Physical Review E*, 79:051907, 2009.

[182] J. Ranft, M. Basan, J. Elgeti, J.-F. Joanny, J. Prost, and F. Jülicher. Fluidization of tissues by cell division and apoptosis. *Proceedings of the National Academy of Sciences of the United States of America*, 107:20863, 2010.

[183] M. Rauzi, P. Verant, T. Lecuit, and P.-F. Lenne. Nature and anisotropy of cortical forces orienting Drosophila tissue morphogenesis. *Nature Cell Biology*, 10:1401, 2008.

[184] A. J. Ridley. Rho GTPases and cell migration. *Journal of Cell Science*, 114:2713, 2001.

[185] M. Rocco, C. Rosano, J. W. Weisel, D. A. Horita, and R. R. Hantgan. Integrin conformational regulation: Uncoupling extension/tai separation from changes in the head region by a multiresolution approach. *Structure*, 16:954, 2008.

[186] B. Rubinstein, M. F. Fournier, K. Jacobson, A. B. Verkhovsky, and A. Mogilner. Actin-myosin viscoelastic flow in the keratocyte lamellipod. *Biophysical Journal*, 97:1853, 2009.

[187] B. Sabass, M. L. Gardel, C. M. Waterman, and U. S. Schwarz. High resolution traction force microscopy based on experimental and computational advances. *Biophysical Journal*, 94:207, 2008.

[188] A. Saez, A. Buguin, P. Silberzan, and B. Ladoux. Is the mechanical activity of epithelial cells controlled by deformations or forces? *Biophysical Journal*, 89:L52, 2005.

[189] C. Schäfer. *Analyse der Zellwanderung am Beispiel von Keratinozyten: Zusammenspiel von Filopodien, Krafterzeugung und Matrix-Sekretion.* Doctoral thesis, Universität Bonn and Forschungszentrum Jülich, 2010. Available online from `http://nbn-resolving.de/urn:nbn:de:hbz:5N-22233`.

[190] C. Schäfer, B. Borm, S. Born, C. Möhl, E.-M. Eibl, and B. Hoffmann. One step ahead: Role of filopdia in adhesion formation during cell migration of keratinocytes. *Experimental Cell Research*, 315:1212, 2009.

[191] G. Schaller and M. Meyer-Hermann. Multicellular tumor spheroid in an off-lattice Voronoi-Delaunay cell model. *Physical Review E*, 71:051910, 2005.

[192] S. Schaub, S. Bohnet, V. M. Laurent, J.-J. Meister, and A. B. Verkhovsky. Comparative maps of motion and assembly of filamentous actin and myosin II in migrating cells. *Molecular Biology of the Cell*, 18:3723, 2007.

[193] B. Schneid. *Simulation der Migration von Keratinozyten: mit Fokus auf zellinterne Aktin- und Myosin-Dynamik*. Bachelor thesis, Universität Bonn, 2012.

[194] R. Schuh, D. Vestweber, I. Riede, M. Ringwald, U. B. Rosenberg, H. Jackle, and R. Kemler. Molecular cloning of the mouse cell adhesion molecule uvomorulin: cDNA contains a B1-related sequence. *Proceedings of the National Academy of Sciences of the United States of America*, 83:1364, 1986.

[195] T. Schwann. *Microscopical researches into the accordance in the structure and growth of animals and plants*. Sydenham Society London, 1845. With appendix "Contributions to phytogenesis" by M. J. Schleiden, all available online from `http://vlp.mpiwg-berlin.mpg.de/library/data/lit28715/index_html`.

[196] S. Sivaramakrishnan, J. V. DeGiulio, L. Lorand, R. D. Goldman, and K. M. Ridge. Micromechanical properties of keratin intermediate filament networks. *Proceedings of the National Academy of Sciences of the United States of America*, 105:889, 2008.

[197] D. B. Staple, R. Farhadifar, J.-C. Röper, B. Aigouy, S. Eaton, and F. Jülicher. Mechanics and remodelling of cell packings in epithelia. *European Physical Journal E*, 33:117, 2010.

[198] M. S. Steinberg. Reconstruction of tissues by dissociated cells. *Science*, 141:401, 1963.

[199] M. S. Steinberg. Does differential adhesion govern self-assembly processes in histogenesis? Equilibrium conficurations and the emergence of a hierarchy among popoulations of embryonic cells. *Journal of Experimental Zoology*, 173:395, 1970.

[200] A. Stéphanou, M. Chaplain, and P. Tracqui. A mathematical model for the dynamics of large membrane deformations of isolated fibroblasts. *Bulletin of Mathematical Biology*, 66:1119, 2004.

[201] A. Stéphanou, E. Mylona, M. Chaplain, and P. Tracqui. A computational model of cell migration coupling the growth of focal adhesions with oscillatory cell protrusions. *Journal of Theoretical Biology*, 253:701, 2008.

[202] J. M. Stewart, W. R. Driedzic, and J. A. M. Berkelaar. Fatty-acit-binding protein facilitates the diffusion of oleate in a model cytosol system. *Biochemical Journal*, 275:569, 1991.

[203] F. B. Straub. Actin. *Studies from the Institute of Medical Chemistry University Szeged*, 2:3, 1942.

[204] R. Strohmeier and J. Bereiter-Hahn. Control of cell shape and locomotion by external calcium. *Experimental Cell Research*, 154:412, 1984.

[205] D. Sulsky, S. Childress, and J. K. Percus. A model of cell sorting. *Journal of Theoretical Biology*, 106:275, 1984.

[206] P. Suraneni, B. Rubinstein, J. R. Unruh, M. Durnin, D. Hanein, and R. Li. The Arp2/3 complex is required for lamellipodia extension and directional fibroblast cell migration. *Journal of Cell Biology*, 197:239, 2012.

[207] A. Szabo, E. Mehes, E. Kosa, and A. Czirok. Multicellular sprouting in vitro. *Biophysical Journal*, 95:2702, 2008.

[208] P. Taddei. Conics intersection. `http://www.mathworks.com/matlabcentral/fileexchange/28318-conics-intersection`, (November 3, 2010) presenting BSD-licensed Octave/Matlab code for intersecting two conics, accessed September 1, 2012.

[209] J. L. Tan, J. Tien, D. M. Pirone, D. S. Gray, K. Bhadriraju, and C. S. Chen. Cells lying on a bed of microneedles: An approach to isolate mechanical force. *Proceedings of the National Academy of Sciences of the United States of America*, 100:1484, 2003.

[210] T. Tauscher. *Zellkörper- und Zellranderkennung von migrierenden Keratinozyten durch iterative Näherungsverfahren.* Bachelor thesis, Universität Bonn, 2011.

[211] K. M. Taute, F. Pampaloni, E. Frey, and E.-L. Florin. Microtubule dynamics depart from the wormlike chain model. *Physical Review Letters*, 100:028102, 2008.

[212] D. L. Taylor, J. S. Condeelis, P. L. Moore, and R. D. Allen. The contractile basis of amoeboid movement i. the chemical control of motility in isolated cytoplasm. *Journal of Cell Biology*, 59:378, 1973.

[213] D. L. Taylor, Y.-L. Wang, and J. M. Heiple. Contractile basis of amoeboid movement vii. the distribution of fluorescently labeled actin in living amebas. *Journal of Cell Biology*, 86:590, 1980.

[214] J. P. Thiery, H. Acoloque, R. Y. J. Huang, and M. A. Nieto. Epithelial-mesenchymal transitions in development and disease. *Cell*, 139:871, 2009.

[215] D. W. Thompson. *Growth and form*. Cambridge University Press, 2nd edition, 1946.

[216] J.-Y. Tinevez, U. Schulze, G. Salbreux, J. Roensch, J.-F. Joanny, and E. Paluch. Role of cortical tension in bleb growth. *Proceedings of the National Academy of Sciences of the United States of America*, 106:18581, 2009.

[217] P. L. Townes and J. Holtfreter. Directed movements and selective adhesion of embryonic amphibian cells. *Journal of Experimental Zoology*, 128:53, 1955.

[218] R. T. Tranquillo and W. Alt. Stochastic model of receptor-mediated cytomechanics and dynamic morphology of leukocytes. *Journal of Mathematical Biology*, 34:361, 1996.

[219] S. Turner and J. A. Sherratt. Intercellular adhesion and cancer invasion: A discrete simulation using the extended Potts model. *Journal of Theoretical Biology*, 216:85, 2002.

[220] A. van Leeuwenhoek. Observations, Communicated to the Publisher by Mr. Antony van Leewenhoeck, in a Dutch Letter of the 9th of Octob. 1676. *Philosophical Transactions of the Royal Society*, 12:821, 1677.

[221] A. B. Verkhovsky, T. M. Svitkina, and G. G. Borisy. Self-polarization and directional motility of cytoplasm. *Current Biology*, 9:11, 1999.

[222] M. Vicente-Manzanares, X. Ma, R. S. Adelstein, and A. R. Horwitz. Non-muscle myosin II takes centre stage in cell adhesion and migration. *Nature Reviews Molecular Cell Biology*, 10:779, 2009.

[223] G. Voronoi. Recherches sur les paralléllοèdres primitifs. *Journal für die reine und angwandte Mathematik*, 134:198, 1908.

[224] J. H.-C. Wang and J.-S. Lin. Cell traction force and measurement methods. *Biomechanics and Modeling in Mechanobiology*, 6:361, 2007.

[225] T. R. Weikl, M. Asfaw, H. Krobath, B. Rozycki, and R. Lipowsky. Adhesion of membranes via receptor-ligand complexes: Domain formation, binding cooperativity, and active processes. *Soft Matter*, 5:3213, 2009.

[226] M. Weliky, S. Minsuk, R. Keller, and G. Oster. Notochord morphogenesis in Xenopus laevis: simulation of cell behavior underlying tissue convergence and extension. *Development*, 113:1231, 1991.

[227] M. Weliky and G. Oster. The mechanical basis of cell rearrangement. *Development*, 109:373, 1990.

[228] `http://wikipedia.org`. Various articles, in various languages, accessed 2007–2012. This web-based encyclopedia was used for reference purposes, as universal and easy-to-access collection of formulas, and for exploring basic concepts that are otherwise practically impossible to discover. Any information from `http://wikipedia.org` that was used in this thesis has been veryfied from conventional scientific publications like books and journal articles, each of which are separately listed in the present bibliography.

[229] C. A. Wilson, M. A. Tsuchida, G. M. Allen, E. L. Barnhart, K. T. Applegate, P. T. Yam, L. Ji, K. Keren, G. Danuser, and J. A. Theriot. Myosin II contributes to cell-scale actin network treadmilling through network disassembly. *Nature*, 465:373, 2010.

[230] P. W. Wiseman, C. M. Brown, D. J. Webb, B. Hebert, N. L. Johnson, J. A. Squier, M. H. Ellisman, and A. F. Horwitz. Spatial mapping of integrin interactions and dynamics during cell migration by image correlation microscopy. *Journal of Cell Science*, 117:5521, 2004.

[231] C. Wollnik. *Quantifying lamella and body dynamics in two-dimensional cell motility.* Diploma thesis, Universität Bonn, 2011.

[232] Y. Xiong, C.-H. Huang, P. A. Iglesias, and P. N. Devreotes. Cells navigate with a local-excitation, global inhibition-biased excitable network. *Proceedings of the National Academy of Sciences of the United States of America*, 107:17079, 2010.

[233] P. T. Yam, C. A. Wilson, L. Ji, B. Hebert, E. L. Barnhart, N. A. Dye, P. W. Wiseman, G. Danuser, and J. A. Theriot. Actin-myosin network reorganization breaks symmetry at the cell rear to spontaneously initiate polarized cell motility. *Journal of Cell Biology*, 178:1207, 2007.

[234] J.-M. Zahm, H. Kaplan, A.-L. Hérard, F. Doriot, D. Pierrot, P. Somelette, and E. Puchelle. Cell migration and proliferation during the in vitro wound repair of the respiratory epithelium. *Cell Motility and the Cytoskeleton*, 37:33, 1997.

[235] Y. Zhang, S. Sivasankar, W. J. Nelson, and S. Chu. Resolving cadherin interactions and binding cooperativity at the single-molecule level. *Proceedings of the National Academy of Sciences of the United States of America*, 106:109, 2009.

[236] J. Zimmermann, M. Enculescu, and M. Falcke. Leading-edge-gel coupling in lamellipodium motion. *Physical Review E*, 82:051925, 2010.

Thanks to ...

the Theoretical Biology group in Bonn for the stimulating working environment, Wolfgang Alt for overwhelming thrust, challenging problems and the calmness of the elder in face of the ardent demands of the younger, Rolf Klein for supervision and expertise on Voronoi diagrams, Klemens Rottner and Juan J. Velazquez for joining the interdisciplinary comittee evaluating this thesis, ...

my wife Annelene Wittenfeld, for proofreading this manuscript, checking the calculations and especially the continuous support, in particular during outbursts of productivity, my family in Beilngries, for sustaining me during significant parts of the writeup of this thesis, ...

Dagmar Bär, for teaching me the necessity and beauty of biological complexity, Eva Deinum, for ~~walking~~ flying discussions about life, the universe and everything, Adrian Klein, for showing me how science can be play, Markus Knappitsch, for casually bringing along the right books at the right time, and professional editing of the ECMTB issue, Esa Kuusela, for solid work to build upon, and the fabulous sofa, Christoph Möhl for the best keratinocyte movies, and stimulating discussions on various occasions, Christina Surulescu for the invitation to Stuttgart, Carina Wollnik for the best keratinocyte pictures ever, professional coauthoring of the ECMTB article, and the unstoppable smile, ...

G. Wayne Brodland for the insights of the engineer and open and enlighting discussions on the cell sorting problem, András Czirók for the quail cell micrograph, and insightful discussions on various occasions, Stephan Grill and Frank Jülicher for the invitation to Dresden, Carl-Philip Heisenberg for permission to reprint the sorting assay picture, Pirta Hotulainen for permission to reprint the stress fiber picture, Josef Käs for pointing me to the position in Bonn, the Käs-lab people for discussions on various occasions, Norbert Kirchgeßner for the invitation to Jülich, Stefan Koestler for stimulating discussions on actin polymerization, the group of Rudolf Merkel at Jülich, in particular David Kirchbüchler and Inka Lauter, Dietmar Ölz for the invitation to Knoxville, Thomas D. Pollard for his motivating yet humbling talk in Regensburg, and the permission to reprint the famous polymerization cartoon, Claudia Schaefer for the best keratinocyte movie ever, Eva-Maria Schötz for permission to extract data from the Zebrafish migrographs, Pierluigi Taddei, for sharing his conic intersection code, and pointing me to the Graphics Gems V book, Juliane Zimmermann and Anders Carlsson for discussions on the physics of actin polymerization, ...

the crowd at “BioMedMath 2008” in Middlefart, Denmark, the crowd at “MECO34 2009” in Leipzig, Germany, the crowd at “SoftFlow 2009” in Cargése, Corsica, France, the crowd at “VW 2009” in Mainz, Germany, the crowd at “Morphogenesis and Dynamics of Multicellular Systems 2009” in Heidelberg, the crowd at “The Physics of Cell Functionality 2010” in Beijing, China, the crowd at “Mechanics of Cell Motion 2010” in Oberwolfach, Germany, the crowd at “ColMot 2010” in Dresden, the crowd at “ECMTB 2011” in Krakau, Poland, the crowd at “VW 2012” in Potsdam, Germany, the crowd at “From Nonlinear Physics to Biology and Medicine 2012” in Cargése, Corsica, France, the crowd at “SMB 2012” in Knoxville (TN), USA the crowd at “Morphogenesis and Dynamics of Multicellular Systems 2012” in Heidelberg, Germany, the crowd at “Actin Dynamics 2012” in Regensburg, Germany, ...

the IZMB, in particular Frau Hertweck, Frau Marikar and the E-Labor, for mostly not noticing their highly appreciated hidden work, all other people that should be mentioned here but are not due to the insufficient capacity of my memory ...

the ECMTB and the BIGS for travel support, ...

the DFG for funding within the SFB 611 “Singular Phenomena and Scaling in Mathematical Models”, and finally the VolkswagenStiftung funding the two projects “Simulation models for cell motility” and “Simulation models for interactive cell motility”, both within the initiative “New conceptual approaches to modeling and simulation of complex systems”.